Simple and Low-cost Manufacturing of Customisable Drug Delivery Devices and Flexible Sensors for Biomedical Applications

Deck Khong Tan

Thesis submitted for the degree of
Doctor of Philosophy

School of Life Sciences
University of Sussex
Brighton, UK

April 2021

Acknowledgements

It would be impossible to finish the work presented in this thesis without the enormous help and support from many individuals.

Firstly, I would like to express my gratitude towards my main supervisor, Professor Ali Nokhodchi, as well as my co-supervisors, Dr. Niko Münzenrieder and Dr. Mohammed Maniruzzaman for giving me an opportunity to complete my PhD under their supervision. Their valuable suggestions throughout the years have helped me move forward to achieve this goal. I would also like to thank Alex Burns, who was the technical and administrative supervisor at the Chemistry department, for his help and support in sorting many of the administrative work.

I would be able to complete my research without the help and support from the members of Sensors Technology Research Centre at the School of Engineering. I would like to thank Júlio Costa for his help and support.

Many thanks to Dr. Qiao Chen, Dr. George Kostakis, Dr. Pascale Schellenberger and Dr. Manoj Tripathi for assisting and allowing me to use the various equipment that are available in their laboratories.

Finally, I would like to thank my parents and my wife for their love and continuous support.

Declaration

I hereby declare that this thesis has not been and will not be, submitted in whole or in part of another University for the award of any other degree.

Signature:

Abstract

In recent years, 3D printing technologies have been adopted into the medical and pharmaceutical industry for the fabrication of personalised medicines, oral dosage forms, medical implants, medical devices, tissue engineering applications, and many more. However, the use of 3D printing, in particular the low-cost Fused Deposition Modelling (FDM) 3D printing technique, has been limited due to the limited number of biocompatible materials suitable for pharmaceutical and biomedical applications. In this study, the FDM 3D printing technique was being explored for the fabrication of pharmaceutical products as it is the most widely available and easily accessible 3D printing technology.

In order to improve the usability of FDM 3D printing for pharmaceutical and biomedical applications, the studies to fabricate several different biocompatible filaments composition that can be used for drug loading were carried out. Firstly, filaments made of several pharmaceutical grade polymers were being developed using hot-melt extrusion (HME). Three types of biocompatible polymeric filaments have been developed. They are (Polylactic Acid) PLA-based, (Hydroxypropyl Cellulose) HPC-based and (Polycaprolactone) PCL-based. These filaments were added with a plasticiser, polyethylene glycol (PEG), to improve their processability and physicochemical properties of the produced filaments so that they can used in an FDM 3D printer. The HPC-based filaments were loaded with a model drug, theophylline, that exhibits poor aqueous solubility, whereas the PCL-based filaments were loaded with a readily soluble model drug, metformin. The studies showed that the filaments were effective in sustaining the release of both drug, and the sustain release properties of the filaments can be adjusted by altering the composition of the polymers.

The studies showed that the HME technology is very compatible with FDM 3D printing as it is able to produce 3D printable filaments by mixing different polymeric materials. The filaments can also be loaded with a desired drug at a required dose to allow the 3D printing of drug delivery systems. This technique allows the fabrication of personalised drug delivery systems in-house. It can be beneficial for clinics and hospitals in remote areas as the lead times can be reduced when in-house fabrication is possible. The ability to fabricate personalised medicines at hand also means that the dose can drug release patterns can be altered for the patients at any point of time when required. Apart from

that, this technique can change way medicines are transported and stored, which could potentially help save cost on transportation and inventory. In addition to medicines, the FDM 3D printing technique can also be used to produce other personalised drug delivery systems such as microneedles, braces and implants of various shapes due to the flexibility of the 3D printing process.

The other aspect of this research was on the fabrication of biomedical sensors that can potentially be integrated with the 3D printed drug delivery systems to form a smart drug delivery device. The idea of smart drug delivery device is that it is capable of continuous monitoring the health of a patient and then administer drug to the patient whenever it is required. The development of such smart medical devices has been one of the hottest interests in the biomedical sector. One of the main issues with such technologies is the high cost which has caused the technologies to be not so affordable for many people. Therefore, the studies to fabricate some simple biomedical sensors such as a temperature sensor and a glucose sensor using simple and cost-effective manufacturing technique were being explored. The fabrication techniques used are FDM 3D printing and a thin-film fabrication technique that involves deposition of material using a thermal evaporator. Low-cost manufacturing techniques were being explored in order to help reduce manufacturing cost which could help improve the affordability of such technologies. The fabricated temperature and glucose sensors exhibit great stability in performance and mechanical flexibility. The flexibility allows the sensors to be conformable to curved surfaces such as the skin. Hence, the sensors are suitable to be used as a wearable device or integrated into some other medical devices to form a smart medical device.

Table of Contents

Acknowledgements i
Declaration ii
Abstract iii
Table of Contents v
List of illustrations ix
List of tables xv
List of equations xviii
List of symbols and units xix
List of abbreviations xx
Chapter 1 : Introduction 1
1.1 Introduction to 3D printing 2
1.1.1 Types of 3D printing 3
1.1.2 FDM 3D printing for biomedical applications 11
1.2 Hot-Melt Extrusion (HME) 14
1.2.1 Hot-Melt Extrusion for Pharmaceutical Applications 21
1.3 Coupling HME with FDM 3D Printing 28
1.3.1 Pharmaceutical Dosage Forms produced using HME and FDM combined 30
1.3.2 Dosage Forms with Multiple Medications 34
1.3.3 Drug-loaded Implants Application 39
1.4 Sensors for Biomedical Applications 41
1.4.1 Examples of Smart Medical Implants 43
1.4.2 Temperature Sensing System 44
1.4.3 Glucose Sensing System 49
1.4.4 Flexible sensors 52
1.5 2D Materials 54
1.5.1 Exfoliation of TMDs layers 57
1.5.2 Molybdenum (IV) Sulphide (MoS_2) 59
1.5.3 Printing of LPE MoS_2 61
1.6 3D Printing of Sensor 63
1.7 Outline of the thesis 65
Chapter 2 : Research aim and objectives 67
2.1 Aim and objectives 67
2.1.1 Aim 68
2.1.2 Objectives 68

Chapter 3 : Investigation on the miscibility of polylactic acid and polyethylene glycols 71
3.1 Introduction 71
3.2 Materials 74
3.3 Experimental Methods 75
3.3.1 Preparation of PEG/PLA Films 75
3.3.2 Characterisation of PEG/PLA blends 75
3.4 Results and Discussion 76
3.4.1 Differential Scanning Calorimetry (DSC) 77
3.4.2 Thermogravimetric Analysis (TGA) 80
3.4.3 Fourier Transform Infrared (FTIR) 81
3.4.4 X-Ray Diffraction (XRD) 83
3.5 Conclusion 84
Chapter 4 : Preliminary study on preparing biocompatible PEG/PLA filaments using a single-screw filament extruder 85
4.1 Introduction 85
4.2 Materials 87
4.3 Experimental methods 88
4.3.1 Coating of the PLA pellets with PEG 88
4.3.2 Preparation of PEG/PLA filaments and pure PLA filaments 90
4.3.3 Differential scanning calorimetry (DSC) 90
4.3.4 Thermogravimetric analysis (TGA) 90
4.3.5 Fourier Transform Infra-Red (FTIR) 91
4.3.6 Mechanical testing of filaments 91
4.3.7 Sample printing using filament produced 92
4.3.8 Scanning Electron Microscopy (SEM) 92
4.4 Results and Discussion 92
4.4.1 Extrusion of filaments 92
4.4.2 Differential scanning calorimetry (DSC) 94
4.4.3 Thermogravimetric analysis (TGA) 97
4.4.4 Fourier Transform Infrared Analysis (FTIR) 99
4.4.5 Mechanical analysis 100
4.4.6 Printability of filaments 103
4.5 Conclusion 105
Chapter 5 : Twin-screw extrusion of PEG/PLA filaments 106
5.1 Introduction 106
5.2 Materials 108
5.3 Experimental Methods 108

5.3.1 Preparation of PEG/PLA films 108
5.3.2 Preparation of PEG/PLA filaments 108
5.3.3 Characterisation of filaments 109
5.4 Results and Discussion 110
5.4.1 Solvent cast films and extruded filaments 110
5.4.2 Diffrential Scanning Calorimetry (DSC) 112
5.4.3 Thermogravimetric analysis (TGA) 115
5.4.4 Fourier Transform Infrared Analysis (FTIR) 117
5.4.5 X-Ray Powder Diffraction (XRPD) 119
5.4.6 Mechanical analysis 120
5.5 Conclusion 122
Chapter 6 : Development and optimisation of novel polymeric compositions for sustained-released theophylline tablets via HME and FDM 3D printing 123
6.1 Introduction 123
6.2 Materials 125
6.3 Experimental Methods 125
6.3.1 Design and Fabrication of Tablet 126
6.3.2 Analysis of the Filament and 3D Printed Tablet 127
6.4 Results and discussion 129
6.4.1 Thermal Analysis 129
6.4.2 X-Ray Powder Diffraction (XRPD) 135
6.4.3 Mechanical properties 136
6.4.4 3D Printing 139
6.4.5 Scanning Electron Microscopy (SEM) 142
6.4.6 *In-vitro* Drug Release Study 144
6.4.7 Dissolution efficiency and kinetics 149
6.4.8 Biocompatibility study 154
6.5 Conclusions 155
Chapter 7 : Development of metformin-loaded filaments for 3D printing of sustained release drug delivery system 157
7.1 Introduction 157
7.2 Materials 161
7.3 Experimental Methods 161
7.3.1 Preparation of metformin-loaded filaments 161
7.3.2 3D printing process 162
7.3.3 Differential Scanning Calorimetry (DSC) 162
7.3.4 Thermogravimetric analysis (TGA) 163
7.3.5 X-ray Powder Diffraction 163

7.3.6 *In-vitro* Drug Release Study 163
7.4 Results and Discussion 164
7.5 Conclusion 171
Chapter 8 : Fabrication of flexible Resistance Temperature Detectors (RTDs) temperature sensors via FDM 3D printing and thin-film fabrication technology 173
8.1 Introduction 173
8.2 Materials 176
8.3 Experimental methods 176
8.3.1 3D printing of temperature sensor 176
8.3.2 Thin-film fabrication of flexible resistance temperature detectors (RTDs) 177
8.3.3 Characterisation of temperature sensors 179
8.4 Results and discussion 180
8.4.1 3D printed temperature sensors 180
8.4.2 Thin-film temperature sensors 188
8.5 Conclusion 193
Chapter 9 : Fabrication of a MoS_2-based thin-film glucose sensing device 195
9.1 Introduction 195
9.2 Materials 200
9.3 Experimental methods 200
9.3.1 Preparation of MoS_2 ink/dispersion 200
9.3.2 Deposition MoS_2 dispersion onto a glass slide 201
9.3.3 Fabrication of thin-film glucose sensor 201
9.3.4 Functionalisation of glucose sensing device 202
9.3.5 Characterisation studies 202
9.4 Results and Discussion 204
9.4.1 Viscosity testing of MoS_2 dispersion 204
9.4.2 Fabrication of glucose biosensor 210
9.4.3 Glucose sensing 213
9.5 Conclusion 217
Chapter 10 : Conclusions and future work 219
10.1 Summary of key findings 219
10.2 Suggestions for future work 223
Appendix: List of publications and conference proceedings 228
Bibliography 230

List of illustrations

Figure 1.1: Mechanism of a Fused Deposition Modelling (FDM) 3D printer (Reproduced with permission from reference [23]). 8

Figure 1.2: A schematic diagram of a typical hot melt extruder (Reproduced with permission from reference [99]) 15

Figure 1.3: Cross-section of a single and twin-screw extruder (Reproduced with permission from reference [99]) 16

Figure 1.4: Twin-screw extruder barrel (a) Counter-rotating screws (b) Co-rotating screws (Reproduced with permission from reference [111]) 19

Figure 1.5: Parameters of a screw in a hot-melt extruder. 21

Figure 1.6: Three different zones of a screw in an extruder: Feeding, compression/melting and metering zone. 21

Figure 1.7: Number of Hot-Melt Extrusion patents issued for pharmaceutical applications between year 1983 to 2006 (the data for chart is extracted from reference [118]) 22

Figure 1.8: Schematic of a combined Hot-Melt Extrusion (HME) and FDM 3D printing into a single continuous process (Reproduced with permission from reference [98]) 30

Figure 1.9: A 3D computer-aided design (CAD) model of capsule-shaped oral drug delivery device (**a**) multilayer device (**b**) two-compartment caplet (Duocaplet) (Reproduced with permission from reference [170]) 36

Figure 1.10: Two-compartment capsular device (**a**) compartments with the same wall thickness (**b**) compartments with different wall thickness (Reproduced with permission from reference [171]) 37

Figure 1.11: Schematic diagram explaining the working principle of a typical biosensor 43

Figure 1.12: A typical electromagnetic spectrum showing the types of electromagnetic waves and their respective wavelengths range (in m) 48

Figure 1.13: Schematic illustration of 2D graphene in honeycomb lattice structure (Reproduced with permission from ref [371]) 55

Figure 1.14: Transition Metal Dichalcogenides materials formed of transition metals (group 4-7) with elements in Chalcogen group (S,Se,Te) highlighted in a periodic table. (Reproduced with permission from ref [376]). 56

Figure 1.15: An illustration of a single layer of TMD material (Reproduced with permission from reference [379]) 56

Figure 1.16: Schematic representation of coordination of MX_2 stacking a) 2H-MX_2 Trigonal Prismatic b) 1T-MX_2 Octahedral (Reproduced with permission from reference [389]) 57

Figure 3.1: Process of producing polylactic acid (PLA) from lactic acid monomer (n is a large number). 72

Figure 3.2: Chemical formula for Polyethylene glycol (PEG), m represents the average number of oxyethylene group. 74

Figure 3.3: An example of dried PEG/PLA film produced from solvent casting. 77

Figure 3.4: DSC thermograms for different PEG/PLA films. 77

Figure 3.5: DSC thermograms for different grades of PEG 79

Figure 3.6: TGA profiles for different PEG/PLA films. 80

Figure 3.7: FTIR spectra for different PEG/PLA films. 81

Figure 3.8: Illustration of hydrogen bonding interaction between PLA and PEG molecules 83

Figure 3.9: XRD spectra for all PEG/PLA films 83

Figure 4.1: Images to show the original form of a) PLA pellets b) PEG 6000 88

Figure 4.2: Set-up of a Caleva mini coater for the coating of PLA pellets with PEG 89

Figure 4.3: Benchtop single-screw filament extruder (FilaFab extruder) 90

Figure 4.4 Texture analyser for mechanical testing a) set-up of tensile testing (before test) b) after tensile testing 91

Figure 4.5: Schematic diagram of cylindrical-shaped model for 3D printing a) front-view b) side-view. 92

Figure 4.6: SEM images of extruded filaments with different compositions a) S10, b) S20, c) S30, d) pure PLA filaments 93

Figure 4.7: DSC profiles for PEG, PLA pellets and different PEG/PLA pellets compositions. 94

Figure 4.8: DSC profiles comparison for different composition of PEG/PLA filaments, pure PLA filaments and commercially available PLA filaments. 95

Figure 4.9: TGA analysis for different compositions of single-screw extruded PEG/PLA filaments, pure PLA filaments and PEG 97

Figure 4.10: FTIR results for different compositions of PEG/PLA filaments, PLA filaments and PEG 99

Figure 4.11: Strength of all extruded PEG/PLA filaments compared with pure PLA filament and commercial PLA filaments 101

Figure 4.12: Cylindrical shaped object printed using different filaments a) 10% w/w PEG/PLA filament b) 20% w/w PEG/PLA filament c) 30% w/w PEG/PLA filament d) pure PLA filament e) commercial PLA filament 103

Figure 4.13: Image of a 3D printed cylindrical shape sample removed from the raft/base. 103

Figure 4.14: SEM images of the cylindrical shaped object printed using different filaments a) S10 filament b) S20 filament c) S30 filament d) pure PLA filament e) commercial PLA filament 103

Figure 4.15: Failed printing due to high printing temperature. PEG/PLA blend filaments were used. 105

Figure 5.1: a) Example of solvent cast PEG/PLA film, b) PEG/PLA films ground into powder form to be fed into the extruder c) twin-screw extrusion process of PEG/PLA filaments 112

Figure 5.2: DSC thermograms for solvent cast PEG/PLA films, PLA film and PEG .. 112

Figure 5.3: DSC for PEG/PLA filaments and pure PLA filaments produced using twin-screw extrusion 113

Figure 5.4: TGA profiles for a) solvent cast PEG/PLA films and PEG, b) extruded PEG/PLA filaments 115

Figure 5.5: FTIR spectra for PEG/PLA, pure PLA solvent cast films and PEG 6000 . 117

Figure 5.6: FTIR Spectra for twin-screw extruded PEG/PLA filaments 117

Figure 5.7: XRPD spectra for PEG/PLA blends, pure PLA and PEG 119

Figure 5.8: Mechanical strength of PEG/PLA filaments compared with pure PLA filament and commercial PLA filament measured using tensile testing 120

Figure 6.1: 3D CAD model of tablet for 3D Printing 127

Figure 6.2: DSC measurements for the pure substances used as powder blend for producing the filaments. The powders are Hydroxypropyl cellulose (HPC), Eudragit® RL PO powder, Polyethylene glycol (PEG) 6000, and anhydrous Theophylline 99+% 130

Figure 6.3: DSC Results obtained for Powder Mixture, HME Extruded Filaments and FDM 3D Printed Tablet 131

Figure 6.4: DSC analysis for theophylline-loaded filament with 2 heating cycles..... 133

Figure 6.5: Thermal degradation profiles for individual materials, powder mixture, extruded filament and 3D printed tablet 134

Figure 6.6: XRPD results for all individual powders, powder mixture, filament and 3D printed tablet 135

Figure 6.7: Stress-strain values from the tensile testing of all Theophylline-loaded filaments 138

Figure 6.8: Stress and strain values of the extruded filaments obtained from 3-point bending test 139

Figure 6.9: 3D printed tablet from the filament F2 a) top view b) side view 139

Figure 6.10: Quality comparison of good and poor quality 3D printed tablets a) F2 tablet on the left (good quality), F6 tablet on the right (poor quality) b) zoom in image of a, c) remnant of F6 tablet stuck on the printing bed after tablet has been removed 141

Figure 6.11: Failed filament during FDM 3D printing a) top view b) side view..... 142

Figure 6.12: SEM images of the powder mixture use for the extrusion of filaments (a-c) and theophylline (d-e) at different magnifications a) 100X b) 500X c) 500X d) 520X e) 1000X 142

Figure 6.13: SEM images of theophylline-loaded filament (a-b) and 3D printed tablet (c-f). a) Surface morphology of filament at magnification of 30X (top view), b) cross-section of filament at magnification of 100X, d) side-view of 3D printed tablet at magnification of 100X, e) side-view of 3D printed tablet at magnification of 250X, f) side-view of 3D printed tablet taken after dissolution at magnification of 100X. 143

Figure 6.14: Dissolution profiles for tablets from filament formulations F1, F2 & F3 144

Figure 6.15: Tablet change in size after drying after dissolution study 145

Figure 6.16: Cross-section image of tablet after (left) and before (right) dissolution .. 147

Figure 6.17: Schematic depiction of: a) IUPAC definition of "dissolution", b) dissolution of a solid drug particle in an aqueous liquid (Adapted with permission from reference [622]) 149

Figure 6.18: Cell count of biocompatibility study on day 0, day 1 and day 4. 155

Figure 7.1: Chemical structure of diabetic drug Metformin Hydrochloride (HCl)..... 158

Figure 7.2: Ring opening polymerisation of ε-caprolactone producing poly-ε-caprolactone (PCL) [671] 160

Figure 7.3: Chemical structure of polycaprolactone (PCL) [672] 160

Figure 7.4: DSC thermograms for all four metformin filaments and the bulk material used: Polycaprolactone (PCL), Hydroxypropyl cellulose (HPC), Eudragit® RL PO, Metformin HCl and PEG 6000 164

Figure 7.5: TGA profiles for all extruded metformin filaments and individual materials 166

Figure 7.6: XRD analysis on the 3D printed metformin tablets and their individual materials 167

Figure 7.7: In-vitro drug release study on the 3D printed metformin tablets 168

Figure 8.1: CAD model designed to be used for 3D printing of RTD sensors 177

Figure 8.2: Schematic diagram for the fabrication process of a thin-film temperature sensor via the lift-off method a) clean polyimide substrate, b) polyimide substrate spin coated with a layer of photoresist solution, c) mask with sensor structures aligned with polyimide substrate coated with photoresist for UV exposure, d) deposition of gold layer, e) removing of unwanted gold layer with uncured photoresist in an acetone bath to form sensor structures required on the substrate 177

Figure 8.3: Mask used for UV patterning of the RTDs structure for the fabrication of thin-film temperature sensor 179

Figure 8.4: 3D printed RTD sensors a) printed using conductive carbon black PLA b) printed using conductive graphene PLA 180

Figure 8.5: Voltage of -5V to 5V applied to obtain the obtain the current vs voltage of the 3D printed sensors 181

Figure 8.6: The change in resistance of the 3D printed temperature sensors as temperature increases from 15 °C to 80 °C 182

Figure 8.7: 5 cycles of resistance measurements from 20 °C to 40 °C for both 3D printed temperature sensors 183

Figure 8.8: Bending test on curved surface with a radius of a) 3.5 cm b) 2.55 cm 184

Figure 8.9: Change in resistance for 5 bending cycles of the 3D printed temperature sensors 185

Figure 8.10: Temperature sensing of different substrate surface at room temperature a) wood surface b) plastic surface 186

Figure 8.11: 3D printed temperature sensors attached on the outer surface of glass vial filled with water at 3 temperature points for temperature sensing 187

Figure 8.12: Images of the fabricated thin-film RTDs a) image of the whole film pattern with RTD structures in gold, b) zoom in image of a), c) enlarged image for the resistor structure on the left, d) enlarged image of the resistor structure in the centre, e) enlarged image of the resistor structure on the right 188

Figure 8.13: The average current vs voltage sweep and average resistance for a bunch of 10 thin film RTD strips 189

Figure 8.14: The I-V sweeps for a single thin film RTD strip at two different temperatures (room temperature and 45 °C) 190

Figure 8.15: The change in resistance of thin film RTDs as temperature increases from 15 °C to 80 °C 191

Figure 8.16: change in resistance for thin-film RTDs for cyclic test from 20 °C to 40 °C 192

Figure 8.17: Optical image taken after measurements 193

Figure 9.1: Schematic diagram of the fabrication of thin-film flexible electrochemical glucose biosensor made of gold/MoS_2/gold layer functionalised with glucose oxidase 201

Figure 9.2: MoS_2 ink/dispersion 205

Figure 9.3: Optical images of MoS_2 dispersion a) 4X magnification b) 10X magnification 205

Figure 9.4: Set up for conductivity measurement of prepared MoS_2 dispersion 206

Figure 9.5: I-V Sweep for the conductivity measurement of annealed MoS_2 in the presence of light and in dark environment 207

Figure 9.6: SEM images of MoS_2 after annealing a) magnification of 500X b) 2000X c) 10,000X 207

Figure 9.7: a) AFM image of spin coated MoS_2 layer on flexible substrate, b) Average height profile of the MoS_2 layer deposited in the rectangular region marked in (a) 209

Figure 9.8: TEM images of exfoliated MoS_2 flakes a) magnification: 3000X b) 30,000X, c) 80,000X 209

Figure 9.9: TEM of exfoliated graphene layer at a magnification of 10,000X 210

Figure 9.10: Microscopic images of the surface of glucose biosensors at 5X magnification. a) gold only (sample A), b) gold/MoS_2/gold glucose sensor (sample B). 211

Figure 9.11: AFM study on the surface of glucose biosensors for a) sample A, b) sample B 211

Figure 9.12: Conductivity measurement of the glucose biosensors 213

Figure 9.13: Cyclic voltammograms of the glucose biosensors 214

Figure 9.14: Amperometeric response of glucose biosensors upon addition of 1mM glucose solution to the electrolyte 216

Figure 10.1: Schematic diagram of an iontophoretic-based biosensor. The working electrode will be made of functionalised MoS_2 for biosensing application (adapted with permission from reference [346]) 225

List of tables

Table 1.1: The most commonly available 3D printing technologies 5

Table 1.2: Printing temperature, properties and applications of different thermoplastic materials used in FDM 3D printing. 10

Table 1.3: Advantages and disadvantages of single-screw and twin-screw extruder. 17

Table 1.4: Information obtained from different in-line process analytical technology (PAT) integrated with HME..... 26

Table 1.5: The different temperature sensing technologies and their applications..... 45

Table 3.1: Formulations of PEG/PLA for different PEG grades 75

Table 3.2: Glass transition temperature (Tg), melting temperature (Tm) and heat enthalpy value (ΔH) extracted from the DSC curves in Figure 3.4 for different PEG/PLA films 77

Table 3.3: Melting temperature and heat enthalpy value for different grades of PEG ... 79

Table 3.4: Temperature at three different degradation points extracted from TGA profiles for all PEG/PLA films..... 80

Table 3.5: Characteristic peaks/wavenumber of different PEG/PLA films..... 81

Table 4.1: Percentage of composition for the three PEG/PLA samples 90

Table 4.2: Glass transition temperature (T_g) and melting temperature (T_m) of pure PLA pellets and PEG/PLA pellets extracted from Figure 4.3. 94

Table 4.3: Glass transition temperature (T_g) and melting point (T_m) of different PEG/PLA blend filaments..... 97

Table 4.4: Temperatures at three degradation points (90%, 50%, 10% wt. remaining) for all compositions of filaments 98

Table 4.5: Strength of extruded filaments..... 100

Table 5.1: Composition of different formulations of PEG/PLA blends 109

Table 5.2: Extracted glass transition temperature (T_g) and melting temperature (T_m) and calculated heat enthalpy value (ΔH) for T_m from DSC curves 115

Table 5.3: Temperature at three degradation points (90%, 50%, 10% wt. remaining) for all compositions of films and filaments. 115

Table 5.4: Wavenumber for the several characteristics peaks extracted from FTIR spectra 117

Table 5.5: Values for the mechanical strength of PEG/PLA filaments, pure PLA filament, and commercial PLA filament 121

Table 6.1: The different ratios of (HPC : Eudragit : PEG : Theophylline) used for the fabrication of different filaments 126

Table 6.2: Temperatures at three degradation points (90%, 50%, 10% wt. remaining) for each individual component, powder mixture, extruded filament and 3D printed tablet 135

Table 6.3: Calculated strength of the Theophylline-loaded filaments from tensile testing 138

Table 6.4: Force, distance, stress and strain values extracted from 3-point bending tests for all filaments 139

Table 6.5: FDM printability and quality of all six theophylline-loaded filaments 141

Table 6.6: Change in mass of the dry tablets after dissolution studies 147

Table 6.7: Difference factor (f_1) for dissolution of tablets formulation F1-F5 151

Table 6.8: Similarity factor (f_2) for dissolution of tablets formulation F1-F5 151

Table 6.9: The four dissolution kinetic models used and their respective equations.... 152

Table 6.10: The Mean Percentage Error (MPE), Coefficient of determinations (R^2/RSQ), Diffusion exponent (n) of the calculated by fitting the dissolution profile in Table 6.7 to the different mathematical kinetic models 154

Table 7.1: Percentage of composition in different formulation of metformin-loaded filaments. The quantities are in percentage (w/w). 162

Table 7.2: Melting temperature (T_m) and the measured heat enthalpy value for melting extracted from the DSC profiles for all metformin filaments and individual materials 165

Table 7.3: Temperature at three degradation points (t90 = 90%, t50 = 50%, t`0 = 10% wt. remaining) for all filaments and the individual materials 167

Table 7.4: Difference factor (f_1) for dissolution of 3D printed metformin tablets 169

Table 7.5: Similarity factor (f_2) for dissolution of 3D printed metformin tablets 169

Table 7.6: The Mean Percentage Error (MPE), Coefficient of determinations (R2/RSQ), Diffusion exponent (n) of the dissolution profiles for all 3D printed metformin tablets when fitted to the different dissolution kinetic models 170

Table 8.1: Resistance measurement for the bending cycles of 3D printed temperature sensors at room temperature 184

Table 8.2: The resistance of the 3D printed temperature sensors when attached to wood and plastic as new substrate 186

Table 8.3: The resistance of 3D printed sensors when attached to the outer surface of a glass vial filled with water at 3 different temperatures 188

Table 9.1: Three different glucose biosensors prepared for comparisons 203

Table 9.2: Viscosity of MoS_2 Ink after the sonication process 204

Table 9.3: Surface roughness parameters of the glucose biosensors from AFM measurements R_a represents the arithmetic average of the absolute values of the surface height deviations measured from the mean plane, R_q represents the root mean square average of height deviation from the mean image data plane 212

Table 9.4: Reduction peak currents of glucose oxidase on the glucose biosensors during cyclic voltammetry 216

List of equations

(Equation 1.1)..... 50

(Equation 1.2)..... 50

(Equation 5.1)..... 121

(Equation 6.1)..... 150

(Equation 6.2)..... 150

(Equation 6.3)..... 152

(Equation 8.1)..... 181

(Equation 8.2)..... 182

(Equation 8.3)..... 185

(Equation 9.1)..... 197

(Equation 9.2)..... 197

(Equation 9.3)..... 212

(Equation 9.4)..... 212

(Equation 9.5)..... 216

(Equation 9.6)..... 216

(Equation 9.7)..... 216

(Equation 9.8)..... 216

List of symbols and units

A – Ampere

dL – Decilitre

°C – Degrees Celsius

ΔH – Change in heat enthalpy value

eV – Electron volt

fM – Femtomolar

GPa – Gigapascal

J – Joule

kg – Kilogram

kPa – Kilopascal

kV – Kilovolt

mg – Milligram

mL – Millilitre

mm – Millimetre

mM – Millimolar

MPa – Megapascal

µm – Micrometre

nm – Nanometre

nM – Nanomolar

Ω – Ohm

θ – Theta

wt% – Weighted percentage

X – Times

List of abbreviations

1T – Octahedral

2D – Two-dimensional

2H – Trigonal prismatic

3D – Three-dimensional

5-ASA – 5-aminosalicylic acid

6-MHA – 6 Mercaptohexanoic acid

.STL – Standard tessellation language

ABS - Acrylonitrile butadiene styrene

AFM – Atomic force microscopy

Ag – Silver

Ag/Cl – Silver chloride

Au – Gold

ALD – Atomic layer deposition

API – Active pharmaceutical ingredient

ATC – Acetyl triethyl acetate

CAD – Computer-aided design

CaSt – Calcium stearate

CAT – Computed axial tomography

CB – Carbon black

CGM – Continuous glucose monitoring

CGMP – Current good manufacturing practice

CJP – Colour jet printing

CNC – Computer numerical control

CNT – Carbon nanotube

Cu - Copper

CV – Cyclic voltammetry

CVD – Chemical vapour deposition

Df-NA – Diclofenac sodium

DIW – Direct ink writing

DLP – Digital light processing

DMF – Dimethylformamide

DNA – Deoxyribonucleic acid

DSC – Differential scanning calorimetry

e^- – Electron

EC – Ethyl cellulose

ECF – Enterocutaneous fistula

ECL – Electrochemiluminescence

EEF – European economic community

EMA – European medicines agency

EVA - Ethylene-vinyl acetate

FBG – Fibre bragg grating

f_1 – difference factor

f_2 – similarity factor

FAD – Flavin adenine dinucleotide

FDA – Food and drug administration

FDM – Fused deposition modelling

FET – Field effect transistor

FTIR – Fourier transform infrared

G – Graphene

GOx – Glucose oxidase

GRAS – Generally recognised as safe

H^+ – Hydrogen ion

H_2O – Water

H_2O_2 – Hydrogen peroxide

HfO_2 – Hafnium (IV) oxide

HME – Hot-melt extrusion

HPC – Hydroxypropyl cellulose

HPMC - Hydroxypropyl methylcellulose

HPMCAS – Hypromellose acetate succinate

I – Current

IPA – Iso-propanol

IUPAC – International union of pure and applied chemistry

IUS – Intrauterine system

IVR – Intravaginal ring

L/D – Length to diameter ratio

LENS – Laser engineered net shaping

LPE – Liquid phase exfoliation

min – minute

MoS_2 – Molybdenum disulphide

MPE – Mean percentage error

MRI – Magnetic resonance imaging

M.W. – Molecular weight

NIR – Near infrared

NMP – N-methyl-2-pyrrolidone

NW – Nanowire

O_2 – Oxygen

ODF – Orodispersible film

PAM – Pressure assisted microsyringe

PAT – Process analytical technology

PBS – Phosphate buffer solution

PCL – Polycaprolactone

PEEK – Polyether ether ketone

PEG – Polyethylene glycol

PEI – Polyether Imide

PLA – Polylactic acid

PLGA – Poly(lactide-co-glycolide)

PLLA – Poly(L-lactide)

POC – Point-of-care

PPE – Personal protective equipment

PSA – Prostate specific antigen

PU – Polyurethane

PVA – Polyvinyl alcohol

PVP – Polyvinylpyrrolidone

R – Resistance

RGO – Reduced graphene oxide

R^2 – Coefficient of determination

RPE – Retinal pigment epithelium

RPM – Revolutions per minute

RTD – Resistance temperature detector

S – Sulphur

Se – Selenium

Si – Silicon

SiO_2 – Silicon dioxide

SLA – Stereolithography

SLM – Selective laser melting

SLS – Selective laser sintering

SMP – Shape memory polymers

SR – Subcutaneous rod

T_{cc} – Cold crystallisation temperature

Te – Tellurium

TEC – Triethyl citrate

TFT – Thin-film transistor

TGA – Thermogravimetric analysis

T_g – Glass transition temperature

T_m – Melting temperature

TMD – Transition metal dichalcogenides

TNF-α – Tumour necrosis factor - alpha

TPU – Thermoplastic polyurethane

USP – United states pharmacopeia

UV – Ultraviolet

VDW – Van der Waal

WHO – World health organisation

XRPD – X-ray powder diffraction

Chapter 1 : Introduction

3D printing has received much interest across many industries due to its manufacturing flexibility as it is able to produce objects of any shapes and designs without the need of a mould. The biomedical industry has also benefited from this manufacturing flexibility, in particular for the manufacturing of personalised medicines and various customised medical devices [1,2]. Hence, the study here investigates the versatility of a low-cost 3D printing technology in producing personalised drug delivery systems when coupled with the hot-melt extrusion (HME) technology.

In recent years, there has also been increasing interest in integrating sensors with medical devices to make them smart medical devices. The purpose of the smart medical devices is to be able to detect and monitor the response of the human body at every single moment. These can often be in the form of wearable devices or implants. These devices can play a crucial role in the detection of any life-threatening conditions. Any medical implants integrated with sensors can be termed smart medical implants. Smart medical implants are able to improve the functionality and longevity of implantable devices. The function of the smart medical implants is to provide real-time information of any part the human body that is of interest. This information is very useful as it can help further improve the quality of life [3]. This is because patients can monitor their own health at any moment and they do not need to consult a healthcare professional all the time which would give them a peace of mind. The data collected on the smart medical device can be uploaded to a database which could also be accessed by the doctors in charge. The system can alert the doctor and patient when the condition of the patient needs attention. Smart medical implants being used as a sensing system also improves patient compliance. As the implant can be used to measure vital health information such as blood pressure, heart rate, body temperature or glucose level, the need for patient to attend appointments just to take some measurement can be avoided. This can also relieve the work pressure of healthcare professionals. Apart from that, even healthy people nowadays would like to monitor how their lifestyle affects their body which has resulted in the increased demand for health monitoring systems. Hence, the field of smart medical devices has been a hot research topic not just for academics, but also for healthcare and technology companies.

The core of these smart healthcare technologies relies on the sensors in the devices for them to function as purposed. Therefore, the reliability and affordability of the sensors

are vital for the function of these devices. The study here also investigates the feasibility of using 3D printing and a thin-film fabrication technique to produce simple biomedical sensors. The use of simple and low-cost fabrication techniques to produce reliable sensors can potentially improve of affordability of the sensors and healthcare technologies.

This chapter presents a literature review on several topics including the different 3D printing techniques used for biomedical applications, the latest developments on integrating HME with fused deposition modelling (FDM) 3D printing as a continuous process to produce various pharmaceutical dosage forms and implants, the use of sensors in biomedical application with a focus on temperature and glucose biosensors, the use of 2D materials for biosensors fabrication, with a focus on the use of Molybdenum (IV) Sulphide (MoS_2), and finally the 3D printing of biosensors. The general outline of the thesis is presented at the end of this chapter.

1.1 Introduction to 3D printing

3D printing, also commonly known as additive manufacturing, is a process that creates a three-dimensional object layer-by-layer from a digital model. The digital 3D models can be generated using computer-aided design (CAD) software or from 3D scanners that capture images of a real-life object and the image being converted into a printable file from a computer [4]. The first 3D printing technology, which is a stereolithography (SLA) method that uses a vat photopolymerisation process, was invented by Charles Hull in the early 1980s [5]. However, 3D printers were only widely available commercially in the early 2010s [6]. 3D printing is also known as rapid prototyping as it was primarily used for making prototypes during the early stages of this technology [7]. This is because 3D printing technology is very cost-effectiveness and has short a production time, where 3D objects can be made very quickly without needing any moulds. Therefore, it played an important role in product design and manufacturing across various disciplines as it is very useful for the design and testing phase in the development of a new product [8]. 3D printing has major advantages over traditional rapid prototyping processes, as the materials used in 3D printers are less expensive and it is able to provide a faster mode of iteration [6]. The rapid growth and improvement in the 3D printing technology have made it not just a rapid prototyping technique, but also a preferred production method in major industries [9–11]. Therefore, 3D printing is considered a very cost-effective manufacturing process, especially in producing objects with high complexity. It is now a preferred method to produce custom-designed objects, which could be very expensive

and time-consuming using conventional manufacturing techniques such as injection moulding, machining and casting [11–14]. Nowadays, 3D printing technology is being used across various industries including architecture [15], construction [16], automotive [17], food [18], fashion industry [19], medical sector [5] and many others. The 3D printing technology has gained much popularity in the healthcare and medical field not just for its cost-effectiveness but also for manufacturing flexibility. It is very useful in creating devices or medicine that are tailor-made for specific patients. The healthcare market in using 3D printing is expected to show significant growth due to the increasing demand for custom-tailored and patient-specific medical products. The ability of 3D printing to produce rapidly only with a CAD model, allows for on demand-fabrication, creating the possibility for medical devices to be produced in-house. Custom made prostheses, hearing aids and some implants have been successfully made using 3D printing technology. It can also fabricate the 3D constructs from a patient's own medical images, such as computed axial tomography (CAT) and magnetic resonance imaging (MRI) [20]. These parts could be very useful for surgeons to practice on before performing a surgery on the real patient, and can also be used as a guidance and explanation of the operation procedure to the patient [21].

1.1.1 Types of 3D printing

As the interest in using 3D printing across different industries is rapidly increasing, different 3D printing technologies have been invented to meet the demand of a wide range of industries. As the technology evolves, it is now possible to create 3D objects of any complex geometries that were previously difficult to make. There is now also a wide range of 3D printable materials, including some advanced materials such as high strength polymers, ceramics, metals, and composites. It is now possible to even 3D print a human organ by using cells as a printing material [22]. All the 3D printing technologies are different in terms of speed, resolution, and printing materials. The working principles will also differ according to the materials being used. The most commonly available 3D printing technologies are as shown in Table 1.1. However, not all 3D printing technologies are suitable for biomedical applications. For example, the direct energy deposition which involve the use of a high energy laser beam may be the main concern for pharmaceutical applications as the laser beam could potentially degrade the drug and pharmaceutical excipients [23]. On the other hand, inkjet-based, extrusion-based and

light-assisted 3D printing systems have successfully been used for bio 3D printing using biomaterials such as cells, biogels and polymers [24–31].

Table 1.1: The most commonly available 3D printing technologies

3D printing technologies	Working mechanisms	Materials	Example System	References
Vat Photopolymerisation	Uses ultraviolet or digital light for photopolymerisation process to cure light sensitive polymers (photopolymers). The molecules of the polymers will be crosslinked during the photopolymerisation process, forming a solid 3D object that does not dissolve in its liquid monomer	Photocurable resins	SLA, DLP	[32–36]
Powder Bed Fusion	Uses laser as a thermal source to induce partial or full fusion between the powder particles then a roller or blade is used to add and smoothen another layer of powder. The two main processes involve are sintering and melting	Polymer, metal, glass	SLS, SLM	[37–42]
Material Jetting	Deposits liquid droplets onto the printing bed to partially soften a layer of the material and solidifies to form a solid object.	Photopolymers, thermoset resins	Polyjet, Inkjet	[43–47]
Material Extrusion	Polymers being melted and pushed out through a heated nozzle, depositing the melted materials on top of each other, allowing each layer to bind with one	Thermoplastic polymers	FDM, PAM	[48–51]

	another, eventually forming a solid 3D object			
Direct Energy Deposition	High power-density laser is focussed onto a continuous stream of metal powders to melt the metal powders, fusing the melted powders together to form a 3D object	Metals including stainless steels, copper, aluminium, titanium, nickel, cobalt and tin	LENS	[52–54]
Binder Jetting	Liquid bonding agent deposited onto a powder bed to bind the powder particle together, forming a 3D object. Does not require support materials during 3D printing.	Ceramic, metal, glass, polymer	CJP	[55–58]

CJP = Colour Jet Printing

DLP = Digital Light Processing

FDM = Fused Deposition Modelling

LENS = Laser Engineered Net Shaping

PAM = Pressure Assisted Microsyringe

SLA = Stereolithography

SLM = Selective Laser Melting

SLS = Selective Laser Sintering

Most 3D printing technologies are still quite expensive and not easily accessible, particularly for technologies that can 3D print object with very high accuracy and resolution. The most easily accessible and affordable 3D printing technology is the material extrusion-based 3D printing. One of the most commonly available systems is Fused Deposition Modelling (FDM). FDM based 3D printers are so common that they are even found in homes for personal use. FDM is one of the 3D printing techniques that is available in open-source, which makes this technology the most affordable, as compared to others such as selective laser sintering (SLS), powder-based 3D printing, and stereolithography (SLA). Open-source means that all information related to the printer can be shared freely with the public and can be easily built by anyone, making it possible for anyone to have an FDM 3D printer as a common household object. RepRap is a 3D printing community that started the open source 3D printer revolution [59]. In FDM 3D printers, thermoplastic materials are typically used as the starting material. These thermoplastics materials that are fed into an FDM printer are usually in the form of a filament. The thermoplastic filaments are melted or softened, and then extruded from a printer head that is able to move in the x- and y-direction. The object is formed by many layers of melted thermoplastic. Each layer fuses and bonds to the layers below [60]. The layers of melted thermoplastic solidify almost immediately after being extruded from the print head. As one layer cools down and solidifies, another layer of the melted filament will be deposited on top of it until the printing of the object is finished (Figure 1.1). Due to the working principle of FDM, the resolution of the 3D printed object is often a limitation. This is because there is always a limitation on how thin the molten filaments can be extruded through the printing head. Currently, the highest resolution that an FDM 3D printer can achieve is 20 µm with a nozzle size of 0.4 mm by Robo 3D R2 (Robo 3D, San Diego, CA, US) [61].

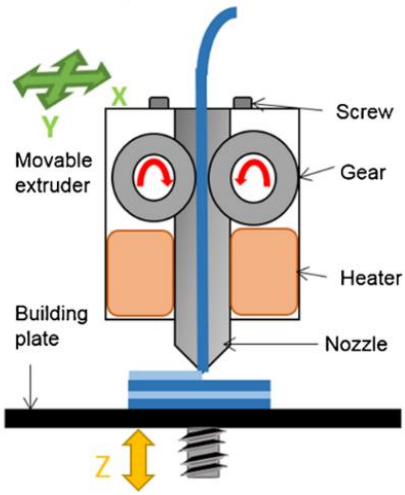

Figure 1.1: Mechanism of a Fused Deposition Modelling (FDM) 3D printer (Reproduced with permission from reference [23]).

Acrylonitrile Butadiene Styrene (ABS) and Polylactic Acid (PLA) are the two most common thermoplastics used in FDM machines [62]. One other commonly used biodegradable polymer in FDM 3D printing is polycaprolactone (PCL). Unlike ABS and PLA, PCL has much lower printing temperature (~60 °C) due to its low melting temperature and low glass transition temperature [63]. As a result, the printing of PCL often does not need a heated printing bed as the material can be easily softened in the presence of heat. PCL can sometimes be soft and flexible even at room temperature, making it a challenge to be 3D printed [64]. High performance thermoplastics such as Polyether Ether Ketone (PEEK) and Polyether Imide (PEI) are some of the newer thermoplastics that are currently used in FDM printers [65]. These materials usually have a very high melting temperature and excellent mechanical properties. They have been considered to be a cost-effective alternative to metal in some applications, as they are strong and also light [66]. PEI is a durable thermoplastic that exhibits physical properties such as high heat, solvent and flame resistance, high dielectric strength, thermal conductivity and overall strength. It has a lower impact strength and working temperature than PEEK [67]. Some of the PEI materials that are compatible with 3D printing have been used to produce plastic parts for aircraft [67]. Table 1.2 shows the comparison of different types of thermoplastics that are currently being used in FDM 3D printing. There are many challenges in using high-performance thermoplastics for FDM 3D printing due to their chemical and physical properties. As these materials possess very high melting temperature, the printing environment needs to be in a high temperature as well. This means that not just the extruder needs to be kept at the melting point of the material, but

that the printing chamber needs to be kept at an evenly distributed high temperature as well during the printing process. This is because any cool areas will cause the material to shrink unevenly, resulting in warping or even a lack of bonding in between the layers of the materials [67]. One of the 3D printers that has been successfully developed by a 3D printing company called INTAMSYS is the FUNMAT HT (Shanghai, China) is capable of printing various 3D printing materials including ABS, PLA, PEI, etc.[68].

Table 1.2: Printing temperature, properties and applications of different thermoplastic materials used in FDM 3D printing.

Thermoplastic Materials	**Acrylonitrile Butadiene Styrene (ABS)**	**Polylactic Acid (PLA)**	**Polycaprolactone (PCL)**	**Polyether Ether Ketone (PEEK)**	**Polyether Imide (PEI)**
Printing temperature (°C)	220–250	190–220	59-64	350–400	355–390
Properties	High strength, flexibility and durability	Biodegradable, biocompatible, brittle	Biodegradable, biocompatible, flexible, excellent impact strength and durability, low glass transition temperature and melting temperature	High mechanical strength, toughness, flexibility, chemical and radiation resistance, self-extinguishing properties	High specific strength (strength-to-weight ratio), flame resistance, chemical resistance
Applications	Pipe systems, automotive, toys, electronic casing	Biomedical, drug delivery systems, food packaging	Tissue engineering, bioprinting, food packaging, implants, drug delivery systems	Electronics, aerospace, automotive, mechanical and medical parts	Medical, chemical instruments, aerospace, automotive, electronics

Some post-processing might be needed for a 3D printed object using the FDM method as the surface finish of the object is often quite rough due to the layering of the melted thermoplastics. Acetone is often used to smoothen ABS so that it has a glossy finish. The 3D printed objects can also be machined or easily sanded after printing to smooth the surface [65]. It has been proven that some FDM 3D printed objects have similar mechanical properties as the objects that are manufactured using traditional injection moulding and machining when the same materials are being used. Therefore, FDM 3D printing can provide a cost-effective alternative for producing these parts. Some high-performance thermoplastics can also provide strength that is similar to metal parts. The advantage of using 3D printer thermoplastics over metal is that the thermoplastics products are much lighter than the metals. Some FDM printers have enhanced features such as having multiple printheads which allow for the printing of several different materials within an object.

1.1.2 FDM 3D printing for biomedical applications

In recent years, FDM 3D printing has been able to attract much attention for use in biomedical and pharmaceutical applications. It has been adopted by the biomedical and pharmaceutical industry as a manufacturing method due to its customisability, flexibility in design and the ability to create complex shapes with precision. FDM 3D printing has successfully been used to produce oral dosage forms [69,70], medical implants [71,72], scaffolds [73,74] and many other biomedical applications. The trend of using 3D printing to produce medicines started to gain much interest since the approval of the first 3D printed drug, Spritam® (levetiracetam), by the U.S. Food and Drug Administration (FDA) in 2015 [75]. However, this medicine is manufactured using the Zipdose technology based on a powder bed-liquid 3D printing technology [76]. In a powder-based 3D printer, a binder solution is required to bind the loose powder together. The binder solution is sprayed onto the successive layers of powder that is being deposited onto the print bed [23]. The traditional methods for producing medicines have very limited process capability and manufacturing flexibility when compared to 3D printing. By using 3D printing, there is much flexibility in designing the products, which can be personally tailored according to the patient's needs. For instance, tablets can be designed to have interesting and complex shapes which can be useful for the fabrication of paediatric medicines or modified-release systems [76,77]. Furthermore, tablets can be designed to contain several drugs that can have different drug release rates.

The research work done by Sadia *et al.* has been able to produce a novel design of a tablet that could accelerate drug release of 3D printed tablets. The 3D printed tablets are made of polymethacrylate and are designed to have built-in channels within the tablet that could increase the surface area/volume ratio of the tablet and also allow media perforation through the structure [77]. The study carried out by Goyanes *et al.* has also proven that the FDM 3D printing technology is feasible for fabricating personalised tablets containing drug doses tailored to individual patients or tablets with specific drug-release profiles [78]. Apart from that, some research work has been carried out on the possibility of housing multiple medications within a dosage form. This multi-active solid dosage form is called 'polypill'. The 'polypill' can also be designed with having different release profiles [70]. One way to achieve this is by changing the exposed surface area or the geometry of the dosage form and by using more than one kind of carrier with different release characteristics. The external shape and volume/mass ratio of a 3D printed tablet can affect the release profile and pattern. The percentage of infill that can be set during the 3D printing process is one of the parameters that can also affect the drug release patterns [77,79]. Thus, 3D printing has opened up the possibility of combining multiple medications in a personalised tablet. This is particularly useful for patients that are currently taking multiple medications through many separate tablets. Besides that, there is also a flexibility to tailor a specific drug combination or drug release profile according to the patient's needs. Therefore, 3D printing is able to fabricate these personalised medicines in a very timely and cost-effective manner.

Apart from using FDM 3D printing to produce oral dosage forms, it has also successfully been used in the medical field for medical modelling, surgical planning and the production of patient-specific implants [5]. Doctors have been using 3D printed models to educate patients, provide surgical training as well as planning the surgical approach [80]. This would help increase the surgery success rate, decreasing any surgical complications during real surgery and reduces the need for intervention [81]. The practice of using 3D printed model for training has been implemented in Spain to train general practitioners (GPs) to carry out minor surgeries [82]. This will reduce the cost of the training by eliminating the need for training on animals. The CAD models that are required for 3D printing can also be easily taken using CT or MRI, which would also provide a better representation of the patient as compared to animal models. Due to the cost-effectiveness of FDM, it has also successfully been used for surgical planning to

reconstruct patients suffering from rhinocerebral mucormycosis [83]. A facial scan of the patient was used to produce an anatomic model using FDM 3D printing that can help the surgeon to plan the free flap reconstruction. This study has shown how the low-cost FDM 3D printer can have a positive impact on the medical field.

It was also reported that FDM 3D printing has been a cost-effective way to produce medical implants. Domínguez-Robles *et al*. reported a study on using an FDM 3D printer to fabricate thermoplastic polyurethane (TPU) vaginal mesh loaded with an antibiotic as an alternative to conventional polypropylene vaginal mesh for the treatment of pelvic organ prolapse or stress urinary incontinence [84]. This study showed the versatility of 3D printing as an alternative when conventional treatments are showing complications. The group also produced PLA/Lignin mixture as an FDM 3D printing material that can potentially be used to 3D print meshes for wound dressing purposes owing to the antioxidant capability of lignin [85]. Fu *et al*. have used FDM 3D printing to produce sustained release progesterone-loaded vaginal rings as a gynaecology drug delivery device [71]. The drug showed release lasting up to 7 days which is more effective than oral administration. Different shapes of vaginal rings have been 3D printed, proving the flexibility and ability of 3D printing to produce custom-shaped products, which could also result in drug release patterns.

A study by Huang *et al*. has successfully 3D printed a fistula stent which was designed from the 3D reconstruction of the patient's fistula image [86]. The stent was fabricated using biocompatible thermoplastic urethane, which is also a material that has been widely used in medical devices such as catheters and vascular grafts [87]. The purpose of the 3D printed stent was to manage enterocutaneous fistula (ECF), which is an abnormal or unintentional connection between the gastrointestinal tract and the skin of a patient. Kim and Lee reported the possibility of fabricating shape transformable bifurcated stents using FDM 3D printing of shape memory polymers (SMPs) that can change its shape as a response to external stimulation [88]. The study reported a 3D printed kirigami structure stent that can travel smoothly in the blood vessel when its initial shape was folded into a compact shape. As the stent reaches the target location, the stent was then activated to expand into its original form, holding up the narrowed blood vessels. This approach is believed to be able to improve the success rate of stent insertion.

FDM 3D printing has also been used extensively in the hearing aids and implants industry [20]. This is because ear canals and shapes are often different from one to another and

these devices would need to be custom made to fit the patient properly. 3D printing has shown to be to the most cost-effective way of producing individualised devices. The shape of the patient's ear is often captured using a 3D scanner. The image will then be translated to an STL file for 3D printing. The advancement in 3D medical imaging techniques has allowed the production of more patient-specific medical implants such as dental implants, prosthetics, hip, knee, etc [89]. The 3D imaging technologies can be coupled with 3D printing technologies to produce any patient-specific devices effectively and locally.

FDM 3D printing can also be used in tissue engineering applications. A study by Khodaei *et al.* produced a porous PLA scaffold that can potentially be used for bone tissue engineering using FDM 3D printing [90]. The study compared the mechanical strength of the scaffold at different porosity level, showing that increasing porosity caused a reduction in the strength of the scaffold. Monshi *et al*. have also used FDM 3D printing to produce electroconductive PLA scaffolds for bone cancer therapy applications [91]. Producing scaffolds through FDM 3D printing allows the flexibility in controlling the desired porosity of the scaffolds which is important particularly for bone tissue engineering. Rajzer *et al*. have successfully 3D printed antibacterial polycaprolactone/graphene scaffolds for growing chondrocytes using FDM 3D printing [74]. Studies have shown that graphene exhibit antibacterial ability and can be effectively incorporated into a polymer matrix [92–94].

Even during the Covid-19 pandemic, FDM 3D printers has played a very important role in producing personal protective equipment (PPE) such as face mask and shields for medical staff dealing with infected patients [95,96]. There are also reports that some 3D printing enthusiasts have used 3D printer to produce parts and valves for ventilators as well as respirators [97]. This campaign has been initiated by the public as hospitals across the world are facing a shortage of PPE. Although there have been doubts on how medically safe and compliant these 3D printed devices are, there is no doubt on the flexibility and versatility on producing any desired parts cost-effectively and locally using FDM 3D printing.

1.2 Hot-Melt Extrusion (HME)

The hot-melt extrusion (HME) technology was established in the early 1930s and was originally used for the manufacturing of plastics and rubber products [98]. It is a

continuous process where heat and pressure are applied to melt or soften materials through an orifice to produce new products of uniform shape and density. The extrusion process can change the physical properties of a substance when it is being forced through an orifice or die on the hot-melt extruder under controlled conditions [99]. The main component of HME is the extruder. Some of the basic elements that are assembled to make an extruder include a motor, an extrusion barrel, rotating screws in the barrel and a die or orifice that is connected at the end of the extruder [99]. The extrusion barrel containing the rotating screws is often made up of several sections that are bolted together. The extruder contains heaters that provide heat for the melting or softening of the materials. The screws in the extruder can provide shear stress and intense mixing of the materials. The friction created by the screws in the barrel and the heat provided cause the polymeric material to melt. The screw then conveys the melted material down the barrel. The extruder is controlled through a central electrical control, which is connected directly to the extrusion unit. Some of the processing parameters that can be controlled are screw speed in revolutions per minute (RPM), feed rate, temperature along the barrel and the die, and the vacuum level for devolatilization. A schematic diagram of a typical extruder is illustrated in Figure 1.2.

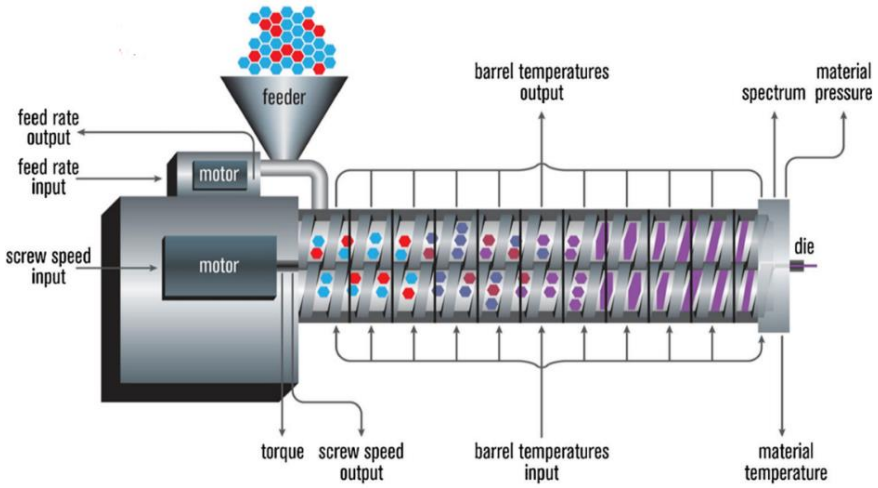

Figure 1.2: A schematic diagram of a typical hot melt extruder (Reproduced with permission from reference [99]).

In general, there are two types of hot-melt extruders: the single-screw extruder and twin-screw extruder (Figure 1.3). Some of the advantages and disadvantages of the single-screw extruder and the twin-screw extruder are compared in Table 1.3. The primary purpose of a single-screw extruder is to melt polymers and extrude them into a continuous shape. In the single screw extruder, there is only one screw in the extruder, which is used

for feeding, melting, devolatilising and pumping [100]. Materials are fed into the extruder from the feeder/hopper and then transported down the barrel using the screw. Most single screw extruders are flood fed, which means the feeder sits over the feed throat and the speed of the screw determines the output rate. Occasionally, the single screw extruder can also be starve fed, where a feed system sets the mass flow rate and the output rate is independent of the screw speed [100]. When the extruder is starve fed, it is fed at a rate less than the forwarding efficiency of the screws [101]. When the screw rotates in the extruder barrel, frictional forces are created between the rotating screw and the surface of the barrel, forming a flow channel that is responsible for transporting the material fed down the barrel to the proximal end of the screw [99]. Increasing the screw speed can increase the frictional forces created, resulting in higher heat energy created. The shearing caused by the rotating screw and the heat energy produced from the heaters will melt the material, which will then result in a melt pool of the material. The molten material will then be pumped through a die, which will give a fixed shape that forms the extrudate [100]. However, high pressure may be created during the melting process in a single-screw extruder. The high pressure will compress the dispersed particulates in the molten material, which could cause agglomeration and poor mixing due to insufficient shear deformation.

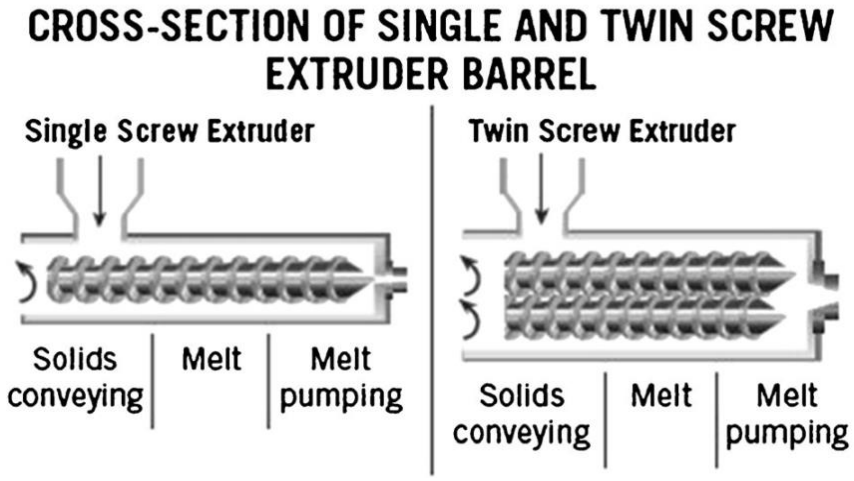

Figure 1.3: Cross-section of a single and twin-screw extruder (Reproduced with permission from reference [99]).

Table 1.3: Advantages and disadvantages of single-screw and twin-screw extruder.

Type of Extrusion	Advantages	Disadvantages
Single-screw extrusion	• Mechanical simplicity • Low maintenance • Low cost	• High tendency of overheating • Not suitable for heat-sensitive materials • Poor mixing
Twin-screw extrusion	• Easier material feeding • Higher kneading and dispersing capacity • Lower tendency to overheat • Higher process productivity and flexibility • Better control of process parameters • Enhanced mixing	• High input energy • Not suitable for shear-sensitive materials

On the other hand, the twin-screw extruder uses two screws arranged side-by-side in the barrel. The twin-screw extruder is used mainly for the purpose of mixing two or more materials together to form a blend. The additional materials that could be melted and mixed with polymers are, for example, pigments (e.g., iron/chromium oxide [102]), fillers (e.g., lactose, starch [103]), APIs (e.g., acetaminophen [104]) and plasticisers (e.g., polyethylene glycols, Triacetin [103]) [105]. Most of the time, a twin-screw extruder will be starve fed with the raw materials. This means that the output rate of the extrudates will depend on the feeder and independent of the screw speed [106]. In a twin-screw extruder, the screws can either be co-rotating (screws rotate in the same direction) or counter-rotating (screws rotate in the opposite direction) (Figure 1.4). The counter-rotating screws can produce very high shear forces as the materials are squeezed into the gaps between the two screws [100]. These two types of twin-screw extrusions can further be classified into fully intermeshing or non-intermeshing. The fully intermeshing twin-screw extruder has a special self-cleaning feature, which can help reduce the non-motion during the extrusion process and also prevents localised overheating of the raw materials when inside the extruder. This is because the raw materials do not rotate along the screw in the configuration of the intermeshing screws. The flight of one of the screws will be able to clean the root of the adjacent screw, removing all the materials away from the extruder assembly during the extrusion process. This can also reduce any product waste that could happen at the end of a production batch. The non-intermeshing extruder has a weaker screw interaction and lower self-cleaning capability, making it not as popular as the intermeshing screws for material mixing applications. The non-intermeshing screws are

often used to process highly viscous materials and can be used to remove large amounts of volatile substances. The non-intermeshing screws are positioned separately from each other, resulting in a lower torque generation, which is suitable for processing highly viscous materials [99].

For twin-screw extruders, the shearing of the materials occurs between the rotating screws and between the screws and the wall of the barrel. The torque and shear created by the rotating screws produce heat energy that is used to melt the materials. When the melted material is being squeezed between the gaps of the rotating screws, it is being continuously stretched like a rubber band, causing viscous heating dissipation to occur [106]. The heat generation in a twin-screw extruder is independent of the screw speed. The configurations of the twin screw can be adjusted depending on the desired level of shear and mixing. This means that there is better control of the melting of the materials in a twin-screw extruder. Hence, there is a lower tendency of overheating, which is particularly useful when processing heat-sensitive materials [99].

The main feature of a twin-screw extruder is the enhanced and homogeneous mixing of materials during extrusion. During twin-screw extrusion, two types of mixing can occur (a) distributive mixing and (b) dispersive mixing. Distributing mixing involves melt division and recombination. This means that the materials can be evenly blended with minimal degradation. Apart from that, the size of the materials is reduced in distributive mixing. Distributive mixing allows for the use of heat and shear sensitive materials such as APIs. Dispersive mixing involves shear and elongational mixing [106]. It induces solubilisation of one component to another component. Dispersive mixing breaks down the droplet or solid materials to fine particles using high energy. The enhanced mixing feature in the twin-screw extruder contributes to the viscous heat dissipation. These make the twin-screw extruder more efficient in heating the materials, and hence, it can readily process thermoplastic polymers [106]. Some other advantages of a twin-screw extruder over a single-screw extruder are easier material feeding, high kneading and dispersing capabilities, lower tendency of overheating and shorter transit time [99]. As twin-screw extrusion provides uniform and homogeneous mixing, the twin-screw extrusion process can be easily scaled up and optimised. The possibility of scaling up the extrusion process makes it a more efficient process for large volume production. Therefore, the majority of the food and plastics industries have been using twin-screw extrusion for their production [107–109]. Apart from that, twin-screw extrusion has also been adopted as a

manufacturing process in the pharmaceutical field [110]. However, there might be an issue for pharmaceutical industry when it comes to the development of a formulation containing some expensive drug/material.

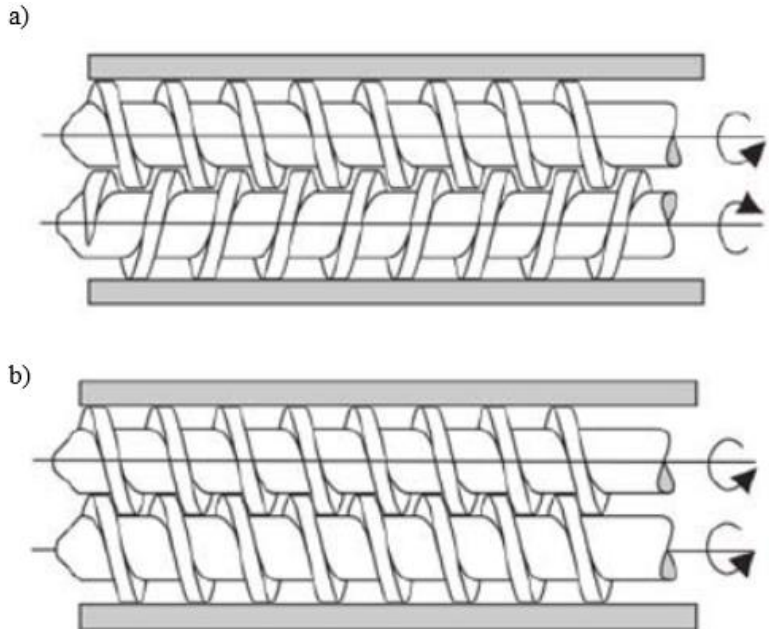

Figure 1.4: Twin-screw extruder barrel (a) Counter-rotating screws (b) Co-rotating screws (Reproduced with permission from reference [111]).

The screw in the hot-melt extrusion process is very important in determining the mixing and extrusion process. Figure 1.5 shows the parameters of a typical screw used in a hot-melt extruder. The dimensions of the screws are normally defined in length-to-diameter (L/D) ratio. Most screws are coated with stainless steel which could reduce friction and avoid chemical reactions with the raw materials. The screw is typically divided into three sections along the length of the barrel: the feed section, melting/compression and metering (Figure 1.6). At the feed section, the screw transfers the materials from the hopper to the barrel. The screw in the feed section has flights that are deeper or of a greater pitch, and the channel depth is also wider. This allows for the raw material to fall easily into the screw for conveyance along the barrel and to facilitate mass flow. The pitch and helix angles determine the output of the extruder at a constant screw speed. The solid raw materials are then conveyed to the compression zone for mixing, compressing, melting and plasticising. The channel depth decreases the compression zone in order to increase the pressure in the barrel which could remove any entrapped air. The polymers will then soften and melt in the compression zone. As the material enters the metering zone, the material should be in a molten state. The metering section is to reduce the pulsating flow and to ensure a uniform delivery rate through the die [99,100].

The last section of the extruder is the die or orifice. The function of the die is to shape the molten material when it is exiting the extruder. It is designed to achieve the required shape and dimensions of the extrudate. The cross-section of the extrudate will increase upon leaving the die and this phenomenon is known as “die swell” [100]. This phenomenon depends on the viscoelastic properties of the polymers [112]. In general, there can be four different shapes for products made by extrusion dies including the extrudate strands, films, sheets and granules [99].

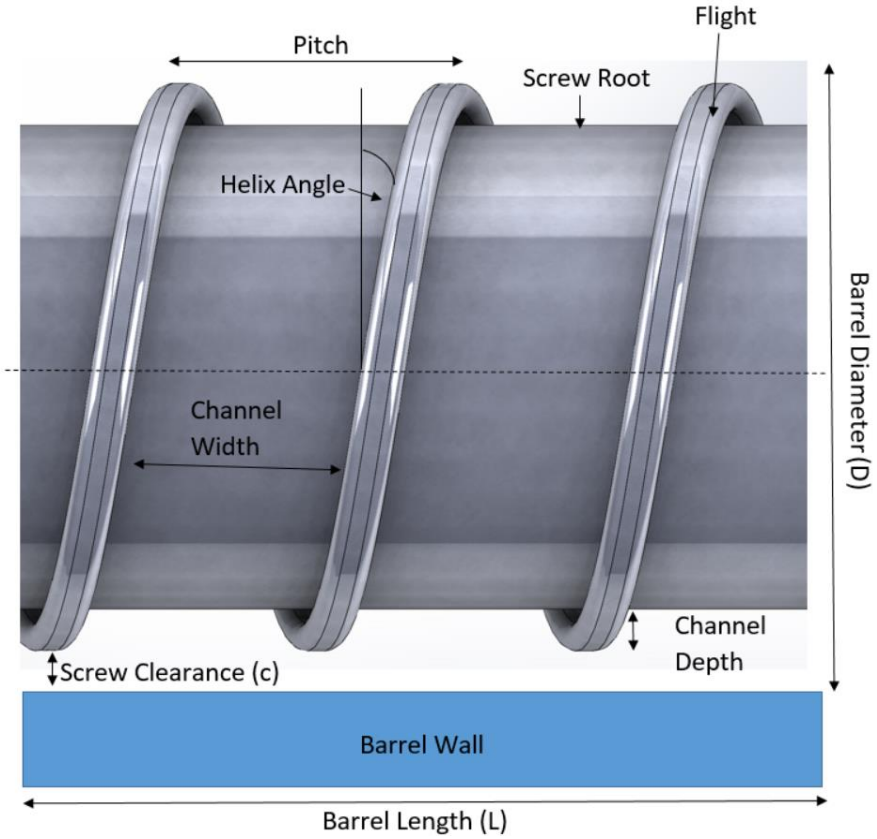

Figure 1.5: Parameters of a screw in a hot-melt extruder.

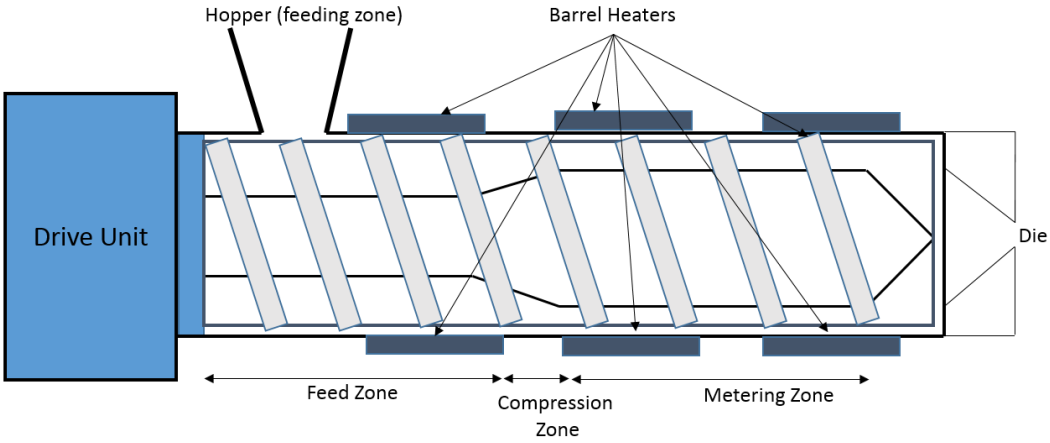

Figure 1.6: Three different zones of a screw in an extruder: Feeding, compression/melting and metering zone.

1.2.1 Hot-Melt Extrusion for Pharmaceutical Applications

Hot-melt extrusion has now emerged as a technology that plays an important role in the production of novel pharmaceutical products in the pharmaceutical industry [113]. Due to its efficiency in mixing and the increasing demand from the regulatory bodies to implement continuous manufacturing processes on the production of pharmaceutical products for better quality control, the HME technology has received much attention from the medical and pharmaceutical industry for the production of

pharmaceutical dosage forms and medical implants [106] [114]. One of the greatest advantages of using HME for pharmaceutical applications is that the process does not require the use of any organic solvents which could then eliminate the possibility of chemical degradation or toxicity caused by the presence of residual solvents after the extrusion process [115]. This technology is also more environmentally friendly as it does not use any organic solvent. Apart from that, HME is a versatile technology in term of its scalability and its ability to integrate with other technologies and process analytical tools for product quality control [116,117]. The number of HME patents issued for pharmaceutical applications has increased significantly since the 1980s (Figure 1.7) [118]. This is because the HME process is able to meet the regulatory requirements in the manufacturing process of dosage forms and also have large flexibility, particularly for the increasing demand for personalised medicines. Regulatory bodies such as the U.S. Food and Drug Administration's (FDA) encourages manufacturing processes that involves process analytical technology (PAT) in order to enhance product and process understanding. The initiative of PAT is to closely monitor some key parameters during the manufacturing process which could help to optimise design, analysis and control within the manufacturing process [101,112,119]. This can be demonstrated and fulfilled in the HME process.

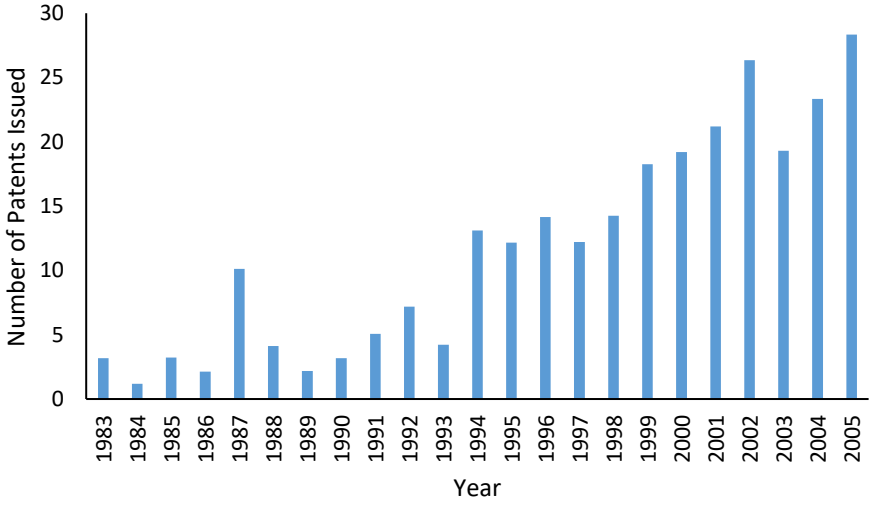

Figure 1.7: Number of Hot-Melt Extrusion patents issued for pharmaceutical applications between year 1983 to 2006 (the data for chart is extracted from reference [118]).

During the hot-melt extrusion process of pharmaceutical dosage forms, APIs, thermoplastic polymeric carrier and processing aids such as plasticisers and antioxidants,

are heated and mixed in the extruder and then being forced through a die into shapes including granules, cylinder or films [120–124], In recent years, much work has proven that HME has the ability to improve the solubility and bioavailability of poorly soluble drugs [125–127]. HME can produce a formulation known as the solid dispersion, where the bioavailability poorly water-soluble APIs can be improved in such formulations. Several studies have shown that the solid dispersion technique has successfully improved the bioavailability of poorly soluble APIs such as Ritonavir, Troglitazone, Anacetrapib, Suvorexant [98,125]. A solid dispersion is a system where one or more APIs are molecularly distributed into a hydrophilic inert carrier matrix. The matrix can either be crystalline or amorphous, and the APIs will be dispersed molecularly in crystalline particles or amorphous particles [99,128]. In the early 1990s and 2000s, the Rezulin® and Kaletra® tablets have been successfully produced using the HME process, which have shown improved bioavailability. These two tablets were produced using twin-screw extrusion as it can provide homogeneous and consistent mixing of multiple ingredients [106]. Since then, the HME process, and in particular, the twin-screw extrusion, has gained much popularity in the pharmaceutical industry.

The powerful processing technology of HME has also attracted much attention in developing different types of drug delivery systems, as it has opened up the opportunity to use some of the molecules that were previously deemed not suitable to be made into pharmaceutical dosage forms [118]. Its ability and efficiency in producing solid dispersions has also made it possible for the development of sustained, modified and targeted drug delivery systems. The different drug release systems can be achieved by controlling the formulations and the processing parameters when using HME [99].

As seen is some early studies, HME has been used to develop sustained release matrix mini-tablets manufactured from ethylcellulose, HPMC and ibuprofen [129,130]. Vegetable calcium stearate (CaSt) was also seen reported in the development of sustained release pellets using as a thermoplastic excipient [131]. A microbicide intravaginal ring (IVR) was also prepared and developed from polyether urethane (PU) elastomers for the sustained delivery of UC781 [132]. There has been also a study where HME was used to produce sustained-release solid lipid matrices of diclofenac sodium (Df-Na), and the extruded products were being compressed into tablets [133]. A lipophilic excipient, Glyceryl dibehenate (Compritol 888 ATO (C-888)) was used for the development of Df-NA sustained-release lipid matrices. The purpose of the study is to investigate the effects

of some parameters (e.g., extrusion temperatures, formulation composition, drug-lipid ratio) on the drug release behavior. It is found that Df-Na can either be in the crystalline or amorphous state depending on the processing conditions. The dissolution rate is affected by the drug–lipid ratio and the extrusion temperatures. There was an excellent distribution of Df-Na on the surface of the compressed tablets. The study has proven that Df-Na sustained-release tablets can be effectively produced by processing solid lipids using HME [133].

Bruce *et al.* have successfully developed tablets to target deliver 5-aminosalicylic acid (5-ASA) to the colon [134]. The tablets, prepared using the HME technique, are able to homogeneously disperse the crystalline 5-ASA throughout the polymeric matrix. The polymeric carriers used are Methacrylic Acid—Methyl Methacrylate Copolymer (1:2) and Eudragit® S 100. Two types of plasticisers (Triethyl Citrate (TEC) and citric acid) were used in the study. TEC was able to reduce the glass transition temperature of the polymer, thus lowering the processing temperature. It can also affect the drug release rates of the tablets due to the leaching of TEC during the dissolution testing. The citric acid causes a slower drug release rate as it causes a decrease of the pH in the microenvironment of the tablet, which suppresses the polymer ionisation. The drug release profiles of the tablets were found to fit both the diffusion and surface erosion model [134].

Apart from developing drug delivery systems with different release patterns, HME can also be used to create drugs that could mask the bitterness of APIs. There are still a significant number of drugs on the market that have very poor organoleptic properties, which makes it unpalatable, especially for paediatric and geriatric medications. In order to improve the palatability of the drugs, taste masking has been an important consideration for the development of a formulation [135]. There are works that have shown that pharmaceutical dosage forms produced using the HME process can mask the bitter taste of APIs. This can be done by mixing the taste-masking polymer with the APIs during the production of a solid dispersion. The solid dispersion can prevent the interaction between the drug molecules and the taste bud by preventing the release of bitter drugs in the saliva [99]. Eudragit E-PO has been widely used as a taste-masking excipient in formulations, as it is insoluble below pH 5, thus preventing the release of the drug in the mouth [135].

In addition, HME is also suitable to be made into rod-shaped implants. Ghalanbor *et al*. used HME to produce protein-loaded poly(lactide-co-glycolide) (PLGA) implants with the incorporation of PEG as a hydrophilic additive, aiming to improve protein stability and release properties [136]. The study showed that the release of the implant can reach 100% in 60-80 days with nearly complete enzyme activity even on the last fraction of the released protein, lysozyme. It has proven that the HME process can maintain protein stability to ensure the effective delivery of protein drugs. Bode *et al*. also carried out a study to prepare PLGA and PLA based implants using HME to achieve a controlled drug release pattern of the drug, dexamethasone [137]. The study was carried out to investigate how the swelling of the polymer can have an effect on the drug release of the implant. HME was chosen to prepare the implants in order to achieve a homogeneous distribution of the drug throughout the implants. The results from the study showed that the water penetration for the implant were limited initially due to the hydrophobicity of the polymers. However, the polymer becomes more hydrophilic over time as the water that penetrated through the polymer cleave the polysters, allowing more water to penetrate and cause swelling of the polymer. Drug release only starts when swelling happens. Salmoria *et al*. showed the possibility of producing implantable polyethylene/fluorouracil rods using HME which would potentially be used as targeted drug delivery in cancer treatment [138]. The implant showed slow and controlled drug release up to 45 days, which is suitable for cancer treatment at the tumour site.

HME has also been used to produce orodispersible films (ODFs), which are sheets of drug-loaded materials that can form a suspension or solution when coming into contact with saliva in the mouth without the need of water intake [139]. This type of dosage form is beneficial for patients who have difficulty in swallowing, for younger patients, or for places where water is scarce. Pimparade *et al*. showed the possibility of producing chlorpheniramine maleate ODF using modified starch and glycerol through the HME process [140]. Sweeteners and saliva-simulating agents were added to the formulations to improve palatability and the disintegration time of the film. Speer and Breitkreutz managed to produce OFDs that have prolonged drug release characteristics by using HME and solvent casting method [141]. Hypromellose was used as a film former and theophylline was used as a model drug. The formulations were first processed using HME to produce drug-loaded matrix particles, then dissolved in distilled water for solvent casting to produce ODFs. Musazzi *et al*. carried out a study to demonstrate the feasibility

of producing maltodextrins ODF by using a combination of HME and 3D printing [142]. The excipients, plasticiser and active ingredient were mixed and made into printable filaments using an in-house HME. The materials were then fed to the printing head for the printing of ODF. The preparation of ODF using HME is still very limited due to the high processing temperature of HME. Most polymers used for ODF preparation are heat sensitive. Therefore, polymeric excipients need to be carefully selected. Apart from that, HME can be combined with other methods such as solvent casting or 3D printing to produce a wider range of ODFs.

As the interest in using HME for pharmaceutical products has grown exponentially over the years, the concept of PAT was introduced which can be combined with HME as a continuous manufacturing process in order to achieve real-time monitoring of the product. This means that the quality of the product can be monitored simultaneously as the product is being extruded from the HME. The implementation of PAT within an HME system can help in the discovery of more novel drug delivery systems and the approach of studies. The most common PAT tools integrated with HME are UV/visible (UV/VIS) spectrophotometry [119,143,144], near-infrared spectroscopy (NIR) [145,146], Raman spectroscopy [147,148]. Table 1.4 shows the information that can be obtained from the in-line PAT during the HME process which would be very useful to provide an insight into how different processing parameters (eg. screw speed, barrel temperature, residence time, feeding rate, etc.) would affect the quality of the extrudates.

Table 1.4: Information obtained from different in-line process analytical technology (PAT) integrated with HME.

In-line Process Analytical Technology (PAT)	**Information**
UV/Vis Spectrophotometer	Particle size, solid state, drug concentration
Near-infrared spectrometer	Effect of processing parameters on product quality, process efficiency, drug content, solid state
Raman spectrometer	End point of mixing process, drug content, solid state characteristics, distribution patterns of formulations

When an extruder is used for pharmaceutical applications, it is required to meet some regulatory requirements. Therefore, some parts are different from the extruder which is used for manufacturing plastics. The metallurgy of the contact parts must not be reactive, additive or absorptive with the product, and these parts are made of medical grade steel.

The oils and lubricants used are also fully FDA-conformant. The equipment needs to be configured for the ease of cleaning within a pharmaceutical environment [100]. A comprehensive documentation of the process is required for monitoring and controlling the parameters such as feed rate, temperature, screw speed, pressure, melt viscosity, drive amperage and torque. The temperature in the barrel needs to be optimised so that the viscosity of the melted material is low enough to be transported down the barrel, but still sufficient for proper mixing. Apart from that, the temperature should also be kept low enough to avoid thermal degradation of the materials. There are also good manufacturing practices (cGMP) guidelines for the cleaning of HME used for pharmaceutical applications. The extruder for pharmaceutical purposes has been redesigned to enhance the ease of disassembling and limit any dead spots, allowing for efficient cleaning and maintenance. The equipment must be cleaned at appropriate intervals and written procedures are required that must be specific and detailed. Cleaned equipment must be protected from contamination while in storage and inspected before being used. Records and equipment logs of all cleaning and inspection must be kept. The time between the end of processing and cleaning steps must be recorded [101]. During cleaning, the extruder assembly is disassembled and any materials present on the screw, barrel and die need to be removed. The surfaces then need to be swabbed and analysed to satisfy cleaning validation requirements [120].

There are many advantages in using HME for pharmaceutical applications, which makes the technology more popular as a manufacturing method for pharmaceutical products. HME can be modified to include appropriate PAT tools, making it a continuous manufacturing process, which is a fabrication method that is highly encouraged by FDA as it meets the goal of PAT scheme to improve the efficiency and effectiveness of manufacturing process design, control and quality assurance [149]. One other reason for HME to be a preferred method is that the process does not require any use of solvent when producing solid dispersions. Traditional formulation methods, such as roll spinning and spray drying, require the use of organic solvents. These organic solvents can cause environmental issues when being disposed of. As HME is a solvent-free process, this makes it an environmentally friendly process, making it a preferred process over conventional methods [135]. Some other advantages of using HME in pharmaceutical applications include shorter production time, higher process efficiency, and increases drug delivery efficiency in patients [120]. The biggest advantage of using HME in

pharmaceutical is the prospect of being able to create new and novel formulations through this technique.

However, there are a few drawbacks in the HME process. HME requires high energy input, which is required for the shear forces and the elevated temperature in the barrel of the extruder. The high temperature may also cause thermal degradation of the APIs and the high shear forces may also cause mechanical degradation to the polymers. However, there has been ongoing research work to overcome these issues, and they can be solved by proper formulation and equipment design, as well as different engineering approaches [118].

1.3 Coupling HME with FDM 3D Printing

HME is now widely used in the pharmaceutical industry dues to its versatility and scalability. However, there is a limitation in terms of the flexibility in the design of the dosage forms or other pharmaceutical products it can produce. This is because the shape of the product produced using HME depends on the shape of the die. Some of the more complex shapes and designs would be impractical to be made into a die. 3D printing seems to be able to overcome this issue as it has large flexibility to produce any pharmaceutical products in any shapes. However, there is a very limited number of 3D printable materials that are suitable to be used for pharmaceutical applications. In the previous section, there were many reports about the ability of HME to produce new polymeric mixture and composition. HME is also the perfect technology to produce filaments that can be used in FDM 3D printers. As a result, HME has been coupled with FDM 3D printing to overcome the limitation of not having the suitable materials available commercially. Apart from that, HME can be used to effectively load drugs onto the filaments which have really made the local production of personalised medicines and implants cost-effective.

The feeding materials in FDM 3D printers need to be in the form of a filament. However, most filaments currently available in the market are not suitable to be used for pharmaceutical applications. This issue has been a major obstacle for FDM 3D printing being used as the main manufacturing method for pharmaceutical products. Apart from that, most traditional polymer excipients that have been used in pharmaceutics do not have the appropriate thermal and mechanical properties that can be used to make into filaments that are needed for FDM 3D printing [150]. Some of the most common

pharmaceutical grade polymers that can be made into filaments are Polyvinylpyrrolidone (PVP), Polyvinyl alcohol (PVA), and PLA [151]. These are suitable to be made into filaments due to excellent mechanical and thermal properties, and have been used to mix with drugs to produce filaments that can be used in an FDM 3D printer to produce oral dosage forms [152,153]. Filaments that are being used in FDM 3D printers need to be of good quality in order to produce a good quality 3D printed product. During the feeding of the filament into the print head of an FDM 3D printer, the filament will experience tensile and compressive forces caused by the extruding gear, as well as a large amount of heat for melting. The filaments will need to be able to withstand the mechanical and thermal stresses in the FDM print head in order to achieve a good printing quality [65]. Good quality thermoplastic filaments can be effectively produced using the HME method. With twin-screw extrusion in the HME technology, almost any kind of polymer can be mixed during the HME process in order to produce polymeric filaments for the desired applications. Therefore, there has been increasing research interest in the development of different types of filaments from different materials for specific applications using the HME technology. For instance, pure Eudragit has not been a suitable material to be made into FDM printable filaments due to its brittleness. Sadia *et al.* have been able to develop Eudragit-based filaments by mixing it with a plasticiser (triethyl acetate) and a filler (tricalcium phosphate) using the HME technique [154]. The mechanical properties such as the flexibility of the Eudragit filament have been further improved and the filaments are suitable to be used in FDM 3D printers for the fabrication of tablets. The 3D printed tablets also possess excellent mechanical strength [154]. Due to the robustness of HME in producing novel polymeric filaments for use in FDM printers, much research has been carried out to explore the possibility of bridging HME and FDM 3D printing to increase the range of polymers that can be used with FDM machines. This approach is seen to be a very efficient and effective way of producing desired materials for FDM printers. It will also further improve the usability of FDM printers across many industries.

The HME technology and 3D printing technology has shown many advantages when being used in pharmaceutical applications. These two technologies can streamline the complex processes of conventional manufacturing methods for pharmaceutical products. Therefore, there has been some research on combining these two technologies into a single continuous process in order to achieve a more effective and efficient manufacturing

process. When these two technologies are coupled into one single process, it opens up the possibility of creating any dosage forms in-house for immediate consumption. This is particularly useful for hospitals in remote areas. Combining these two processes makes the fabrication of dosage forms more cost-effective, efficient and economical. Figure 1.8 shows a schematic of the HME combined with FDM 3D printing into a single continuous process.

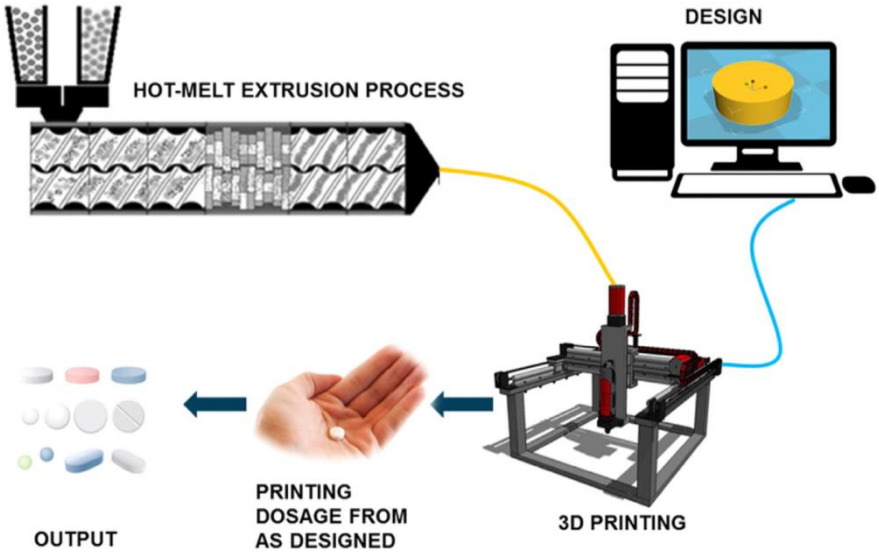

Figure 1.8: Schematic of a combined Hot-Melt Extrusion (HME) and FDM 3D printing into a single continuous process (Reproduced with permission from reference [98]).

1.3.1 Pharmaceutical Dosage Forms produced using HME and FDM combined

The study reported by Zhang *et al.* showed the combination in the use of two technologies, the HME and FDM 3D printing, in a single process to produce controlled-release tablets [98]. Different types of pharmaceutical polymers were made into filaments using HME and they were loaded with Acetaminophen as a model drug. The drug release profiles of the 3D printed tablets and the directly compressed tablets were being compared. The study shows that the 3D printed tablets have better extended drug release rates than the directly compressed tablets as they have smoother surfaces and tighter structures. The study has proven that it is possible to produce different formulations required using a single process [98]. Zhang *et al.* have been able to develop controlled-release 3D printed tablets by using hydroxypropyl methylcellulose (HPMC) as a hydrophilic matrix polymeric material in the drug [155]. HME was used to prepare solid dispersion filaments with an API dispersed in HPMC based matrix. The filaments produced are fed into an FDM 3D printer to produce controlled-release tablets with different structural design in order to obtain different drug release profiles. Nine tablets

with the same overall tablet dimensions (diameter, 10 mm; thickness, 4.5 mm) but with different outer shell thicknesses and core densities were 3D printed. The geometry of 3D printed tablets can affect the dissolution and drug release rates. The study has proven that 3D structure design is effective and efficient for optimising controlled drug release rates [155]. Goyanes *et al.* have also fabricated controlled-release budesonide tablets using FDM 3D printing. The work is to explore the feasibility of using FDM with HME and fluid bed coating to fabricate modified-release budesonide dosage forms. Budesonide is loaded into PVA filaments using HME. An FDM 3D printer is then used to produce capsule-shaped tablets (caplets) containing 9 mg of budesonide. The caplets were then overcoated with a layer of enteric polymer. The 3D printed caplet formulation started to release the drug in the mid-small intestine, but release then continued in a sustained manner throughout the distal intestine and colon. This work has demonstrated the possibility of combining FDM 3D printing, HME and film coating for the fabrication of modified-release oral dosage forms [156].

The work by Okwuosa *et al.* coordinates FDM 3D printing and liquid dispensing for the fabrication of individualised dosage form on demand in a fully automated fashion. This work has the potential of modifying drug dose and release. Polymethacrylate shells (Eudragit EPO and RL) were made using FDM 3D printing and the shells were simultaneously filled using a computer-controlled liquid dispenser loaded with a model drug solution (theophylline) or suspension (dipyridamole). The shell thickness of 1.6mm, and concentric architecture allowed for successful containment of the liquid core whilst maintaining the release properties of the 3D printed liquid capsule. Modifying the shell thickness of Eudragit RL capsule allowed for a controlled extended drug release without the need for formulation change. This type of hard shell capsule is better for taste and odour masking, improving the patient's compliance. This low cost and versatile approach can be adapted to a wide spectrum of liquid formulation such as small and large molecule solutions. This method also eliminates the need for material compatibility with the high temperature of FDM. This is the first time that an example of a fully automated additive manufacturing process for a liquid capsule with the ability to control the dispensed dose has been demonstrated. A dual head FDM 3D printer is used here. However, one of the printing heads has been modified to include a syringe-based liquid dispenser. The drug-free Eudragit filaments were produced using HME. Dimethylaminoethyl methacrylate, butyl methacrylate, and methyl methacrylate (Eudragit EPO) are used for the shell of

immediate release dosage forms and Eudragit RL is used for time-controlled drug release. The dosage can be controlled by manipulating the dispensed volume and the capsule shell thickness. This work has again proved the capability of FDM producing individualised dosage forms [157].

Chai *et al.* have used HME to produce hydroxypropyl cellulose (HPC) filaments that are loaded with Domperidone (DOM) to be used in FDM 3D printers. The DOM loaded HPC filament is used to 3D print intragastric floating sustained-release tablets that have a hollow structure, which makes the tablet has a lower density and allows it to float. The hollow structure of the tablet can be achieved by adjusting the shell numbers and the infill percentage of the FDM 3D printing process. The study shows that the capability of FDM 3D printers, a cost-effective platform, to produce hollow tablets is a promising manufacturing method to fabricate intragastric floating drug delivery devices [158]. Okwuosa *et al.* have also used FDM 3D printers to produce delayed-release shell-core gastric resistant tablets. A dual extruder FDM 3D printer has been used to produce an enteric-coated tablet in a single fabrication process. In this study, PVP has been used as a polymer for the core and methacrylic acid polymer for the shell for gastric protection. Similarly, the drug loaded filament for the core and the filament for the shell were manufactured using HME. This work has proven that the FDM 3D printer is able to perform enteric coating to produce delayed release solid dosage forms [152]. Goyanes *et al.* have been able to use FDM 3D printing to produce modified-release paracetamol tablets without the need of an enteric coating [159]. Again, HME has been used to produce paracetamol-loaded filaments for the use in FDM 3D printers. In this study, paracetamol is mixed with three different grades of excipients hypromellose acetate succinate (HPMCAS) (grades LG, MG and HG) respectively. The HPMCAS-based tablets exhibit delayed-release properties, and tablets made from lower pH-threshold release drug faster (LG has the lowest pH threshold of 5.5, MG at 6.0, and HG at 6.5). This study shows that FDM 3D printing is able to produce delayed-release tablets without the need for an outer enteric coating. The work by Li *et al.* has been able to combine HME and FDM to produce a novel controlled-release drug delivery device for diabetic treatment [160]. HME was used to load Glipizide onto PVA to form the drug-loaded filaments. A dual extruder FDM 3D printer was used to produce a double chamber device, where a tablet is embedded within a larger tablet (DuoTablet), and both chambers contain different doses of glipizide. The different concentration of the drug at two chambers is

able to achieve a sustained-release profile of the drug. The drug in the external layer is first released and the drug in the second layer will only be released when the first layer has been completely dissolved, delaying the drug release profile of the solid dosage form. This study shows the feasibility of producing a DuoTablet with controlled-release profile in a single process [160].

Verstraete *et al.* conducted a study to develop high drug-loaded (>30%, *w/w*), thermoplastic polyurethane (TPU)-based dosage forms using FDM 3D printing. This is because TPU has shown potentials for the manufacturing of highly dosed oral sustained-release matrices via HME [161]. The drug-loaded TPU filaments were prepared using HME. Different grades of TPU were mixed with model drugs of different particle size and solubility. Only the TPU-based filaments that exhibit consistent filament diameter, smooth surface morphology and good mechanical properties were used in FDM printers to be printed into tablets. It is proven that TPU-based filaments could be loaded with 60% (*w/w*) fine drug powder. The hot-melt extruded hard TPU filaments were successful in producing 3D printed tablets with a high concentration of the crystalline drug (up to 60%, *w/w*). The drug release profile of the 3D printed tablet was dependent on the matrix composition and the tablet infill degree. The dosage and release rate can be adjusted according to the patient's needs by changing the matrix composition and the percentage of tablet infill. The study shows that TPU-based filaments can offer much formulation freedom for the development of personalised dosage forms [162].

Although there is much work that has proven the ability of FDM 3D to produce various drug delivery systems, it has not been a favoured technique when it comes to the fabrication of immediate-release tablets. This is because FDM 3D printed tablets generally have a slower dissolution rate when compared to tablets produced using conventional methods [163]. For instance, the FDM 3D printed theophylline tablets by Okwuosa *et al.*, which is made from Eudragit®E and PVP with plasticisers required 30 min for the drug to be completely released [153]. However, Kempin *et al.* explored the possibility of improving the dissolution speed of FDM 3D printed tablets by using different types of polymeric carriers [163]. The study carried out shows that when suitable pharmaceutical grade polymer is being used, FDM can be used to produce immediate-release tablets that contains thermolabile drugs. The drug release profiles of pantoprazole sodium tablets made from five different polymers (PVP K12, PEG 6000, Kollidon® VA64, PEG 20000 and poloxamer 407) were compared. The drug was loaded onto each

polymer using the HME technology to produce drug-loaded filaments. The results show that the drug incorporated in PVP has the fastest release and can be completed within 10 min. The dissolution rate can also be further improved by reducing the infill rate during printing to increase the porosity of the tablet [163]. Apart from that, the study has also proven that FDM 3D can produce tablets at processing temperatures below 100°C. FDM 3D printers are known to have very high printing temperatures (170–230°C) due to the high melting temperature of the traditional polymeric filaments used and could be inappropriate for the incorporation of thermos-sensitive drugs. However, the processing temperature of FDM 3D printers can be lowered when suitable polymers can be made into filaments chosen as a drug carrier. Kollamaram *et al.* have also been able to produce immediate-release formulations (Ramipril) through FDM 3D printing at a lower printing temperature. The drug is mixed with Kollidon VA64 and Kollidon 12PF to achieve the immediate-release effect. Drug loaded filaments were first produced using the HME technology at 70 °C. The 3D printer was able to print the tablets from the filaments produced at 90 °C and there were no signs of thermal drug degradation on the printed tablets. The work has proven that FDM 3D printing can also be used to produce thermolabile and low-melting point drugs when the drug is mixed with appropriate excipients [164]. The study by Solanki *et al.* have produced FDM 3D printed tablet for rapid drug release. The model drug used is haloperidol and the drug-loaded filaments were prepared using HME. Different type of polymers were used to be made into filaments (Kollidon® VA64, Kollicoat®IR, Affinsiol TM 15 cP and HPMCAS). Tablets of 100% and 60% infill were printed at 210 °C and dissolution test were conducted at pH 2 and 6.8. For the 60% infill tablet, complete drug release was achieved in 45 min, which was significantly faster than the 100% infill tablet. This is because the 60% infill tablet is porous and the 100% tablet is non-porous. The filaments made of Kollidon®VA-64-Affinisol TM 15 cP mixtures were flexible and had optimum mechanical strength for 3D printing. The 1:1 mixture of Kollidon® VA-64 and Affinisol TM 15 cP was the most suitable polymer system to be used for 3D printing and rapid drug release. The study has proven that FDM 3D printing can also be used to fabricate immediate release dosage forms [165].

1.3.2 Dosage Forms with Multiple Medications

In recent years, there has also been increasing interest in developing a dosage form that contains multiple medications [150,166,167]. Having more than one API in a dosage form

can improve patient compliance and cost-effectiveness [168]. This type of multi-active solid dosage form, also known as polypill, is particularly useful for patients with complicated diseases, who are required to take multiple medications in a day. The polypill can reduce the frequency of medications intake in a day for the patient. The work by Gioumouxouzis *et al.* discovered the capability of FDM 3D printing to fabricate dosage form containing two APIs. The bilayer dosage form contains two anti-diabetic drugs (metformin and glimepride). Metformin was mixed with Eudragit®RL to achieve a sustained-release effect and glimepride was mixed with polyvinyl alcohol (PVA) for an immediate release system. In this study, the two APIs were incorporated into two different polymeric carriers to achieve distinct release characteristics. The 3D printed bilayer dosage form allows for the simultaneous usage of two APIs that are administered at different times of the day according to the patient's needs. The drug-loaded filaments were also manufactured using the HME technology. This study shows that FDM 3D printing can be a promising technique for the fabrication of complex personalised medicine consisting of different APIs that exhibit different release patterns [169]. Goyanes *et al.* used a dual-extruder FDM 3D printer to fabricate two different capsule-shaped oral drug delivery devices. One is a multilayer device and the other is a two-compartment caplet (Figure 1.9). The multilayer device is designed in such a way, that two adjacent layers contain different type of drugs. The two-compartment caplet is a smaller caplet embedded in a larger caplet (Duocaplet), with each compartment containing a different drug. In this study, PVA-based filaments were used and they were loaded with paracetamol or caffeine. The filaments were prepared using the HME method. The drug release study shows that for the multilayer device, drug release rates were similar for both drugs. However, if one layer has a higher drug loading than the other, the release rate will be faster for higher drug loading. For the Duocaplet, the drug on the external layer is being released first. The time lag of the release of drug in the inner caplet depends on the characteristics of the external layer. The study has proven that tablets that are 3D printed in different shapes can have different release profiles [170].

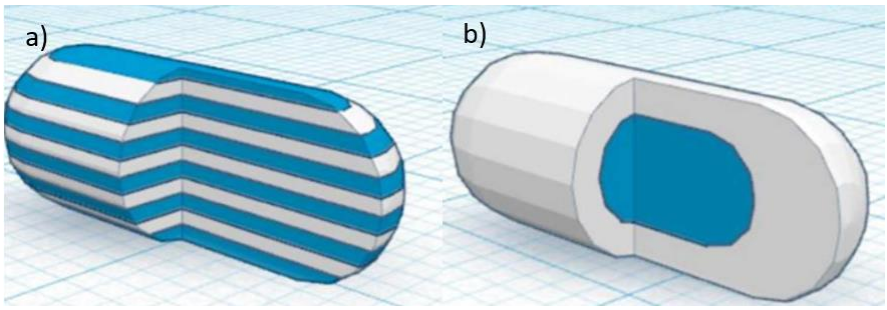

Figure 1.9: A 3D computer-aided design (CAD) model of capsule-shaped oral drug delivery device (**a**) multilayer device (**b**) two-compartment caplet (Duocaplet) (Reproduced with permission from reference [170]).

Maroni *et al.* used FDM 3D printing to fabricate a two-compartment capsular device for two-pulse oral drug delivery purposes. The study carried out in this work involves the combination of two compartments with different wall thickness and compositions. Promptly soluble, gastroresistant and swellable/erodible compartments were developed, which allowed for immediate, enteric and pulsatile release to be achieved respectively. Therefore, different types of polymeric filaments have been used to achieve different effects. The polymeric filaments were prepared using twin-screw extrusion. Apart from different materials, the compartments were also made to be of different wall thickness (600 µm and 1200 µm) (Figure 1.10). Such a device is intended to yield multiple release kinetics. The two separate compartments are to be filled either with different APIs or with varying doses and/or formulations of one particular drug. These devices with different compartment characteristics show two pulse release patterns. These two-compartment capsular devices are able to convey incompatible drugs or different drug formulations [171].

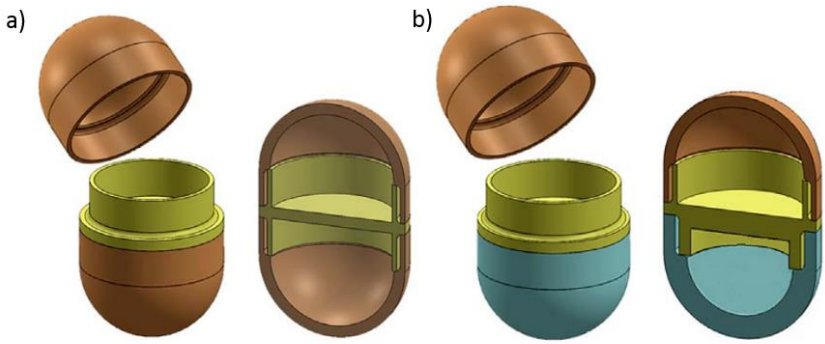

Figure 1.10: Two-compartment capsular device (**a**) compartments with the same wall thickness (**b**) compartments with different wall thickness (Reproduced with permission from reference [171]).

Tagami *et al.* were able to fabricate 3D-printed composite tablets consisting of two components, a drug and a filler, using a dual head FDM 3D printer. PVA containing calcein was used as the drug component and drug-free PVA or PLA was used as the water-soluble or water-insoluble filler respectively. The filaments were produced using a twin-screw extruder. Different designs of the tablets were being used. There were eight kinds of calcein-loaded PVA/PVA composite tablets and four kinds of calcein-loaded PVA/PLA tablets that were 3D printed. All composite tablets were designed to have different surface areas of calcein-PVA but all have a drug component/filler component ratio of 2/3 (*v/v*). The composite tablets showed various drug release profiles. The higher surface area of calcein-PVA had a higher dissolution rate. The study shows that the polymer filler component was effective in controlling drug release and will be particularly useful for personalised medicine [172]. The study carried out by Melocchi *et al.* has successfully proven the feasibility of FDM 3D printing in the manufacturing of capsular devices for oral pulsatile release using HPC-based filaments. Pharmaceutical grade HPC-based filaments are not commercially available and they were produced using HME. The capsular device produced using FDM 3D printing exhibited satisfactory physico-technological properties. The release test of the capsular device shows that there is a lag phase before the rapid and quantitative liberation of the drug. The morphological of the device when in contact with water and the release performance is comparable to the analogous systems fabricated using injection moulding. Since it is possible to rapidly prototype capsular devices using FDM 3D printing, the screening of formulation and design characteristics of these devices are also expected to be accelerated [173].

Pereira *et al.* carried out a study to demonstrate the ability of FDM 3D printing to produce patient-specific polypills as a treatment of cardiovascular diseases [174]. The polypill fabricated was PVA based and contained 4 model drugs (lisinopril dihydrate, indapamide, rosuvastatin calcium and amlodipine besylate). The PVA filaments containing each of these drugs were extruded using HME. Then a multilayer polypill was printed using FDM 3D printer using the PVA filaments containing each drug. A novel approach of using distilled water as a plasticiser was used in this study and it was found that the extruding and 3D printing temperature was much lower due to the plasticising effect. The release profile of each drug depends on the position of its layer in the pill. This approach showed a low-cost manufacturing method of a multidrug delivery system for individualised medications, and the release profile of the drug can be modified by changing the sequence of the drug layer in the multiplayer polypill.

As FDM 3D printing can be used to produce complex personalised medicines, Arafat *et al.* have been able to use 3D printers for flexible on-demand precision tailored dose adjustment [175]. This type of medication has been beneficial for anticoagulant therapy. For anticoagulation therapy, regular coagulation monitoring and dose modification is required in order to ensure the patient's International Normalised Ratio (INR) remains in the target range. Therefore, dose modification is required from time to time, depending on the patient's condition, as the patient's INR profile may be constantly changing. The 3D printing technology is able to produce a precise dose and has been a platform to fabricate personalised medicine with the required dose. The technology allows the administration of the lowest effective dose of the drug to maintain the target INR due to its flexible and precise manufacturing capability. Arafat *et al.* have used FDM 3D printers to produce a tailored dose of a narrow therapeutic index drug, warfarin, and have successfully fabricated this purposefully designed solid dosage form in ovoid tablets. The study showed that FDM 3D printing can be used to engineer and control the dose of immediate-release warfarin tablets by controlling the mass and volume of the 3D printed tablet. The drug-loaded filaments were produced using a twin-screw hot-melt extruder and Triethyl citrate was mixed into the drug-loaded filament formulation in order to lower to the glass transition temperature of the filament [175].

Apart from that, the work done by Scoutaris *et al.* has also proven that a continuous process of HME coupled with FDM 3D printing can be used to prepare chewable tablets in the shapes of "Starmix®" sweets [76]. This is a very effective method to produce

paediatric medicines as the HME is able to provide taste masking of bitter APIs, and FDM 3D printing has the capability to produce complex shapes tablets that could attract the attention of children. In this study, the drug used is Indomethacin and the thermoplastic polymer used is HMPCAS. HME has efficiently dispersed the indomethacin in the HPMCAS matrix, providing excellent taste masking efficiency. FDM 3D printing has shown to have high reproducibility, accuracy and content uniformity of the Starmix® shapes. This study has proven an alternative route of producing palatable paediatric dosage forms. Jamróz *et al.* carried out a study that used FDM 3D printer to prepare orodispersible films (ODFs) containing a poorly water-soluble substance, Aripiprazole. The study proves the feasibility of fabricating ODFs using FDM technology to improve the dissolution rate of the poorly water-soluble substance through 3D printed films. The Aripiprazole loaded PVA filaments were prepared using HME. The study shows the amorphisation of the aripiprazole and the porous structure of 3D printed film is able to improve its dissolution rate. The mechanical properties of the 3D printed films were also comparable to the films prepares using the casting method [176].

Beck *et al.* also carried out a study regarding an innovative approach to produce customised drug delivery systems using FDM 3D printing. This work produced a multi-functional drug delivery system, which is a solid dosage form loaded with nano-sized carriers. The possibility of fabricating solid dosage form containing drug-loaded nanocapsules using FDM 3D printing has been discovered. This work integrates the FDM 3D printing technology and nanotechnology to produce innovative nanomedicines. PCL and Eudragit®RL100 filaments were produced using HME. The 3D printed tablets were then loaded with polymeric nanocapsules. The study proposed a new platform for the development of oral dosage forms, biodegradable implants with tailored dose and drug release profiles, as personalised medicines [51].

1.3.3 Drug-loaded Implants Application

Kempin *et al.* have used HME to produce quinine loaded filaments that can be used in FDM 3D printers to produce drug-loaded implants. The drug release of different type of polymers (Eudragit® RS, Polycaprolactone (PCL), poly(L-lactide) (PLLA), and ethyl cellulose (EC)) were being compared. The study shows that PCL has the fastest drug release whereas Eudragit and EC have the slowest drug release. The study has proven the feasibility of FDM 3D printing to manufacture drug loaded-implants as FDM 3D printing can produce a product of almost any shape, which could be designed to function as an

implant, and at the same time, be able to incorporate a desired drug delivery system [177]. Besides that, Genina *et al.* used ethylene vinyl acetate (EVA) as a drug carrier to produce drug-loaded EVA filaments using HME. The EVA filaments were loaded with indomethacin using HME. The filaments produced were used in FDM 3D printers to fabricate custom-made T-shaped intrauterine system (IUS) and subcutaneous rods (SR). The aim of this work is to investigate the printability of different grades of EVA copolymers as new feedstock material for FDM 3D printing in the fabrication of drug delivery devices. The IUS and SR were successfully printed at a temperature just above the melting point of the drug. The study has proven that EVA 5 polymer has the required properties to be made into filaments for the FDM 3D printing of drug delivery systems such as IUS and SR devices [178]. Holländer *et al.* have also been able to produce indomethacin loaded PCL filaments using HME. The drug-loaded PCL filaments were then used in FDM 3D printers to produce drug-containing T-shaped prototypes of IUS. This study shows that the fabrication of controlled-release implantable devices can be achieved using FDM 3D printing and HME technology [179]. Fu *et al.* have been able to use FDM 3D printing to produce personalised progesterone-loaded vaginal rings. Progesterone was mixed with Polyethylene Glycol (PEG) 4000 to form a solid dispersion and was cut into pieces. The mixture of PLA and PCL (8:2), Tween 80 and the progesterone-loaded PEG were mixed in a desktop single screw extruder and hot melt extruded in the form of filaments. The filaments were fed into FDM 3D printers to print vaginal rings in the shape of “O”, “Y”, or “M”. The work shows that “O” ring had a higher dissolution rate due to its higher surface area/volume ratio. The vaginal rings also have long-term sustained-release of progesterone for more than 7 days with diffusion-controlled release behaviour. It is again been proven that HME and FDM 3D printing is an effective method to prepare personalised and customised medications [71].

Stewart *et al*. developed several biodegradable subcutaneous implants that were loaded with different APIs and have different designs to achieve a prolonged drug release from the implants using FDM 3D printing [180]. A study on how the geometry of the implant can affect the drug release kinetics was also carried out. The materials used were PLA and PVA and the filaments were produced using HME from these materials. The printed implants have a different degree of porosity by the presence of a different number of ‘windows’ to investigate the drug release. The main implant body was printed out of PLA filaments and the windows were printed out of PVA filaments. PCL was then used to coat

the implants in order to obtain a more sustained drug release pattern. The study successfully proved that how effective the HME and FDM 3D printing technologies are in terms of producing personalised drug delivery implants on-demand as the 3D printing technology can easily produce different implant design to achieve the desired drug release pattern.

The work carried out by Melocchi *et al*. proposed a novel approach of 3D printing a retentive intravesical drug delivery system based on the water-induced shape memory response of PVA [181]. Shape memory polymers are considered as smart materials that carry a shape memory effect, which is the ability to deform and recover to their original shape when triggered by an external stimulus such as light, humidity, change in temperature, electric current or magnetic field [182–185]. The PVA filaments containing glycerol as plasticisers and caffeine as an active ingredient was produced using HME. The filaments were fed into an FDM 3D printer to print the desired shape of the implant. The printed implant required programming steps to change it into a temporary shape so that it will be suitable for administration via a catheter. It is then transformed to its desired permanent shape for bladder retention when it is in the human body caused by the body temperature of 37°C. The implant showed prolong release due to the material's slow interaction with aqueous fluid. This new concept of 3D printing is now commonly known as 4D printing, where the 3D printed object is capable of self-transforming to achieve its designed functionality as a response to external stimuli. Such drug delivery devices which can self-transform are highly beneficial as it can be designed to a shape which can have administered conveniently into the human body. This study has shown the feasibility and possibility of using 4D printing for pharmaceutical applications.

1.4 Sensors for Biomedical Applications

Nowadays, sensors are ubiquitous and have been playing an important role in our daily lives. Sensors can be easily found in a wide range of applications, ranging from consumer products such as mobile phones to many manufacturing industries. Apart from that, sensors are also very critical in healthcare and biomedical applications. Sensors have always been important for health monitoring and diagnostic as we rely on sensors to provide us with information regarding our health.

A widely used definition for a sensor is a device that can produce a useful output in response to a specified measurement [186]. Typically, the output of a sensor can be

optical, electrical, chemical or mechanical and the targeted measurement can be of physical, chemical or biological property [187]. In biomedical applications, sensors have been used to measure much important information regarding the human body such as blood pressure, body temperature, oxygen level, glucose level, heart rate, different hormones and antibodies, magnetic and electric fields, etc [188–196]. The reliability, sensitivity and accuracy are highly important in the development of biomedical sensors in order to provide the most accurate health diagnostic and measurement of a person. One other key consideration is biocompatibility of the sensor, particularly for sensors that need to be implanted and have direct contact with the human body so that the sensor material will not cause any toxicity or harm to the human body.

In recent years, the integration of sensors with traditional medical implants has gained much research attention. The purpose of integrating implants with sensors is to immediately detect and monitor the response of the human body in all conditions. This can play an important role in the detection of life-threatening diseases. Therefore, medical implants integrated with sensors are also called smart implantable devices. In general, smart medical implants are able to improve the functionality and longevity of implantable devices. The function of smart medical implants is to provide real-time information of any part of the human body that is of interest. This information is very useful as it can help to further improve the quality of life.

As smart medical implants integrated with sensors are used to detect the changes in the body, the main functioning sensor is often called a biosensor. A biosensor can be known as a device that measures the biological and chemical reactions in the body which can also be used as a diagnostic tool in clinical applications. Biosensors are nowadays ubiquitous and have been widely used for point-of-care monitoring of treatment and disease progression [197]. The applications of biosensors are not only limited to biomedical application such as disease monitoring, drug discovery, detection of vitals or diseases in our human body [197], but also used in other fields such as national security [198], forensic studies [199] and environmental monitoring [200]. In general, the working principle of a biosensor can be explained in 5 components: analyte, bioreceptor, transducer, electronics and display (Figure 1.11). An analyte is a substance that is of interest and needs to be detected by the biosensor. For example, glucose can be an analyte for a glucose biosensor. A bioreceptor is a molecule that specifically recognises the analyte, where it could be enzymes, cells, deoxyribonucleic acid (DNA), antibodies etc.

The response or signal generated from the interaction of the analyte with the bioreceptor is called bio-recognition. The transducer is an element that converts a form of energy into another. In a biosensor, the transducer converts the bio-recognition event into a measurable signal. The process of energy conversion is called signalisation. Most transducers produce either optical or electrical signals. The electronics is where the produced signal is being processed and prepared for display. This is normally a complex electronic circuit that performs signal conditioning such as amplifying and converts the signals from analogue to digital. The display is where the detected information are being displayed in a form which is comprehensible by the user [197]. Some of the main features to consider when manufacturing a biosensor are selectivity, reproducibility, stability, sensitivity and linearity.

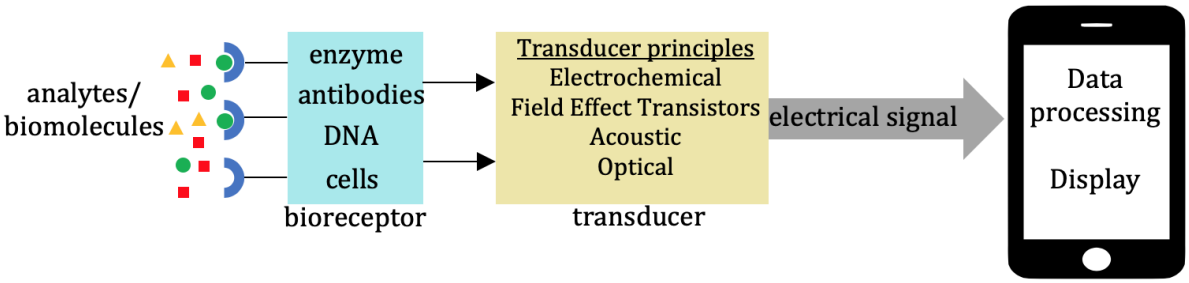

Figure 1.11: Schematic diagram explaining the working principle of a typical biosensor.

1.4.1 Examples of Smart Medical Implants

Some orthopaedic implants, especially for artificial joints used for joint replacement surgery, are currently integrated with sensors. This is because there has been an increasing number of complications related to bacterial biofilm infections at the artificial joint prostheses which could cause chronic infection, resulting in aseptic loosening of the prostheses. By integrating sensors to these implants, it is then possible to detect and monitor the response of the human body to the implants after the surgery is performed. This could also help to monitor the progress of the patients' recovery. The sensor can also detect any unusual activity at the implanted site through enzymatic reactions caused by the development of bacteria. The implant could have a drug reservoir where the drug will be released to target the infected area. The smart orthopaedic implants could prolong the life of the implant, reduce the risk the infection, and reduce the need for revision surgery.

Another type of smart medical implant that has received much research attention contains sensors that could measure some metabolites through the body fluid to provide vital information regarding the health of the human body. Typically, these implants consist of a needle-type sensor which is inserted under the skin to measure the targeted information

from biomolecules in the body fluid. Our body fluid such as sweat and interstitial fluid contains several potential analytes related to human health status such as sodium, chloride, potassium, carbonates, ammonia, calcium, glucose, lactate etc [201–203]. The most commonly available sensors are used to detect the glucose level in the body.

1.4.2 Temperature Sensing System

The measurement of body temperature is very basic but also a very critical parameter for a diagnostic procedure in medical practice [204]. It is suggested that body temperature is one of the main vital signs and should be used as part of the initial assessment for acute illnesses in adults [205]. The human body regulates its temperature by balancing the heat generated through metabolism and the heat loss to ensure a stable body temperature [206]. This is known as the homeostatic thermoregulation mechanism which help maintain the core body temperature at around 37.5 °C [207,208]. A body temperature that is too high or too low may indicate some early signs of disorders and illnesses [209]. Therefore, the measurement of body temperature needs to be very accurate as inaccuracy can lead to misdiagnosis and compromise patients' health.

As the reliability and accuracy of temperature sensors are highly important particularly in the healthcare industry, there has been increasing effort in developing safe and reliable biomedical temperature sensors. Temperature sensors can be produced using different technologies and are often categorised into the following types: thermocouples [210], thermistors [211], resistance temperature detectors (RTDs) [212], fibre optic temperature sensors [213], and infrared sensors [214]. Table 1.5 below shows a brief summary of the different techniques that have been used for temperature sensing and their applications across various industries. However, the applications of all the temperature sensors are not limited to the applications mentioned. The approximation of the operating temperature range of each technology is very dependent on its application and the type of material it is made of. Hence, it is not an accurate representation of the actual temperature range that the temperature sensing system can operate.

Table 1.5: The different temperature sensing technologies and their applications.

Type of temperature sensor	Approximate operating temperature range (°C)	Applications
Thermocouple	-40 – 1500 (depending on type of wire used) [215]	Oil/Gas [216,217], Pharmaceutical [218], Kitchen appliances [219]
Thermistor	-55 – 150 [211]	Textile manufacturing [220,221], Plastics manufacturing [222], medical applications [223,224], air, gas and liquid temperature measurement [225–227]
Resistance Temperature Detectors (RTDs)	-250 – 1000 [228]	Air conditioning [229], food processing [230], micro-electronics [212,231], Nuclear plant [232]
Fibre Optic Temperature Sensors	-250 – 250 [233]	Pharmaceutical [234], Medical [235,236], Aerospace [237,238], Wind energy [239], Oil/Gas [240]
Infrared Temperature Sensors	0 – 1000 [214,241]	Heating/Air conditioning [242,243], Food safety [244,245], Agriculture [246,247], Biomedical [248,249]

A thermocouple is typically made of two different metal wires that are of different electrical properties at different temperatures. One end of both wires are welded together to create a junction which is used to measure temperature. The other open ends of the two wires are used to measure the voltage created between the two dissimilar metal wires when there is a change in temperature. The change in voltage is used to measure the difference in temperature [250]. The set-up of thermocouples is very simple, easy to manufacture and inexpensive. They are offer good reliability and mechanical flexibility. As they are often made of extremely fine metal wires, thermocouples can be used to measure temperatures in locations that are difficult to access such as human organs, autoclave and nuclear reactors [251–253]. As an example, a flexible thermocouple temperature sensor integrated with a soft pneumatic balloon actuator to function as a

robotic microfinger for operations in inaccessible environments was demonstrated by Konishi *et al.* [210]. Such devices are particularly useful as minimally invasive surgeries are more preferred nowadays for safer operations [254].

A thermistor is generally a thermally sensitive resistor, where its resistance changes when there is a change in temperature. Most thermistors have a negative temperature coefficient, which means the resistance decreases as the temperature increases. Some could also exhibit positive temperature coefficient, where the resistance increases as the temperature increases. Thermistors have been widely used in healthcare applications due to their stability, precision, reliability, fast response and low cost [255,256]. An example where thermistors have been used in medical application is that thermistors are used to measure the temperature of cells during cancer treatment when using heat to destroy diseased cells in tumours [257–259]. Thermistors can also be found in dialysis machines for diabetic patients where the temperature of the blood being filtered during dialysis are being monitored. The machine will then reheat the blood to normal body temperature after filtering before it is returned to the patient's body [260]. Thermistors are used extensively in catheters as well which are inserted into the heart muscles to monitor the temperature during a heart surgery [261,262]. The catheters integrated with thermistors are important for cardiac diagnostic and procedures.

RTDs are similar to thermistors as they also function like resistors in which the resistance changes as the temperature changes. RTDs often offer greater stability, accuracy and repeatability when compared to thermocouples. However, a power source will be required for RTDs to operate as it operates using electrical resistance. Yang *et al.* showed an example of a flexible implantable micro temperature sensor that is made of RTDs which can potentially be used in various biomedical applications [263]. This is because the RTDs were fabricated on a flexible polymer capillary with very thin layers of platinum, allowing the temperature sensor to be highly flexible for precise and sensitive temperature measurement. One example discussed by the authors where such implantable temperature sensors can be useful is for microwave hyperthermia during cancer treatment. The temperature sensor can be implanted into the tumour during treatment to monitor the temperature in order to prevent excessive heat from the hyperthermia to prevent the burning healthy tissues around the tumour [263].

Fibre optic temperature sensors use optical fibres to measure temperature. There are many types of fibre optic temperature sensors with different principles of operations. These sensors can be generally categorised into intensity-modulated sensors, phase-modulated sensors and wavelength-modulated sensors [264–267]. In an intensity-modulated temperature sensor. The intensity of the light through an optical fibre changes according to the change in temperature. For a phase-modulated sensor, the sensor compares different phases of light in the sensing fibre at different temperature. The wavelength-modulated sensors measure the change in the reflected wavelength of the light due to the change in temperature. One of the most widely used techniques is the Fibre Bragg Grating (FBG)-based sensors [268]. The basic principle of this sensor is that it uses wavelengths that satisfy the Bragg condition, where these wavelengths are reflected using a grating inside the core of an optical fibre. When there is a change in temperature on the optical fibre, the spacing between the gratings will change resulting in a change in the refractive index. This means that a change in temperature will cause a shift in the reflected wavelength [269]. This type of temperature sensors are highly sensitive as they are able to measure extremely small temperature changes. Fibre optic temperature sensors have been very valuable for biomedical applications and can be found in various applications such as electromagnetic heating for cancer therapy, catheter with temperature sensors and patient temperature monitoring during magnetic resonance imaging (MRI) [270–273]. Fibre optic temperature sensors do not exhibit conductive properties, unlike the temperature sensors previously mentioned. As a result, it offers the advantage of not interfering with electromagnetic, radio waves or microwaves. Hence, it can be used with MRI and still provide stable and reliable temperature measurements [274]. Apart from MRI, fibre optic temperature sensors have also been used in radio frequency and microwave treatments [275–277]. The Luxtron fibre optic thermometer from LumaSense (LumaSense Technologies, Santa Clara, CA, USA) is an example of an optical fibre temperature sensor that uses the light fluorescent technique to provide real-time temperature measurements during ablation procedures involving MRI, radio frequency or microwave [278–280]. An in-depth review of how different optical fibre-based temperature sensing technologies have been developed for various biomedical applications have been prepared by Roriz *et al.*[233].

Infrared temperature sensors use a non-contact temperature and non-destructive measurement method as the technique involves the use of infrared radiant energy to

measure the temperature from a distance by measuring the energy of the wavelength being emitted [281]. It uses the principle that objects with the temperature above absolute zero (-273.15 °C = 0 Kelvin) emits electromagnetic radiation from its surface which is proportional to its intrinsic temperature [282]. This radiation is an infrared radiation and can be used to measure the temperature of the object. Infrared radiation is one of the electromagnetic waves as shown in the electromagnetic spectrum in Figure 1.12. The wavelength of infrared is typically in the range of 0.78 – 1000 µm [283]. In an infrared temperature sensor, a lens is used to focus the infrared beams into a detector element which generates an electrical signal that is proportional to the infrared radiation. The signal is then transformed to produce a temperature value that corresponds to the temperature of the measured object. Examples of infrared temperature sensors are commonly found as fever thermometers such as ear thermometers and non-contact thermometers [284].

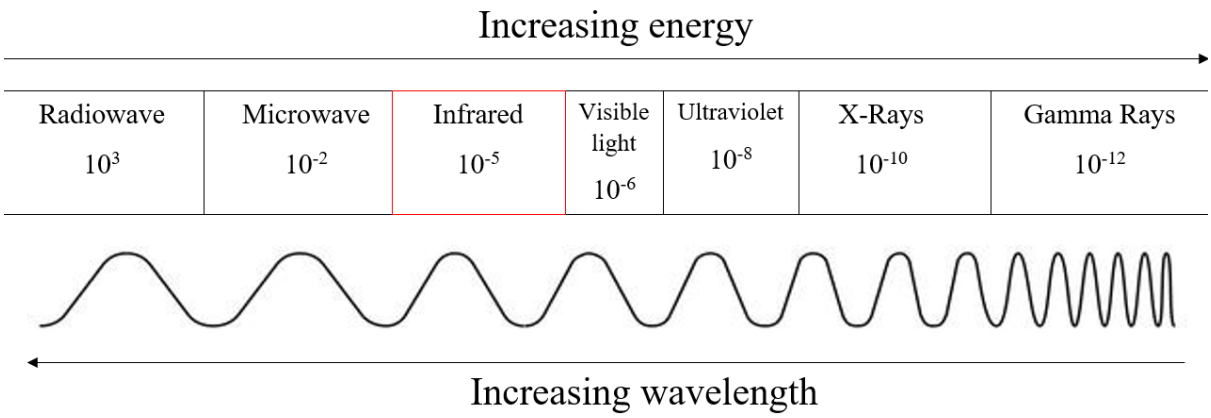

Figure 1.12: A typical electromagnetic spectrum showing the types of electromagnetic waves and their respective wavelengths range (in m).

Most current temperature sensors for medical applications are often integrated with some medical diagnostic and treatment devices [285]. For instance, some temperature sensors integrated sensors can measure the calorimetric flow of the blood or respiratory flow as well temperature at the same time [286–288]. Some of the temperature sensors are integrated with surgical tools for better surgical outcome [289]. Nevertheless, temperature sensors are highly important and have many applications, not just in the medical field.

1.4.3 Glucose Sensing System

Glucose is the main energy carrier in the human body. It is a type of sugar that is derived from the digestion of carbohydrates in the body which is absorbed into the bloodstream and circulated throughout the body for cells to convert them into energy. The sugar level is regulated by a hormone called insulin which is produced in the pancreas by the Islet of Langerhans. Typically, the glucose level in a healthy person 4-5.9 mmol/L [290]. In some people, however, the body's ability to produce or respond to insulin is impaired, resulting in a high concentration of sugar in the blood, also known as hyperglycaemia. This chronic condition is called diabetes. The two most common types of diabetes are Type I and Type II. Type I diabetes is an autoimmune disease where the body's immune system attacks and destroys the cells that produce insulin. Type II diabetes is an condition where the production of insulin is insufficient or ineffective in regulating the uptake of glucose from the blood [291,292]. In general, Type II diabetes is more common than Type I. According to the report from the World Health Organisation (WHO), there were 422 million diabetic patients in the year 2014 around the globe. Diabetic can be fatal, and it is a major cause of blindness, kidney failure, heart attacks, stroke and lower limb amputation. WHO estimates that diabetes was the seventh leading cause of death in the year 2016 [293]. Diabetic patients need to constantly monitor their blood sugar level throughout the day so that they can manage their activities such as diet pattern, physical exercise and drug therapy in order to regulate their blood sugar level [294,295]. Therefore, systems that can efficiently monitor the glucose level in our body is essential and has received much research effort not just in academia but also in the pharmaceutical industry.

The most conventional method of measuring glucose in the human body is by glucose meters. This method requires pricking of the fingertips with a lancet to access the capillary blood and a drop of blood is used to measure the sugar level [296]. The glucose meter measures the enzymatic reaction of blood glucose with glucose oxidase (GOx) that is on the strip of the glucose meter. GOx is a specific enzyme that oxidises glucose to form gluconic acid and hydrogen peroxide (H_2O_2) in the presence of water (H_2O) and oxygen (O_2). H_2O_2 is then electrochemically oxidised on an anode electrode to give an amperometric signal (current) which is proportional to the concentration of glucose in the blood. The glucose meter contains a current-to-voltage converter which converts the current produced into a voltage reading proportional to the glucose level in the blood [297].

$$\text{Glucose} + H_2O + O_2 \xrightarrow{\text{GOx}} \text{Gluconic acid} + H_2O_2 \quad \text{(Equation 1.1)}$$

$$H_2O_2 \rightarrow O_2 + 2H^+ + 2e^- \quad \text{(Equation 1.2)}$$

The use of an enzyme, such as GOx and dehydrogenase, is the most common approach used in glucose sensors to convert glucose into a readable electrochemical signal [298–301]. This is mainly due to its simplicity, efficiency, and reliability [302,303]. Unfortunately, this method of measuring glucose level is not the most patient compliant as the patients could easily forget to measure. Fingertips pricking can also cause a certain degree of pain. Apart from that, this method of measuring glucose level does not provide any information on how the glucose level changes with the activities carried out within a certain timeframe [304]. To better understand the fluctuation of the glucose level in the human body, an alternative approach involves the use of Continuous Glucose-Monitoring (CGM) systems. CGM systems are being used to live to monitor the glucose level in the human body and glucose readings can be taken at any time. The data obtained shows the history and the direction of the glucose level is heading in the body. The CGM can help patients to track the fluctuation of the glucose level throughout the day so they can adapt to the lifestyle that benefits them the most. CGM is also more patient-friendly as these technologies are mostly wearable and non/minimally invasive [305–308]. Given the many advantages of CGM compared to conventional methods of measuring glucose, the global CGM system is projected to reach around $9,000 million by 2027 [309].

In-vivo measurements are attractive as it provides patients for quick self-assessment. Most CGMs currently available in the market employs the glucose-oxidase electrochemical sensing principle [310]. It uses a minimally invasive needle sensor which is usually inserted under the skin in the abdomen or on the arm. The device measures the electrical current generated by the glucose-oxidase reaction, which is proportional to the glucose concentration in the interstitial fluid. Some examples of the first commercially available CGM products are Medtronic Guardian (Medtronic Minimed, Northridge, CA, USA), the Dexcom Seven Plus (Dexcom, San Diego, CA, USA) and the Abbott Navigator (Abbott Diabetes Care, Alameda, CA, USA) [304]. Abbott and Dexcom are currently the main suppliers of CGMs for diabetes care in the market. The latest product from Abbott is a flash glucose monitoring system called the FreeStyle Libre System. The glucose sensor in a microneedle can is inserted under the skin which measures the glucose level every 5 minutes and stores the readings for up to 8 hours. A hand held device or a

smartphone can be used to read the glucose reading and the history of the glucose level [311]. The latest CGM from Dexcom is the G6 CGM System. The system can also transmit the readings wirelessly to the a smart device or a smartwatch which shows the direction of the glucose level is heading [312]. There are some challenges in using enzymes-based glucose. Enzymes are relatively expensive and are highly sensitive to its surrounding environment [313]. It can be easily denatured when there is a change in temperature, humidity and pH values [313,314]. Besides that, the need for the immobilisation of enzymes on the electrode surface is often a complicated process [315,316]. In order to overcome these limitations, researchers have been focusing on using enzyme-free approaches for glucose sensing. For instance, some CGM suppliers have employed the optical sensing approach which uses near infrared detection [317,318], Raman spectroscopy [319,320], or fluorescent-based sensors. One example of CGM that has successfully applied the optical sensing technique is the Senseonics (Senseonics, Inc., Germantown, MD, USA) which is a fully implantable CGM system [304]. Zhu *et al.* reported a nonenzymatic wearable sensor for electrochemical analysis of perspiration of glucose [314]. Human sweat has been widely used as a sampling medium for most wearable chemical sensors. The electrochemical detection method in sweat-base sensors are simple, sensitive and consumes low electrical power [321,322]. Hence, sweat or perspiration sensing has been focused as it is a promising alternative to invasive or even self-monitoring glucose tests [202,323,324]. The electrocatalytic oxidation of glucose often requires an alkaline condition, where pH is greater than 11, for acceptable selectivity and sensitivity. Multipotential steps including a high negative potential step for the pretreatment of the sample which produces a localised alkaline condition on the electrode surface, moderate potential for glucose detection under the alkaline condition and a positive potential to clean the electrode surface were applied onto the Au electrode. Fluorocarbon-based materials were coated onto the electrode for improving the selectivity and robustness of sensors [314].

Some CGM are implanted subcutaneously which detects the glucose level of the human body through the fluid in the subcutaneous tissues. This allows the user to monitor glucose level under any conditions and determine how different activities carried out can affect the glucose level. Therefore, CGM has attracted intense research interest because of the need for better diabetes management. There has also been increasing effort to improve the accuracy, reliability, usability, size and the lifetime of CGM [304]. Some of

the CGM systems can only last for a small period of time and needs frequent changing of the sensors. These systems can become expensive and could compromise patients' comfort due to continuous implantation procedures [325]. The continuous improvement of CGM is crucial and could revolutionize the treatment of diabetes. There is also a need for low-cost devices so that the smart CGM devices can be affordable by the public. These devices are not just suitable for diabetic or pre-diabetic patients, but also can be used my healthy individuals to monitor their own body conditions.

1.4.4 Flexible sensors

The miniaturization of implants, in particular for implants with continuous monitoring purposes, has become a hot research topic as it has proven to be beneficial not just for the patients, but also for the device performance. A miniaturized implant is more patient compliant as it can be implanted in a minimally invasive way. The presence of a miniaturized implant will not be noticed by the patient and would not affect the patient physically or mentally. In terms of the device performance, micro- to nano-scale sensors can provide a better signal-to-noise ratio and only small volumes of samples is required. Apart from that, a smaller sensor means the surface-to-volume ratio is increased, which could increase the sensing efficiency. Nowadays, there has been reported that biosensors can have very low limits of detection, some can even achieve single-molecule detection [326].

However, there is a limit to the miniaturization of implants to ensure the device performance and reliability. Apart from that, most surfaces on the human body are not flat. The technologies developed for use in healthcare, particularly for implantable devices need to conform to convoluted surfaces. Hence, the development of flexible electronics has quickly emerged as the best solution to achieve this goal. Flexible electronics have shown many advantages such as being conformable, light-weight, biocompatible, biomimetic [327,328]. It has been very promising for novel and innovative application such as smart labels [329,330], wearable devices [322,331–334], smart patches [335], artificial skins [336–338], e-tattoos [339–341], and advanced surgical tools [342–344]. Apart from that, the development of flexible sensors has received much attention due to the increasing popularity of biosensors for non-invasive medical applications. This is because flexible sensors are thinner and flexible, which makes them to have higher conformability to uneven surfaces, especially to the human body [345]. An example where a flexible sensor has been used is to fabricate an all-

printed tattoo-based glucose sensor for non-invasive glucose monitoring by Bandodkar *et al.* [346]. This non-invasive glucose monitoring system is worn on the skin. The glucose biosensor is functionalised using reverse iontophoretic extraction of interstitial glucose and an enzyme-based amperometric biosensor. Another 3D printed flexible electrochemical biosensor for glucose detection has been introduced by Nesaei *et al.* via a dual 3D printing method of Prussian modified electrode and glucose oxidase enzyme layer [347]. The electrodes were printed onto a temporary tattoo paper and the performance of the printed biosensor was compared with the conventional screen-printed electrodes. The study showed that the 3D printed electrodes have higher uniformity and defect-free surface which has improved the electrochemical sensing ability [348].

Flexible electronics are made of circuits built on flexible materials such as plastic films, which can be rolled up or can conform to any non-planar surfaces. Transistor is one of the most common components in electronics and has been the building block of all electronics devices. It is also often deposited on top of the flexible films to form flexible electronics, often known as flexible thin-film transistors (TFTs). In general, the principle of a TFT is similar to a field effect transistor (FET). It consists of two electrodes (source and drain) and a semiconductor channel that bridges the source and drain. There is another electrode called the gate placed on top of the semiconductor channel which would determine the flow of the current through the channel depending on the electric field provided by the gate. The ratio of the current and the gate voltage dictates whether the transistor will turn on, or off, or amplify a signal. As for biosensors, the same configuration is used, but the gate is replaced with a functionalised receptor layer that selectively binds to a biomolecule analyte which changes the conductivity of the semiconductor. The source/drain voltage will be fixed and the electrical current changes according to the amount of analyte detected. Transistor has been used to fabrication biosensors due to its high sensitivity, rapid measurement, low power consumption, label-free detection and compatibility with large-scale integrated circuit [349–353]. Biosensors that have high sensing capability, stability and sensitivity to biomolecules are important for the early detection of a disease. The first TFT was made of a metal oxide semiconductor on a glass substrate [354]. Since then, the interest in fabricating TFTs using different metal oxides for biosensing applications has grown rapidly [355–357]. Nowadays, TFTs can also be fabricated using organic materials [358–361]. There are also studies that have fabricated FET-based biosensors using nanowires (NWs) and carbon

nanotubes (CNTs) to detect several biomarkers, including cancer and proteins, in the concentration range of nM to fM [362–366]. Such high sensitivity nanoscale FET-based biosensor that can achieve fM-level limit-of-detection (LOD) of biomarker concentration could enable label-free, single-molecule-level detection of the trace-level amount of biomarkers. This would serve as a reliable lab-on-a-chip platform for precisely determining the kinetics of various biomolecule interactions. However, the main issue with using these one-dimensional nanostructures for the nanofabrication of the highly sensitive biosensor is its affordability and high processing costs. This is because high quality, small size NWs and CNTs are required and these materials are usually produced using the bottom-up synthesis methods (such as Chemical Vapour Deposition). The high processing cost makes it not suitable for practical clinical biosensing applications. A more affordable alternative for the fabrication of highly sensitive FET biosensor is by using 2D materials [367]. 2D materials are generally single layer crystalline materials and they exhibit excellent electrical, mechanical and optical properties. They have attracted great attention to electronics applications as these materials can be easily modified to achieve conducting, semiconducting and insulating properties [368,369].

1.5 2D Materials

2D layered materials, such as graphene and Transition Metal Dichalcogenides (TMDs) have received great attention due to their intrinsic properties and their great potential to be used in a wide range of applications such as nanoelectronics, optoelectronics, energy harvesting and storage [370], and most importantly biosensing and biomedical applications. Graphene is a type of carbon in which single sheets of carbon atoms are bind to each other in a honeycomb lattice [371](Figure 1.13). The unique structure of graphene has allowed it to exhibit excellent chemical and electrical properties, which makes it an interesting material for use in the development of highly sensitive and selective biosensors [372–374]. Interestingly, another category of 2D materials, TMDs, have also shown great potential for ultra-sensitive biosensor applications [353,375]. These materials are appealing due to their intrinsic electrical properties, excellent physical properties, large abundance and compatibility with planar nanofabrication processes [376–380]. These materials are also highly sensitive to external stimuli, which makes them suitable for the production of highly sensitive FET-based biosensors. FET made of 2D layers has high quality FET channels with low densities of scattering centers (resulting in low Flicker noise level) due to the low density of dangling bonds on the surface. This

makes the biosensor to be highly sensitive and low noise level for the detection of biomolecules.

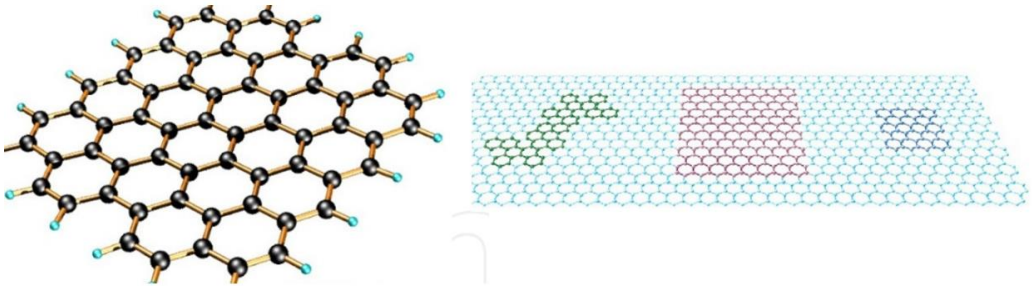

Figure 1.13: Schematic illustration of 2D graphene in honeycomb lattice structure (Reproduced with permission from ref [371]).

TMD is a family of 2D materials with a general chemical formula of MX_2. M are the transition metals from group VI-VII whereas X is a chalcogen from group VI (S, Se or Te) in the periodic table (Figure 1.14). Most TMDs have a layered structure. For layered MX_2, each X-M-X layer contains three atomic layers. The M atoms layer is sandwiched between two X atomic layers with strong covalent M-X bonds (Figure 1.15). These X-M-X layers are also bonded to each other by weak van der Waals forces [381]. Hence, TMDs can be easily thinned down and exfoliated to monolayer or several layers [382]. The oxidation states of M and X atoms are +4 and -2 respectively, forming a general formula of MX_2. The stacking of layered MX_2 can exist in two configurations: a trigonal prismatic (2H) phase or octahedral (1T) phase (

Figure 1.16). Depending on the combination of M and X, one of these two configurations will be more thermodynamically stable than the other. For example, 2H-MoS_2 is a more thermodynamically stable phase whereas 1T-MoS_2 is metastable. Although 2H-MoS_2 can be converted to 1T-MoS_2 via the intercalation of sodium or potassium ion [383,384], the 1T phase will gradually return to the 2H phase at room temperature [385,386]. The versatility of TMDs and customizability makes it a promising candidate for the fabrication of 2D electronic devices with the potential for large-scale production [387]. Due to the layered structure of TMDs, the materials have a bandgap that can be adjusted by changing the layer thickness. The existence of a bandgap can contribute to the fabrication of a highly-sensitive FET-based biosensor [388]. The single layer or few monolayers structure of these materials cause it to have a high surface-to-volume ratio which could be used to produce highly sensitive and selective biosensors. Atomically layered TMDs also exhibit the potential for next-generation low-cost transistor biosensors

that allows single-molecule-level quantification of biomolecules. In order to achieve its biosensing capability, the device needs to be calibrated for the response to enable quantification of biomolecule interaction. 2D TMDs also opens up the opportunity for short channel FETs.

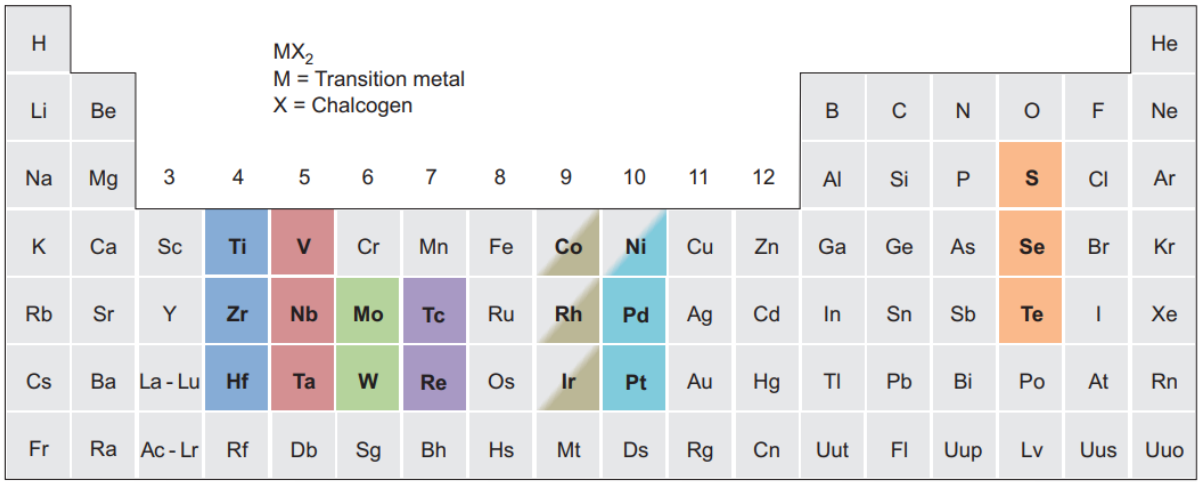

Figure 1.14: Transition Metal Dichalcogenides materials formed of transition metals (group 4-7) with elements in Chalcogen group (S,Se,Te) highlighted in a periodic table. (Reproduced with permission from ref [376]).

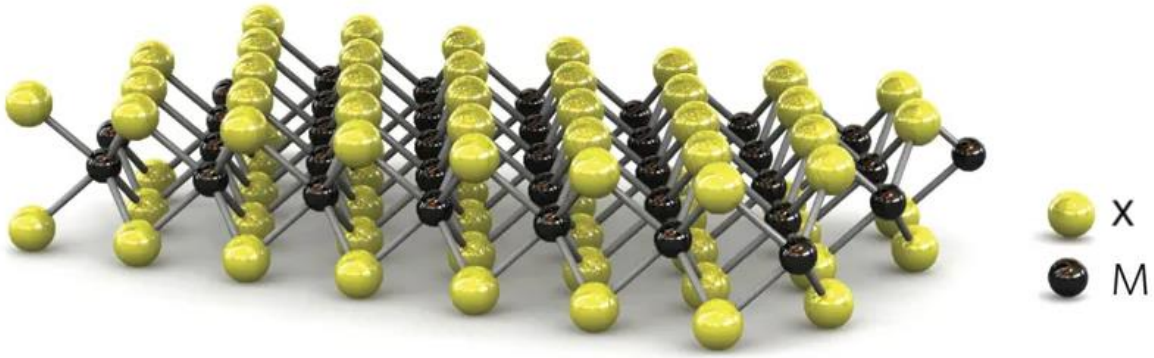

Figure 1.15: An illustration of a single layer of TMD material (Reproduced with permission from reference [379]).

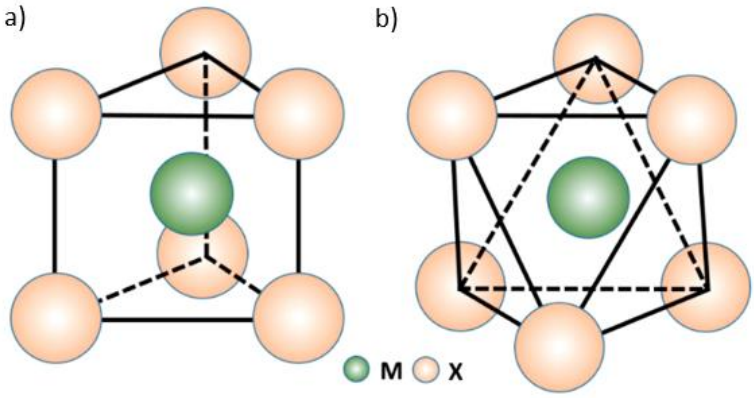

Figure 1.16: Schematic representation of coordination of MX_2 stacking a) 2H-MX_2 Trigonal Prismatic b) 1T-MX_2 Octahedral (Reproduced with permission from reference [389]).

1.5.1 Exfoliation of TMDs layers

In order to achieve the potential of these 2D materials for the use in flexible electronics applications, an exfoliation process is required so that the 2D materials are in their monolayer or multilayer forms from their bulk material. Exfoliation can be achieved mechanically or chemically [390–392]. Some of the preparation methods currently available include mechanical exfoliation with scotch tape [393], chemical exfoliation in a liquid phase and coating [394,395], chemical vapour deposition (CVD) [396], and hydrothermal synthesis and coating [397]. The scotch tape method was first used to exfoliated graphene from bulk graphite [393]. It has also been used on TMDs and there are some high performance MoS_2 devices using films of a few monolayers of MoS_2 produced by the mechanical exfoliation of MoS_2 from bulk MoS_2 single crystal using the scotch-tape method [379,382]. Although this method can produce high quality monolayer materials, it is not practical for large scale fabrications due to its low yield. The other limitation of this technique is that it is difficult to control the size and thickness of the flakes produced. Chemical approaches such as ion-intercalation can achieve a high yield of single-layer materials [398]. This method uses the concept of ion insertion in between the layers of 2D materials in order to widen the layer gaps. Generally, lithium ions are commonly used for intercalation. During the process, water is introduced to react with the intercalated ions, forming hydrogen gas in the layers that forces the layers apart [399]. Ion intercalation process can be time consuming and the process is extremely sensitive to environmental conditions, which could cause some structural deformation onto the 2D materials [400,401]. The removal of ions can cause the reaggregation of layers in the 2D materials.

The CVD approach is one of the more popular techniques as it has shown promising potential for practical applications in producing high quality layered materials [402,403]. This method can prepare a continuous layer with controllable uniform thickness directly onto a substrate from precursors of the 2D materials [404]. For example, the synthesis of MoS_2 layers uses MoO_3 as a precursor with the presence of sulphur [405,406]. The CVD process can eliminate the need for transferring the layered materials which could prevent interfacial contamination. Although CVD-grown 2D materials seem promising, they may cause some defect that could affect their electrical properties [407]. The process is also extremely expensive and has some limitation to scale up for massive production [408]. For practical concerns, the preparation of 2D material layers need to be low cost and easily scalable for large-scale production.

Liquid Phase Exfoliation (LPE) is a powerful technique to produce defect-free 2D nanosheets in large quantities. Coleman *et al*. are one of the first to propose the effectiveness of LPE for large scale exfoliation for 2D layered materials using organic solvents such as (N-methyl-2-pyrrolidone) NMP, (Dimethylformamide) DMF and (Iso-propanol) IPA [409]. In general, this method uses sonication or shearing of the 2D layered materials in selected suitable solvents to separate the layer of materials held together by VDW forces [391,409,410]. The presence of suitable ionic liquid in the exfoliation process also inserts ionic liquid molecules into the atomic layers, making the 2D materials into liquid suspensions [411]. These liquid suspensions can then be used to process into different structures such as films, coatings and composites [412–414]. This is a very cost-effective technique especially when it is required for large-scale production [415]. The surface energy of the solvent chosen for LPE plays an important role in determining the quality of the dispersion. The solvent must have similar surface energies to the 2D material [416]. Studies have proven that ultrasonication of layered materials including MoS_2 and graphene is an easy and effective way to obtain single and multilayer of these materials [391,409,417–419]. However, enhancing the yield of the single layers and maintaining the lateral dimensions of the exfoliated nanosheets can be challenging. In order to improve the yield, appropriate surfactant or polymeric solutions can be used to stabilise the nanosheets and prevent reaggregation [410,416,420]. Ideally, ionic surfactants are preferred as stabilisers as they will bind to the exfoliated nanosheets via VDW, allowing electrostatic stabilisation. Backes *et al.* reported a method based on iterative centrifugation cascades which could efficiently produce the desired nanosheet

size and also provide monolayer enrichment [410]. This method allows the production of nanosheets of desired sizes and thickness distribution which is particularly useful as the exfoliation of nanosheets can be controlled according to the need of the application.

1.5.2 Molybdenum (IV) Sulphide (MoS_2)

MoS_2 is a semiconductor and has been the most appealing material amongst all TMDs. This is mainly due to its unique intrinsic properties such as mechanical flexibility, high electron mobility properties and large tuneable bandgaps. MoS_2 crystals are vertically stacked and the interacting layers are held together by weak van der Waals forces [379]. The natural lamellar structure of MoS_2 with three atom layers (S-Mo-S) stacked together allows the thickness of MoS_2 layers to have good scalability. MoS_2 also exhibit no surface dangling bonds and has thermal stability of up to 1100°C, which makes it an attractive material for use in nanoelectronics applications [353,379]. The absence of dangling bonds is attributed to the lone-pair electrons on the sulphide atoms, terminating the surfaces of the layers. MoS_2 also exhibit high mechanical flexibility (Young's Modulus 240-270 GPa) due to their 2D nanosheet structure [421]. This makes it a suitable material to be used as a flexible sensor and can be used for the development of wearable and implantable biosensor devices. MoS_2 has a similar structure to graphene and has attracted great attention in the field of nanoelectronics [379]. Another material that is very similar to MoS_2 is graphene, which is also a very popular 2D layered material that has been used in the fabrication of nanoelectronics. However, graphene has no bandgap, which causes insufficient current on-off ratio and little voltage gain. This can be a disadvantage as it compromised the sensitivity and selectivity when it is being used to fabricate sensors [352]. On the other hand, MoS_2, in its monolayer, typically has a direct bandgap of 1.8eV. Unlike graphene, the presence of bandgap in MoS_2 can be used to produce transistors with high on/off ratio and intrinsic voltage gain [378,422–424]. Studies have shown that MoS_2-based transistor can have high on/off current ratios of up to 10^8, which is essential to produce a highly sensitive biosensor [379,425]. Moreover, MoS_2 has great potential for biosensors as the binding event at the interface between MoS_2 and the charged biomolecules can be monitored by a direct change of the transistor performance metrics [426]. As for graphene, the graphene surface needs to be functionalised to achieve high sensitivity which introduces additional complexity to the fabrication process [427]. The potential of MoS_2 is so great that if it can be effectively used to fabricate large area and defect-free film, it could revolutionise the flexible electronics industry. MoS_2-based

transistors fabricated on rigid silicon wafers or glass substrates have shown superior electronic properties [428,429]. However, the main challenge remains in the preparation of high quality monolayers or several layer MoS_2. Currently available methods such as mechanical exfoliation and chemical vapour deposition (CVD) are suitable for lab settings and seems to be challenging for large scale production.

The first high mobility single-layer MoS_2 channel on SiO_2/Si wafers of was reported by Perkins *et al*. The monolayer flakes of MoS_2 were exfoliated from bulk samples using the scotch tape method and were used to produce a chemical vapour sensor. The results showed that the sensor had great selectivity and was unaffected by the presence of many other analytes or gases [427]. A highly sensitive glucose biosensor fabricated using a bilayer molybdenum disulphide (MoS_2) based field-effect-transistors (FETs) was introduced by Shan *et al*. [430]. The study has shown that the biosensor has a sensitivity and can detect glucose even at extremely low glucose concentration solution. The MoS_2-based biosensor glucose biosensor also showed short response time (<1s), good stability and wide linear detection range (300nM to 30 mM). This study has proven the bilayer MoS_2-based FET has a great potential to be used for the fabrication of next generation biosensor [430]. Sarkar *et al*. also demonstrated that MoS_2 is a suitable material to be used as a channel material for a FET biosensor. A highly sensitive MoS_2-based pH sensor was introduced. The sensor also showed specific protein sensing ability and the sensitivity of MoS_2-based sensor surpassed the graphene-based sensor by more than 74-fold. The study has proven again that MoS_2 exhibit excellent electrostatics and sensitivity due to its atomically thin nature and presence of bandgap. Its excellent mechanical properties also allows easy patternability and scalability [388]. Lee *et al*. also created a MoS_2 biosensor that can electrically detect prostate-specific antigen (PSA) [426]. However, unlike to biosensor from Sarkar *et al*., the MoS_2-FET-based biosensor has no dielectric layer which improves the sensitivity and simplifies the sensor design. This is because the dielectric oxide surface layer is hydrophilic which makes the surface functionalization difficult and binding event inefficient. On the other hand, the hydrophobic nature of MoS_2 makes it an excellent candidate for functionalizing antibody and protein. The study has proven the potential of fabricating a highly sensitive dielectric-free MoS_2-based biosensor [426]. The group also demonstrated an improvement in the reliability and the quantitative detection of biomolecules in a non-aqueous environment by excluding non-specific binding using this MoS_2-FET biosensor can provide reliable and quantitative in a further work [431].

Yoo *et al*. have also reported the use of MoS_2-FET biosensor for real-time biomolecule detection that can be used as a point-of-care diagnostic tool. The study presented an FET-based biosensor that can allow real-time detection of PSA up to a concentration of 1pg/mL without specific surface treatment for anti-PSA immobilisation on the MoS_2 surface. The anti-PSA antibody can be physically absorbed to the MoS_2 channel without pre-surface chemical treatment due to the hydrophobicity of MoS_2 surface [432]. Zheng *et al.* also reported a sensitive MoS_2-based FET H_2O_2 sensor but was constructed using MoS_2/reduced graphene oxide (RGO) interface. Here, MoS_2 was used as a catalytic layer and RGO was used as the conductive layer [352]. However, the limitation of this method is that the nanosheet thickness distribution is broad monolayer content can be low. Wang *et al*. have also demonstrated that ultrasonication of MoS_2 can produce MoS_2 nanoparticles which were then used to fabricate a sensitive biosensor that can detect small concentrations of H_2O_2 [419]. The high activity of MoS_2 nanoparticle modified electrode toward the reduction of H_2O_2 creates the possibility of fabricating a glucose biosensor. Many research work has proven that MoS_2 is a promising material and exhibit significant potential for the fabrication of next-generation low-cost electronic devices with high biosensing capabilities. Despite the promising results, these achievements are mostly limited to laboratory level.

1.5.3 Printing of LPE MoS_2

MoS_2 nanosheets produced using the LPE technique can be used as functional inks which is suitable to be used in printing [433,434]. Printing techniques can be effective for the fabrication of electronic devices as it has the ability to produce well-defined shapes without masking which is often required for traditional screen printing or photolithography [435]. For instance, Direct-Ink-Writing (DIW) is an additive manufacturing technique that dispenses ink through a nozzle within the range of mm to μm scale. This method is capable of depositing ink with high levels of spatial control and accuracy [436]. Printing of sensors is a promising method particularly for the fabrication of flexible sensing devices [437]. This is because the printing of flexible electronics has simplified processing steps, the ability to produced organised patterns, and can reduce materials waste [327,438]. The flexibility of printing technologies also opens up the possibility of developing sensors and electronics on non-planar surfaces. This has led to the development of printed electronics on flexible substrates that has been successfully used as electronic skin applications and other biomedical applications [439,440]. In

general, printing technologies can be categorised into two different methods: the contact printing and the non-contact printing. The contact printing process is where there is contact between the patterned structure of the inked surfaces with the substrate. In non-contact printing, the ink is dispensed onto the substrate and the pattern structures are obtained through the moving substrate holder that is pre-programmed [437]. The non-contact printing techniques are more popular as the process is more simple and easy to control with only a few parameters to adjust, the patterns have higher resolutions, and the process is quicker with less material waste [441–444].

Kelly *et al*. have demonstrated the feasibility of inkjet printing thin-film transistors (TFTs) using the LPE prepared nanosheets of various 2D materials [445]. The printed TFTs are vertically stacked, where graphene was used as source, drain and gate electrodes, a channel of TMD and boron nitride were used as a separator. It was shown that the nanosheet dispersion sprayed onto flexible alumina-coated polyethylene-terephthalate substrates form a uniform porous nanosheet network over length scales greater than 10 µm. The study also showed that the nanosheets can be thermally activated as the electrical conductivity increases as the temperature increases [446]. The on-currents of the nanosheet network channels depend on the network thickness and volumetric capacitance. It was found that the all-printed TFTs can carry high currents and relatively low drive voltages [445]. The suitability of LPE prepared MoS_2 for inkjet printing has also been demonstrated by Li *et al*. [447]. In this study, MoS_2 ink was prepared using solvent exchange and polymer stabilisation technique so that the prepared ink has the right viscosity for inkjet printing. The prepared multilayer MoS_2 nanosheet has a thickness of 5-7 nm and can be used to print conformal and uniform patterns with a resolution of about 80 µm. The study managed to print MoS_2-based TFTs integrated with printed silver nanoparticles to enhance the photoluminescence properties of the MoS_2. In addition, Nam *et al*. were able to fabricate a highly sensitive transistor-based biosensor using few-layer of MoS_2 as a sensing channel. The MoS_2 transistor was fabricated using a microprinting method [448] and the channel thickness was controlled to be 15-20 nm. The MoS_2 channel was then functionalised by depositing an HfO_2 layer using atomic layer deposition (ALD). The biosensor was able to measure the concentration of analyte solutions and the affinity and kinetic properties of the analyte-receptor pair. The biosensor had a tumour necrosis factor – alpha (TNF-α) detection limit of as low as 60fM [326].

1.6 3D Printing of Sensor

3D printing seems to be a suitable technology to be used in the manufacturing of sensors as it is a highly precise technique and is known to be able to produce geometrically complex shapes easily. Comparing with the conventional fabrication techniques of sensors such as lamination and lithography, 3D printing seems to have the advantage of being low cost, less time consuming and fewer processing steps that are complicated. Due to these advantages, 3D printing has gained much attention in the fabrication of sensors. Researchers have successfully produced different types of sensors, including pressure sensors [449–451], biosensors [452–454], and wearable sensors [455–457] using 3D printing. There are two types of 3D printing of sensor, 3D printing the structure or substrate where sensors can be embedded onto it [458], and printing the entire sensor [459]. A study carried out by Emon *et al.* has developed a custom made 3D printer consists of 3 printing nozzle that is capable of fabricating a multimaterial soft pressure sensor [460]. This pressure sensor was built of an ionic liquid-based pressure-sensitive layer sandwiched between carbon nanotube-based stretchable electrodes and encapsulated with stretchable insulating layers printed out of a photopolymer TangoPlus. This method of printing the entire sensor without any manual handling could be revolutionary and allows design flexibility of the sensors

The inkjet printing technology is one of the first successful applications for the fabrication of sensors via printing methods [461]. Inkjet printing has been successfully used to produce a flexible temperature sensor capable of measuring the temperature on the surface of the human body [462,463]. The low cost FDM 3D printing technology has been used for strain sensor fabrication [464]. Kwok *et al*. has successfully used FDM 3D printing to produce a 3D printed circuit using self-extruded conductive filaments [465]. The study showed that there is a potential for low-cost 3D printing to produce sensors. A study by Adams *et al.* showed the first attempt of 3D printing a graphene-based glucose sensor using a low-cost FDM 3D printer [454]. This is a proof-of-concept study that successfully showed that the 3D printed sensor was able to detect physiological glucose concentrations between 0 and 400 mg/dL. The study has shown that 3D printed glucose sensor is a promising alternative to self-monitoring blood glucose devices. Gowers *et al.* also used 3D printing technologies to produce a microfluidic platform that can be integrated with biosensors that can measure real-time glucose and lactate levels subcutaneously [466]. The microfluidic chip and the needle holders which is integrated

into the microfluidic platform were printed using two different 3D printers. The needle biosensors are removable and can be joined to a clinical microdialysis probe for continuous monitoring. The novel 3D printed microfluidic device is modular, which means the biosensors can be changed easily, making it suitable for a wide range of clinical, as well as fitness applications.

Other 3D printing methods such as stereolithography has been successfully used for the printing of fluidic devices for various types of analysis [467–471]. A stereolithography based 3D printing technique was used to produce a plastic closed-channel fluidic device as part of a biosensor that can carry out electrochemiluminescence (ECL) measurements using DNA-coated graphite electrodes [472]. ECL typically has excellent sensitivity and specificity as the electrogenerated optical signal eliminate the background signals. The results showed that a relatively low concentration of co-reactant DNA can still be detected through ECL measurements. The 3D printed fluidic device is low-cost, customisable and allows quick modifications and revisions to be carried out to adapt other electrochemical sensing abilities. Another study by Li *et al.* used a multimaterial FDM 3D printer that is capable of printing up to 5 different materials to fabricate a fluidic device for the measuring of pharmaceuticals in biological fluids [473]. Such devices can be used as Lab-on-Chip applications which have now attracted much attention due to their simplicity, portability and cost-effectiveness [468,474]. The whole fluidic device was printed using 4 different materials and can be produced in a single uninterrupted 3D printing process. The device was capable to simultaneously extract and concentrate small molecule pharmaceuticals from urine samples. Electrophoretic separation can also be carried out on the sample on the concentrated targets for quantitative analysis. It was reported that this 3D printed fluidic device allowed the direct quantification of ampicillin in untreated urine sample within 3 min.

Direct-ink-writing (DIW), which is similar to FDM has also been used to fabricate strain sensors [475,476]. Apart from that, a study to prove the concept of manufacturing a flexible electrochemical biosensor for glucose monitoring using the DIW printing method was carried out [347]. The study uses a custom-built DIW printer where the printing nozzle has a diameter of 200 µm. The printing head is connected to a positive pressure pump for ink dispensing. Prussian blue modified electrode was first printed onto a tattoo paper, then dried at 100 °C under vacuum condition before the printing of the glucose oxidase enzyme was carried out on top of the dried carbon electrode. The performance of

the electrode is compared with the conventional screen-printed electrodes for its glucose-sensing capabilities. The study showed that the 3D printed electrodes were more uniform and have smoother surfaces, hence improving its sensitivity for glucose sensing. The 3D printed glucose biosensor was able to detect micro-molar levels of glucose with the presence of other interfering molecules. Conventional screen printing is more time-consuming and material wastage as compared to DIW. Apart from that, the sensors produced by DIW also have better reproducibility, repeatability and long-term stability.

Dirkzwager *et al*. demonstrated the possibility of 3D printing an aptamer-based point-of-care diagnostic (POC) device which could potentially be used for the diagnosis of malaria [477]. This is a proof-of-concept study that was carried out to offer an alternative to the conventional malaria diagnosis using light microscopy which can only be used in a lab setting. The development of such POC devices have the advantages of being portable, simple to interpret, and require limited expertise. 3D printing was used to produce a paper-based syringe test and magnetic bead-based well test. The syringe test was more sensitive, but more preparation steps were required to prepare the sample, whole blood, before the testing was carried out. On the other hand, whole blood can be tested directly using the well test without any preparation steps prior to testing, which seems to be more suitable and convenient as a POC diagnostic device. These devices were designed with a simple colorimetric assay in which the results can be interpreted easily by visual analysis. The study has proven that such diagnostic devices are very cost-effective due to their simplicity and stability for storage of up to 2 months at room temperature.

1.7 Outline of the thesis

This thesis contains the research work that has been designed and carried out to fulfil the aims and objectives that will be discussed further in chapter 2. The research findings and results are discussed in detail in the following chapters and the content of the thesis can be summarized as follow:

Chapter 1 provided an in-depth review on the technologies that are being used to carry out the research and a few other research topics regarding sensors for biomedical applications. The two main technologies being reviewed are the Fused Deposition Modelling (FDM) 3D printing and the hot-melt extrusion technology. The review on how these two technologies can be combined to help promote the applicability of FDM 3D

printing for pharmaceutical and biomedical applications was also carried out. Different biomedical sensors, the materials used for the sensors and the fabrication techniques of the sensors were also covered in this review.

Chapter 2 discussed the aim and objectives of the research.

Chapter 3 showed an investigation on the miscibility of a biocompatible polymer, polylactic acid (PLA), with a widely used pharmaceutical plasticiser, polyethylene glycol (PEG), to produce a biocompatible and biodegradable polymeric matrix that can be suitable for a wide range of biomedical applications. The study focused on the effect of different PEG grades when mixed with PLA to form PEG/PLA blends.

Chapter 4 showed a preparation study for producing 3D printable biocompatible filaments made of PEG/PLA blends using a single-screw filament extruder.

Chapter 5 extended the investigation of the PEG/PLA filaments with enhanced physico-chemical properties by using a twin-screw extruder.

Chapter 6 aimed to develop and optimise a polymeric composition that can be made into filaments in which the filaments can be loaded with a drug and used for the FDM 3D printing of a drug delivery device.

Chapter 7 showed a study of loading metformin as an active ingredient in some polymeric blends extrudable into 3D printable filaments with the aim to produce sustain-release metformin containing medical device/implant.

Chapter 8 showed two different simple techniques that can be used to fabricate flexible temperature sensors which can be used for biomedical applications.

Chapter 9 investigated a simple preparation method of Molybdenum (IV) Sulphide (MoS_2) solution which was then used as one of the materials for the fabrication of a flexible glucose biosensor.

Chapter 10 contained a conclusion and a short summary of the research findings. Suggestions for possible future investigations were also discussed.

Chapter 2 : Research aim and objectives

2.1 Aim and objectives

Three-dimensional (3D) printing, also known as additive manufacturing, has appeared as an emerging manufacturing technology across various industries. Unlike conventional fabrication methods such as injection moulding or Computer Numerical Control (CNC) machining, 3D printing can easily produce complex-shaped objects. Hence, the technology allows much more flexibility and freedom in designing an object. The most easily accessible 3D printers are the desktop 3D printers that use the Fused Deposition Modelling (FDM) printing technology. This type of 3D printers and the printing materials are low-cost and very affordable. Due to the affordability of this technology, it has gained much popularity across many industries. However, the use of the FDM 3D printing technique is somehow limited mostly to prototyping product. This is because the printing technique uses thermoplastic polymers as the feedstock material and most plastics do not exhibit excellent mechanical properties. Apart from that, most polymers used for FDM 3D printing are not biocompatible and biodegradable, which makes it to have limited applications in biomedical and pharmaceutical applications.

In recent years, much research has been carried out on developing biocompatible filaments in order to promote the usage of FDM 3D printing for biomedical and pharmaceutical applications. This is because there has been an increasing interest in personalised and patient-specific products in the biomedical industry. Personalisation in the biomedical application has been a much discussed topic as it can improve treatment efficacy, help reduce any treatment-related side-effects, and most importantly lead to a better quality of life. However, the production of personalised devices using traditional manufacturing method can be expensive and disruptive as most traditional manufacturing methods are designed for mass production. Hence, 3D printing has attracted much attention as its additive manufacturing technique is more suitable and cost-effective for producing customised devices.

In addition to personalised medical devices, smart medical devices have become increasingly popular as well. Smart medical devices play an important role in healthcare monitoring and diagnostics as they are designed to continuously monitor and measure the vital signs of our human body. For example, various minimally invasive continuous glucose monitoring systems have been developed in recent years. This has made glucose

level monitoring more patient-friendly as diabetes patients do not have to regularly measure their own blood sugar level by pricking their own fingers using the finger stick blood test. The continuous glucose monitoring system also shows the trend of the glucose level in the patients, which could provide warning signs of hypo and hyperglycaemic events to the patients [478]. There are many other examples of smart medical devices. Nevertheless, the function of these smart devices depends heavily on reliable sensors. Sensors that are used for biomedical applications can be called biosensors. There have been much interest on developing reliable biosensors using simple fabrication techniques in order to reduce the cost of biosensors [479–482]. Reducing the cost of biosensors can improve the affordability of such technologies so that more people can enjoy the benefit of improved healthcare.

2.1.1 Aim

The research aim is to utilise the potential of 3D printing technology as a simple and cost-effective method to fabricate pharmaceutics and biomedical devices. The FDM 3D printing technique will be the focus as is the most affordable and widely available 3D printing technology. Apart from that, the fabrication of reliable biosensors using simple manufacturing techniques such as 3D printing and thin-film deposition is also investigated.

2.1.2 Objectives

As most of the widely available thermoplastic filaments used in FDM 3D printing are not biocompatible, the filaments cannot be used for pharmaceutical and biomedical applications. One of the objectives is to produce biocompatible filaments with enhanced physico-chemical properties so that the filaments can be used for a wide range of biomedical applications. The fabrication of filaments can be easily achieved in-house using a benchtop hot-melt extruder.

Apart from that, most thermoplastic filaments require a relatively high temperature for it to melt or soften during the 3D printing process. The high heat exposure to the materials may not always be desirable especially for pharmaceutical applications. This is because most active pharmaceutical ingredients and excipients are thermally sensitive. Prolonged exposure to high temperature may cause degradation. Hence, the study to produce filaments that exhibit lower melting temperature was carried out. This was carried out by

investigating the effect of a plasticiser on a biocompatible polymer that has been widely used to produce 3D printable filaments.

The research also involved an investigation to fabricate customisable drug-loaded filaments for the 3D printing of pharmaceutics. The drug can exhibit different release patterns when being loaded onto different polymeric compositions. The ability to produce customisable filaments with a desired drug release profile using simple technologies such as the hot-melt extrusion and FDM 3D printing can promote the use of personalised treatments even in local hospitals situated in remote areas.

The possibility of using 3D printing to fabricate other biomedical diagnostic devices such as temperature sensors was also investigated. 3D printing and thin-film fabrication technique were used to produce flexible temperature sensors than can be used for biomedical applications. The flexible temperature sensors are modular and can be transferred and integrated with other biomedical or drug delivery devices for better treatment efficacy.

A novel and simple technique for fabricating a thin-film and flexible glucose biosensor was also investigated. The use of a novel 2D material, Molybdenum (IV) Sulphide, that exhibit intrinsic electrical properties was evaluated by using it to fabricate a conducting thin-film for glucose biosensing. The conducting thin-film was immobilised with glucose oxidase enzyme to perform glucose oxidation for glucose sensing purposes. Similarly, the thin-film glucose biosensor is modular and can be integrated with a drug delivery system to produce a smart medical device.

In general, the major objectives and deliverables of the research work in this thesis can be summarised as follows:

- Investigate the plasticising effects of different polyethylene glycol (PEG) grades on a biocompatible polylactic acid (PLA) polymer.

- Evaluate the fabrication of PEG/PLA biocompatible polymeric mixture into 3D printable filaments using a single-screw filament extruder.

- Evaluate the effectiveness of producing PEG/PLA mixture into filaments using the twin-screw hot-melt extrusion technique.

- Develop and optimise polymeric compositions to achieve different release patterns for an API, theophylline. The drug-loaded polymeric mixtures were made into 3D printable filaments using the twin-screw extrusion technique to achieve better mixing efficiency. The drug-loaded filaments were then used to produce 3D printed tablets for the investigation on drug release. The study also investigates the effectiveness and feasibility of coupling the hot-melt extrusion (HME) technique with FDM 3D printing as a continuous manufacturing process.

- Develop sustained-release metformin systems via twin-screw extrusion and 3D printing by utilising the optimised compositions for theophylline. Another polymeric composition that is capable of 3D printing at a much lower temperature and still exhibits sustained-release pattern was investigated.

- Develop flexible temperature sensors for biomedical applications via FDM 3D printing and thin-film fabrication technique which is widely used for the production of microelectronics. The 3D printed temperature sensors were printed using conductive PLA filaments, one contains carbon black and the other contains graphene. The temperature sensors produced suing the thin-film fabrication technique is made of a thin layer of gold on a flexible polyimide film. The performances of the different temperature sensors were evaluated.

- A flexible glucose biosensor was developed using a similar thin-film fabrication technique for the temperature sensor. The conductive electrode of the glucose biosensor consists of gold and MoS_2. The glucose biosensor surface was functionalised with glucose oxidase enzyme, which would create electrons during the oxidation of glucose. The current produced can be used as a measure for glucose detection.

Chapter 3 : Investigation on the miscibility of polylactic acid and polyethylene glycols

3.1 Introduction

Plastics are now very common materials that are used in daily lives and they are made up of long-chain of molecules called polymers. Polymers are a large chain of molecules made of repeating smaller units called monomers [483]. The monomers are bonded together to form polymers via a process called polymerisation [484]. Bioplastics have been a great area of interest for research due to environmental concerns [485,486]. They are usually produced from renewable sources such as derivatives from plants or microorganisms and are degradable by nature over a reasonable period of time [485,487–490]. Bioplastics not only are better for the environment, but they are also suitable candidates to be used for the production of biomedical and pharmaceutical products [491–494]. For the bioplastics to be used for biomedical and pharmaceutical applications, they need to be biocompatible with the human body. Biocompatibility means materials that are acceptable to the human body and are not harmful nor toxic when being used in the human body [495,496].

Polylactic acid (PLA) is one of the most commonly available biopolymers that is typically made from plants such as corn starch, dextrose or other biomass [497,498]. There are many different methods of producing biocompatible PLA [499]. One of the more commonly materials used are corn kernels, which are milled to extract dextrose, and then further fermented to obtain lactic acid [500]. Typically, lactic acids are not directly polymerised into PLA as water will be produced. The water molecules can prevent the growing chain of lactic acid molecules from staying together. Therefore, smaller chains of polylactic acids are first formed, called polylactic acid oligomers, from the lactic acid monomers. The water produced from this processing step can be removed before the polymerisation reaction is carried out to produce PLA. The final long-chain PLA is produced via ring-opening polymerisation. Lactide is an intermediate product for the production of PLA, which is the ring-firmed dimer of lactic acid [501]. The process of PLA polymerisation is depicted in Figure 3.1.

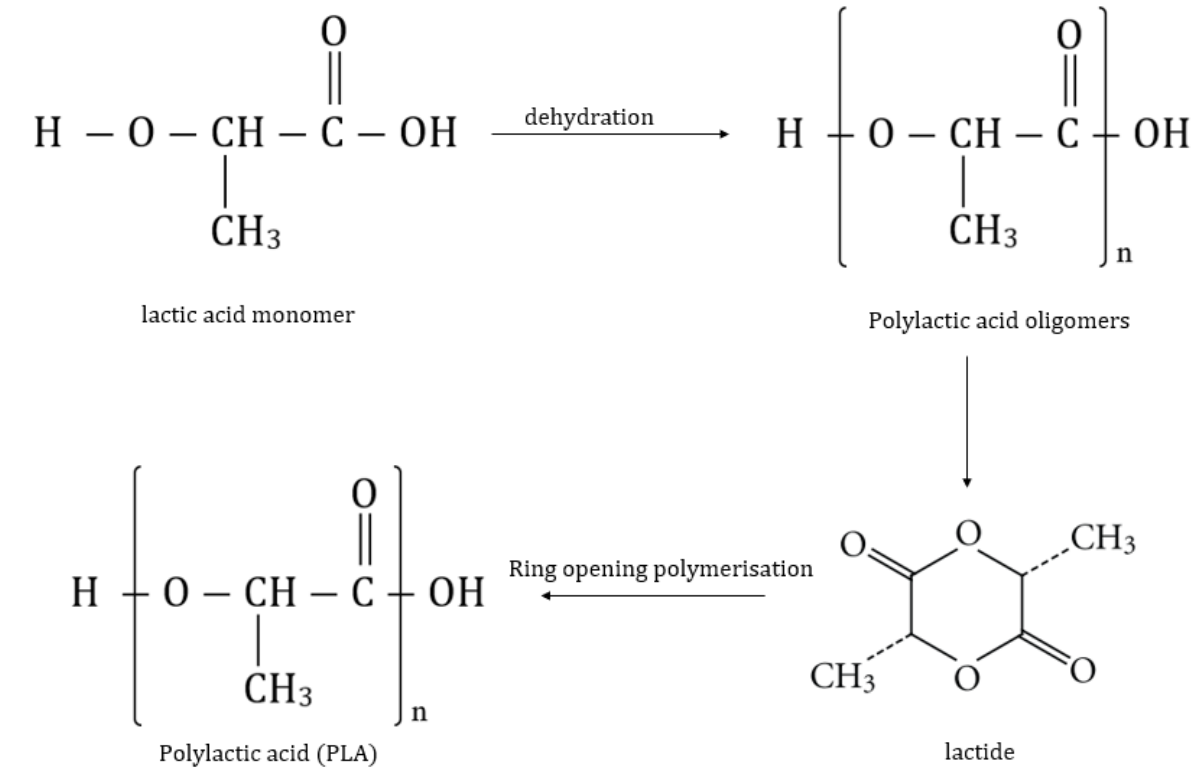

Figure 3.1: Process of producing polylactic acid (PLA) from lactic acid monomer (n is a large number).

PLA is classified as 'not dangerous' according to the European Directive 67/548/EEC. It is also being listed in the United State Food and Drug Administration (FDA) inactive ingredients for approved drug products database as well as being classified as generally recognised as safe (GRAS) material by the FDA [502,503]. PLA is a biodegradable thermoplastic polymer. It can be easily found as a material to produce carrier bags [504], food packaging [505], plastic containers [506], and textiles [507]. Apart from that, it has also received much attention from the medical industry to produce wound dressings [508], sutures [509], stents [510], scaffolds for tissue engineering [511], bone and dental fixations [512,513], as well as drug delivery systems [514]. PLA has been used in pharmaceutical applications as coating agents and controlled-release agents [515–517]. It has successfully been used to produce implants, injections and other drug delivery systems [518–521]. However, the applications in PLA for implants are often limited due to its poor mechanical properties. For instance, pure PLA is brittle in nature, exhibit poor flexibility and strength [522,523]. Therefore, additives were often used to produce a polymer composition for the enhancement of their mechanical properties [524].

Plasticisers are one of the most commonly used additives in the polymer industry to improve the flexibility and processibility of polymers [525]. According to the council of International Union of Pure and Applied Chemistry (IUPAC), plasticiser can be defined as a substance or material incorporated in a material to increase its flexibility, workability, or distensibility [524]. The purpose of a plasticiser can help reduce the hardness, increase the chain flexibility, processability, resistance to fracture and dielectric constant of a polymer [526,527]. The addition of plasticisers can also lower the glass transition temperature (T_g) of the polymer as it acts as spacers between the molecules so that less energy is required for the molecules to rotate and move around [522]. Plasticisers are also commonly used in pharmaceutical applications as one of the ingredients in the composition of solid oral dosage forms. Biocompatible plasticisers are often preferred when designing polymeric compositions for use in pharmaceutical applications. Some of the most commonly used biocompatible plasticisers include polyethylene glycol (PEG), ethyl cellulose (EC), triethyl citrate (TEC), acetyl triethyl citrate (ATC) and glycerol [523,524,528–530]. In this study, the effect of PEG as a plasticiser on PLA was investigated.

PEG has a general formula of $H(OCH_2CH_2OH)_nOH$ and the chemical formula is depicted in Figure 3.2. PEG polymers are formed via the ring-opening polymerisation reaction of ethylene oxide and water under pressure in the presence of a catalyst [531,532]. Similar to PLA, it is also listed in the FDA inactive ingredients for approved drug products database. PEG can exist in different molecular weights, ranging from 200 to 20000 g/mole [533]. Depending on the molecular weight, PEG can exist in liquid or solid. Typically, low molecular weight PEG exists in liquid form at room temperature, whereas higher molecular weight PEG is in solid form at room temperature. The different molecular weight of PEG exhibit different functionalities. Bolourchian *et al*. carried out a study to investigate the effect of different molecular weights PEG as a drug carrier in a solid dispersion system on the dissolution behaviour. The study reported that PEG with higher molecular weight showed higher phase solubility of drug [534].

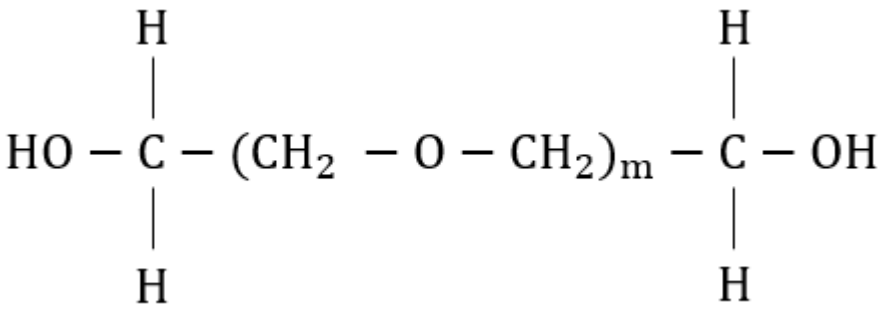

Figure 3.2: Chemical formula for Polyethylene glycol (PEG), m represents the average number of oxyethylene group.

PEG is commonly found in pharmaceutical products as an ointment base, plasticiser, suppository base, tablet and capsule lubricants [535–538]. PEG is hydrophilic in nature and can be used to enhance aqueous solubility or dissolution characteristics of poorly soluble compounds [534]. Higher molecular weight PEG is known to be more effective as tablet binders and it can better impart plasticity to the blend [539,540].

It is a well-known issue that PLA has some poor mechanical properties such as brittleness, and blending PLA with plasticisers is cost-effective to improve its flexibility [541]. Improving its mechanical properties can improve the usability of PLA particularly for biomedical applications. PEG is generally regarded as non-toxic and non-irritant, hence it is suitable to be mixed with PLA to form a biocompatible polymer blend [531,542]. Some studies have shown that PEG is an effective plasticiser for PLA [543–545]. Other reports showed that incorporating PEG into PLA can lower the T_g of PLA [545–547]. This study aims to investigate the effect of different molecular weight PEGs on the properties of PLA. The PEG/PLA blend was produced using a low-cost solvent casting method. The PEG/PLA blends were produced in the form of films and the chemical, thermal and degradation properties of the PEG/PLA films were being studied.

3.2 Materials

Polylactic acid (PLA) pellets (Ingeo™ Biopolymer 2002D grade) were purchased from NatureWorks (Minnetonka, US). Different grades of Polyethylene glycol (PEG) used were purchased from Fisher Scientific (Loughborough, UK). The different PEG grades used were 200, 400, 600, 1000, 6000, 8000, 10000. Analytical grade dichloromethane was purchased from Sigma Aldrich (Gillingham, UK). All chemicals were used as received.

3.3 Experimental Methods

3.3.1 Preparation of PEG/PLA Films

The PEG/PLA films were prepared using the solvent casting method. PLA was mixed with different grades of PEG and the formulation for each PEG/PLA films were shown in Table 3.1. The higher the PEG grade, the higher the molecular weight of the PEG. PLA pellets were first dissolved in dichloromethane at a concentration of 10% w/v. The PLA was dissolved using a magnetic stirrer at around 800 rpm until a clear solution was obtained. PEG was then mixed into the clear PLA solution until fully dissolved. The concentration of PEG in PLA for all blends were 20% w/w. The PEG/PLA solution was then cast onto glass petri dishes and allowed to dry. The films were then dried in the oven at 45°C for 24 hours to ensure the full evaporation of dichloromethane.

Table 3.1: Formulations of PEG/PLA for different PEG grades.

Formulation No.	Grade of PEG	State of PEG at room temperature	Composition of PEG/PLA (%)
P1	200	Liquid	20/80
P2	400	Liquid	20/80
P3	600	Semi-solid	20/80
P4	1000	Solid	20/80
P5	6000	Solid	20/80
P6	8000	Solid	20/80
P7	10000	Solid	20/80

3.3.2 Characterisation of PEG/PLA blends

3.3.2.1 Differential Scanning Calorimetry (DSC)

A DSC 4000 system (Perkin Elmer, Waltham, MA, US) was used to study the glass transition temperature and the melting temperature of the PEG/PLA films. The samples used were about 5mg. The samples were placed in an aluminium pan, and an empty aluminium pan was used as a reference. The chamber was heated from 30 °C to 200 °C at a rate of 10 °C/min. Nitrogen gas was used as the purged gas at a flow rate of 20 mL/min in all the DSC experiments. The data were collected and analysed with Pyris software (Perkin Elmer).

3.3.2.2 Thermogravimetric Analysis (TGA)

The thermal stability of PEG/PLA blends was analysed using TGA. The analysis was carried out using Q40 Thermogravimetric analyser (TA Instruments, New Castle, DE, US). The samples were weighed to be about 10 mg and were placed in an open aluminium pan. The furnace was heated from 30 °C to 500 °C at a rate of 10 °C/min. Nitrogen gas

was used as a purge gas at a flow rate of 20 mL/min. The results were collected and analysed using the Advantage/Universal Analysis Software (TA Instruments)

3.3.2.3 Chemical structure characterisation

Fourier Transform Infra-Red (FTIR) analysis was carried out to study the interaction of the intermolecular chains between PEG and PLA. The FTIR analysis was performed using a Spectrum Two FT-IR Spectrometer (PerkinElmer, Waltham, MA, USA). The spectra were collected using 16 scans between wavenumber 4000-500 cm^{-1} with a resolution of 4.0 cm^{-1}. The results were analysed using the PerkinElmer Spectrum^{TM} 10 software and were displayed as a percentage of transmission.

3.3.2.4 X-ray Diffraction (XRD)

XRD was carried out on the PEG/PLA and pure PLA solvent cast films. The samples were first ground into smaller particles and were assessed using a Siemens D500 X-ray Diffractometer (Siemens, Germany). The samples were scanned between 2 Theta(θ) =5° to 50° using 0.01° step width and 1s time count. The divergence slit was 1mm and the scatter slit was 0.6mm. The X-ray wavelength was 0.154 nm in Cu source and at a voltage of 40 kV.

3.4 Results and Discussion

The PLA pellets used are yellowish-white opaque pellets which have a very high hardness and cannot be mechanically ground. It is insoluble in water, but is soluble in organic solvents such as dichloromethane, ethyl acetate, chloroform, and acetone. Since the pellets cannot be easily ground into fine powders, the most cost-effective way of mixing PLA with PEG is by first dissolving PLA in dichloromethane. The different PEG grades were then further mixed with the PLA solution. Examples of a dried PEG/PLA film obtained was shown in Figure 3.3. The films are white in colour and completely opaque when dried. These films were used for the different studies that are carried out below.

Figure 3.3: An example of dried PEG/PLA film produced from solvent casting.

3.4.1 Differential Scanning Calorimetry (DSC)

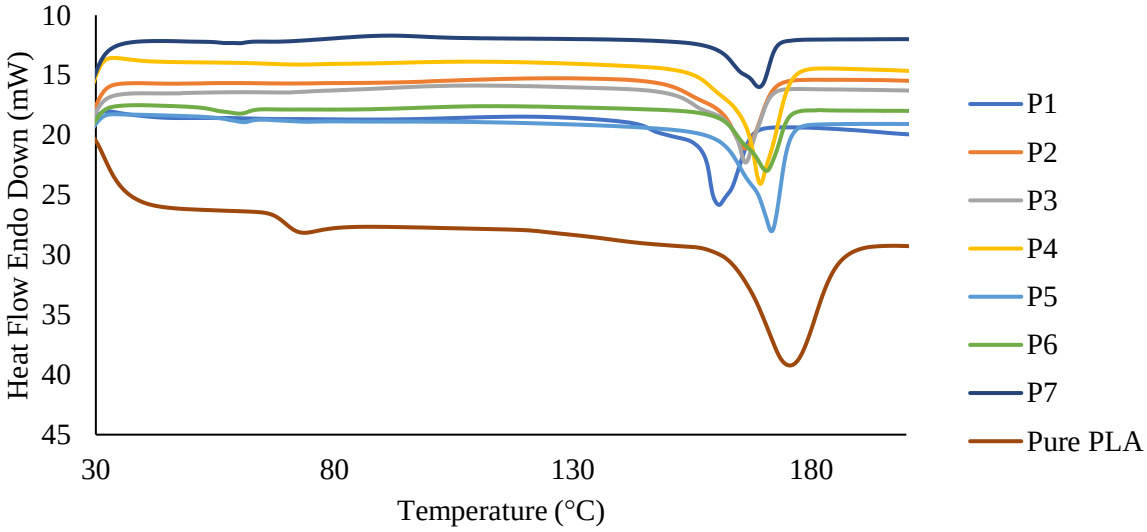

Figure 3.4: DSC thermograms for different PEG/PLA films.

Table 3.2: Glass transition temperature (Tg), melting temperature (Tm) and heat enthalpy value (ΔH) extracted from the DSC curves in Figure 3.4 for different PEG/PLA films.

Samples	T_g (°C)	T_m (°C)	Heat enthalpy value (ΔH) for T_m (J/g)
Pure PLA	73.66	175.78	47.6
P1	-	160.19	70.5
P2	-	166.43	73.0
P3	-	166.42	61.7
P4	-	169.29	72.0
P5	61.53	172.01	98.4
P6	61.03	170.94	50.7
P7	60.90	169.49	38.9

Figure 3.4 shows the DSC results for all the PEG/PLA blends and pure PLA. Pure PLA and formulations P5, P6, P7 showed two endothermic peaks. On the other hand,

formulations P1-P4 showed only one endothermic peak. The first smaller endothermic peak showed in pure PLA and P5-P7 happened at a lower temperature of between 60-70 °C represents the glass transition temperature (T_g) of the samples. The second or larger endothermic peak that occurred at a higher temperature and was present for all samples represents the melting temperature (T_m) of the samples. The results showed that all PEG/PLA blends have T_g and T_m lower than the pure PLA film. This is due to the plasticising effect of PEG. PEG as a plasticiser occupies the intermolecular spaces between the PLA polymer chains, which could change the orientation of the molecules in the polymer blend. The decrease in T_g and T_m is caused by the increase in mobility within the polymer chains, causing the polymer to be in a more amorphous state. This is because less energy is required for the molecules in the blend to move around and to transition from one stage to another. Therefore, the molecules of PEG/PLA blends can change state at lower temperatures when compared to pure PLA as the molecular mobility is higher in the PEG/PLA blends than pure PLA. The lower T_g and T_m of the PEG/PLA blends showed the effectives of PEG as a plasticiser. Such compositions with lower T_m can be beneficial when thermal processes were employed as they can be processed at lower temperatures. This is particularly useful for processing polymers for use in pharmaceutical and biomedical applications as lower processing temperature can prevent the thermal degradation of materials. The benefit of PEG as a plasticiser in 3D printable filament compositions will be further investigated.

However, the PEG/PLA blends that contain lower molecular weight PEG have lower T_m. As the molecular weight of PEG increases in the blend, the T_m increases. This shows the plasticising effect of lower molecular weight PEG is higher. The decrease in plasticising effect in the blends with higher molecular weight PEG could be caused by the decrease in solubility of the higher molecular weight PEG in PLA. This is because lower molecular weight PEG has lower T_g and T_m, causing them to exist in liquid form at room temperature. Formulations P1-P4 do not exhibit a T_g from the DSC results. This could be because the T_g of the material is much lower than the start temperature of the test (30 °C). The T_g and T_m of each formulation and pure PLA films were shown in Table 3.3.

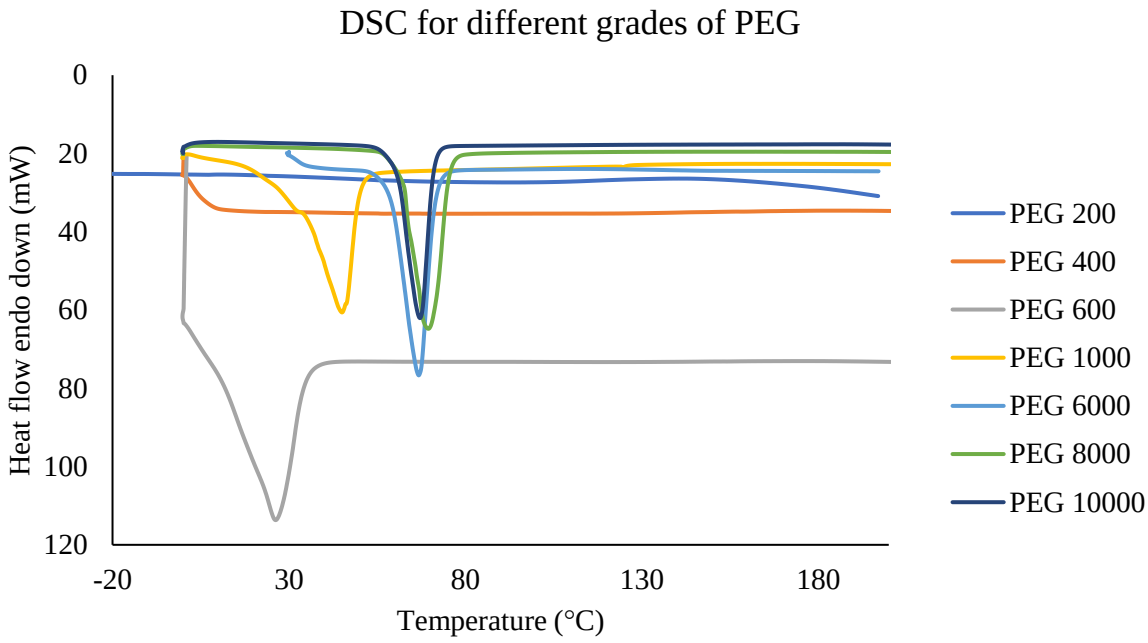

Figure 3.5: DSC thermograms for different grades of PEG.

Table 3.3: Melting temperature and heat enthalpy value for different grades of PEG.

Samples	T_m (°C)	Heat enthalpy value (ΔH) for T_m (J/g)
PEG 200	-	-
PEG 400	-	-
PEG 600	26.2	920.2
PEG 1000	45.1	617.3
PEG 6000	65.4	252.7
PEG 8000	69.4	488.2
PEG 10000	67.2	361.7

DSC was carried out for the different PEG grades being used as a plasticiser for different PEG/PLA blend. The DSC curves obtained were shown in Figure 3.5 and the extracted values of T_m for each PEG grade were shown in Table 3.3. PEG 200 and PEG 400 did not show a melting endothermic peak. This could be the actual melting point of these lower molecular weight PEGs that are out of the operating temperature range on the DSC. PEG 200 and 400 exist as colourless viscous liquid at room temperature. It was reported that the melting/softening point of PEG 200 and PEG 400 could be around the range of -65 °C to -50 °C and -6 °C to 8 °C respectively [548]. As the molecular weight of the PEG increases, the melting temperature increase. The measured melting temperature of PEG 600 was around 26.2 °C. Hence, PEG 600 seems to be at a semi-solid paste at room temperature (~20 °C). PEGs above 1000 are all white solid flakes at room temperature and their melting temperature are above 45 °C. The DSC results of the different PEG grades agree with the physical state of the material at room temperature.

3.4.2 Thermogravimetric Analysis (TGA)

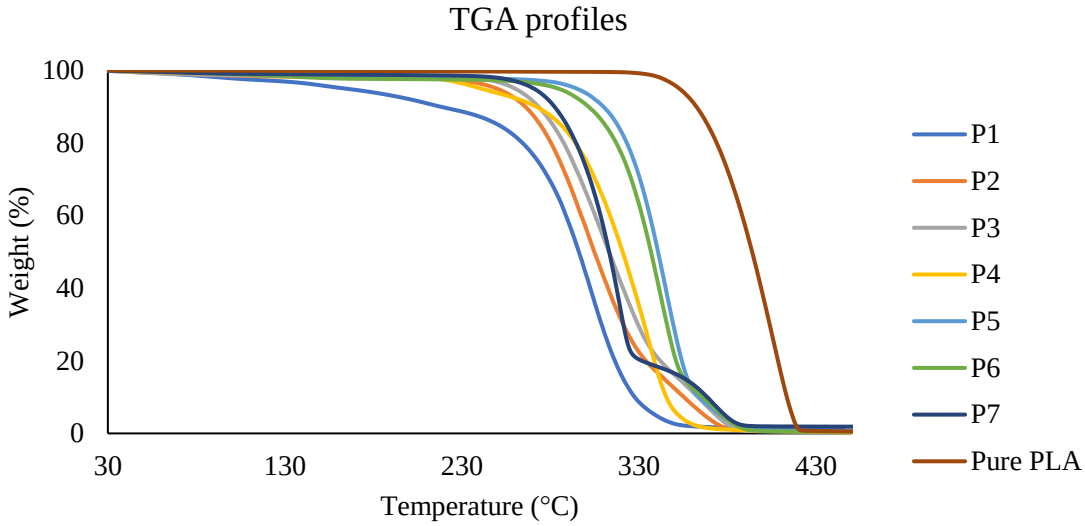

Figure 3.6: TGA profiles for different PEG/PLA films.

Table 3.4: Temperature at three different degradation points extracted from TGA profiles for all PEG/PLA films.

Temperature at weight %	**t_{90} (°C)**	**t_{50} (°C)**	**t_{10} (°C)**
P1	218.79	296.23	327.89
P2	265.55	304.87	355.13
P3	272.75	312.25	363.67
P4	270.71	320.85	354.44
P5	310.19	340.94	364.34
P6	301.2	336.6	365.81
P7	282.5	313.31	368.94
Pure PLA	340.43	358.09	367.89

The thermal degradation profiles of the different PEG/PLA blends and pure PLA were measured using TGA and the obtained profiles were shown in Figure 3.6. Three different degradation points were extracted from the TGA profiles and the temperatures were shown in Table 3.4. The three degradation points were the temperature when 10% of the sample had degraded (t_{90}), 50% of the sample had degraded (t_{50}), and 90% of the sample had degraded (t_{10}). The degradation study shows that pure PLA has the highest resistance to thermal degradation since 340.4 °C is required to degrade 10% of the sample. The PEG/PLA film with lower molecular weight PEG seems to have a lower degradation temperature. This is because low molecular weight PEG has smaller polymeric chains which require less heat energy to break. One interesting observation from the TGA results is that the PEG/PLA films containing higher molecular weight PEG exhibit a second degradation profile. The degradation profiles for P5, P6, P7 do not only have a smooth

profile such as the ones for P1-P4 and pure PLA. P5, P6, P7 showed another step degradation at around 364 °C,357 °C, 327 °C respectively. The higher second degradation temperature in these blends could be caused by the longer polymeric chain of PEG which in turn act as a barrier protective layer on the surface of the polymer matrix. The protective layer could delay and slow the degradation process as the plasticiser can increase the permeability of the volatile compound during the degradation process [549,550]. However, all PEG/PLA blends showed good thermal stability and could be thermally processed up to 200 °C before experiencing any degradation. This information is important as the PEG/PLA blends will be used for thermal processing as described in the latter chapters.

3.4.3 Fourier Transform Infrared (FTIR)

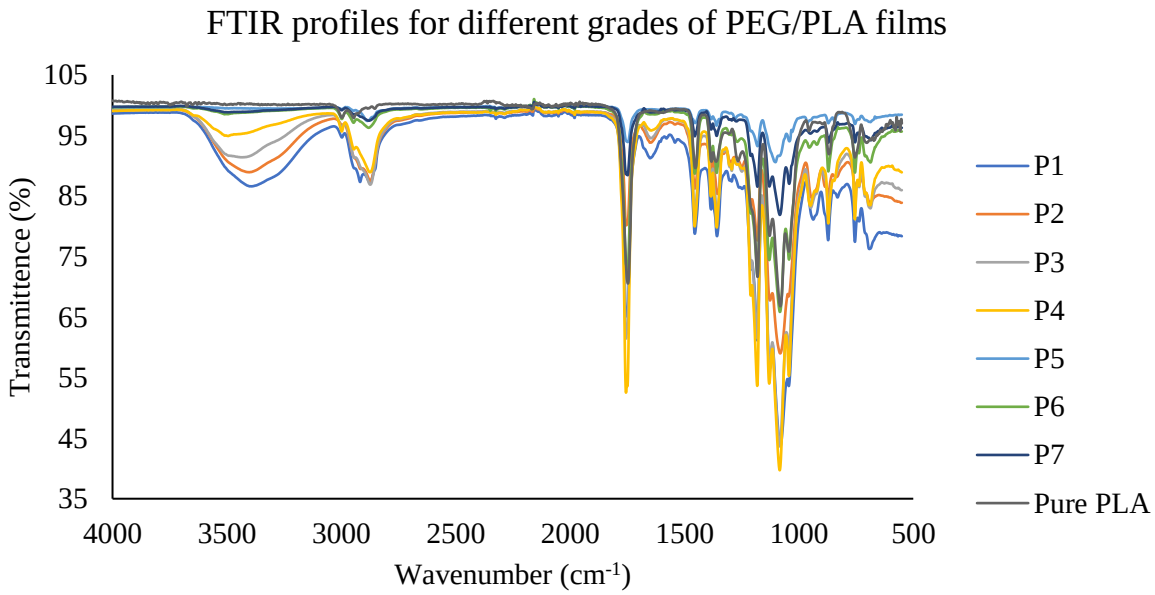

Figure 3.7: FTIR spectra for different PEG/PLA films.

Table 3.5: Characteristic peaks/wavenumber of different PEG/PLA films.

Formulation	Wavenumber (cm^{-1})	Vibration
Pure PLA	2997	-CH_3 asymmetric
	2946	-CH_3 symmetric
	1747	C=O stretching
	1081	C-O stretching
P1	3393	-OH stretching
	2875	C-H stretching
	1755	C=O stretching
	1081	C-O stretching
P2	3403	-OH stretching
	2873	C-H stretching

	1755	C=O stretching
	1082	C-O stretching
P3	3437	-OH stretching
	2873	C-H stretching
	1756	C=O stretching
	1084	C-O stretching
P4	3492	-OH stretching
	2878	C-H stretching
	1749	C=O stretching
	1084	C-O stretching
P5	3507	-OH stretching
	2883	C-H stretching
	1748	C=O stretching
	1101	C-O stretching
P6	3508	-OH stretching
	2881	C-H stretching
	1748	C=O stretching
	1083	C-O stretching
P7	3506	-OH stretching
	2879	C-H stretching
	1749	C=O stretching
	1083	C-O stretching

FTIR was carried out to analyse the chemical interaction of PEG with PLA for every PEG/PLA solvent cast films. The FTIR spectra of all the PEG/PLA films and pure PLA were shown in Figure 3.7. The characteristic absorption peaks for each formulation were extracted from the spectra and shown in Table 3.5. The FTIR spectra contained all typical absorption features of a semicrystalline PLA. The characteristics peaks for C-O and C=O of pure PLA were found at wavenumber 1081 cm^{-1} and 1747 cm^{-1} respectively, whereas the absorption at wavenumbers at 2997 cm^{-1} and 2946 cm^{-1} corresponds to the band absorption of asymmetric and symmetric stretching of C-H in pure PLA respectively. In the PEG/PLA films, the presence of PEG was reflected as the presence of a broader peak that corresponds to the -OH stretching in the FTIR spectra. The broader peak occurred at around a wavenumber of 3500 cm^{-1} for all the PEG/PLA films, which was a confirmation of the chemical interaction between the PEG and PLA [544,551]. This also showed that PEG is compatible with PLA and the interaction between these two polymers could be in the form of hydrogen bonding. The hydrogen bonding between PLA and PEG occurs between the oxygen on the carbonyl group (C=O) of PLA and the hydroxyl end group (-OH) in the PEG chain, and the interaction is depicted in Figure 3.8. The smaller peak was seen for P6 and P7 where the blends contain higher molecular weight PEG. The smaller peak showed a reduced chemical interaction between the two polymers, which could be

caused by a reduction in solubility of higher molecular weight PEG in the PLA matrix [546]. The results were consistent with the DSC analysis that showed lower molecular weight PEG was more effective in depressing the melting temperature of PLA.

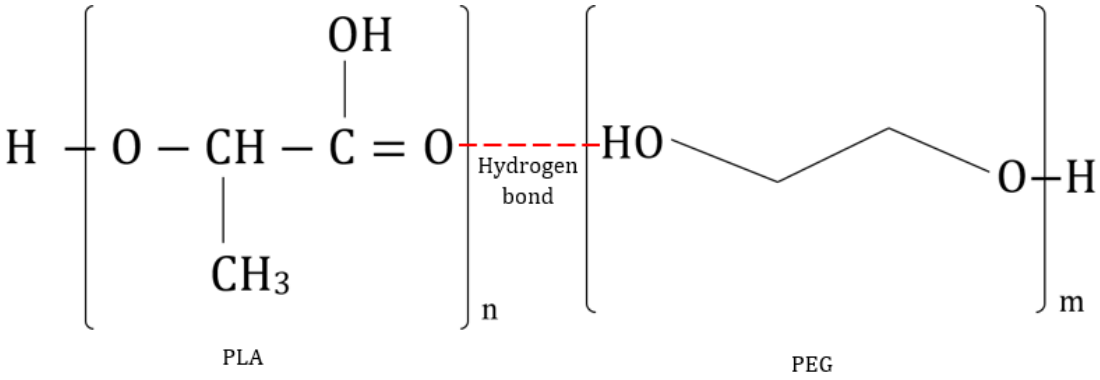

Figure 3.8: Illustration of hydrogen bonding interaction between PLA and PEG molecules.

3.4.4 X-Ray Diffraction (XRD)

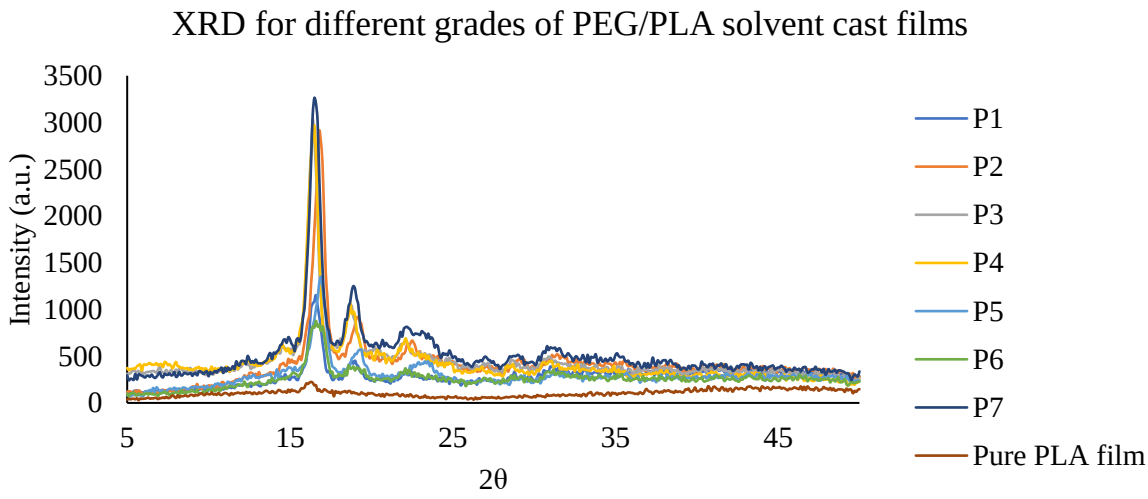

Figure 3.9: XRD spectra for all PEG/PLA films.

XRD was used to study the crystallinity of the PEG/PLA films. It has been reported that the introduction of PEG can improve the crystallinity behaviour of the PLA polymer matrix [551]. The XRD spectra for all PEG/PLA and pure PLA films were shown in Figure 3.9. Pure PLA showed very weak intensity for crystallinity, indicating that pure PLA is almost amorphous. This corresponds to the semicrystalline nature of PLA. All PEG/PLA blends showed strong crystallinity peaks as compared to pure PLA. PEG is a highly crystalline polymer. The presence of strong crystalline peaks in the PEG/PLA

blends reflects the plasticising effect of PEG on PLA, causing the PLA to be more crystallised. However, it was shown that increasing PEG molecular weight causes a reduction in the crystallisation ability of PLA/PEG blend. This may be due to the smaller PEG molecules at lower molecular weight, allowing the PEG molecules to be easier to insert into PLA molecules thus introducing a better plasticising effect. This finding is consistent with the DSC results, where lower molecular weight PEG seemed to have more effectively depressed the melting point of PLA.

3.5 Conclusion

PLA is a very popular biocompatible polymer that has been extensively used in the food and industrial packaging industry. It has also received much attention to be used in the biomedical field due to its excellent biocompatibility, biodegradability, and non-toxic degradation products. However, its application in the biomedical industry is somewhat limited due to poor mechanical properties, degradation rate and hydrophobicity. To overcome these drawbacks of PLA, blending it with plasticisers such as PEG is a simple, practical and efficient way. PEG also exhibit excellent biocompatibility and hydrophilicity. Hence, it is a preferred plasticiser to be blended with PLA to preserve its biocompatibility. A simple solvent casting method was used in this study to prepare different PEG/PLA blends with different PEG grades for characterisation.

It was found that lower molecular weight PEG seemed to have better plasticising efficiency to PLA. The PEG/PLA blends with lower molecular weight PEG showed lower melting temperature, lower degradation temperature, stronger -OH vibration and higher crystallinity. This is because lower molecular weight PEGs have a smaller molecular chain which could be easier to interact within the intermolecular space of PLA. Nevertheless, the studies confirmed that PEG has very good miscibility with PLA as the terminal hydroxy group in PEG can interact with the carboxyl groups in PLA molecules to form a hydrogen bond. The presence of PEG can reduce the intermolecular force and enhanced the mobility of PLA chains.

Chapter 4 : Preliminary study on preparing biocompatible PEG/PLA filaments using a single-screw filament extruder

4.1 Introduction

Three-dimensional (3D) printing, also widely known as “additive manufacturing” or “rapid prototyping”, is a manufacturing technique whereby an object is constructed in a layer-by-layer fashion. It is currently being used as a fabrication method in many different fields and industry, including aerospace, defence, automotive [17], consumer products [552,553], construction [16], healthcare [5] and many others. It has been projected that the 3D printing market is expected to reach USD 34.8 billion by 2024 [554]. Some experts also forecast that 3D printing has the potential to become the next industrial revolution [69]. 3D printing has now changed the way many things are being created, transported and stored [170]. This is because 3D printing allows people to create and build things easily and quickly, which can also be done at home. People can also easily share the things that they have made on the internet so that other people can reproduce the same thing on a 3D printer by just simply clicking and downloading the file that needs to be printed.

Currently, the main challenge that has hindered the growth of 3D printing in the medical and pharmaceutical field is the availability of medical grade materials. Most of the commercially available filaments are not compliant with the requirement to be made into medical products. The materials available are mostly toxic and not suitable to be used in the human body as the filaments contain many types of additives to achieve the required mechanical properties.

Many researchers are trying to improve the availability of medical and pharmaceutical grade filaments. The two most common and widely used filaments are made of Acrylonitrile Butadiene Styrene (ABS) and Polylactic Acid (PLA). ABS is mainly derived from petroleum and it is not biocompatible. PLA is a corn-based plastic and is considered biodegradable and biocompatible [556]. This is because monomers used for the polymerisation of PLA, lactic acid, is mainly produced via the fermentation of sugar obtained from bioresources such as corn starch [557,558]. Hence, PLA is safe to be used in medical products as it has obtained FDA approval for use in medicines and the human body [11–13]. This material is highly attractive across various industries due to its

sustainability, and renewability and is environmentally friendly. Due to its biocompatibility and biodegradability, it is suitable not just for the industrial packaging field, but also for medical applications.

PLA is a biodegradable polyester and exhibits semicrystalline properties in nature [562,563]. It is one of the most widely used materials in clinical applications due to its tuneable mechanical properties, wide availability, and its ability to degrade into natural metabolites [564,565]. The semicrystalline properties of PLA have allowed it to be made into filaments for use in FDM 3D printing. However, the printing of PLA requires a relatively high temperature of up to 200 °C, hence it may not be suitable for many pharmaceutical applications. This is because some drugs are thermally sensitive and printing at such a high temperature can cause thermal degradation. Apart from that, the limited ductility of PLA is a limitation for its use in a wide range of medical and pharmaceutical 3D printing applications. Therefore, PLA has limitations as it can break at very low stress and has poor thermal stability [541]. The mechanical and thermal properties of PLA can be improved by adding plasticisers to the PLA polymer matrix [566]. A plasticiser improves the mechanical properties by acting as a spacer between the molecular chains of the polymers. Some of the most commonly used plasticisers include polyethylene glycol (PEG**),** triethyl citrate (TC), acetyl triethyl citrate (ATC) and glycerol [20–24].

The most effective way of producing polymeric filaments for 3D printing is through Hot Melt Extrusion (HME). The HME technique is a long-established technology that has been used to produce plastics since the 1930s [105]. HME has also been used in the pharmaceutical industry to produce a wide variety of drug delivery systems and modified release solid dosage forms [101,118].

This chapter describes a preliminary study of an attempt to produce a type of PLA-based filaments that can be printed a lower temperature when being used in an FDM 3D printer. The aim is to demonstrate the used of HME to produce a type of biocompatible filament suitable for pharmaceutical applications. PLA is mixed with a plasticiser, polyethylene glycol (PEG), to produce a PEG/PLA blends. This polymeric composition can improve the mechanical properties of pure PLA and can be used for pharmaceutical applications. PEG can be blended with PLA to form a polymer matrix as PEG has good miscibility with PLA [567]. When being mixed with PLA, PEG can act as a plasticiser as its

hydrophilic group interacts with the hydrophobic group in PLA. The PEG/PLA blend can also act as an effective drug carrier as it improves the hydrophilicity of the pure PLA. The PEG/PLA blend can release drug easier than pure PLA.

The PEG/PLA blend filaments were produced using a single screw FilaFab filament extruder. Three compositions of PEG/PLA filaments were produced (10%, 20%, 30% w/w PEG/PLA) and were compared with pure a PLA filament and a commercial PLA filament. The PEG grade used in this study was PEG 6000. This is because PEG 6000 exists in solid form at room temperature and can be processed more easily than other lower molecular weight PEGs that typically exist in liquid or semi-solid at room temperature. Apart from that, PEG 6000 exhibit excellent thermal degradation behaviour according to the thermal degradation study carried out in Chapter 3. As the extrusion process and FDM 3D printing process expose the materials being processed to high temperatures, the materials need to exhibit excellent thermal properties.

The presence of PEG in PLA was confirmed by Fourier transform infrared (FTIR) spectra. The thermal properties of the different filaments were investigated through differential scanning calorimetry (DSC) and thermogravimetric analysis (TGA). The printability of the filaments was also investigated by printing a cylindrical shape object using the different filaments. The study shows that 30% w/w PEG/PLA filaments has the best properties among the three blends and all PEG/PLA filaments can print at 175°C, lower than pure and commercial PLA (190°C). The PEG/PLA filaments can have a wider medical and pharmaceutical applications than pure PLA.

4.2 Materials

Biodegradable high molecular weight polylactic acid (PLA) pellets (Ingeo^{TM} Biopolymer 4032D, made of >98% of polylactide resinCAS: 9051-89-2) were purchased from (NatureWorks, Minnetonka, MN, US). Poly(ethylene glycol), average M.W. 6000 was purchased from Fisher Scientific (Loughborough, UK). Commercial Makerbot Red PLA filaments were purchased from Creat3d Ltd (Wokingham, UK). All materials were used as received.

4.3 Experimental methods

4.3.1 Coating of the PLA pellets with PEG

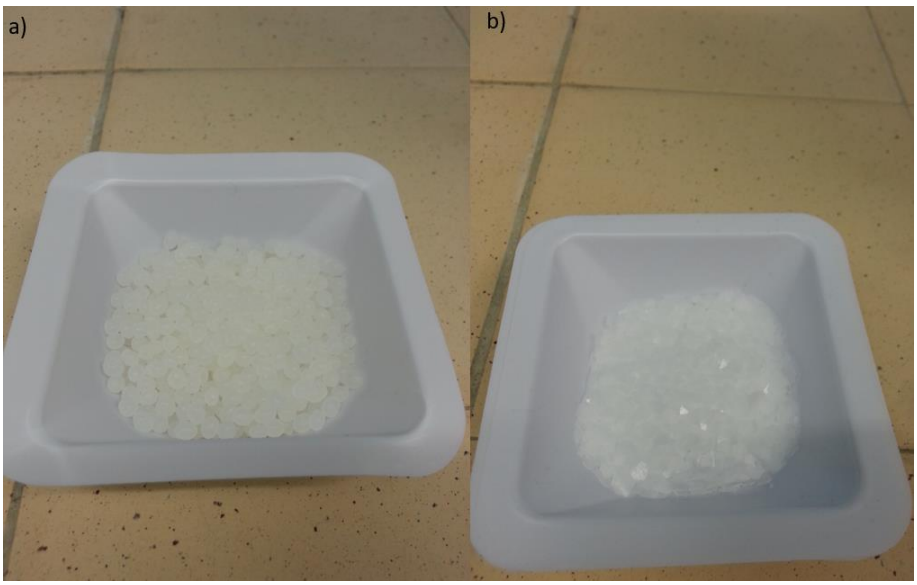

Figure 4.1: Images to show the original form of a) PLA pellets b) PEG 6000.

The preparation of PEG/PLA was required to ensure the mixing can be homogenous when being fed into the single screw extruder. As shown in Figure 4.1, PLA are in the form of small round pellets of around 3 mm whereas PEG 6000 used were in the form of thin waxy flakes. The PLA pellets are very hard whereas the PEG solids are very fragile which could be easily ground into powder. Due to the difference in size and mechanical properties, an extra step was required to better prepare the samples before extrusion. This is because during the extrusion process, it is highly likely that the rotating single screw will segregate the PLA pellets from the PEG instead of mixing due to the screw configuration. Coating the PEG on the surface of PLA can ensure both PEG and PLA can be transported down the extruder through the rotating single screw throughout the extrusion process.

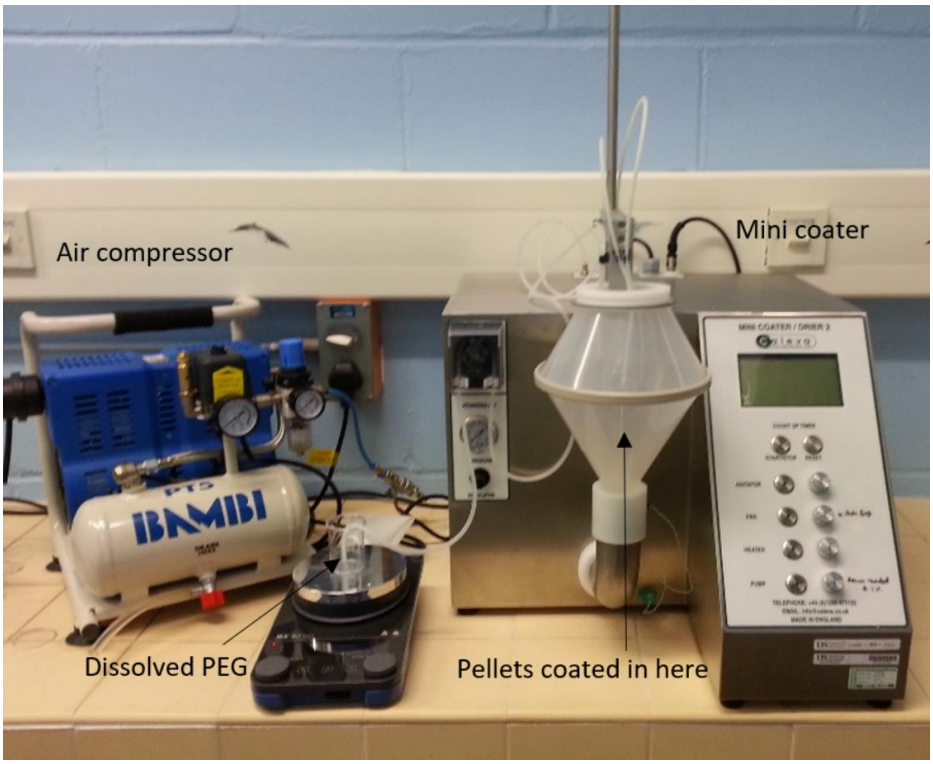

Figure 4.2: Set-up of a Caleva mini coater for the coating of PLA pellets with PEG.

For the coating process, PEG 6000 was dissolved in distilled water using a magnetic stirrer at a temperature of 60°C and rotation speed of 400 rpm for 10 mins. The concentration of PEG in water is 20% w/v. The dissolved PEG was then used to coat the PLA pellets using the Caleva mini coater (Sturminster newton, UK) (Figure 4.2). Three different compositions were produced (10%, 20%, 30% w/w PEG/PLA blends) (Table 4.1). Each batch size of 25 g PLA coated with PEG was produced. The mass of the PLA pellets was weighed before the coating of PEG and after the coating of PEG to quantify the amount of PEG being coated onto the PLA pellet were as desired. For the coating process, the peristaltic pump was set to 2.2 rpm. The agitator was set at a frequency of 20.5 Hz. The fan speed was set to 16 m/s and the air temperature was set to 35°C. The atomizing air pressure was set to 0.7 bar. The PEG solution was kept under stirring condition throughout the coating process to prevent any possible PEG precipitation or clogging up of tubes. The PLA pellets were coated with PEG to ensure homogeneous mixing during the single-screw extrusion process. PLA pellets are much larger than PEG solids and a simple blend of both materials may not be the most effective to achieve a homogeneous mixing of both materials. This is because the PEG powder will segregate from the PLA pellets in the blend during the extrusion process due to the very large size difference between the two materials. Therefore, a coating process was carried out to

ensure all PLA pellets are coated with a layer of PEG so that both materials are effectively mixed during the extrusion process.

Table 4.1: Percentage of composition for the three PEG/PLA samples.

Sample code	wt (%)	
	PEG	PLA
S10	10	90
S20	20	80
S30	30	70

4.3.2 Preparation of PEG/PLA filaments and pure PLA filaments

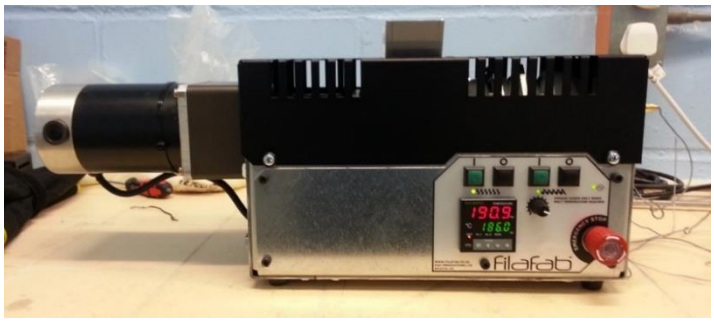

Figure 4.3: Benchtop single-screw filament extruder (FilaFab extruder).

The coated pellets were then being extruded into 3D printable filaments using a single-screw extruder, Filafab extruder (D3D Innovations Ltd, Bristol, UK) (Figure 4.3). PLA pellets without PEG coating were also used to be made into pure PLA filaments. The extruder is heated up to 190°C and soaking was allowed for 10 mins before the extrusion process. The nozzle on the dies of the extruder is 1.75 mm.

4.3.3 Differential scanning calorimetry (DSC)

A DSC 4000 system (Perkin Elmer, Waltham, MA, US) was used to study the glass transition temperature and the melting temperature of the filaments. The samples used were about 5 mg. The samples were placed in an aluminium pan, and an empty aluminium pan was used as a reference. The chamber was heated from 25 °C to 250 °C at a rate of 10 °C/min. Nitrogen gas was used as the purged gas at a flow rate of 20 mL/min in all the DSC experiments. The data were collected and analysed with Pyris software (Perkin Elmer).

4.3.4 Thermogravimetric analysis (TGA)

TGA was carried out using Q40 Thermogravimetric analyser (TA Instruments, New Castle, DE, US) to obtain the degradation profile of the filaments. The samples used were about 10 mg and were placed in an open aluminium pan. The furnace was then heated

from 30 °C to 550 °C at a rate of 10 °C/min. Nitrogen gas were used as purge gas at a flow rate of 20mL/min. Data were collected and analysed using the Advantage/Universal Analysis Software (TA Instruments).

4.3.5 Fourier Transform Infra-Red (FTIR)

Fourier Transform Infra-Red (FTIR) analysis was carried out to study the interaction of the intermolecular chains between PEG and PLA. The FTIR analysis was performed using a Spectrum Two FT-IR Spectrometer (PerkinElmer, Waltham, MA, USA). The spectra were collected using 16 scans between wavenumber 4000-500 cm^{-1} with a resolution of 4.0 cm^{-1}. The results were analyse using the PerkinElmer Spectrum™ 10 software and were displayed as percentage of transmission.

4.3.6 Mechanical testing of filaments

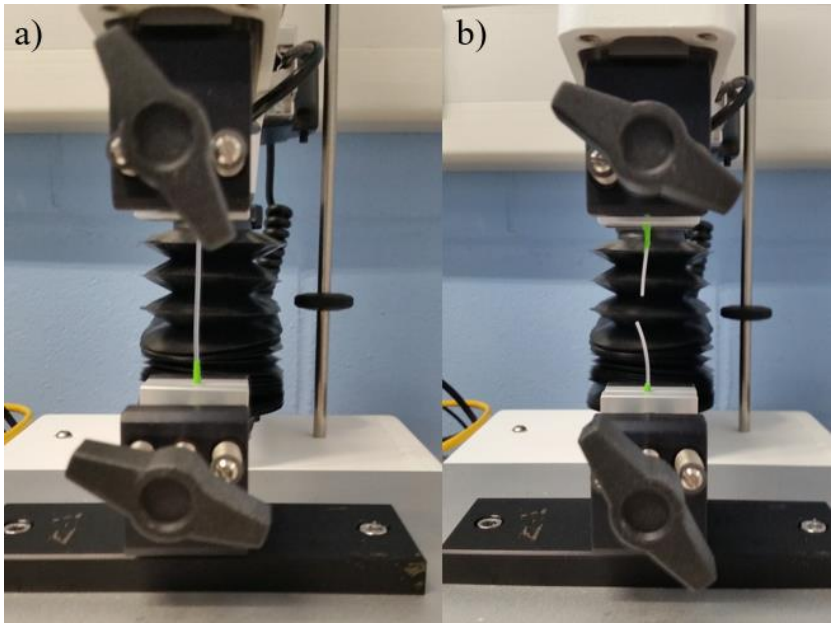

Figure 4.4 Texture analyser for mechanical testing a) set-up of tensile testing (before test) b) after tensile testing.

Tensile testing was carried out on all the extruded filaments using TA.XT Plus Texture Analyser (Stable Micro Systems, Godalming, UK) as depicted in in Figure 4.4. For each formulation of extruded filaments, five 10 cm samples were cut at random from the same batch of filaments produced. All samples have a diameter of 1.5 mm ± 0.1 mm. The samples were then stretched using the texture analyser as shown in Figure 4.4. A load cell of 50 kg was used and a tensile grip probe set was used to measure the tensile strength of the filaments. The test was set up as a tension test with a maximum applied force of 50 kg. The test was stopped as soon as the filament breaks. The data were collected and

analysed using the Exponent Software version 7.0.3.0 (Stable Micro Systems, Godalming, UK).

4.3.7 Sample printing using filament produced

A cylindrical-shaped CAD model with a diameter of 0.8 mm and length of 15 mm was created in Solidworks (Dassault Systemes, Waltham, MA, US). A schematic diagram containing the front and side view of the cylindrical model was depicted in Figure 4.5. The 3D model was then saved as an .STL file and imported to Cura for Robo 2.5.0 software (Robo3D, San Diego, CA, US) for slicing. The sliced 3D model saved as .gcode file and is printed using a Robo R2 FDM 3D printer (Robo3D, San Diego, CA, US). The cylinder has a diameter of 0.8 mm and a length of 15 mm. The layer height for printing was set to 0.06mm. A printing temperature of 190 °C and bed temperature of 60 °C is set when pure PLA and commercial PLA are used. When filaments of PEG/PLA blends are used, the printing temperature is set around 175 °C. The bed temperature is set at 60 °C.

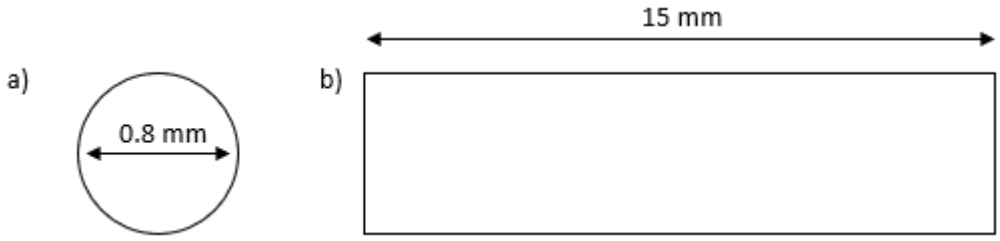

Figure 4.5: Schematic diagram of cylindrical-shaped model for 3D printing a) front-view b) side-view.

4.3.8 Scanning Electron Microscopy (SEM)

SEM was carried using the JEOL JMS 820 (Freising, Munich, Germany) to obtain a close-up image of the structure of the printed sample. The samples were sputter-coated with gold under vacuum conditions using the Edwards S-150 sputter coater (Edwards High Vacuum Co. International, Albany, NY, US). The accelerating voltage was at 3 kV and the magnification was 20X.

4.4 Results and Discussion

4.4.1 Extrusion of filaments

Filaments of three different PEG/PLA blends and pure PLA were successfully prepared using the single screw extrusion method. The Filafab single screw was built specifically for filament extrusion to be used in FDM 3D printers. Therefore, the control settings were simple and only has one temperature control which set the temperature for the whole

extruded, from the hopper to the extruder die. The minimum temperature required to process the PLA pellets were 190 °C. The time taken for the whole extruder to reach the temperature suitable for extrusion was approximately 10 mins. The extruder screw for the Filafab extruder has a wide screw pitch and channel depth. Such a screw configuration does not provide a homogeneous and even mixing of different materials. Therefore, the preparation of PEG/PLA pellets using the coating method was required. This will ensure the extruded filaments have a more even PEG mixing in PLA. SEM was used to image the morphology of the filaments at the cross-section and the images were displayed in Figure 4.6.The images showed that the filaments produced have smooth surfaces and a very consistent round shape.

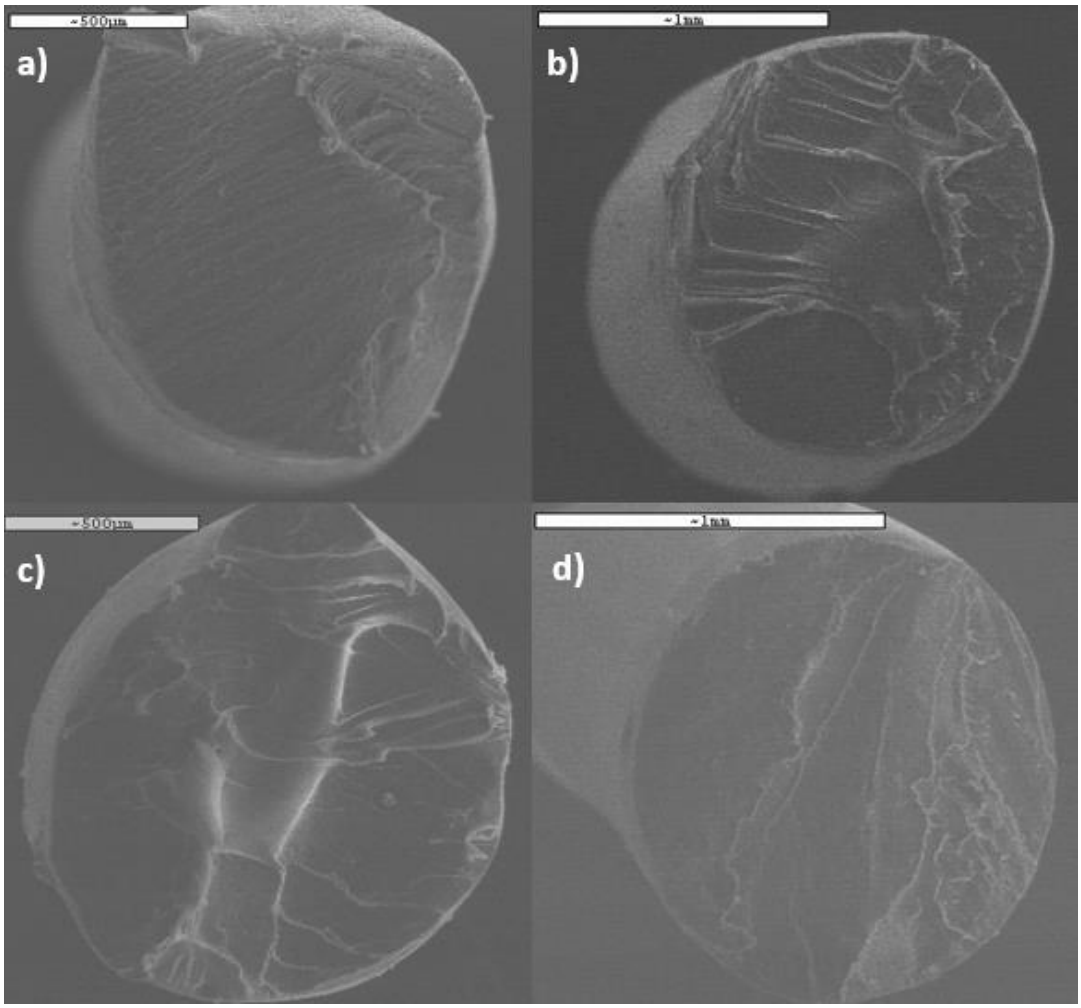

Figure 4.6: SEM images of extruded filaments with different compositions a) S10, b) S20, c) S30, d) pure PLA filaments

4.4.2 Differential scanning calorimetry (DSC)

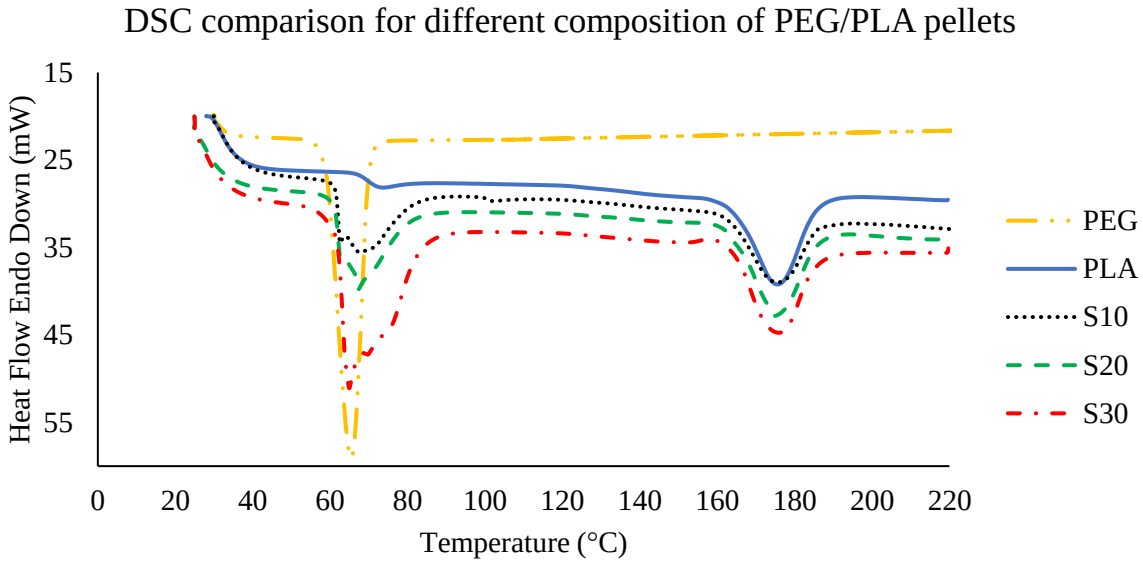

Figure 4.7: DSC profiles for PEG, PLA pellets and different PEG/PLA pellets compositions.

DSC is a highly sensitive technique to study the thermal transition as a function of heating. DSC is the most often used thermal analysis method, primarily because of its speed, simplicity and availability. It is mostly used for quantitative analysis. The thermograms obtained show information for the glass transition and melting temperature of the studied material. The DSC analysis of PEG 6000 which was blended with PLA to form 3 different concentrations of PEG/PLA blends is depicted in Figure 4.7. The analysis shows that PEG 6000 has a melting point of 65.4 °C. The calculated heat enthalpy value (ΔH) of PEG is approximately 252.7 J/g. PEG is known to be a semicrystalline polymer. However, the plot of PEG did not show any glass transition temperature. According to the literature, PEG 6000 has a glass transition temperature of -22.7 °C. PEG 6000 is a semicrystalline solid at room temperature and will transition into a liquid state when the temperature reaches its melting point [568,569].

Table 4.2: Glass transition temperature (T_g) and melting temperature (T_m) of pure PLA pellets and PEG/PLA pellets extracted from Figure 4.7.

PLA Pellet Composition	**Glass transition temperature, T_g (°C)**	**Melting point, T_m (°C)**	**Heat enthalpy value (ΔH) for T_m (J/g)**
Pure PLA	72.8	175.6	20.2
10% PEG/PLA (S10)	67.7	175.5	14.1
20% PEG/PLA (S20)	67.3	174.9	18.1
30% PEG/PLA (S30)	69.9	174.9	15.8

The DSC analysis depicted in Figure 4.7 also shows the thermographs of pure PLA pellets and the 3 different compositions of PEG-coated PLA pellets. The graph shows that all PLA pellets exhibit two endothermic events. The first endothermic event that happened around 70 °C shows PLA was going through the glass transition state. At this temperature, the molecules in the polymer received enough heat energy to move around, transitioning from a hard, brittle state into an elastic or rubbery state. The second endothermic event occurred around 170 °C, here the PLA started to melt. Figure 4.7 shows that with increasing concentration of PEG in the blend, the glass transition temperature (T_g) and melting temperature (T_m) of the PLA pellets were not affected. The T_g and T_m of all the pellets can be found in Table 4.2. This was expected as the PEG was only coated onto the surface of the PLA pellets with no molecular interaction between the two polymers. This can also explain the increase in the size of the peak for the glass transition event. This is because PEG 6000 has a melting point around the same temperature as the T_g of PLA. Hence, the overlapping melting of PEG and glass transition of PLA was reflected by a larger peak at around 70 °C. The size of the endothermic peak increases as the concentration of PEG increases.

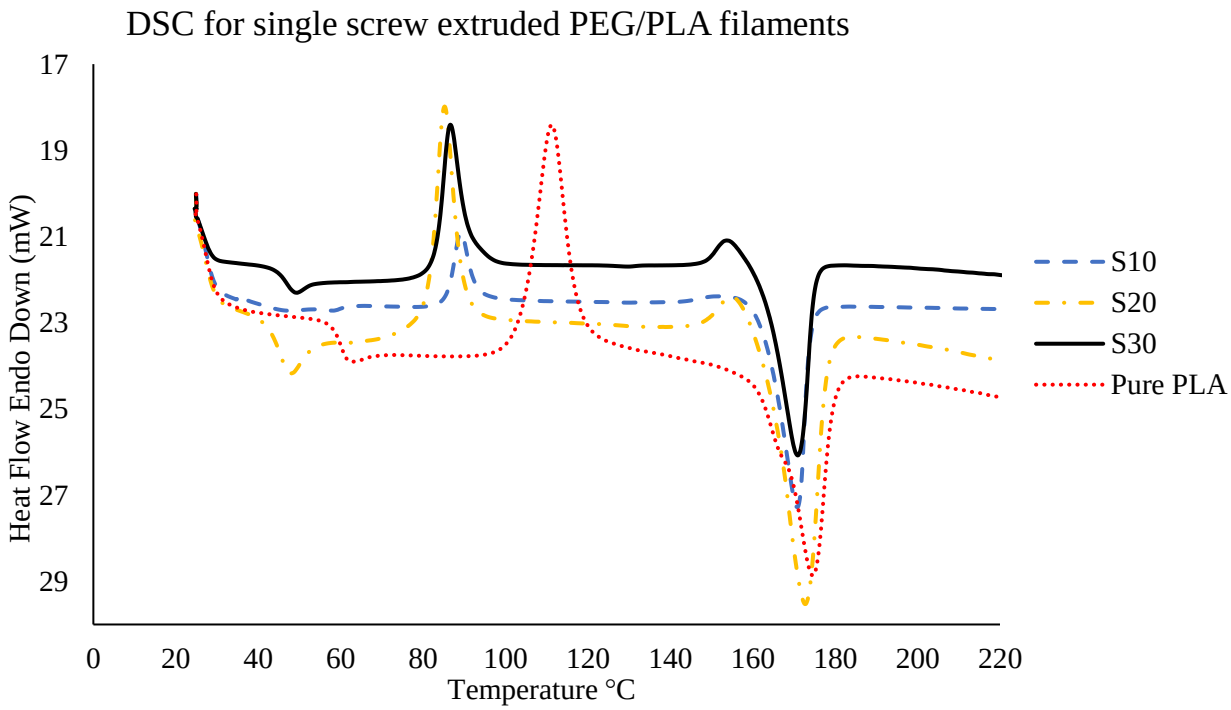

Figure 4.8: DSC profiles comparison for different composition of PEG/PLA filaments, pure PLA filaments and commercially available PLA filaments.

Figure 4.8 shows the DSC thermographs of the PEG/PLA filaments and pure PLA filaments extruded using the FilaFab extruder. The extrusion process heats and melts the

PLA and PEG polymer. The screw provides the effect of kneading and mixing of the two polymers, forming a PEG/PLA polymer matrix. The polymer mixture was then forced through a die, producing a continuous filament. Unlike the DSC results in Figure 4.7, the results in Figure 4.8 showed 3 peaks, 2 endothermic events and 1 exothermic event, which occurred between the 2 endothermic events. The first endothermic peak is the glass transition temperature and the second endothermic peak would be the melting point of the filaments. The exothermic occurred could possibly be the cold crystallisation temperature (T_{cc}) of the filaments. In addition, the results showed the melting temperature of the PEG/PLA filaments is slightly lower than the melting point of pure PLA. The glass transition temperatures of the PEG/PLA filaments are also significantly lower than the pure PLA filaments. The T_g and T_m extracted from the thermographs in Figure 4.8 were tabulated in Table 4.3.

As the concentration of PEG increases in the blend, the T_g decreases. This is caused by the plasticising effect of PEG in PLA. This is because the plasticiser reduces the intermolecular forces in PLA, improving the flexibility and ductility of the polymer at lower temperatures [570]. The pure PLA has a melting point of 174.5 °C. The 10% PEG/PLA blend (S10) shows a melting point of 170.7 °C. The 20% PEG/PLA blend (S20) shows the melting point to be 172.7 °C. The 30% PEG/PLA blend (S30) shows a melting point of 170.9 °C. There was only a slight decrease in the melting point of all three PEG/PLA filaments as the filaments were still predominantly PLA. The lower melting point means that the printing temperature can also be lowered. A lower printing temperature is particularly beneficial for medical and pharmaceutical applications. This is because thermal degradation can be avoided when printing at lower temperatures. The T_{cc} peaks showed in the DSC thermographs for the filaments could be associated with the change in the distribution of crystallinity in the polymer after the extrusion process. This is because there were no exothermic peaks shown on the PEG/PLA pellets in Figure 4.7. The results from DSC shows that PEG has effectively mixed with PLA in the filaments through the single screw extrusion process.

Table 4.3: Glass transition temperature (T_g) and melting point (T_m) of different PEG/PLA blend filaments

Composition of filaments	**Glass transition temperature (°C)**	**Melting point (°C)**	**Heat enthalpy value (ΔH) for T_m (J/g)**
Pure PLA	62.3	174.5	22.3
10% PEG/PLA (S10)	58.9	170.7	33.1
20% PEG/PLA (S20)	47.9	172.7	33.0
30% PEG/PLA (S30)	49.2	170.9	39.5

4.4.3 Thermogravimetric analysis (TGA)

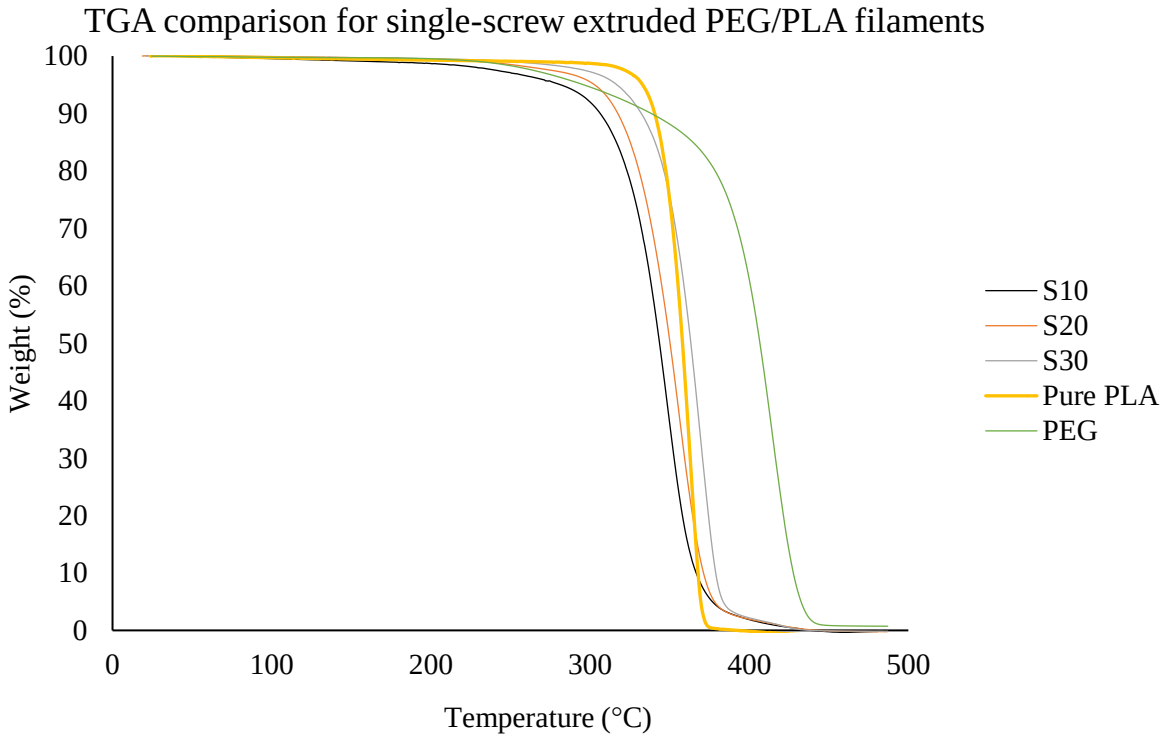

Figure 4.9: TGA analysis for different compositions of single-screw extruded PEG/PLA filaments, pure PLA filaments and PEG.

Table 4.4: Temperatures at three degradation points (90%, 50%, 10% wt. remaining) for all compositions of filaments.

Filaments	T_{90} (°C)	T_{50} (°C)	T_{10} (°C)
S10	306.4	343.6	366.7
S20	317.4	350.2	371.3
S30	332.2	363.3	379.0
Pure PLA	340.4	358.1	367.9
PEG	338.3	406.7	427.8

TGA was carried out on the different compositions of PEG/PLA filaments, pure PLA filament, and PEG 6000. The results from Figure 4.9 shows the degradation profile of the different filaments and PEG. The TGA data shows excellent stability for PEG/PLA blends, PLA and PEG. The presence of PEG did not affect the stability of PLA. T_{90} is the temperature when 10% weight loss is observed. T_{50} is the temperature when the polymer has 50% weight loss and T_{10} is the temperature when the polymer has 90% weight loss. The temperature at these three stages of degradation for the filaments was shown in Table 4.4. 10 % weight loss of all the filaments were observed around 300°C and 90% weight loss occur around 400°C. The results show that both PEG and PLA polymers when being mixed still have excellent stability in the presence of high temperature which would be suitable to be used in 3D printing for pharmaceutical applications. The study also showed that when PEG was added to PLA, the PEG/PLA blends starts to degrade at a lower temperature than pure PLA. The results show that as the concentration of PEG increases, the temperature at which the sample starts to degrade decreases. As the temperature at which degradation starts is still around 300 °C, the blends are still considered stable for thermal processes such as hot melt extrusion and FDM 3D printing. The maximum printing temperature was below 200 °C, which is well below the degradation temperature.

4.4.4 Fourier Transform Infrared Analysis (FTIR)

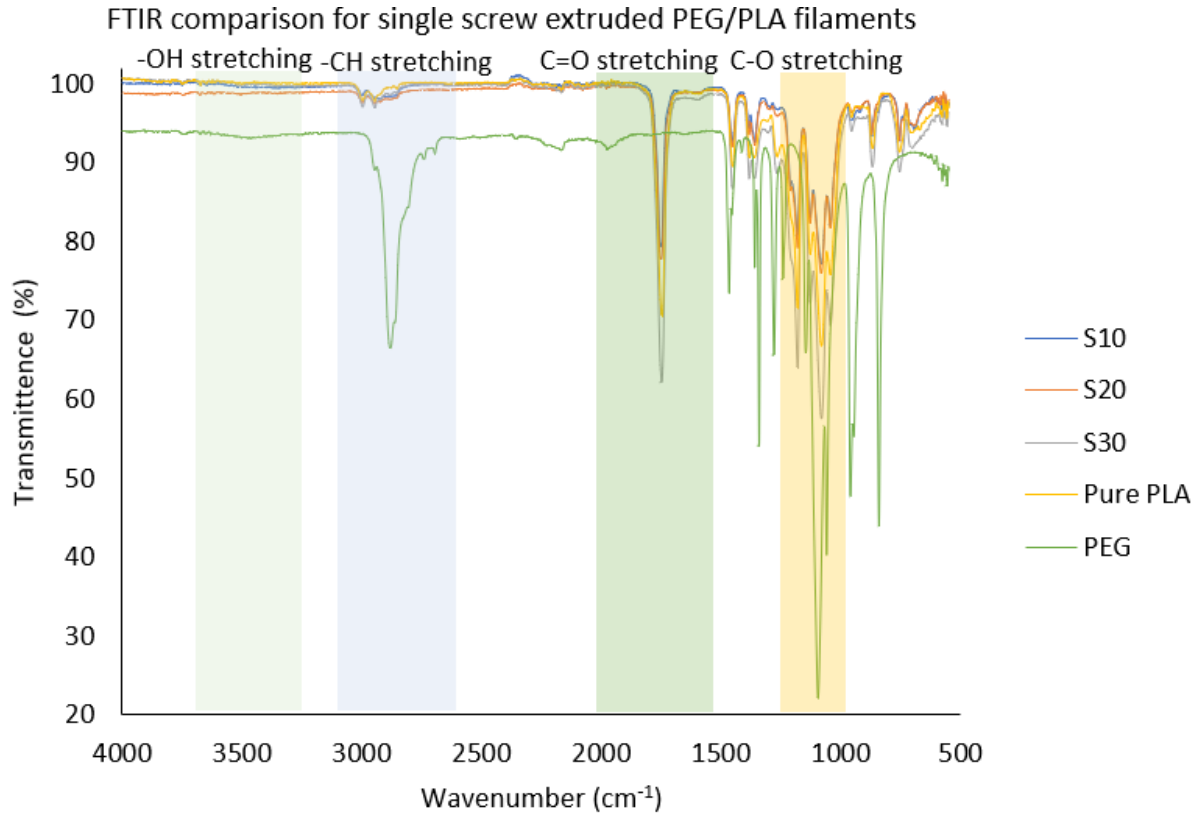

Figure 4.10: FTIR results for different compositions of PEG/PLA filaments, PLA filaments and PEG.

FTIR is used to determine the molecular composition in the different compositions of PEG/PLA filaments and pure PLA filament. The FTIR uses the absorbance of infrared light of the sample at different wavelengths to determine its composition. Figure 4.10 shows the results from the FTIR analysis for all PEG/PLA filaments, pure PLA filaments, and PEG 6000. In all the PEG/PLA and PLA filaments, the absorption of wavenumber of around 2996 cm^{-1} and around 2940 cm^{-1} shows the characteristic absorption bands corresponding to the band absorption of asymmetric and symmetric stretching of C-H. The C=O stretching occurs around 1746 cm^{-1} and The CH_3 stretching occurs at 1453 cm^{-1}, C-H deformation at 1362cm^{-1} and CH asymmetric at around 1359 cm^{-1}. The C-O stretching modes of the ester group appear at around 1265 cm^{-1}. The C-O stretching bands in -CH-O- and -O-C=O of PLA also appear at around 1181 cm^{-1} and 1080 cm^{-1} respectively. The absorption bands at 869 cm^{-1} can be attributed to the amorphous phase whereas the band at 755 cm^{-1} is the crystalline phase. These peaks found in the FTIR spectra showed the typical absorption features of a semicrystalline PLA [571].

In PEG 6000, the absorption band at around 2882 cm^{-1} is attributed to the aliphatic C-H stretching of PEG. The C-O-C groups can be found at the peak around 1096 cm^{-1}. From the FTIR results, the three PEG/PLA blends have a similar spectra pattern as the pure PLA. One of the reasons is because of the similarity in the structure of PLA and PEG as they both consist of carbon and oxygen atoms. As the PEG is mixed with the PLA polymer matrix, it shows that the PEG has good compatibility as it mixed well with PLA. There are slight differences in the intensity of the peak, which is the absorption at the infrared, for different compositions of PEG/PLA blends. The absorbance intensity increases as the concentration of PEG increases in the PEG/PLA blend. The 10% PEG/PLA blend (S10) has the lowest absorbance and the 30% PEG/PLA (S30) filament has the highest absorbance. The increased intensity is due to the presence of PEG as PEG has very high absorbance itself. The incorporation of PEG into PLA did not produce any new configuration or chemical properties on the filaments. This also means that there are no significant changes occur in the surface chemistry of the PLA. The increase in intensity can be explained by improving bonding in the polymer when PEG in blended with PLA. The results from FTIR confirmed the compatibility and miscibility of PEG with PLA.

4.4.5 Mechanical analysis

Table 4.5: Strength of extruded filaments

Filament	**Yield Strength (kPa)**	**Elongation at break (%)**
S10	507.5 ± 211.6	16.4 ± 6.4
S20	239.6 ± 155.7	20.9 ± 3.8
S30	359.9 ± 62.1	30.7 ± 2.2
Pure PLA	437.3 ± 61.6	27.9 ± 3.6
Commercial PLA	804.3 ± 13.2	6.6 ± 0.8

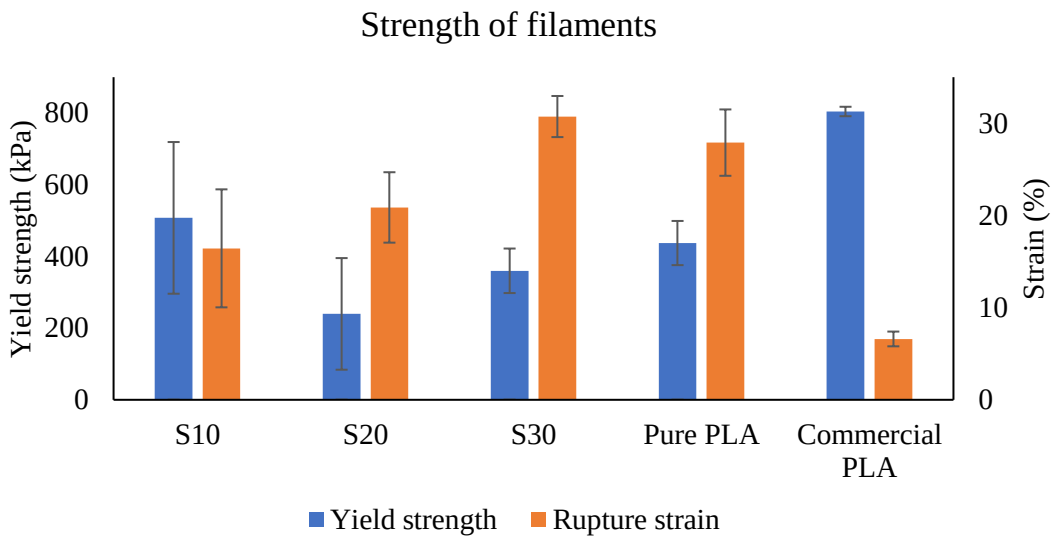

Figure 4.11: Strength of all extruded PEG/PLA filaments compared with pure PLA filament and commercial PLA filaments.

Tensile testing was carried out to determine the mechanical resilience of the different PEG/PLA filaments, pure PLA filament and a commercial PLA filament. The strength of the PEG/PLA filaments were compared with pure PLA filament and commercially available PLA filament. The mechanical properties of the filaments are important to determine their printability in FDM printers. This is because the FDM printing process stretches the filament as gear is used to feed the filament into the printing head. Hence, the filaments require adequate ductility to ensure they would not break easily while being stretched. The results from the tensile testing of the filaments were expressed as the yield strength and the maximum strain values of each of the filaments. The strength of the filaments was displayed in Table 4.5 and Figure 4.11. Yield strength is the minimum stress under which the material deforms permanently (i.e. the stress at which the material stops behaving elastically is called the yield strength). This is the highest point where the strain increases proportionally with stress. Typically, materials undergo elastic deformation below the yield stress, which means the material being stretched will be able to return to its original length. When the force applied is above the yield strength, the material will be plastically deformed, which means the material will not be able to return to its original form when the force stretching it was released. The testing showed that, the yield strength of S10 filaments was the highest amongst all the filaments. However, as the concentration of PEG increased, the yield strength decreased. This means that filaments with a higher concentration of PEG has a lower elastic limit. This could be that PEG does not stretch elastically as well as PLA. This value does not represent the overall

strength of the material, representing the amount of force it could withstand before breaking. Hence, a better reference for the strength of the filaments may be the rupture strain.

Strain is often a better measure as it is used to determine the ability to stretch from its original length before breaking, representing the plasticity and elasticity of the material. It can be defined as the change in length over the original length ($\frac{\text{Change in length}}{\text{Original length}} \times 100 = \text{Strain}(\%)$) of an object [572]. As the concentration of PEG increased, the rupture strain of the filaments increased. The highest concentration of PEG blend seems to have a better ability to be stretched as compared to pure PLA. This showed the plasticising effect of PEG in PLA. Nevertheless, PEG/PLA blends have proven to have good mechanical properties and they are quite similar to the pure PLA filament, which could be suitable to be used in the FDM 3D printers. The strength of the self-prepared filaments was comparable to a commercially available filament that can be readily used for FDM 3D printing. The PEG/PLA filaments even make more superior strain values, meaning they can be stretched much more than the commercial PLA filament before breaking. Nevertheless, the PEG/PLA filaments and pure PLA filaments showed adequate mechanical properties which were confirmed suitable for used in 3D printing.

4.4.6 Printability of filaments

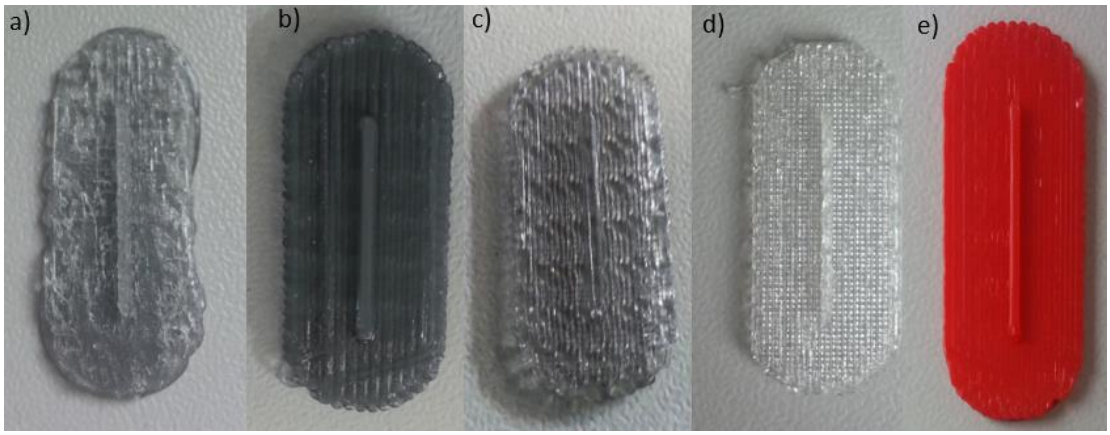

Figure 4.12: Cylindrical shaped object printed using different filaments a) 10% w/w PEG/PLA filament b) 20% w/w PEG/PLA filament c) 30% w/w PEG/PLA filament d) pure PLA filament e) commercial PLA filament.

Figure 4.13: Image of a 3D printed cylindrical shape sample removed from the raft/base.

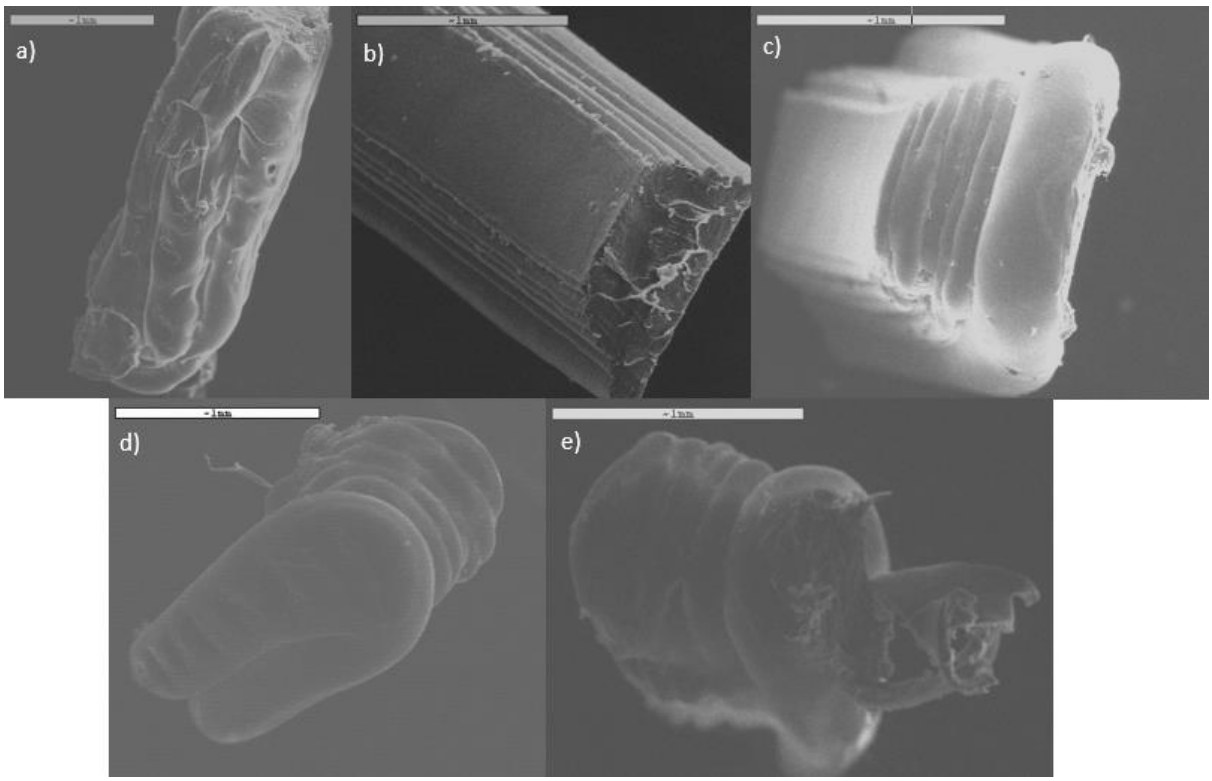

Figure 4.14: SEM images of the cylindrical shaped object printed using different filaments a) S10 filament b) S20 filament c) S30 filament d) pure PLA filament e) commercial PLA filament.

Figure 4.12 shows the printability of the different PEG/PLA filaments, pure PLA filament, and commercial filament. The object being printed is a cylindrical shape which has a diameter of 0.8 mm and a length of 15 mm. The layer height for printing was set to 0.06 mm. The miniaturised cylinder was printed on a raft as a base for the printed object to attach to whilst printing. The cylinder can be removed from the base as shown in Figure 4.13. The quality of the printed cylindrical shape object was considerably good as compared to the pure PLA and commercial PLA. Figure 4.14 are the SEM images of the printed cylindrical shape object. The layers of printing can be seen very clearly and it can form the shape required. A printing temperature of 190°C and bed temperature of 60°C was set when pure PLA and commercial PLAs are used. When filaments of PEG/PLA blends are used, the printing temperature is set around 175°C. The bed temperature is set at 60°C. The printing temperature is critical for the success of a print when using the PEG/PLA blend filaments. The printing temperature is around 175°C. The temperature needs to be adjusted accordingly in order to obtain the right viscosity of the melted filament that can successfully print an object. When the printing temperature is too high, the filament will become too viscous when melted. The extruded material cannot rapidly cool down and solidify when being laid on the print bed. This will cause the print to fail as the material will fail to lay on top of each layer as shown in Figure 4.15. With the right printing parameters, it was showed that 3D printing was able to produce an object with intricate details up to a resolution of 0.06 mm. This may be useful for pharmaceutical and biomedical applications particularly for producing personalised items as these items will need to fit the patients' requirements. Apart from that, the ability to print such a miniaturised object showed the potential of 3D printing miniaturised implants.

One thing to note from Figure 4.12a-c, which were the samples printed using the PEG/PLA filaments showed some darker colour than the one printed using pure PLA. This is discolouration of the PEG through the thermal process of 3D printing. PEG is generally stable up to 300 °C as shown from the TGA analysis. The darkening of the polymer after being processed at elevated temperature is most probably caused by oxidation during heating. It has been reported that the darkening can be prevented by preventing the oxidation of PEG using suitable antioxidant to the blend or processing the material in an inert atmosphere [573].

Figure 4.15: Failed printing due to high printing temperature. PEG/PLA blend filaments were used.

4.5 Conclusion

PLA is one of the most common materials that is being made into 3D printable filaments. However, commercially available PLA filaments are not biocompatible and cannot be used for the 3D printing of biomedical application. Apart from that, pure PLA often have poor mechanical properties. The properties of PLA can be improved by blending the polymer with plasticisers such as PEG using a simple HME method. A single-screw Filafab filament extruder was used to produce PEG/PLA filaments at different concentrations of PEG, as well as pure PLA filaments. The study showed that PEG/PLA filament shows good mechanical and thermal properties. The presence of PEG was confirmed and showed good miscibility with PLA in the polymer matrix. The PEG/PLA blend filament has a lower melting point than the pure PLA filament. The printing temperature of the PEG/PLA filament is also lower than the pure PLA filament. Pure PLA is hydrophobic and PEG is hydrophilic. By incorporating PEG into PLA, the PEG/PLA has better hydrophilicity which is expected to have better drug release. Therefore, the PEG/PLA filament can be used to carry drugs and used for the 3D printing of drug delivery systems. The lower printing temperature allows the loading of thermolabile drugs. The PEG/PLA filament is suitable to be used in 3D printing for a wide range of medical or pharmaceutical applications. The filaments can be used to 3D print medical implant, drug delivery systems, or personalised tablets.

Chapter 5 : Twin-screw extrusion of PEG/PLA filaments

5.1 Introduction

Hot-melt extrusion (HME) was first introduced in the food plastics industry since the 1930s. industries [100,114]. In general, HME is a process of shearing and mixing different materials using the screw elements at an elevated temperature to melt and intimately mix two or several compositions. It has then been introduced into the pharmaceutical industry in the 1970s and many patents related to the use of HME in pharmaceutical applications have been filed since then [120,574,575]. HME can be generally classified into two categories: single-screw extrusion and twin-screw extrusion. The single-screw extruder is commonly used to produce filaments [576] and films [577,578], whereas the twin-screw extruder has found utility in producing pharmaceutical products such as amorphous solid dispersions [579] (ASD) and pharmaceutical co-crystals [580]. In most applications, twin-screw extrusion is often preferred when mixing of materials is involved as it is more effective in achieving homogeneous mixing of several different materials. It is also more versatile and allows more control on the process parameters which could ensure better consistency and repeatability [581]. Twin-screw HME is also easily scalable which allows cost-effective large volume production.

One of the main drawbacks of HME is the high processing temperature may not be suitable for certain materials that are thermally sensitive. However, this issue only applies when there are materials with high melting point studies involved in the mixture that is processed. Studies have shown that this can be overcome by adding suitable plasticisers or surfactants to the mixture [585,586]. The addition of plasticiser or surfactant can lower the processing temperature as the API and the polymer that melts at higher temperatures were solubilised [120]. For instance, the study by Zhang *et al*. successfully lowered the HME processing temperature to produce an amorphous solid dispersion (ASD) of Baicalein (BAC), with the use of a plasticiser, Cremophor RH, to improve the bioavailability of the API [587]. The plasticiser was able to soften the polymeric carrier and decrease the glass transition temperature as well as the melt viscosity of the polymeric carrier, allowing BAC to solubilize at a lower temperature. In addition to improving the API's dissolution and bioavailability, the study showed that careful selection of a compatible plasticiser improves the processability of a high melting point API via HME.

Zhao *et al*. also studied the effect of plasticisers on the ASD of ritonavir as API and copovidone as a polymeric carrier produced via HME [588]. The study investigated the impact of two different plasticisers (Span 20, hydrogenated soybean phosphatidylcholine (HSPC)). The results showed that the plasticisers are effective in not just in lowering the extrusion temperature, but also in improving the dissolution profile and bioavailability of the ritonavir ASD.

In this chapter, the twin-screw extrusion method of producing biocompatible polymeric composition was investigated. Biocompatible and biodegradable polymers have attracted increasing attention due to their suitability to be used in biomedical applications as well as environmental concerns. However, biopolymers typically have poor physical and chemical properties that could limit thier potential for applications. In the previous chapter, a study to enhance polylactic acid (PLA) was carried out by blending PLA with a plasticiser, polyethylene glycol (PEG). The blend was produced in the form of filament using a single-screw extruder. The fabricated filaments were used in a Fused Deposition Modelling (FDM) 3D printing to investigate the suitability of the polymeric composition being used for the 3D printing for biomedical applications.

The aim of this study is to compare the properties of filament extruded using twin-screw extrusion with single-screw extrusion from the previous chapter. The twin-screw extrusion equipment available can only be fed with materials in smaller particle size. The PLA pellets were too large to be processed. Therefore, the PLA pellets need to be ground into smaller particle sizes before being fed into the twin-screw extrusion. However, PLA pellets are naturally very hard and require expensive equipment and processes such as cryo-milling to properly grind them. Hence, a more cost-effective method is required. Smaller PLA particles were produced through grinding solvent cast PLA films using a normal coffee grinder. The solvent casting method is cost-effective compared to other grinding or milling technologies. In the solvent casting method, PEG was mixed into PLA solution. The solution was then poured onto a petri dish and allowed to dry to obtain a thin film. The dried films were ground into smaller particles that can be fed into the feeding zone of the twin-screw extruder. The solvent casting method offers the benefit of providing better miscibility and mixing in addition to shear mixing provided through twin-screw extrusion.

5.2 Materials

Biodegradable high molecular weight polylactic acid (PLA) pellets (Ingeo™ Biopolymer 4032D, made of >98% of polylactide resin CAS: 9051-89-2) were purchased from (NatureWorks, Minnetonka, MN, US). Poly(ethylene glycol), average M.W. 6000 was purchased from Fisher Scientific (Loughborough, UK). Dichloromethane was purchased from Sigma Aldrich (Gillingham, UK). Commercial Makerbot Natural PLA filaments were purchased from Creat3d Ltd (Wokingham, UK). All chemicals and materials were used as received.

5.3 Experimental Methods

5.3.1 Preparation of PEG/PLA films

The PEG/PLA films were prepared using the solvent-casting method. PLA pellets were dissolved in dichloromethane (DCM) at a concentration of 10% w/v. The PLA pellets were dissolved in DCM using a magnetic stirrer at a rotation speed of 800 rpm until a clear solution was obtained. PEG was then mixed into the clear PLA solution until fully dissolved. Three different concentrations (10%, 20% 30% w/w) of PEG/PLA blends were prepared. The PEG/PLA solution was then cast onto glass petri dishes and allowed to dry. The films were then dried in the oven at 45°C to ensure the full evaporation of dichloromethane. Table 5.1 shows the three formulations of PEG/PLA films.

5.3.2 Preparation of PEG/PLA filaments

The prepared films were blended into smaller particle size using an 800W Cookhouse coffee blender (UK). The ground PEG/PLA produced then were made into filaments using a customised 10mm L/D co-rotating twin-screw extruder by Twin Tech Extrusion Limited (Stoke-on-Trent, UK). The extruding temperature for the 4 zones (Z1 : Z2 : Z3 : Z4) were (120°C : 140°C : 150°C : 150°C) and the die was set to 150°C. The heat soak time of the extruder was set to 5 minutes. The extruding hole on the die has a diameter of 2.0mm and the screw speed was set to 50 rpm. Table 5.1 shows the formulation for the three filaments produced.

Table 5.1: Composition of different formulations of PEG/PLA blends.

Code of sample		Percentage of PEG (%)	Formulation ratio (wt. %)	
Solvent cast films	**Filaments**		**PEG**	**PLA**
P10	PF10	10	10	90
P20	PF20	20	20	80
P30	PF30	30	30	70

5.3.3 Characterisation of filaments

5.3.3.1 Differential Scanning Calorimtery (DSC)

DSC was carried out on a DSC 4000 system (Perkin Elmer, Waltham, MA, USA) to study the thermal properties of the PEG/PLA blends. The measured samples used were about 5 mg and were placed in an aluminium pan, with another empty aluminium pan used as a reference during measurement. The chamber was heated from 25 °C to 250 °C at a heating rate of 10 °C/min. Nitrogen gas was used as a purge gas at a flow rate of 20 mL/min in all DSC measurements. All results were collected and analysed with Pyris software (Perkin Elmer).

5.3.3.2 Thermogravimetric analysis (TGA)

TGA was carried out using a Q40 Thermogravimetric analyser (TA Instruments, New Castle, DE, US) to obtain the degradation profile of the PEG/PLA blends. The samples used were about 10 mg and were placed in an open aluminium pan. The furnace was then heated from 30 °C to 550 °C at a rate of 10 °C/min. Nitrogen gas were used as purge gas at a flow rate of 20mL/min. Data were collected and analysed using the Advantage/Universal Analysis Software (TA Instruments).

5.3.3.3 Fourier Transform Infrared (FTIR)

Fourier Transform Infra-Red (FTIR) analysis was carried out to study the interaction of the intermolecular chains between PEG and PLA. The filament sample was cut to approximately 5 mm in length for characterisation. The FTIR analysis was performed using a Spectrum Two FT-IR Spectrometer (PerkinElmer, Waltham, MA, USA). The spectra were collected using 16 scans between wavenumber 4000 cm^{-1} and 500 cm^{-1} with a resolution of 4.0 cm^{-1}. The results were analysed using the PerkinElmer Spectrum^{TM} 10 software and were displayed as a percentage of transmission.

5.3.3.4 X-ray Powder Diffraction

The crystallinity of the solvent cast films was assessed using a Siemens D500 X-ray Diffractometer (Siemens, Germany). The samples were first ground into powder form and were scanned between 2 Theta(θ)=5° to 50° using 0.01° step width and 1s time count. The divergence slit was 1mm and the scatter slit was 0.6mm. The X-ray wavelength was 0.154 nm in Cu source and at a voltage of 40 kV.

5.3.3.5 Mechanical Characterisation (Texture Analyser)

Tensile testing was carried out on the filaments using a TA.XT Plus Texture Analyser (Stable Micro Systems, Godalming, UK). A load cell of 50 kg was used and a tensile grip probe set (A/TG) was used as an attachment to measure the strength of the filaments.fFor each formualtion, Five 10 cm filaments were randomly cut at different sections to be used for sample measurements. The test was set up as a tensile test with a maximum applied force of 50 kg. The test was stopped as soon as the filament broke or until the maximum length of the texture analyser was reached. The data were collected and analysed using the Exponent Software version 7.0.7.0 (Stable Micro Systems, Godalming, UK).

5.4 Results and Discussion

5.4.1 Solvent cast films and extruded filaments

A combination of solvent casting and twin-screw extrusion tehcnique was used to produce biocaomptible PEG/PLA filaments. Solvent casting is a simple method that involves the use of an organic solvent to produce polymeric films containing a mixture of different polymers. This is an effective way to produce PEG/PLA films as described in Chapter 3. Once the PEG/PLA films were produced using the solvent casting method, they were ground into smaller particles and fed into a tabletop twin-screw extruder to produce biocompatible PEG/PLA filaments. As PLA has poor mechanical properties, it may have limited applications particularly for biomedical and pharmaceutical applications. Hence, blending it with plasticisers should improve its mechanical properties, as well as physical properties such as its degradation behaviour. This is because the presence of PEG as a plasticiser may affect the crystallisability and morphology of PLA [589]. The maximum concentration of PEG in the PEG/PLA blends being studied was 30%. This is because plasticisers are typically required at lower concentration in a polymeric composition to be effective. A study by Yang *et al*. suggested that PEG were miscible in PLA up to 30 wt% [589]. The compositions of the filaments produced are similar to Chapter 4.

However, the method of preparation was slightly different. The method described in Chapter 4 uses a single-screw filament extruder whereas the method described in this chapter uses a twin-screw extruder. The image of the twin-screw extruder used can be seen in Figure 5.1. The twin-screw extruder used here extruder has a smaller feeder and screws with smaller pitch and depth. Hence, it was not possible to process the PLA pellets directly. The PLA pellets itself had a very high hardness and cannot be mechanically ground. A cost-effective way to pre-process the PLA pellets is by dissolving it in a suitable solvent which has a low boiling point so that the solvent can be easily removed. Hence, the solving casting method was adapted by using DCM as it has a high vapour pressure, and its boiling point is approximately 39.6 °C [590]. PLA was first dissolved in DCM, then PEG was added to the PLA solution. The PEG/PLA solution was then cast onto a petri dish and allowed to dry, forming PEG/PLA dry films as shown in Figure 5.1a. The PEG/PLA films produced were then mechanically ground using a domestic coffee grinder to obtain a powder form of the blends (Figure 5.1b), which could then be processed using the twin-screw extruder. As the PEG/PLA blends were pre-mixed using the solvent casting method and thin films were produced, the films were much easier to be broken and ground as compared to the PLA in pellet form.

The twin-screw extruder has 5 different temperature controls, one at each zone (i.e., Z1, Z2, Z3, Z4, Die). The separate temperature controls allow more effective heating of the extruder and each zone can be controlled individually to set the temperature that is required. This can prevent the overheating of the samples and thermal degradation. The time taken for the whole extruder to achieve the desired temperature was shorter than that of the single-screw extruder, as it can be achieved in approximately 5 mins. The maximum temperature used for processing the PEG/PLA filaments was 150°C, which was much lower than the temperature used in the Filfab single-screw extruder (190 °C). This showed that the twin-screw extruder zone heating is much more effective and even across the barrel. Apart from that, the shearing forces provided from the two screws placed side-by-side also contributed to the mixing and melting of the polymeric mixture. Hence, the temperature can be lowered as less heat energy may be required. The heat and shearing action of the screws both contributed to the energy required to mix and melt the polymeric mixture in the twin-screw extruder. The extruded filaments showed excellent consistency round shape with smooth surfaces and have an average diameter of 1.5 mm which is suitable to be inserted into the printing head of an FDM 3D printer.

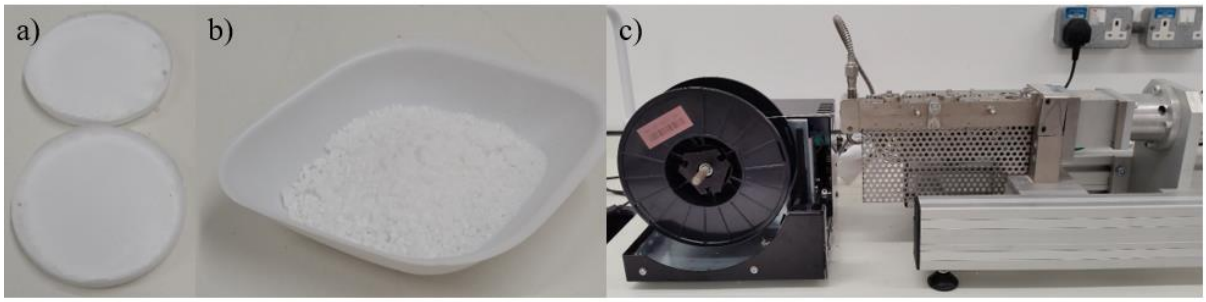

Figure 5.1: a) Example of solvent cast PEG/PLA film, b) PEG/PLA films ground into powder form to be fed into the extruder c) twin-screw extrusion process of PEG/PLA filaments.

5.4.2 Diffrential Scanning Calorimetry (DSC)

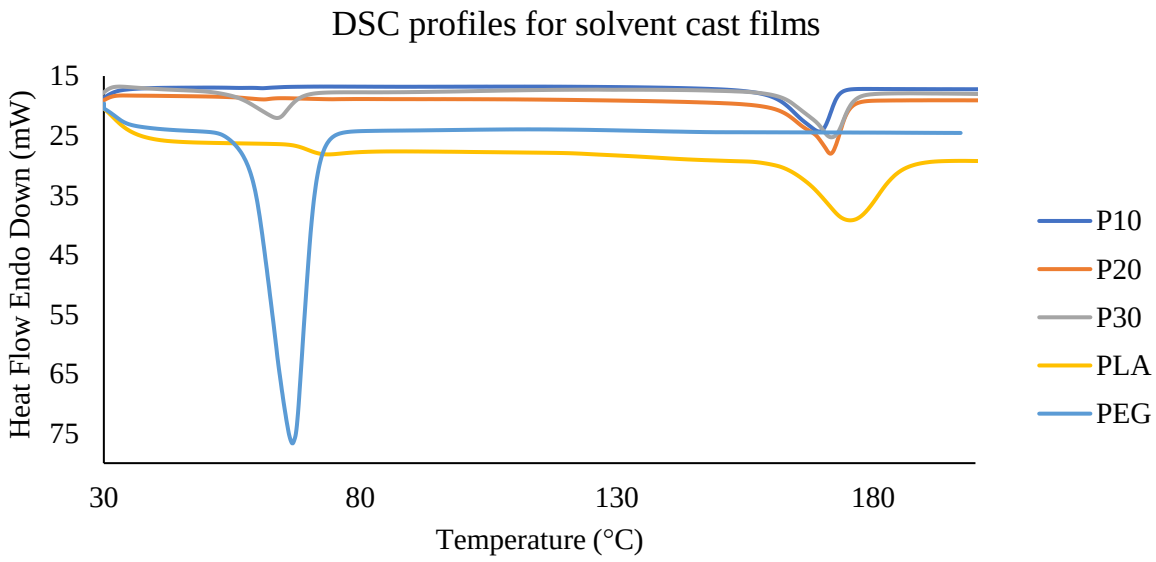

Figure 5.2: DSC thermograms for solvent cast PEG/PLA films, PLA film and PEG.

Figure 5.2 shows the DSC curves for the three different compositions of PEG/PLA solvent cast films, solvent cast PLA film and PEG. The DSC results showed two endothermic events for all films. The peaks for the first endothermic event are associated with the glass transition temperature of the films and the second peak can be interpreted as the melting point of the blends. The size of the glass transition peak seems to increase as the concentration of PEG increases. This could be caused by the overlapping of melting point of PEG with the glass transition of PLA. The DSC results of PEG shows that PEG has a melting temperature of around 66.67°C. The amount of energy required for melting is larger than the amount of energy required for glass transition in the polymer. Hence, the peak of melting is larger. The films with a lower concentration of PEG showed that PEG does not have as much effect on the PLA as reflected from the DSC results in Figure

5.2. Comparing the DSC results from the PEG/PLA films to the pure PLA, PEG seems to have a plasticising effect on the PLA. This is because the T_g of the PEG/PLA blends were much lower than the T_g of pure PLA. The T_g of pure PLA is around 73.66 °C whereas the P10, P20 and P30 showed a T_g of 61.36 °C, 61.69 °C, and 63.92 °C respectively. The lower T_g reflects that the amount of energy required for the molecules to move from the glassy state to the elastic state is lower. This also means that PEG has been effective as a plasticiser and the PEG/PLA blends are more flexible than PLA [522,591]. The T_m of all PEG/PLA films were slightly lower than pure PLA film. However, the decrease in T_m is smaller than the decrease in T_g. This is because the concentration of the PEG is still considerably low and the compositions are still predominantly PLA.

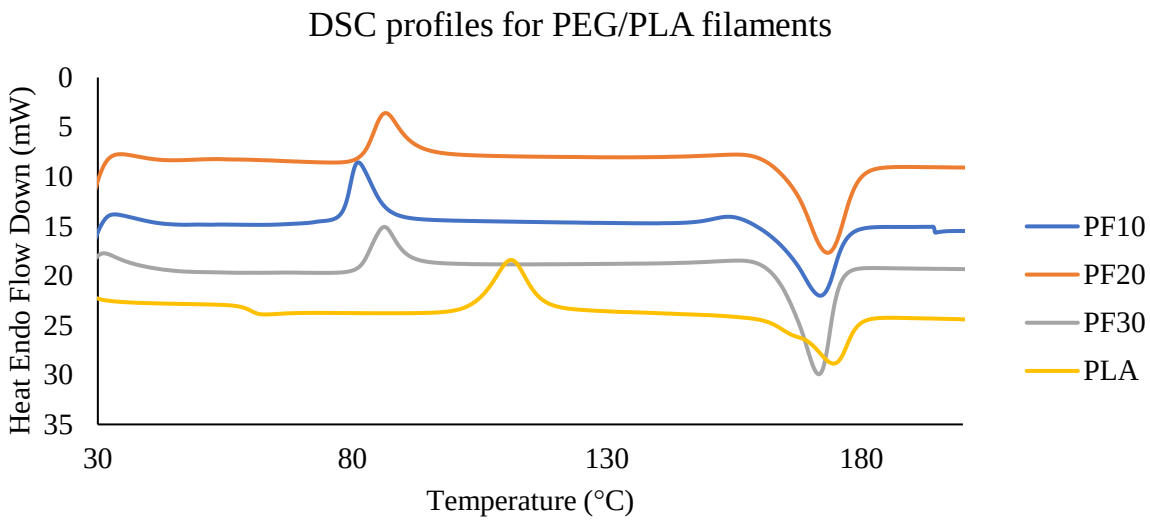

Figure 5.3: DSC for PEG/PLA filaments and pure PLA filaments produced using twin-screw extrusion.

Figure 5.3 shows the DSC results for PEG/PLA filaments and PLA filament using twin-screw extrusion. The T_g and T_m of PLA filament are around 61.9°C and 175°C respectively. However, the PEG/PLA filaments (PF10, PF20, PF30) does not seem to exhibit an obvious T_g from the DSC analysis. The T_m of PF10, PF20 and PF30 are 171.72°C, 172.96°C and 171.40°C respectively (Table 5.2). T_g was not observed in the DSC for PEG/PLA filaments and this could be caused by the loss of crystallinity due to the presence of PEG, causing the filaments to be in a more amorphous state [528]. This can also prove the compatibility of PEG with PLA. The results also showed a slight decrease in the T_m of the filaments from the pure PLA filaments. This means the presence of PEG has managed to reduce the T_m resulted from the plasticising effect of PEG. From

the DSC curves in Figure 5.3, we can also see an exothermic peak for all the filaments. This could be the cold crystallisation temperature (T_{cc}) of the filaments. The T_{cc} of PF10, PF20, PF30 and PLA filaments are 79.99°C, 87.25°C, 87.22°C, and 111.81°C respectively. The T_{cc} of the filaments seems to increase as the concentration of PEG increases. However, the presence of PEG has lowered the T_{cc} when comparing to the pure PLA filament. Cold crystallisation in the filaments might be caused by the development of irregular crystals during the cooling process after extrusion [592]. During the extrusion process, the polymers were melted at a temperature close to their melting point and there will be a sudden drop in temperature when the materials were being extruded out of the extruder die. This uncontrolled and rapid cooling process can create nucleating points that does not allow the polymer to crystallise into a more ordered structure, causing the development of irregular crystal aggregates [593]. Higher T_{cc} means PLA crystallised later and indicates a slower crystallisation rate. The presence of PEG in PLA has promoted the crystallisation rate of the PEG/PLA blends. The new crystalline region is reflected as T_{cc} in the DSC analysis and this is typically above the T_g and below T_m.

The results confirmed the presence of PEG in the films and the filaments. This because the T_g in the films with PEG were lower than the T_g of pure PLA film. However, no endothermic events that represent the T_g were recorded from the DSC analysis for the PEG/PLA filaments. This could be due to the cooling process after the extrusion. During the extrusion process, the filaments were being extruded from the die and allowed to cool naturally at room temperature without any cooling assistance. Apart from a decreased in T_g, there was an increase in the heat enthalpy value required for melting recorded for all PEG/PLA blends. This could be due to the lubricating effect of the PEG in the polymeric matrix as the presence of PEG can increase the mobility of PLA molecules.

Table 5.2: Extracted glass transition temperature (T_g) and melting temperature (T_m) and calculated heat enthalpy value (ΔH) for T_m from DSC curves

Samples	**T_g (°C)**	**T_m (°C)**	**Heat enthalpy value (ΔH) for T_m (J/g)**
Pure PLA film	72.83	175.62	20.2
P10	61.36	170.54	65.3
P20	61.69	171.68	72.0
P30	63.92	172.02	74.1
Pure PLA filament	61.79	174.53	22.2
PF10	-	171.72	86.1
PF20	-	172.96	116.4
PF30	-	171.40	100.0

5.4.3 Thermogravimetric analysis (TGA)

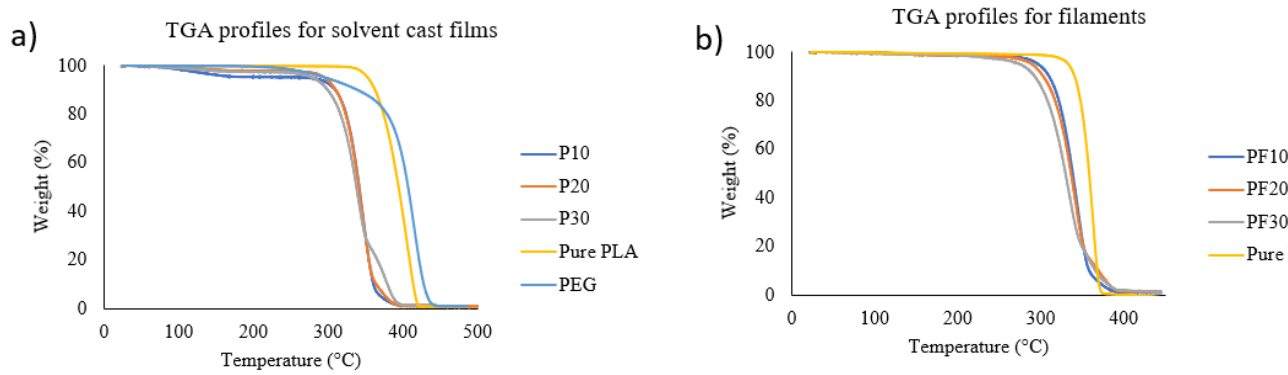

Figure 5.4: TGA profiles for a) solvent cast PEG/PLA films and PEG, b) extruded PEG/PLA filaments.

Table 5.3: Temperature at three degradation points (90%, 50%, 10% wt. remaining) for all compositions of films and filaments.

Temperature at weight %	**t_{90} (°C)**	**t_{50} (°C)**	**t_{10} (°C)**
Pure PLA	340.43	358.09	367.89
PEG 6000	338.31	406.72	427.75
Solvent Cast Films			
P10	309.27	341.4	360.51
P20	310.19	340.94	364.34
P30	299.34	337.54	379.24
Extruded Filaments			
PF10	309.69	338.34	358.13
PF20	303.06	336.25	369.42
PF30	291.88	329.57	365.24

Figure 5.4 shows the TGA profiles for all solvent cast films and extruded filaments. TGA can be used to investigate the degradation of the blends and pure PLA. The temperature

at three degradation points was noted from the TGA plots. The temperature when 10% of the sample was degraded (t_{90}), 50% of the sample was degraded (t_{50}), and 90% of the samples have degraded (t_{10}) were shown in Table 5.3. The TGA study shows that when PEG was added to PLA, the PEG/PLA blends starts to degrade at a lower temperature than pure PLA. The exact temperatures of degradation for the samples at three different points were recorded in Table 5.3. The results show that as the concentration of PEG increases, the temperature at which the sample starts to degrade decreases. As the temperature when it starts to degrade is still around 300 °C, the blends are still considered stable at the temperature required for hot melt extrusion. The maximum temperature used for extrusion was only 150 °C, which is well below the degradation temperature. Hence, the blends were still stable even when PLA was incorporated with PEG.

Figure 5.4b shows the TGA profiles for all twin-screw extruded filaments. Similar to the solvent cast films in Figure 5.4a, the degradation of the filaments started around 300 °C. As the concentration of PEG in the filament increases, the degradation temperature for the first 10% wt. (t_{90}) decreases. The study shows that the filaments are still thermally stable even after the extrusion process. This means that the filaments can be safely used for 3D printing as the melting temperature for 3D printing is around 170 °C. The TGA profiles for the PLA and PEG showed a smooth degradation profile. When PEG was blended into PLA, there seems to be a second degradation point appearing around 350 °C. The samples P10, P20, P30 have a second degradation temperature at 364.09 °C, 360.54 °C, 351.84 °C respectively. Samples PF10, PF20, PF30 have a second degradation at around 360.25 °C, 353.68 °C, 346.97 °C respectively. The occurrence of these second degradation temperature might have caused by the plasticising effect of PEG, where the PEG act as a protective barrier on the surface of the PLA matrix [546]. However, this second degradation profiles were not seen in the single-screw extruded PEG/PLA filaments as studied in Chapter 4 (Figure 4.9). This could be because due to the more effective mixing of PEG with PLA in twin-screw extrusion and single-screw extrusion. Hence, the effect of PEG was more evident in twin-screw extruded PEG/PLA filaments. In general, PLA when blended with PEG has a lower degradation temperature than pure PLA materials. Studies have shown that the incorporation of PEG could reduce the crystallinity in the PLA polymer hence causing it easier to degrade [594,595].

5.4.4 Fourier Transform Infrared Analysis (FTIR)

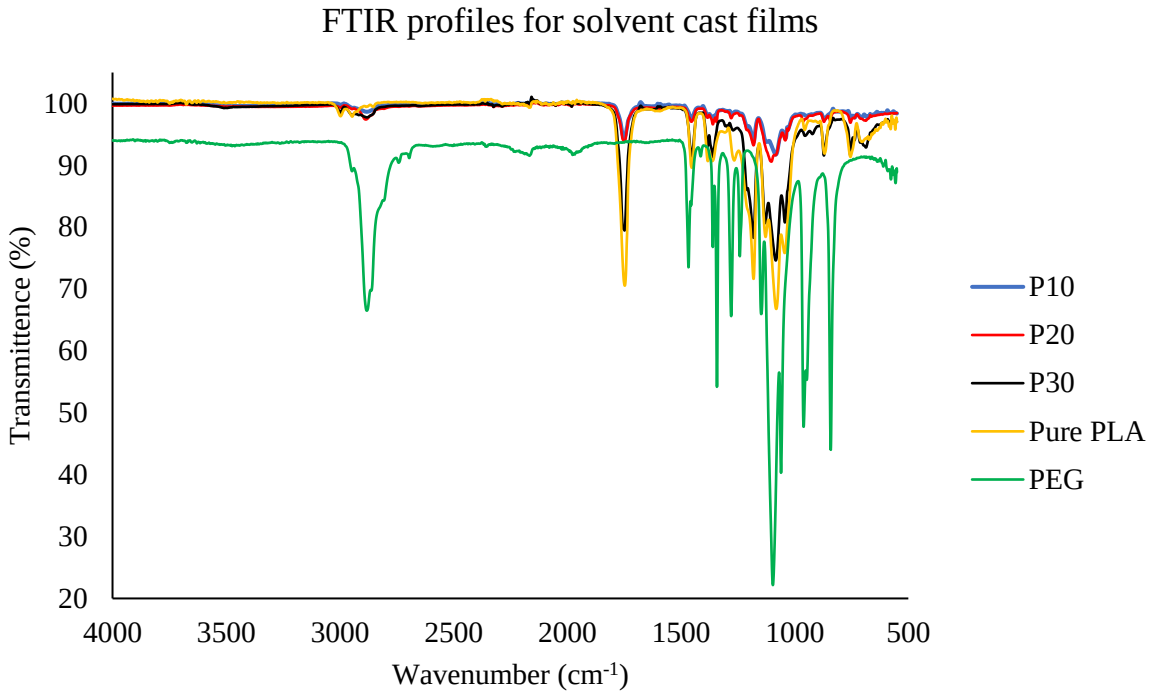

Figure 5.5: FTIR spectra for PEG/PLA, pure PLA solvent cast films and PEG 6000.

-

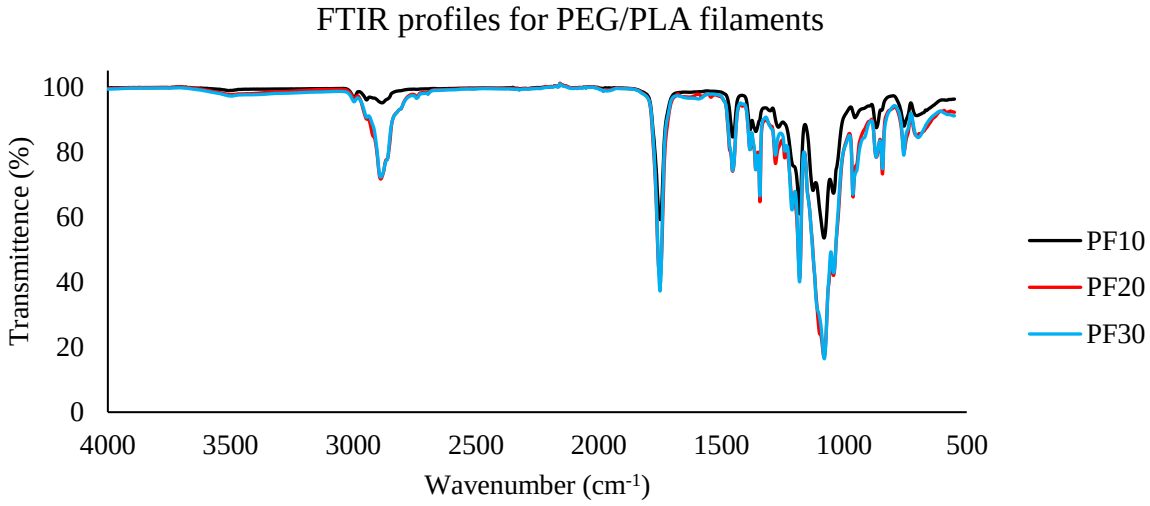

Figure 5.6: FTIR Spectra for twin-screw extruded PEG/PLA filaments.

Table 5.4: Wavenumber for the several characteristics peaks extracted from FTIR spectra.

Formulation	Wavenumber (cm^{-1})	Vibration
Pure PLA film	2997	$-CH_3$ asymmetric
	2946	$-CH_3$ symmetric
	1747	C=O stretching
	1081	C-O stretching

PEG	2882 1467 1096	-CH stretching C-H bending C-O stretching
P10	3504 2878 1747 1084	-OH stretching C-H stretching C=O stretching C-O stretching
P20	3507 2883 1748 1101	-OH stretching C-H stretching C=O stretching C-O stretching
P30	3505 2877 1748 1081	-OH stretching C-H stretching C=O stretching C-O stretching
PF10	3507 2881 1749 1081	-OH stretching C-H stretching C=O stretching C-O stretching
PF20	3504 2888 1750 1081	-OH stretching C-H stretching C=O stretching C-O stretching
PF30	3493 2888 1750 1080	-OH stretching C-H stretching C=O stretching C-O stretching

FTIR can be used to determine the molecular interaction of PEG and PLA in the polymeric matrix. Figure 5.5 and Figure 5.6 display the FTIR spectra for the PEG/PLA solvent cast films and their extruded filaments respectively. In all the PEG/PLA blends and PLA, the absorption at wavenumbers from 2998 cm^{-1} to 2944 cm^{-1} shows the characteristic absorption bands corresponding to the band absorption of asymmetric and symmetric stretching of C-H. The characteristic peaks at wavenumber around 1080 cm^{-1} and 1750 cm^{-1} were attributed to the C-O and C=O of PLA. The absorption bands at 869 cm^{-1} can be attributed to the amorphous phase whereas the band at 755 cm^{-1} correspond to the crystalline phase. These peaks showed a typical characteristic band of a PLA. Hence, the chemistry of the PEG/PLA blend was not modified. The wavenumber of the characteristic peaks for each of the PEG/PLA films and filaments were shown in Table 5.4.

The bands at 2873 cm^{-1} seen in all the PEG/PLA blends were attributed to the stretching of PEG. As PEG was added to PLA, the peak intensity at 2988 and 1759 cm^{-1} were reduced. In general, the intensity of the peaks increases as the concentration of the PEG increases for the PEG/PLA films and extruder filaments. The increased intensity is due to the presence of PEG which has a high absorbance itself. The increase in intensity can also be explained by improved bonding in the polymer when PEG is blended with PLA. As the PEG is mixed with the PLA polymer matrix, it shows that the PEG has good compatibility as it mixed well with the PLA. In the PEG/PLA extruded filaments, there are slightly broadened peaks in the region of -OH stretching at approximately 3500 cm^{-1}. According to Peng *et al.*, the presence of chemical interaction (hydrogen bonding) between the two compatible polymers can be determined as a note by band shift and or broadening of the IR spectra of hydroxyl groups. Hence, the broadened peak in the region of OH stretching is attributed to the chemical hydrogen bonding interaction between PEG and PLA. Comparing the FTIR results of the twin-screw extruded filaments with the single-screw extruded filaments in Chapter 4 (Figure 4.6), the broadening of the peaks in the twin-screw extruded filaments were more evident. This could be caused by the better mixing of PEG and PLA during the twin-screw extrusion process due to shear mixing at an elevated temperature. Apart from that, the materials used for twin-screw extrusion have better mixing since the two materials were mixed by a common solvent [596].

5.4.5 X-Ray Powder Diffraction (XRPD)

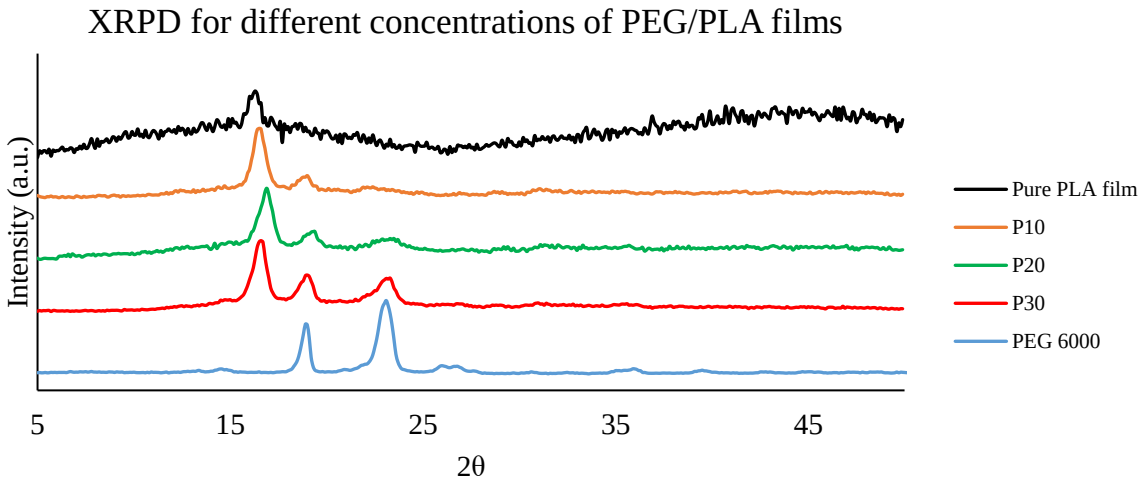

Figure 5.7: XRPD spectra for PEG/PLA blends, pure PLA and PEG.

All three PEG/PLA solvent cast films, pure PLA film and PEG were ground into powder form and the crystallinity of the materials was determined using X-Ray power diffraction.

The results from the XRPD were shown in Figure 5.7. The study confirms that PLA is a semicrystalline material as seen in the spectrum. PLA showed a small crystalline peak at around 16° but the spectrum showed amorphicity in PLA as well. On the other hand, PEG showed clear crystalline peaks confirming that PEG has high crystallinity in its bulk form. The spectra for all three PEG/PLA films showed characteristics of both PLA and PEG combined. This confirmed the effective mixing and the presence of PEG in PLA. As expected, the spectrum showed more obvious PEG crystalline peaks as the PEG concentration increase. The presence of PEG at a higher concentration induced a higher crystallinity in the PEG/PLA film. This could mean that a higher concentration of PEG may cause brittleness on the polymeric mixture.

5.4.6 Mechanical analysis

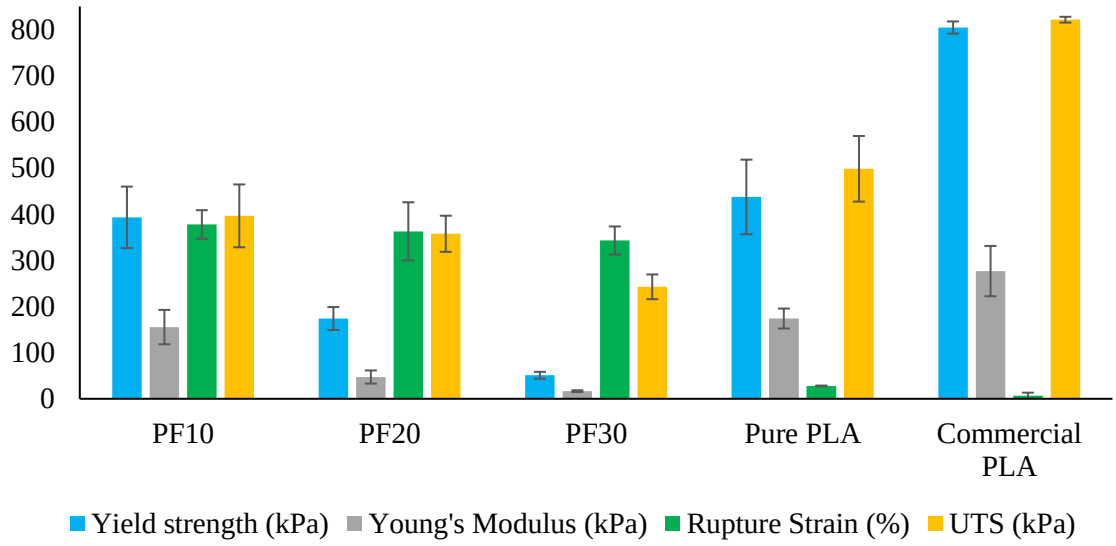

Figure 5.8: Mechanical strength of PEG/PLA filaments compared with pure PLA filament and commercial PLA filament measured using tensile testing.

Tensile testing was carried out to determine the mechanical strength of the filaments. The strength of the extruded PEG/PLA filaments and pure PLA filament were being compared to a commercially available PLA filament. The results from the tensile testing were presented in different strength measurements including yield strength, ultimate tensile strength (UTS), Young's modulus and rupture strain/elongation at break as shown in Figure 5.8. Yield strength represents the minimum stress under which the material deforms permanently (i.e. the stress at which the material stops behaving elastically is called the yield strength). This is the highest point where the strain increases proportionally with stress. Ultimate tensile strength is the maximum stress that a material

can withstand while being stretched beyond the yield strength before breaking. Young's modulus measures the stiffness of the material. It describes the elastic properties of the filament undergoing tension in one direction. This can be obtained by calculating the gradient below the point of yield strength, in which the material stretches elastically and the distance being stretched increases proportionally to the force applied. The rupture strain, which can also be called elongation at break, showed how much the material has been extended before it breaks. This can be calculated using the equation:

$$\frac{\text{Change in length}}{\text{Original length}} \times 100 = \text{Strain}(\%) \quad \text{(Equation 5.1)}$$

The strength values for the tested filaments were shown in Table 5.5. The results showed that tensile strength, elongation/strain and young's modulus decrease as the concentration of PEG increases in the PEG/PLA filaments. This could be because the filaments with a higher concentration of PEG has reached the PEG saturation in the polymer matrix. When PEG in PLA reaches its saturation point, the PEG/PLA blend may become brittle due to phase separation [597]. This finding was consistent with results from XRPD in Figure 5.7, where the crystallinity of the PEG/PLA blend increased as the concentration of PEG increased. Hence, the strength of the filaments decreased. However, the strain values showed than the twin-screw extruded PEG/PLA filaments have far more superior elongation capabilities than the pure PLA and commercial PLA filament. The superior elastic properties of the twin-screw extruded filaments as compared to the commercial PLA filaments reflects the plasticising effect of the PEG in the PLA polymer. Nevertheless, the plasticising effect of PEG in PLA can be seen and the strength was comparable with the commercial PLA filament.

Table 5.5: Values for the mechanical strength of PEG/PLA filaments, pure PLA filament, and commercial PLA filament.

Filament formulation	**Yield Strength (kPa)**	**Ultimate Tensile Strength (kPa)**	**Young's Modulus (kPa)**	**Elongation at break/Rupture strain (%)**
PF10	393.2 ± 66.6	396.3 ± 68.1	155.4 ± 37.2	377.6 ± 31.0
PF20	174.0 ± 24.8	357.5 ± 39.1	47.2 ± 14.2	362.8 ± 63.0
PF30	50.9 ± 7.5	242.6 ± 26.8	16.5 ± 1.91	342.9 ± 30.5
Pure PLA	437.3 ± 80.8	498.3 ± 21.6	173.9 ± 71.1	27.9 ± 0.8
Commercial PLA	804.4 ± 13.2	821.3 ± 6.3	276.7 ± 54.5	6.55 ± 2.8

5.5 Conclusion

Twin-screw extrusion is a very versatile technique and is preferred when different polymeric materials are mixed together. In this study, the properties of PLA was enhanced by blending it with PEG as a plasticiser using the twin-screw extrusion technique. The effect of PEG in PEG/PLA blends was more evident when using twin-screw extrusion as compared to single-screw extrusion in Chapter 4. This has suggested that twin-screw extrusion provides better mixing as it provides more control over the temperature of the extruder and provides more intimate mixing through the shearing that occurs between the materials and the twin-screw. As the twin-screw extruder was not able to process PLA pellets due to their size, the PEG/PLA blends were required to be pre-processed into films through the solvent casting method. The films were then ground into smaller particles so that they can be fed into the twin-screw extruder. The presence of PEG has lowered the T_g and T_m of the PEG/PLA blends. The plasticising effect of PEG can also be confirmed through the FTIR analysis and mechanical testing. Although the yield strength of the PEG/PLA filaments were not as strong as the commercially available filament, the elongation of the PEG/PLA filaments were at least 5 times better than the pure PLA filaments and 50 times better than the commercial filaments. This is because PLA has very low ductility and high brittleness at room temperature. The presence of PEG can impart elasticity and allows the filaments undergo more plastic deformation. The improved mechanical properties can be particularly useful for biomedical applications, where such blends can be used as an implantable drug delivery device, sutures, skin patches and scaffolds.

Chapter 6 : Development and optimisation of novel polymeric compositions for sustained-released theophylline tablets via HME and FDM 3D printing

6.1 Introduction

Since the discovery of additive manufacturing, many industries have been able to adopt this technology due to the benefits it could bring. One of the most attractive features of 3D printing is its ability to produce objects of any shape in a cost-effective way at any time [598]. For this reason, 3D printing has a large potential in the use of pharmaceutical and biomedical applications. Due to the current rise in the development of personalised medicines, there is a need for a cost-effective method to produce these patient-tailored medicines in a short time frame after diagnosis [599]. In theory, 3D printing should be able to produce these medicines, in particular the solid dosage forms that are adjusted according to the patient's need [600]. The use of 3D printing in producing medicines also allows hospital and pharmacies to manufacture the medications to patients immediately after the consultation. This is particularly beneficial for hospitals in remote areas so that they can supply their own patients with medications.

Since the U.S. Food and Drug Administration (FDA) approval of the first 3D printed drug, Spritram®, there has been plenty of research involves 3D printing for various types of drug delivery systems [71,158,601]. The most easily accessible and low-cost 3D printing is Fused Deposition Modelling (FDM). There has been much research on the polymeric filaments for FDM 3D printers that can be used in biomedical application. This is because there is still a lack of pharmaceutical grade filaments currently available in the market. Apart from that, there are no commercially available drug-loaded filaments [602]. In this study, Active Pharmaceutical Ingredient (API)-loaded pharmaceutical grade filament has been produced using HME. HME is a well-established technique that has been used for pharmaceutical applications [99,100,104,120]. Many studies have also proven that using HME to produce API-loaded filaments that can be used for FDM 3D printing is feasible [98,603–605]. However, the main concern of the filaments produce is mechanical resilience, which is a main factor that determines its printability. During FDM 3D printing, the filament is being fed into the heated nozzle head for the melting of the filament through a motorised gear. The gear exerts stress and strain onto the filament during the feeding process. Therefore, the filaments should be rigid and stiff enough so

that it does not break during the 3D printing process. It should also have enough plasticity so that it can withstand the stress exerted transversely. The mechanical resilience of the filament is largely dependent on the type of polymers that are being used as a drug carrier.

This study was carried out to analyse the feasibility of combining HME and FDM 3D printing in order to achieve a cost-effective fabrication platform for a patient-tailored drug delivery system. A type of biocompatible filament has been produced by mixing several pharmaceutical grade polymers and an active pharmaceutical ingredient (API). The polymers are Hydroxypropyl Cellulose (HPC), Eudragit® RL PO and Polyethylene Glycol (PEG). The model drug loaded is theophylline. Different ratios of the mixture were used for the extrusion for the optimization of filament composition. The properties and the printability of the extruded filaments were being studied. The filament produced need to have good flexibility and ductility so that it can be fed into the printing head of the FDM 3D printer. HPC is a derivative of cellulose and is a type of thermoplastic with high amorphous content. As a result, it has high molecular mobility and plasticity [606]. Due to its physical properties, HPC has been chosen to be made into FDM printable filament. HPC has been widely used in the pharmaceutical industry as a tablet binder, thickening agent, viscosity increasing agent and coating agent [606]. A study carried out by Sarode *et.al* shows that HPC can be used to produce chemically stable solid dispersions of poorly and highly water soluble drugs [607]. The polymer HPC has been used effectively to form amorphous solid dispersions containing crystalline drug, which has resulted in improved dissolution and also making the drug sustained release. However, HPC is highly hygroscopic and has the tendency to absorb moisture from the atmosphere. Eudragit® RL PO is an amorphous polymer and is an ammonio methacrylate copolymer type A. It has been used for sustained release products [608]. It is highly permeable to water but not water soluble. According to the Heckel analysis by Dave *et al*., the deformation behaviour of Eudragit® RL PO is similar to a typical plastic material [609]. A study carried out by (Kotiyan 2001) shows that Eudragit® RL PO can be used to prevent crystallisation [610]. PEG is a semi-crystalline polymer that has been used in a wide variety of pharmaceutical formulations for controlled release systems. It is biodegradable, stable and hydrophilic. Its hydrophilicity can improve aqueous solubility and bioavailability of solid dispersion. PEG can also impart plasticity into the polymer matrix [606]. By adding Eudragit and PEG into the formulation, the plasticity and the flexibility of HPC filament can be improved so that it can be used for 3D printing. Apart

from that, the use of higher molecular weight PEG is less hygroscopic, which could bring stability to the formulations [531]. The model drug, theophylline, is an odourless white crystalline powder with a bitter taste. Theophylline is chosen as it has a high melting point of 273°C, which appears as an ideal candidate to withstand thermal processing. Due to its thermal stability at high temperature, it is suitable to be used both in HME and FDM 3D printing. However, theophylline is only slightly soluble in water and alcohol. Due to the advantages of HPC and PEG in solid dispersions, these polymers were chosen. HME is a technology that can create a solid dispersion effectively [117,133,611]. The shear mixing and kneading during the extrusion process allows homogeneous mixing of the polymers and the drug as the drug is molecularly dispersed in the polymer matrix. Such formulation is known as solid dispersion and the solid dispersion is known to be able to improve the solubility of a drug with poor solubility [583].

Therefore the aim of this study was to develop and optimise various novel polymeric compositions for FDM 3D printing of sustained-release drug delivery systems by means twin-screw extruder. The printability of the filaments was assessed thoroughly for outlining the scope 3D printing a tablet out of these filaments. The mechano-chemical properties as well as *In-vitro* drug release of the filaments and the 3D printed tablets were studied. The release mechanism of the 3D printed tablets was determined using mathematical kinetic models such as zero-order, first-order, Higuchi, and Korsmeyer-Peppas models. Studies have shown that different 3D printing settings can have an effect on the release kinetics and mechanisms of a 3D printed tablet [79,612,613]. The biocompatibility of the filaments produced was also studied via cell studies.

6.2 Materials

Nisso Hydroxy Propyl Cellulose (HPC) (Grade SSL) from Nippon Soda Co., LTD. (Tokyo, Japan) was used. Eudragit® RL PO powder used was from Evonik Industries (Darmstadt, Germany). Poly (ethylene glycol), average M.W. 6000 was purchased from Fisher Scientific (Loughborough, UK). Theophylline 99+% anhydrous purchased from Fisher Scientific (Loughborough, UK) was used as a model drug. All materials were used as received.

6.3 Experimental Methods

HPC powder, Eudragit® RL PO powder, PEG, and model drug theophylline were used and mixed together in a pestle and mortar. The mixed powder was then transferred into a

bottle and further mixing was carried out using a Turbula shaker mixer, Eskens (Alphen aan den Rijn, Netherlands) for 15 mins. The ratio of the (HPC : Eudragit : PEG : theophylline) used to make into filaments were shown in Table 6.1. The mixed powder was then produced into filaments using a table-top custom-built L/D 10 twin-screw extruder by Twin Tech Extrusion Limited (Stoke-on-Trent, UK), assembled by Point1Controls/R Controls (Stoke-on-Trent, UK). The extruding temperature for the 4 zones (Z1 : Z2 : Z3 : Z4) were (70 °C : 100 °C : 110 °C : 110 °C) and the die was set to 110°C. The heat soak time of the extruder was set to 5 minutes. The extruding hole on the die has a diameter of 2.0 mm and the extrusion speed was set to 60 rpm. A standalone filament winder was used to collect the filaments extruded. A Vernier calliper was used to measure the diameter of the filaments and only filaments with a diameter of 1.75 mm were used for 3D printing as the size of the 3D printing nozzle can only fit filaments with diameter below 1.75 mm.

Table 6.1: The different ratios of (HPC : Eudragit : PEG : Theophylline) used for the fabrication of different filaments.

Formulation No.	**Ratio of (HPC : Eudragit : PEG : Theophylline)**
F1	0 : 8 : 1 : 1
F2	2 : 6 : 1 : 1
F3	4 : 4 : 1 : 1
F4	5 : 3 : 1 : 1
F5	6 : 2 : 1 : 1
F6	7 : 1 : 1 : 1

6.3.1 Design and Fabrication of Tablet

The extruded filaments were printed into tablets using the Makerbot Replicator 2X (Makerbot Inc., NY, USA). The CAD model of the tablet was designed using Solidworks (Dassault Systemes, Waltham, MA, USA). Figure 6.1 shows a computer-generated 3D model of the tablet used for 3D printing. The 3D model was then saved as an .STL file and imported to Makerbot Desktop software (Makerbot Inc., NY, USA) for slicing. The tablet has a height of 5 mm, width of 10 mm and length of 20 mm. The layer height for printing was set to 0.15mm. A printing temperature of 195°C and bed temperature of 60°C was used. Tablet infill for printing was set to 100%.

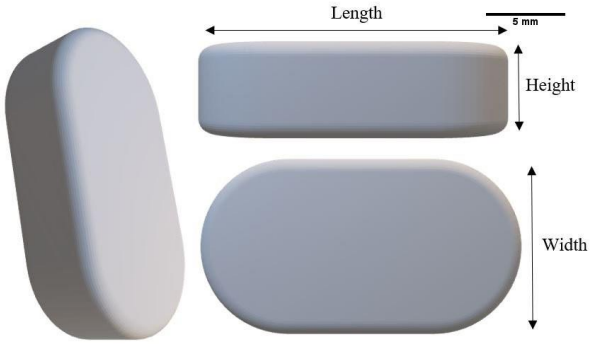

Figure 6.1: 3D CAD model of tablet for 3D Printing

6.3.2 Analysis of the Filament and 3D Printed Tablet

6.3.2.1 Differential Scanning Calorimetry (DSC)

A DSC 4000 system (Perkin Elmer, Waltham, MA, USA) was used to study the glass transition temperature and the melting temperature of all the filaments. The samples used were about 5mg. The samples were placed in an aluminium pan, and an empty aluminium pan was used as a reference. Nitrogen gas was used as the purged gas at a flow rate of 20 mL/min in all the DSC experiments. The data were collected and analysed with Pyris software (Perkin Elmer, Waltham, MA, USA).

6.3.2.2 Thermogravimetric analysis (TGA)

TGA was carried out using a Q40 Thermogravimetric analyser (TA Instruments, New Castle, DE, US) to obtain the degradation profile of the PEG/PLA blends. The samples used were about 10mg and were placed in an open aluminium pan. The furnace was then heated from 30 °C to 550 °C at a rate of 10 °C /min. Nitrogen gas was used as purge gas at a flow rate of 20mL/min. Data were collected and analysed using the Advantage/Universal Analysis Software (TA Instruments).

6.3.2.3 X-ray Powder Diffraction

The crystallinity of the powder mixture, each individual powder, filament and 3D printed tablet were assessed using a Siemens D500 X-ray Diffractometer (Siemens, Germany). The samples were scanned between 2 Theta (θ)=5° to 50° using 0.01° step width and 1s time count. The divergence slit was 1mm and the scatter slit was 0.6mm. The X-ray wavelength was 0.154 nm in Cu source and at a voltage of 40 kV.

6.3.2.4 Mechanical Testing (Texture Analyser)

Tensile testing and three-point bending test were carried out on the filaments using TA.XT Plus Texture Analyser (Stable Micro Systems, Godalming, UK). A load cell of

50 kg was used and a tensile grip probe set was used to measure the tensile strength of the filaments. For each filament formulations, five 10 cm filament samples were cut from the batch for mechanical testing. The test was set up as a tension test with a maximum applied force of 50 kg. The test was stopped as soon as the filament breaks. For the three-point bending test, a 3D printed custom made three-point bend probe tool was attached to the tensile grip. The filaments were securely taped onto a tester platform with a 25-mm gap. The data were collected and analysed using the Exponent Software version 7.0.3.0 (Stable Micro Systems, Godalming, UK).

6.3.2.5 Scanning Electron Microscope (SEM)

SEM was carried out using the JEOL JMS 820 (Freising, Munich, Germany) to study the morphology of the filaments and the printed samples. The samples were sputter-coated with gold under vacuum conditions using the Edwards S-150 sputter coater (Edwards High Vacuum Co. International, Albany, NY, US) for electrical conductivity. The accelerating voltage was at 3 kV at various magnifications.

6.3.2.6 Biocompatibility Study

Cell studies were carried out on the powder mixture and the filaments to ensure their biocompatibility. Retinal Pigment Epithelium (RPE) cells were used and the cells were seeded at a density of 4 x 104 on the first day. The number of cells was counted again on the second day and fifth day after seeding and treated with the powder mixture and filaments.

6.3.2.7 *In-vitro* Drug Release Study

In-vitro dissolution test was carried out on three randomly selected tablets from each batch for 3D printed tablets for drug release study. The mass of the samples was first weighed before dissolution and then weighed again after the dissolution test when the samples were dried. The dissolution parameters were chosen according to the US Pharmacopeia (USP) 36 monograph 'Theophylline Extended-Release Capsules Test 6'. Determination of the *In-Vitro* drug release was performed using USP type I dissolution apparatus (708-DS Dissolution Apparatus, Agilent Technologies, Santa Clara, CA, USA) in 1000mL of 0.05M phosphate buffer solution (pH 6.6) at 37±0.3 °C with a rotation speed of 100 rpm. The drug concentration of the dissolution medium was measured using a Cary 60 UV-Vis Spectrophotometer (Agilent Technologies, Santa Clara, CA, USA) at a wavelength of 271 nm in a 2 mm cell versus a blank solution consisting of a phosphate buffer (pH 6.6). The samples were drawn automatically using an Agilent 810 peristaltic

pump (Agilent Technologies, Santa Clara, CA, USA) and sampling was done every 5 min for the first hour, every 20 min of the following 2 hours and every 60 min for the last 10 hours. The release profiles were plotted as a percentage of cumulative drug release versus time.

6.3.2.8 Statistical Analysis

Statistical analysis was carried out on the 3D printed tablets to study the differences in the 3D printed tablets due to the difference in formulation composition. The mass of all tablets used for dissolution studies were measured before and after the dissolution studies in dry conditions. One-way ANOVA test, followed by a post-hoc Tukey HSD test was use for the analysis on the change in mass on all tablets for all formulations.

The dissolution data for all tablet formulations were also compared using model independent approaches (difference factor (f_1) and similarity factor (f_2)) to show whether the dissolution patterns of each formulation are different from each other.

6.4 Results and discussion

6.4.1 Thermal Analysis

DSC is a highly sensitive technique to study the thermal transition as a function of heating of materials. In the HME process, the powder mixture was thermally stressed. It has been proven that the API used, theophylline, has good thermal stability and can be processed using HME [153,602,614]. However, DSC measurements have been carried out on the pure substances, the powder mixture, the extrudates and the 3D printed products to ensure its thermal stability as well as miscibility.

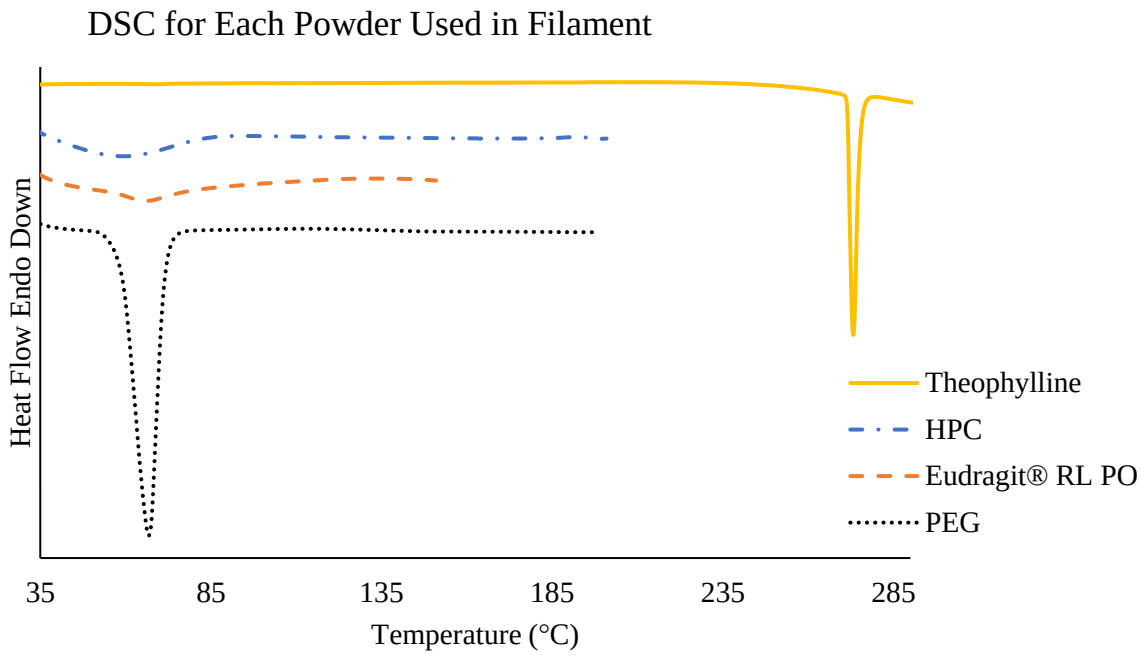

Figure 6.2: DSC measurements for the pure substances used as powder blend for producing the filaments. The powders are Hydroxypropyl cellulose (HPC), Eudragit® RL PO powder, Polyethylene glycol (PEG) 6000, and anhydrous theophylline 99+%.

Figure 6.2 shows the DSC measurements for each individual powder before mixing. The study shows that HPC and Eudragit® RL PO have high amorphous content as the DSC curves for both materials do not show obvious endothermic events. However, amorphous materials were expected to show an endothermic slope which represents the glass transition temperature (T_g). The T_g is the temperature when the molecules in the material starts to transition from a glassy state to a soft, rubbery state [615]. This is the temperature when the materials soften. According to the technical data sheet of the HPC Grade SSL from the manufacturer, it exhibits two softening temperature, one at 75 °C and the second at 183 °C [616]. From the DSC curve, the T_g of HPC was found to be around 76 °C. The dip before the slope of the glass transition could be caused by the plasticising effect due to the presence of moisture in the HPC polymer. The T_g for Eudragit was around 66 °C which is similar to the literature [617,618]. PEG is a semi-crystalline polymer and the DSC showed a melting peak at around 67°C. The calculated heat enthalpy value (ΔH) of PEG is approximately 252.7 J/g. Theophylline is a crystalline drug and has a sharp endothermic peak, which is the melting point at around 273 °C. The DSC result of theophylline shows that the ΔH value of theophylline is around 68.14 J/g. This shows that

theophylline would be a suitable model drug for HME and FDM 3D printing processes as these processes require high temperature.

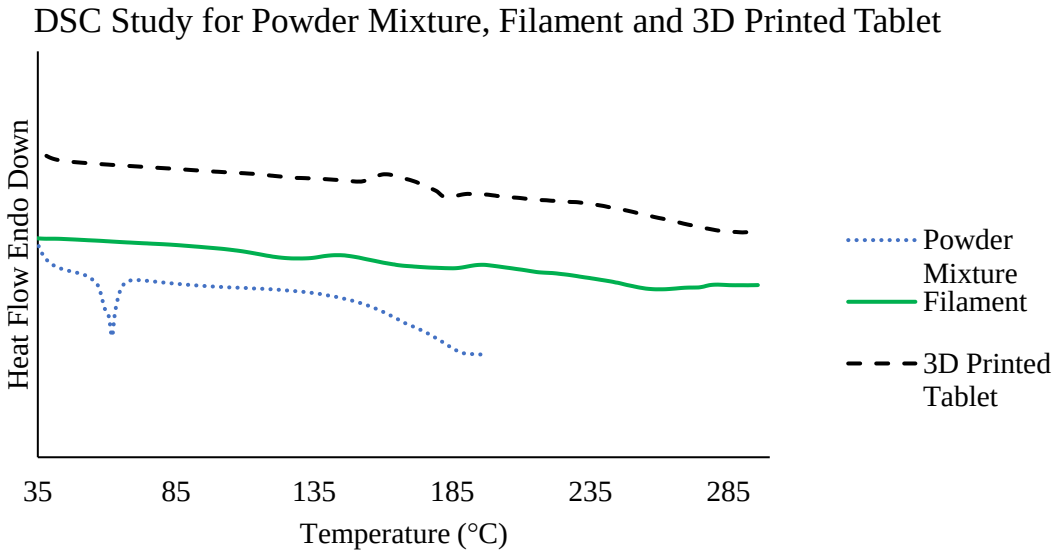

Figure 6.3: DSC Results obtained for Powder Mixture, HME Extruded Filaments and FDM 3D Printed Tablet.

The DSC curve for the powder mixture in Figure 6.3 mimics the temperature cycle of the powder mixture went through during the extrusion process and the printing process. This is to ensure the thermal stability of the powder mixture as it is required to go through processes of high temperature. The powder mixture of HPC, Eudragit, PEG and theophylline was placed in the sample pan for heating. However, the results obtained only reflect the thermal process experienced by the powder. In the process of extrusion, the mixture underwent kneading and shear mixing which is not reflected in the DSC result. The extrusion process was carried out at a maximum temperature of 110 °C. The extruded filament was then being fed into a hot printing head at a temperature of 195 °C. Therefore, the heating of the powder mixture in the DSC study was carried out up to 200 °C. The DSC curve only showed a small endothermic step at around 60 °C for the heating of the powder mixture. This could be the T_g of HPC and Eudragit® RL PO. The DSC curve in Figure 6.2, which shows the DSC results of the individual components shows that HPC and Eudragit have a very similar T_g. The endothermic peak at around 62 °C, following the small step that occurred before, could be the melting point of PEG on the powder mixture. As the T_g of HPC and Eudragit are very close to the T_m of PEG, the DSC curve showed just on the endothermic peak that coincides with each other when these materials are all physically mixed to form a powder mixture.

The DSC curves in Figure 6.3 also contain the DSC study for the HME produced theophylline-loaded filament. As shown in the DSC results from Figure 6.2, HPC and Eudragit have very high amorphous content with a low T_g (around 56 °C and 63 °C respectively). PEG is a semi-crystalline polymer with a melting point of around 68 °C. The model drug, theophylline, is an odourless white crystalline powder with a bitter taste, and has a melting point of 273 °C. From the DSC results for the filament, we can see that the peaks for the PEG and theophylline melting points have been depressed. There were no obvious endothermic peaks on the DSC curve due to the lack of crystallinity in the filament. This has proven that the theophylline has been molecularly dispersed into the polymer matrix, making it amorphous through the process of twin-screw extrusion. It has also been reported that HPC can effectively convert the crystalline drug to amorphous form, which is also shown in the DSC results obtained. The DSC results for the filament showed a very small step change at around 160 °C, which could be the T_g of the new amorphous filament. This means that the filament could be softened above this temperature. DSC was also carried out on the FDM 3D printed tablet. The results show that the tablet contains amorphous content as there was no occurrence of endothermic peaks during the heating cycle. There is a small step change at around 170°C which could be the T_g of the 3D printed tablet. The high temperature of 3D printing could have slightly shifted the T_g of the tablet from the filament. Similar to the filament, the melting point of the theophylline could not be seen, which further confirmed that the process of HME has converted the crystalline theophylline to amorphous. The DSC study shows that the mixture is thermally stable to be used for HME to be extruded into filament at 110 °C, and the filaments produced are suitable for FDM 3D printing at a temperature of 195 °C. The extruded filament and the 3D printed tablet also have thermal stability of up to 300 °C.

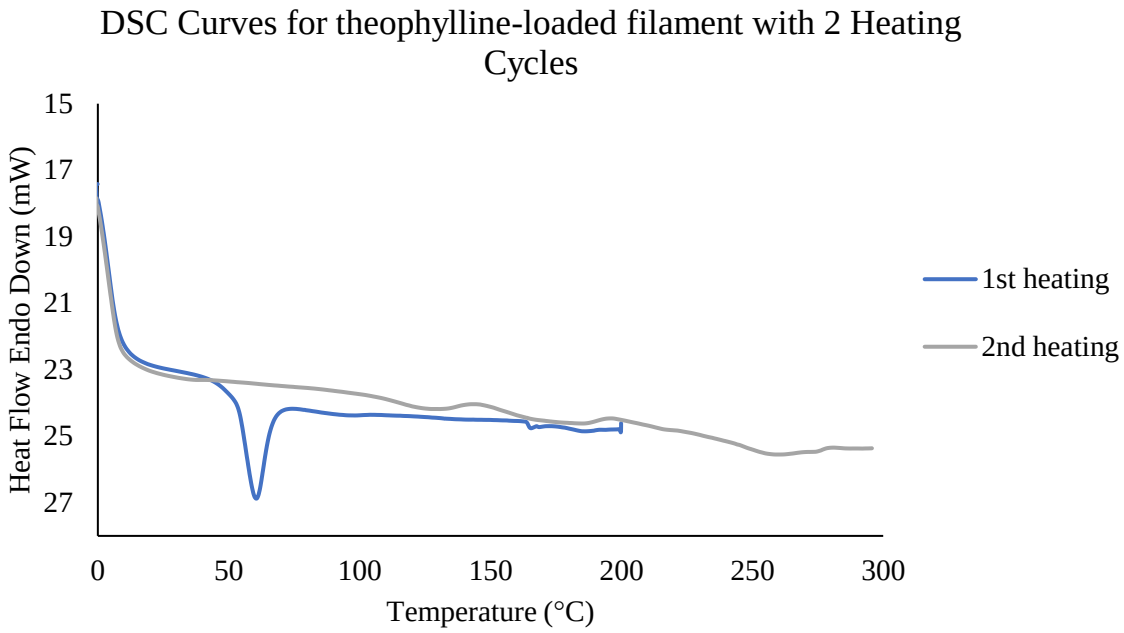

Figure 6.4: DSC analysis for theophylline-loaded filament with 2 heating cycles.

The DSC results in Figure 6.4 shows the measurement for the extruded theophylline-loaded filament on 2 heating cycles. The first heating cycle was carried out up to 200 °C, then a cooling cycle down to 0 °C, finally the 2nd heating of up to 300 °C. It has been recommended that 2 heating cycles can be carried out during a DSC analysis for materials consisting a mixture of different materials to remove any possible artefacts and any thermal history on the results in order to obtain a better representation of the thermal properties of the newly formed material [619]. The first endothermic peak (around 60 °C) seen on the first heating cycle could be caused by the presence of a volatile substance or a plasticiser. This is because, during the second heating cycle, this endothermic peak disappears from the curve. This could be explained by the presence of moisture in the filament that is absorbed from the environment. The presence of water in the filament caused a plasticizing effect on the polymer mixture, causing the polymer to show an endothermic event when being heated. The water in the filament has been evaporated during the first heating cycle, hence the endothermic does not happen again on the second heating cycle. The Tg of the filament is around 160 °C in the first heating cycle, and the step change is very small. A small endothermic peak occurred after the Tg of the filament. This could be an artefact that is caused by the relaxation of the molecules at the glass transition. This is because the molecules go from a rigid to a flexible structure and stress is released. After cooling, the filament is reheated again. In the second heating cycle,

there are no endothermic peaks, showing that the filament is amorphous. This can prove that the HME is effective in producing amorphous material through the shearing and mixing by the co-rotating screws.

TGA was used to study the degradation profile of each of the individual component used in for the formulations, the powder mixture of the formulation, the extruded theophylline-loaded filament, and the 3D printed tablet (Figure 6.5). The temperature when 10% of the sample degraded (t_{90}), 50% of the sample degraded (t_{50}), and 90% of the sample degraded (t_{10}) were extracted from the TGA curves and were tabulated in Table 6.2. The TGA results confirmed that the individual components and the mixture only start to degrade at a temperature of at least above 260 °C. This result suggests that the drug and the polymer mixture would not degrade during the HME process and the 3D printing process as the operating temperature of both processes were well below the temperature when the material starts to degrade. The TGA on the filament and 3D printed tablet also further confirmed that the processes did not degrade the materials. Despite the shearing provided during the HME process, the extruded theophylline-loaded filaments still maintain great thermal stability as the torque applied during the process was relatively low (approximately 5 Nm).

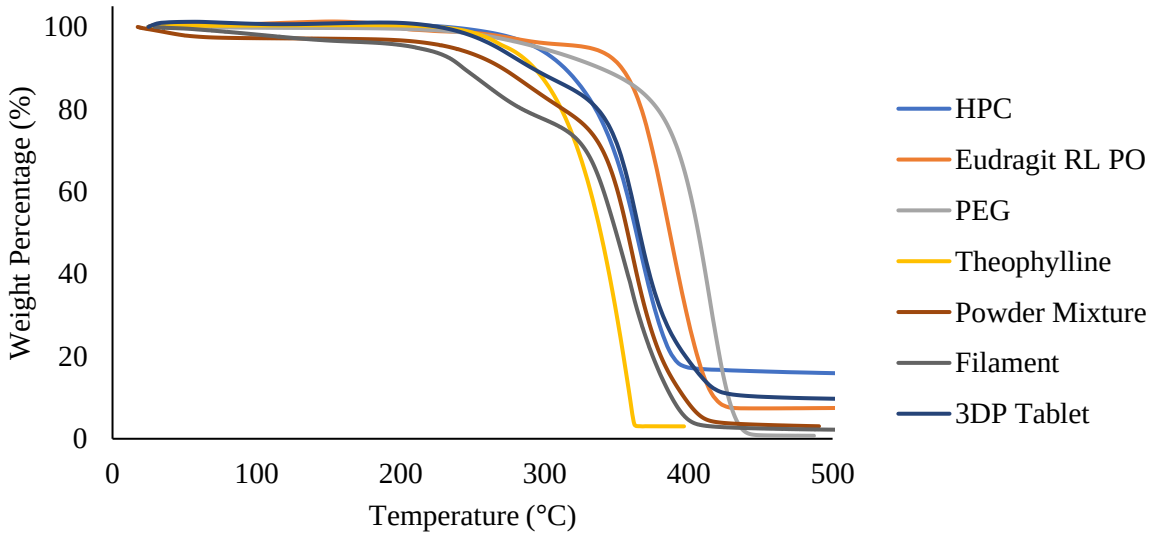

Figure 6.5: Thermal degradation profiles for individual materials, powder mixture, extruded filament and 3D printed tablet

Table 6.2: Temperatures at three degradation points (90%, 50%, 10% wt. remaining) for each individual component, powder mixture, extruded filament and 3D printed tablet.

Temperature at weight %	t_{90} (°C)	t_{50} (°C)	t_{10} (°C)
HPC	269.9	363.3	-
Eudragit	351.7	386.7	415.8
PEG	338.3	406.7	427.8
Theophylline	306.4	343.6	366.7
Powder Mixture	270.8	357.7	396.9
Extruded filament	243.2	349.8	388.2
3D Printed Tablet	291.4	366.0	468.8

6.4.2 X-Ray Powder Diffraction (XRPD)

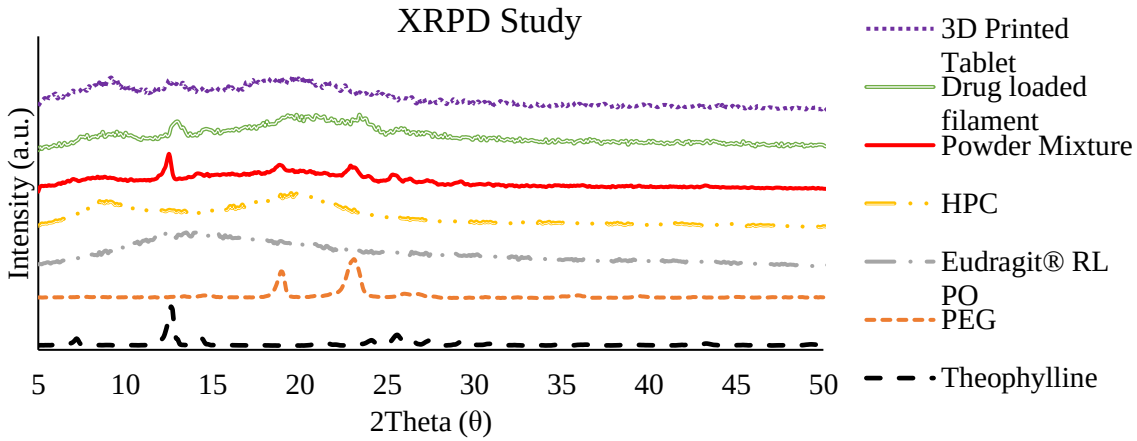

Figure 6.6: XRPD results for all individual powders, powder mixture, filament and 3D printed tablet.

XRPD has always been used for qualitative analysis to determine the crystallinity of a material. XRPD study has been carried out on all the individual bulk powders, the powder mixture, the extruded filament and the 3D printed tablet. The results from the XRPD is shown in the figure above (Figure 6.6). The scans from theophylline and PEG show obvious crystalline peaks, which means these two materials have high crystallinity in their bulk powder forms. The diffractograms for HPC and Eudragit® RL PO confirm that these two powders are highly amorphous reflected by no obvious peaks. The powder blend shows some crystallinity as expected as the powders were only physically mixed together at room temperature. The crystallinity in the powder mixture was due to the presence of crystalline theophylline and PEG. As the powders were physically mixed, there is not much reaction between the powders which could highly affect the crystallinity of the mixture. However, the crystallinity is slightly lower in the powder mixture than the pure theophylline and PEG individually. This is expected due to the presence of amorphous polymers (Eudragit and HPC) in the formulations. As for the theophylline-loaded

filament, the result shows that the filament is highly amorphous with a very small amount of crystallinity as the crystallinity peaks are very small. A quite similar phenomenon was observed on the 3D printed tablets. The peaks that can be seen on the PEG and theophylline are not obvious in the 3D printed tablet. This has proven that the process of twin-screw extrusion has successfully converted the crystalline theophylline into amorphous form by molecular dispersion of the drug molecules into the polymer matrix. These results are in line with the studies from the DSC of filament and 3D printed tablets which further confirms that the model drug, theophylline, has been converted to its amorphous forms as a function of being molecularly dispersed into the polymer matrix.

6.4.3 Mechanical properties

The mechanical strength of the extruded filament is very important as the FDM printing process exerts a considerable amount of force onto the filament. The filaments must have the right balance between ductility and stiffness for them to the printable. In an FDM 3D printing process, a gear is used to feed the filament into the printing head. The gear exerts shearing and tensile stresses onto the filament. Therefore, the filament must be ductile and strong enough to withstand the transversally applied pressure. Tensile testing and 3-point bending test were carried out to determine the mechanical resilience of the extruded filaments. Using the results obtained from the tensile testing, the strength of the filaments can be calculated through the stress-strain curve. The strength of the filaments was presented in four aspects: yield strength, ultimate tensile strength, Young's modulus and elongation at break. Yield strength is the minimum stress under which the material deforms permanently (i.e. the stress at which the material stops behaving elastically is called the yield strength). This is the highest point where the strain increases proportionally with stress. Ultimate tensile strength is the maximum stress that a material can withstand while being stretched before breaking. Young's modulus measures the stiffness of the material. It describes the elastic properties of the filament undergoing tension in one direction. This can be obtained by calculating the gradient of the proportional section on a stress-strain curve. The elongation at break is the percentage of filament sample that can be stretched without breaking and this value can be calculated using the change of length over the original length of the sample. This is also presented as a strain values in Figure 6.7. Figure 6.7 shows the results from the tensile testing for the filaments, displaying the stress and strain values. The results for the yield strength, ultimate tensile strength, Young's modulus and elongation at break are in Table 6.3.

The study shows that F1 and F2 have two of the highest strain values amongst all the filaments. F1 has the highest strain, which means it can be stretched the most before failing. This could be due to the high percentage of Eudragit in the filament as Eudragit induces high flexibility and plasticity. As the percentage of HPC increases in the filament, formulation, the strain values of the filaments decrease. From the chart in Figure 6.7, F1 has the highest stress values, which means it can withstand the most force. There seems to be no linear pattern on the stress values as the composition of the polymers change. The stress values showed are actually the yield strength of the filaments. The stress values only mean that was the maximum stress before the plastic deformation of the filaments. It seems that both Eudragit and HPC can impart elasticity when only one of itself is at high concentration. When both are mixed at a ratio closer to 1, the strength decreases. However, the stress that the filament can withstand is already sufficient for FDM 3D printing as all filaments have been successfully used for printing. The result from tensile testing can only be used as a reference as it only represents the uniaxial force that the filaments can withstand. The values of stress for the filaments, although can be used to represent the actual stiffness of the filaments, is often the ratio of force to the cross-sectional area of the filament. The amount of stress applied when the filament breaks was considered the maximum 'load' and the distance when it breaks was considered as 'deformation'. In most cases, the filaments manufactured do not have homogeneous diameters due to the processing parameters during the HME process (eg. feeding rate, rotating speed of the standalone filament winder). The values obtained in Figure 6.7 and Table 6.3 are the average values of several measurements.

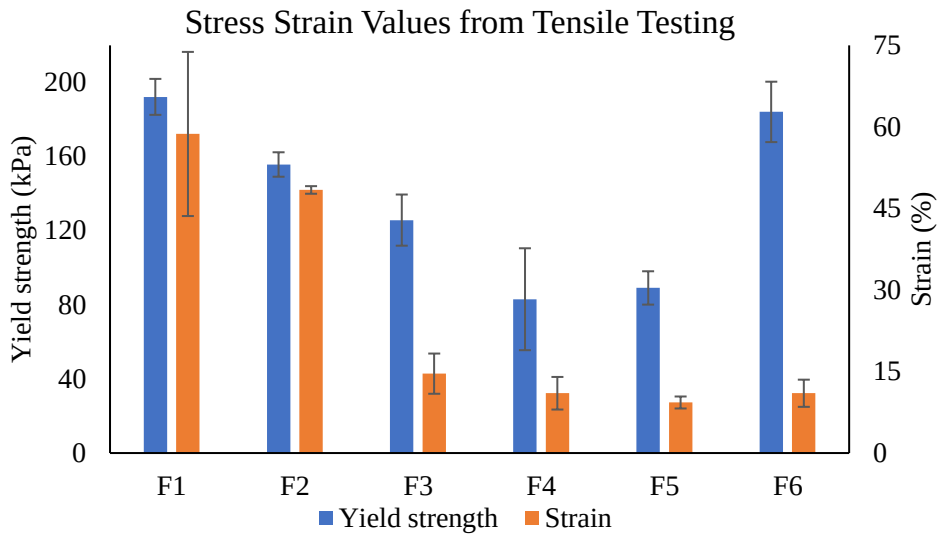

Figure 6.7: Stress-strain values from the tensile testing of all theophylline-loaded filaments.

Table 6.3: Calculated strength of the theophylline-loaded filaments from tensile testing.

Filament Formulation No.	Yield Strength (kPa)	Ultimate Tensile Strength (kPa)	Young's Modulus (kPa)	Elongation at Break (%)
F1	192.2 ± 9.7	216.7 ± 2.6	46.0 ± 5.3	58.7 ± 15.1
F2	155.7 ± 6.6	188.3 ± 2.5	46.0 ± 6.6	48.4 ± 0.7
F3	125.7 ± 13.8	139.6 ± 17.5	47.0 ± 5.3	14.6 ± 3.7
F4	83.0 ± 27.5	105.0 ± 28.9	30.1 ± 6.9	11.0 ± 3.0
F5	89.1 ± 9.0	109.4 ± 6.7	30.3 ± 2.1	9.3 ± 1.1
F6	184.1 ± 16.3	200.0 ± 10.9	55.0 ± 2.6	11.0 ± 2.5

A 3-point bending test was carried out to measure the flexural strength of the filaments. The setup of this test means it is suitable to be used to assess the breaking force, breaking distance and the rupture strain of the filament. During the printing process, the filament is pushed by a rotating gear in which the force exerted can be replicated through a 3-point bending test. The stress and rupture strain values were extracted from the 3-point bending tests and results were shown in Figure 6.8 and Table 6.4. The test showed that filament F1 has the highest stress and strain values. As the percentage of HPC increases in the filament, the strength of the filament seems to decrease. This is due to the semi-crystalline properties of HPC, causing HPC to be brittle at room temperature. The presence of Eudragit improves the flexibility and plasticity of the filament. Despite the decreasing strength of the filaments as the concentration of Eudragit decreases, the filaments are still suitable to be used to FDM 3D printing as the filaments can still withstand the forces exerted by the printing gear.

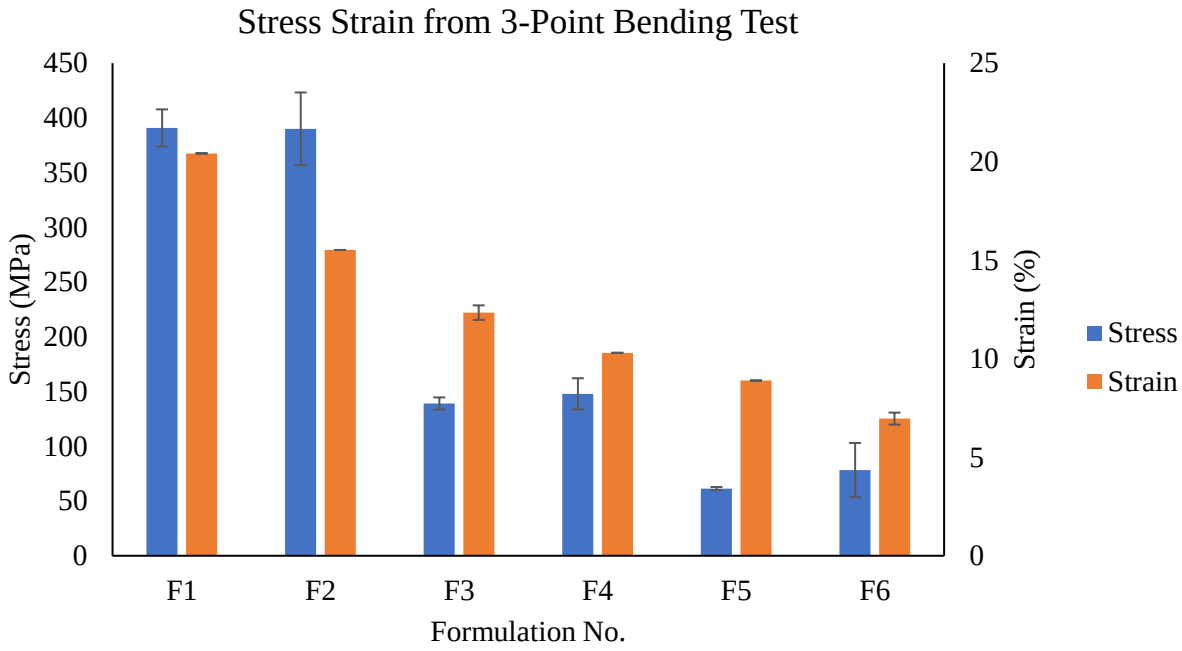

Figure 6.8: Stress and strain values of the extruded filaments obtained from 3-point bending test.

Table 6.4: Force, distance, stress and strain values extracted from 3-point bending tests for all filaments.

Formulation No.	Force (g)	Distance (mm)	Stress (MPa)	Strain (%)
F1	5008.80 ± 216.27	10.63 ± 2.5e-15	390.88 ± 16.91	20.42 ± 5e-15
F2	2867.84 ± 395.07	9.51 ± 3.1e-15	390.042 ± 33.22	15.52 ± 1.39e-14
F3	1620.33 ± 251.31	8.051 ± 2.43	139.12 ± 8.55	12.34 ± 0.37
F4	1275.54 ± 124.62	5.43 ± 0.77	147.891 ± 14.31	10.30 ± 1.8e-15
F5	1170.42 ± 91.55	4.01 ± 0.12	61.39 ± 1.42	8.89 ± 1.3e-15
F6	1067.90 ± 106.98	3.12 ± 0.44	78.26 ± 24.77	6.96 ± 0.30

6.4.4 3D Printing

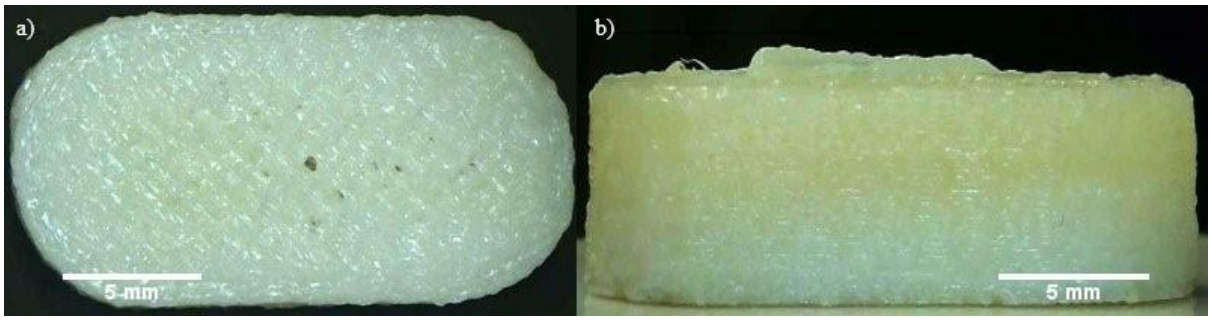

Figure 6.9: 3D printed tablet from the filament F2 a) top view b) side view.

The theophylline-loaded filaments were used to 3D print into tablets using a Makerbot Replicator 2X FDM 3D printer. The temperature of printing was 195°C, which is very close to the normal printing temperature of PLA filaments (around 190°C). Despite

filament not being as strong as the commercial filaments available, as proven from the tensile testing, the filament can still withstand the shear forces and stress experienced through the extruder of the FDM 3D printer. The printing of a tablet took approximately 10 minutes including the heating up of the printing nozzle and printing bed. Once the printer is heated up, the printing time required for one tablet is only 5 minutes. Figure 6.9 shows an example of a 3D printed tablet produced using the filament of formulation F2. All six filaments were printable. All filaments apart from filament F6 can produce good quality 3D printed tablets. The quality of tablets F6 was unacceptable (see Figure 6.10). The quality was assessed by visual inspection of the shape and the surface finish of the printed tablet. The quality of printing was also assessed by the difficulty in removing the printed tablet from the printing bed after printing without damaging the tablet. Tablets printed from F1-F5 filaments can be removed easily and cleanly from the printing bed. They also have a smooth surface finish. F5 tablets were printable and the quality was considered acceptable. The surface finish was not as smooth and the tablets were more brittle, causing some difficulties in being removed from the printing bed (Figure 6.10). However, the F5 tablets can still be removed from the bed cleanly without damaging it with extra care and attention. F6 printed tablets also had good adhesion to the printing bed, causing it difficult to be removed. When being removed, there were some bits that were still adhered to the bed which makes the shape of the tablet to be altered. There was no way to remove the tablets cleanly from the printing bed without damaging it. The surface finish was not as good as the others. Apart from that, the F4 printed tablets were brittle. Some parts of the tablet can be easily damaged when removing because of their brittleness. This is not ideal particularly for the fabrication of tablet as the consistency of each tablet will be affected. The high content of HPC in F5 and F6 could have contributed to its brittleness. To achieve a good quality print, the filament needs to have enough plasticity and smoothness which is provided by the presence of Eudragit. The higher the content of Eudragit, the higher the plasticity and flexibility of the filament. However, the plasticity of the filament cannot be too high as it may lose its ductility which is needed to withstand the forces exerted onto the filaments during printing. The filament that has too much plasticity could be easily deformed which could be an issue during the feeding process of FDM 3D printing. This is because the teeth of the gear may leave an imprint on the filament and change the shape of the filament, which is shown in Figure 6.11. Filament that has high flexibility is also difficult to keep its shape and remain straight, which makes it difficult to be fed into the small hole of the printing head. However, high

plasticity allows smoother surface finish as the melted filament has a higher viscosity, making the extrusion during 3D printing easier. The printability of all four filaments was shown in Table 6.5

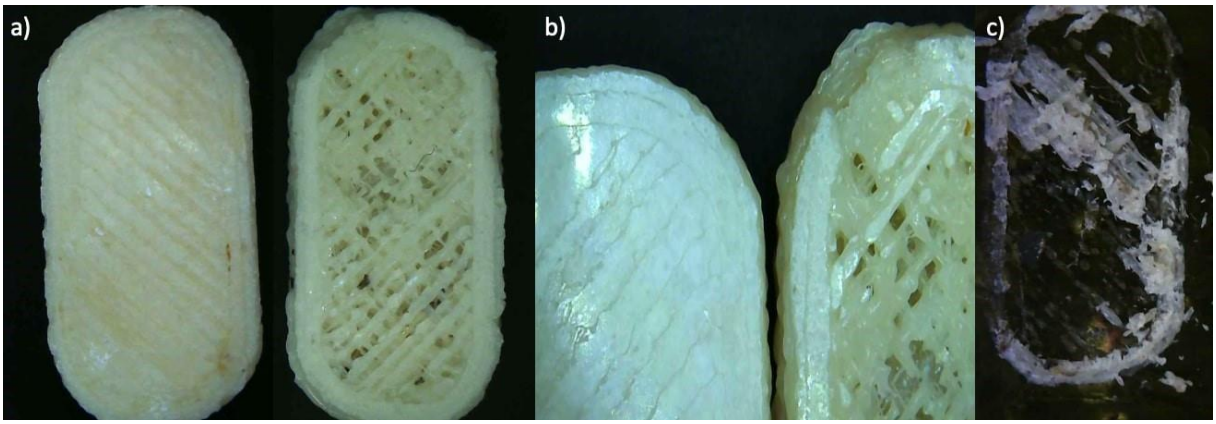

Figure 6.10: Quality comparison of good and poor quality 3D printed tablets a) F2 tablet on the left (good quality), F6 tablet on the right (poor quality) b) zoom in image of a, c) remnant of F6 tablet stuck on the printing bed after tablet has been removed.

Table 6.5: FDM printability and quality of all six theophylline-loaded filaments.

Filament of Formulation No.	Quality of Printing
F1	Printable & Good Quality
F2	Printable & Good Quality
F3	Printable & Good Quality
F4	Printable & Good Quality
F5	Printable, Acceptable Quality
F6	Printable, Poor Surface Finish

Extra attention is required for the storage condition of the filament extruded. This is because the filament can absorb moisture from the environment more easily than PLA filaments. Although it was reported that the use of higher molecular weight PEG in a formulation can be less hygroscopic, HPC typically has high affinity to water molecules [531]. If the filament is left in the air for a long period of time, the filament will turn brittle due to the absorption of moisture. A brittle filament will fail at the gear during the feeding of the filament into the printing nozzle. The brittle filament will be crushed by the force exerted by the feeding gear. Therefore, it is recommended that the filament should be used immediately for printing after being produced using the twin-screw extruder. Otherwise, the filament needs to be stored in a dry environment to preserve and prolong the life of the filament. The filaments can be kept in a desiccator or in a sealed bag when not is used. The filament should always be stored in low humidity condition.

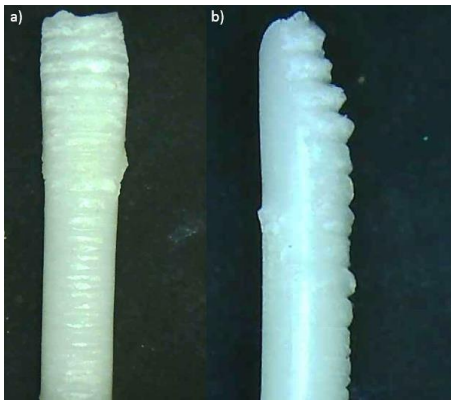

Figure 6.11: Failed filament during FDM 3D printing a) top view b) side view.

6.4.5 Scanning Electron Microscopy (SEM)

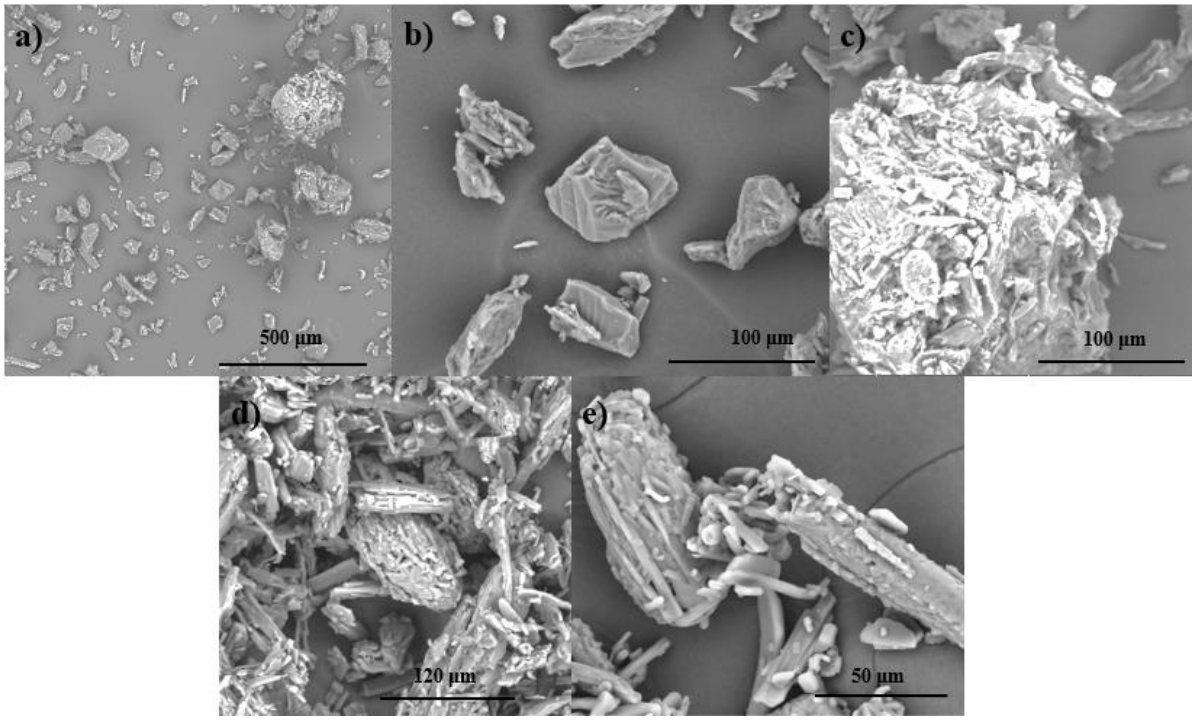

Figure 6.12: SEM images of the powder mixture use for the extrusion of filaments (a-c) and theophylline (d-e) at different magnifications a) 100X b) 500X c) 500X d) 520X e) 1000X.

The SEM images shown in Figure 6.12 are the powder form of the materials used for the polymeric composition of the filament. Figure 6.12a-c showed the powder mixture at different magnifications before it was being extruded into filaments. The mixture contained HPC, Eudragit, PEG and theophylline. The SEM images showed that the powder mixture contained some crystallinity mixed with amorphicity. This is because some of the powder particles exist as solid crystalline and some do not have a definite shape. The amorphicity was due to the presence of HPC and Eudragit as both polymers exhibit high amorphicity. The crystallinity was mainly attributed to theophylline. Figure

6.12d & e showed the SEM images of theophylline powder, where they exist in crystalline shapes. The structure of the powder mixture reflects the results obtained from XRD.

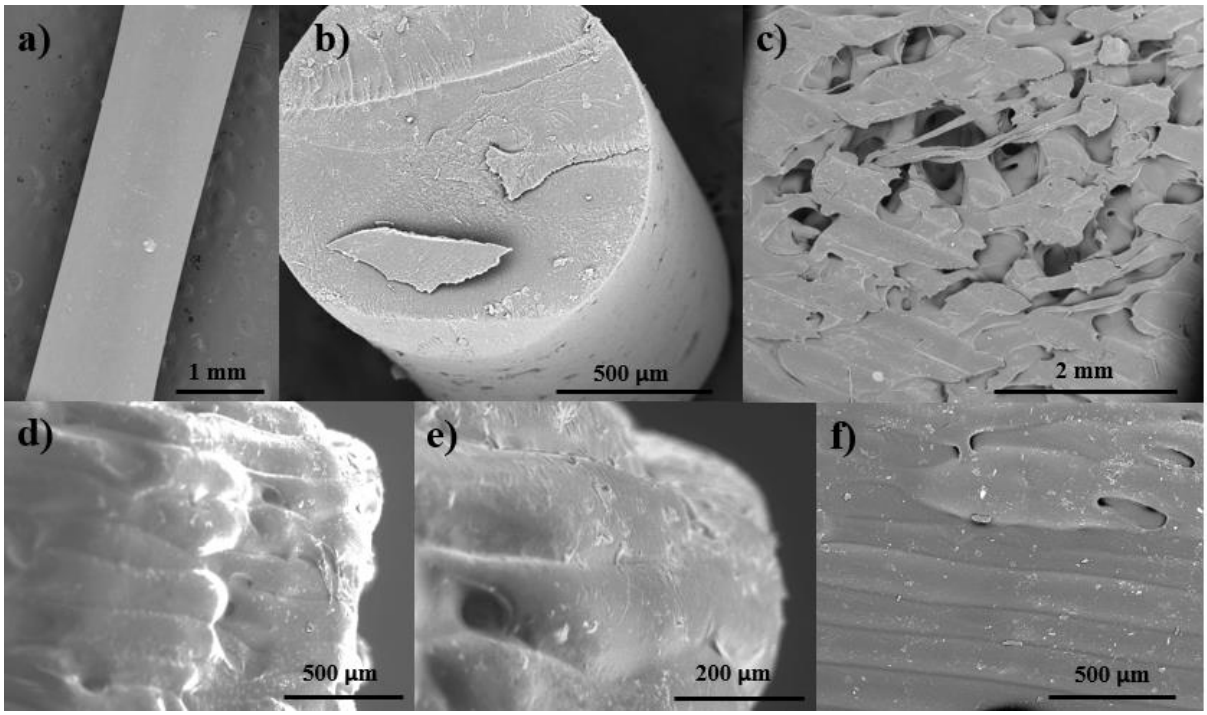

Figure 6.13: SEM images of theophylline-loaded filament (a-b) and 3D printed tablet (c-f). a) Surface morphology of filament at magnification of 30X (top view), b) cross-section of filament at magnification of 100X, d) side-view of 3D printed tablet at magnification of 100X, e) side-view of 3D printed tablet at magnification of 250X, f) side-view of 3D printed tablet taken after dissolution at magnification of 100X.

SEM images were also taken to study the morphology of the filament and the 3D printed tablets. The images of the filament surface and the filament cross-section were shown in Figure 6.13a-b. The SEM images showed that the filament has smooth surfaces and a very consistent round shape. There was no drug aggregation seen on the images which further confirms the twin-screw extrusion has successfully converted the theophylline crystals into amorphous form. SEM images of the 3D printed tablet were shown in Figure 6.13(c-f). The SEM images clearly showed the multiple layers of the tablet that were laid down during the FDM 3D printing process. It can be seen from the images that the thickness of each layer is quite consistent. The thickness of each layer is 0.15 mm. This has proven that FDM 3D printing can achieve high precision and accuracy despite being a low-cost 3D printing technique. Due to the layering method of FDM 3D printing, there also exist some pores on the tablet as seen in Figure 6.13c. This is unavoidable even with the printing of 100% infill being set. Figure 6.13f shows the side-view of the 3D printed tablet after dissolution has been carried out. The tablet did not dissolve in the dissolution

medium but retained its shape. The layering of materials was still present and distinguishable.

6.4.6 *In-vitro* Drug Release Study

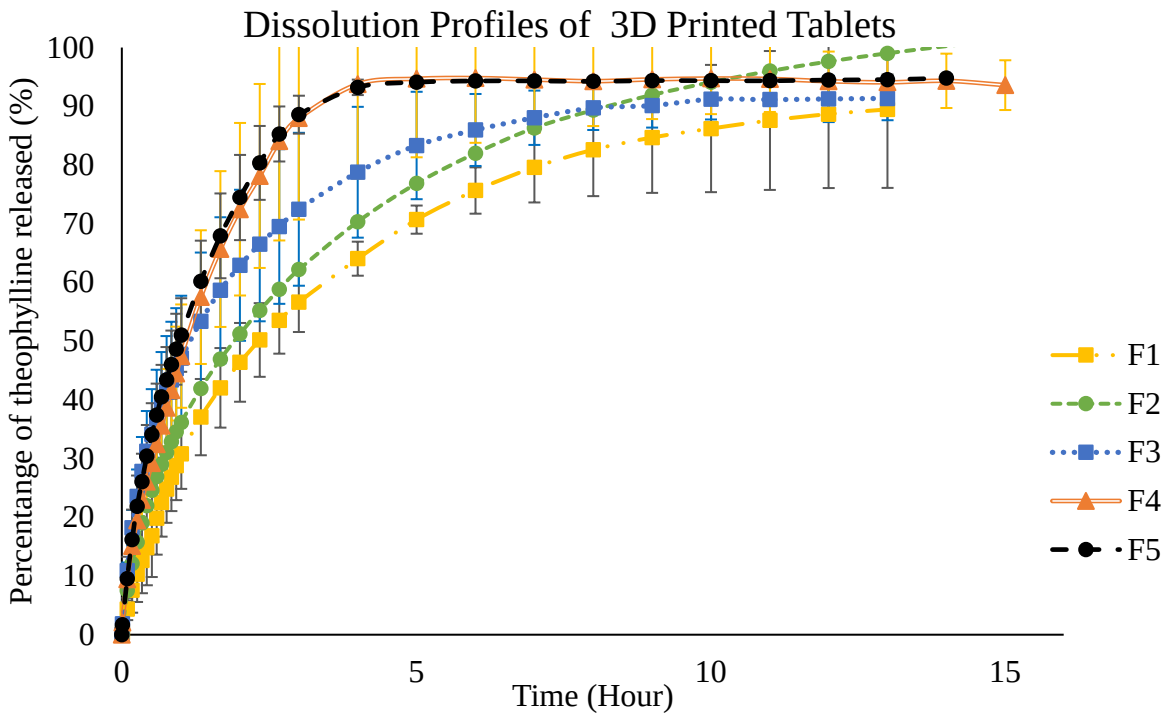

Figure 6.14: Dissolution profiles for tablets from filament formulations F1-F5.

After the development of theophylline-loaded filaments and the 3D printing of tablets, the drug loading of the filaments and the 3D printed tablets were determined. The samples were dissolved in ethanol and the drug concentration was measured using a Biochrom WPA Biowave II UV/Visible spectrophotometer (Biochrom Ltd., Cambourne, UK) at a wavelength of 271 nm. The percentage of theophylline in the filaments was 93.76% ± 2.76 and the drug content in the tablets was 92.46% ± 5.73. This shows that there was no major degradation of the drug caused by thermal processing i.e. HME and the FDM 3D printing. Dissolution studies were carried out on the 3D printed tablets. The drug release profiles were shown in Figure 6.14. Only F1-F5 tablets were studied as the 3D printed tablet of F6 did not show good quality. F1 tablets show the slowest release profile, whereas F4 and F5 tablets have similar release profiles. Theophylline is generally a poorly water-soluble API. The particles of API were dispersed or dissolved into the polymer matrices to form solid dispersion during the HME process, which is also confirmed through results from DSC and XRPD. During the dissolution process, a steep concentration gradient is formed at the media/tablet interface when tablets come into

contact with the dissolution medium. The steep concentration gradient allows the diffusion of theophylline from the tablet to the medium. There is no burst release at the beginning of the dissolution process, seen on the dissolution profiles in Figure 6.14. It is suggested that 3D printed tablets often have compact structure and high density which may restrict the drug release through diffusion [620].

The dissolution results showed that the time taken for theophylline to completely release in F1 tablets was around 10 hours. The drug release F4 and F5 tablets plateaued after 4 hours. The drug release study shows that all formulations are suitable for the purpose of controlled release as release continued for over 5 hours. The higher the percentage of Eudragit, the slower the release of theophylline. All the tablets showed drug release of more than 80% within 14 hours. This confirms that there was no API or excipient degradation occurred during the HME and 3D printing process. The 3D printed tablet using such polymeric composition seems to be successful in producing a controlled-release profile.

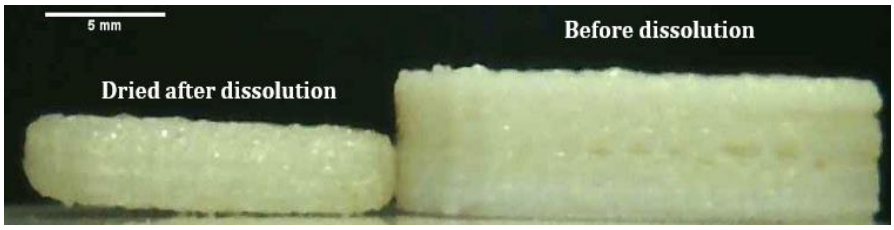

Figure 6.15: Tablet change in size after drying after dissolution study.

The tablets for all the formulations did not dissolve completely during the dissolution studies and the original shape of the tablet was retained. This is because Eudragit is not soluble in the dissolution medium used and it has managed to keep the shape of the tablet even after the drug has been completely released. Figure 6.15 above shows that the tablet size changed after the tablet was dried after dissolution. The size of the tablet did not change when the tablet was removed from the dissolution medium as the dissolution medium has been absorbed by the polymer that makes the tablet. The two polymers used (HPC and PEG) are soluble in water but only one polymer, Eudragit is not soluble. Eudragit is permeable to water, hence it is likely that Eudragit absorbed the dissolution medium. During the dissolution process, the HPC and PEG fully dissolved with the drug loaded. When the tablet was removed from the dissolution medium, the size and shape of the tablet were retained by the Eudragit. Once the medium absorbed by the Eudragit has completely evaporated, the shape of the tablet remains but it shrank in size. The tablets

were weighed before and after the dissolution studies for the comparison of the change in mass. The changes were shown in Table 6.6. There may some variations in the mass of the tablets. This is because 3D printed structures cannot be completely solid even with 100% infill due to the method of fabrication and the resolution of printing. It will always incorporate small internal voids and pores in the printed structures. This causes mass deviations. A one-way ANOVA, followed by a post-hoc Tukey HSD test were carried out on the change in the mass of the tablets. The results from the statistical tests were shown in Table 6.7. The statistical studies showed that the p-value corresponding to the F-statistic of one-way ANOVA is much lower than 0.05, suggesting that one or more of the 3D printed formulations were significantly different from each other. To identify which pair of the formulations are significantly different from each other, the Tukey HSD test was then carried out. The results showed that all formulations of 3D printed tablets were also significantly different from each other when being compared in pairs. This has shown that the different percentage of polymers in the formulation have a significant effect in the dissolution of the 3D printed tablets, which causes the change in mass.

Although all tablets experience a change in mass, they still retained their frame and shape after the drug release. This could be useful for the development of a medical implant. Figure 6.16 shows the cross-section of the tablet after and before the dissolution. The white colour of the tablet was due to the presence of theophylline and HPC. Once the drug has been released, the tablet becomes translucent. The image shows that the drug has been completely released. This study shows that such polymeric composition could be useful for the development of a medical implant. This type of formulation is particularly useful to be used as a medical implant for drug delivery or monitoring the condition of the body. This is because the insoluble part of the system can still hold the sensing devices on the implant after the drug has completely been released.

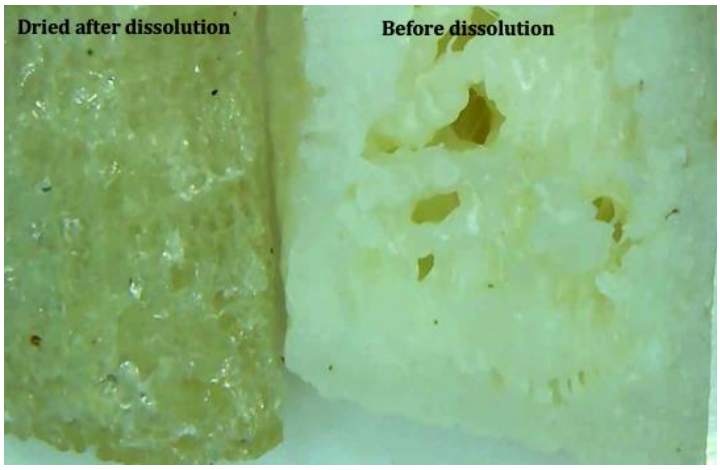

Figure 6.16: Cross-section image of tablet after (left) and before (right) dissolution.

Table 6.6: Change in mass of the dry tablets after dissolution studies.

Formulation No.	Tablet No.	Mass Before Dissolution (mg)	Mass of Dry Tablet After Dissolution (mg)
F1	1	734.4	627.0
	2	624.4	528.6
	3	818.4	722.5
F2	1	695.5	478.5
	2	610.8	403.8
	3	622.2	424.5
F3	1	629.6	280.9
	2	631.9	287.1
	3	653.2	286.4
F4	1	791.4	291.7
	2	784.0	272.3
	3	806.7	292.6
F5	1	633.3	194.6
	2	632.3	192.5
	3	625.5	190.8

Table 6.7: One-way ANOVA results, followed by post-hoc Tukey HSD test results for the change in mass of dry tablets before and after dissolution from Table 6.6.

ONE-WAY ANOVA		
	p-value (α = 0.05)	**Significant**
Change in mass of tablets after dissolution	2.1e-13	Yes
POST-HOC TUKEY HSD TEST		
Group compared	**Q statistic**	**Significant**
F1 vs F2	22.25	Yes
F1 vs F3	53.13	Yes
F1 vs F4	85.59	Yes
F1 vs F5	70.78	Yes
F2 vs F3	30.61	Yes
F2 vs F4	63.08	Yes
F2 vs F5	48.26	Yes
F3 vs F4	32.47	Yes
F3 vs F5	17.65	Yes
F4 vs F5	14.82	Yes

6.4.7 Dissolution efficiency and kinetics

According to the International Union of Pure and Applied Chemistry (IUPAC), the term "dissolution" is defined as the mixing of two phases resulting in a new homogeneous phase (i.e. the solution) [621] (see Figure 6.17a). In the case of the dissolution of a solid drug particle, the drug will dissolve in the phase of an aqueous liquid as depicted in Figure 6.17b.

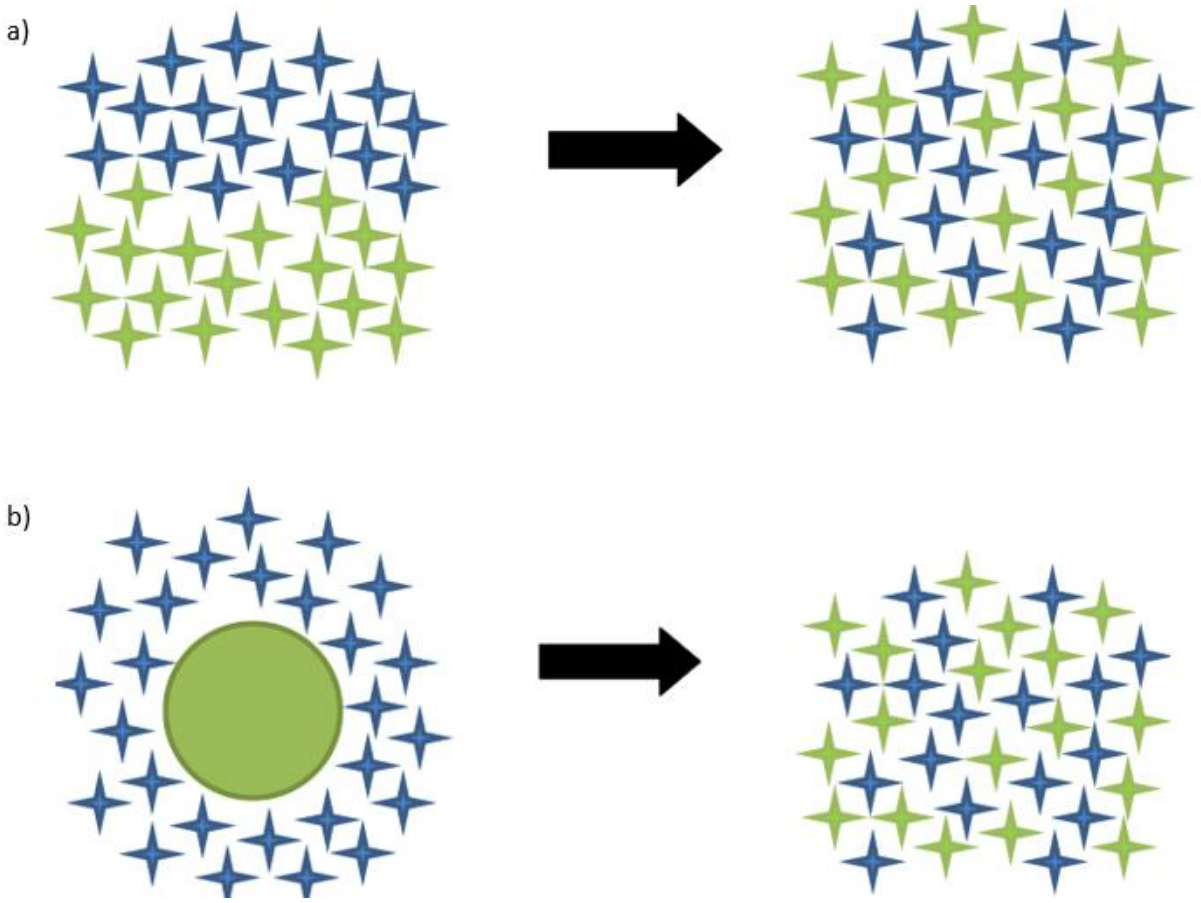

Figure 6.17: Schematic depiction of: a) IUPAC definition of "dissolution", b) dissolution of a solid drug particle in an aqueous liquid (Adapted with permission from reference [622]).

In general, drugs will dissolve upon contact with aqueous body fluids. However, all drugs have different dissolution rate and the rate of drug release can be dependent on the water penetration into the drug delivery system, polymer swelling and dissolution, as well as drug diffusion through polymeric networks [622]. Some drugs with poor solubility do not dissolve as easily. As all drugs have different solubility, a better understanding of the physico-chemical reactions of the drugs, their solubility and dissolution rates can be helpful for designing drug delivery systems. Quantitative analysis and the study of drug

release mechanism can be achieved using realistic mathematical modelling of the process of drug dissolution. The dissolution efficiency and pharmacokinetics are the most popular ways for mathematical analysis of drug dissolution. The study of dissolution efficiency compares different dissolution profiles using the mathematical analysis of difference factor (f_1) and similarity factor (f_2). The difference factor (f_1) measures the percent difference between the two curves over all time points.

$$f_1 = \frac{\sum_{j=1}^{n}|R_j - T_j|}{\sum_{j=1}^{n} R_j} \times 100 \text{ (Equation 6.1)}$$

where n is the sampling number, R_j and T_j are the percent dissolved of the reference and test products at each time point j. The percent difference is zero when the test and drug reference profiles are identical and increase proportionally with the dissimilarity between the two dissolution profiles. On the other hand, the similarity factor (f_2) is a logarithmic transformation of the sum-squared of differences between the test T_j and the reference products R_j over all time points:

$$f_2 = 50 \times \log\{[1 + \frac{1}{n}\sum_{j=1}^{n} w_j|R_j - T_j|^2]^{-0.5} \times 100\} \text{ (Equation 6.2)}$$

where w_j is an optional weight factor. The result of the similarity factor calculation falls between value 0 and 100. It is 100 when the test and the reference profiles are identical and tends to 0 as the dissimilarity increase. All dissolution profiles for the 3D printed formulations were being compared using the difference factor (f_1) and the similarity factor (f_2). The results for f_1 *and* f_2 *are* tabulated in Table 6.8 and Table 6.9 respectively. In order to consider dissolution profiles to be similar, the f_1 values should be close to 0 and the f_2 values should be close to 100. In general, f_1 values between 0 and 15 and f_2 values between 50 and 100 indicates similarity of the dissolution profiles. Such classification is also recognised by the FDA and European Medicines Agency (EMA). This means that when hen the values of f_1 falls out of the range of 0-15 (i.e. above 15) and f_2 falls out of the range of 50-100 (i.e. below 50), the two dissolution profiles that are being compared can be declared dissimilar. The results in Table 6.8 and Table 6.9 showed that F1 is similar to F2 only; F2 is similar to F1 and F3; F3, F4 and F5 are all similar to each other. Therefore, it can be said that F3, F4 and F5 have a similar dissolution profile but they are different from F1 and F2. This can be explained by a difference in dissolution mechanism as formulation F1 does not contain any HPC and F2 has a very small percentage of HPC

present. The calculated f_1 and f_2 values correspond to each other and the similarity of the dissolution profiles was also reflected in Figure 6.14.

Table 6.8: Difference factor (f_1) for dissolution of tablets formulation F1-F5.

Formulation No. Compared	F1	F2	F3	F4	F5
F1	-	11.83	25.89	35.82	39.01
F2	13.42	-	14.48	24.34	28.10
F3	32.54	16.80	-	12.63	11.46
F4	55.81	32.18	13.33	-	5.26
F5	63.95	39.08	12.73	5.54	-

Table 6.9: Similarity factor (f_2) for dissolution of tablets formulation F1-F5.

Formulation No. Compared	F1	F2	F3	F4	F5
F1	-	60.01	42.84	36.47	34.16
F2	60.01	-	53.60	42.79	40.17
F3	43.19	53.60	-	55.99	55.18
F4	36.47	42.79	55.99	-	74.70
F5	34.16	40.17	55.18	74.70	-

Comparing the dissolution profiles is a simple method to determine whether the different formulations show the same drug release mechanisms and patterns. In addition to computing f_1 and f_2 values of two different dissolution profiles, the different dissolution profiles can be further analysed by fitting them to different mathematical models. Mathematical models can be used to describe the release mechanism of the 3D printed tablet. Several models have been developed over the years. These models are also known as pharmacokinetic models and are used to speculate the release mechanism of a drug delivery system. They also play an important role in the process of designing pharmaceutical formulations and evaluating the process of drug release. Mathematical modelling can help to optimise the design of the new drug delivery systems and improve the efficacy of the systems. In this study, the dissolution profiles for each of the 3D printed tablets were analysed by fitting the dissolution data into several different kinetic models such as zero-order, first-order, Higuchi and Korsmeyer-Peppas models. The kinetic models were used to speculate the release mechanisms that the tablet exhibit. The results from fitting the dissolution data to the mathematical equations were shown in Table 6.11. The model that showed the maximum R^2 (RSQ) and minimum mean percentage error (MPE) is the best kinetic model fit for that particular dissolution profile. The equations of the four different kinetic models used were shown as below:

Table 6.10: The four dissolution kinetic models used and their respective equations

Dissolution kinetic models	Equation
Zero-order	$\frac{M_t}{M_\infty} = k_0 t + C$ [623]
First-order	$ln(1 - \frac{M_t}{M_\infty}) = -k_1 t + C$ [624]
Higuchi	$\frac{M_t}{M_\infty} = k_H t^{\frac{1}{2}} + C$ [625]
Korsmeyar-Peppas ("Power Law")	$\frac{M_t}{M_\infty} = k t^n + C$ [626]

where $\frac{M_t}{M_\infty}$ represents the cumulative drug release percentage at time t, k_0, k_1, k_H, and k are the release constant of each model equation and n is the release exponent. The zero-order release model is often used when the dug release rate is constant over a period of time and it represents an ideal situation of a controlled release drug delivery systems. The first-order model is used to describe the absorption and/or elimination of drugs [627]. It is often used to describe dosage forms containing water soluble drugs in a porous matrix [628]. The Higuchi model is the first model that describes the drug release rate from a matrix system. It is also one of the preferred models for drug release in different geometries and porous model [629–631]. However, it is often not applicable to many controlled release systems [625]. The mathematical equation of the Higuchi model is related to the API particles dispersed into a homogeneous matrix being submitted to a diffusing medium. The equation above is a simplified version of the first Higuchi equation [632]:

$$\frac{M_t}{M_\infty} = \sqrt{D(2C - C_s)C_s t} \quad \text{(Equation 6.3)}$$

where $\frac{M_t}{M_\infty}$ is the accumulative drug released from time t, C is the initial amount of drug contained in dosage form, C_s is the solubility of active agent in the matrix medium and D is the diffusion coefficient in the matrix medium. The Higuchi model was derived under pseudo-steady states and carried several assumptions [633]:

1) The initial drug concentration in the matrix is much higher than the solubility of the drug
2) The diffusion is unidirectional with negligible the edge effects
3) The size of the dosage form is much larger than the size of the drug molecules

4) The swelling or dissolution of the polymer matrix is negligible
5) The drug diffusion coefficient is constant
6) The perfect sink conditions during drug release

The Korsmeyer-Peppas, also known as the "Power law" model, is often used to describe the drug release of a polymeric system when the drug release mechanism is not known, or drug release mechanism that happen simultaneously such as diffusion, swelling and dissolution of the polymer matrix [634]. The constant 'k' depends on the structural and geometrical characteristic of the system, and the value 'n' is the exponent of drug release in the function of time t [626]. The power law is a more comprehensive semi-empirical equation to describe drug release from polymeric systems. This equation shows an exponential relationship between drug release and time.

The dissolution for each formulation above was fitted to four different mathematical models (zero-order, first-order, Higuchi and Korsmeyer-Peppas model) to determine the best description of its drug release mechanism. The model fitted to that shows the lowest mean percentage error (MPE) and the highest coefficient of determination (R^2) is typically considered the best model to describe the dissolution. The MPE and R^2 for all the dissolution of the 5 3D printed formulations were displayed in Table 6.11. The fitting data shows that the two best models that could be used to represent the 3D printed formulations are Higuchi and Korsmeyer-Peppas models. This is because MPE and R^2 for the formulation were the lowest and highest respectively. The MPE and R^2 of these two models are very also close to each other. It is shown that the dissolution of formulation F1, F2 and F5 can be best described using the Higuchi model, whereas F3 and F4 can be represented using the Korsmeyer-Peppas model. According to the Korsmeyer-Peppas equation, when the value of n falls between 0.45 and 0.89, the drug release mechanism can be described as non-Fickian (anomalous). This means that the drug release can be caused by diffusion and swelling of the polymer matrix [635]. If the n value is small ($n < 0.43$), this indicates the drug release mechanism is diffusion-controlled, representing a Fickian diffusion release mechanism [636]. The study indicates all formulations may have multidirectional diffusion and polymer swelling during the dissolution process as the n values are greater than 0.45. The swelling of the polymer matrix happened when the dissolution medium penetrates into the polymer matrix. This could be caused by the presence of Eudragit. Eudragit is permeable to water but not dissolvable. Hence, swelling of the polymer occurs. The results from the kinetic model

analysis showed the dissolution data for all formulation seem to fit both Higuchi and Korsmeyer-Peppas models. This could be because these pharmacokinetic models were developed for tablets produce in traditional pharmaceutical methods. 3D printing of tablets has not been established as a tablet processing technique. This is because 3D printed tablets could have variations as shown in Table 6.6 and the 3D printing may change some properties of the polymeric matrix due to the thermal stress exerted during the 3D printing process. The change on properties could easily affect the release rate and release kinetic of the drugs. However, some studies have shown that Higuchi model may not be the most suitable model for 3D printed dosage forms as polymeric 3D printed drug delivery devices may exhibit multidimensional diffusion and swelling of the polymer matrix is often not negligible [155,637]. It is suggested that the Korsmeyer-Peppas model may be a better representation of the dissolution profile for 3D printed tablets.

Table 6.11: The Mean Percentage Error (MPE), Coefficient of determinations (R^2/RSQ), Diffusion exponent (n) of the calculated by fitting the dissolution profile in Table 6.8 to the different mathematical kinetic models.

Formulation	**Zero-order**		**First-order**		**Higuchi**		**Korsmeyer-Peppas**		
No.	**MPE%**	**RSQ**	**MPE%**	**RSQ**	**MPE%**	**RSQ**	**MPE%**	**RSQ**	**n**
F1 (0811)	212.48	0.905	142.49	0.984	25.86	0.992	21.89	0.950	0.911
F2 (2611)	163.52	0.894	111.82	0.989	30.13	0.994	24.37	0.920	0.810
F3 (4411)	78.13	0.831	59.82	0.968	28.48	0.972	14.47	0.96	0.710
F4 (5311)	42.73	0.957	7.14	0.995	12.18	0.996	5.86	0.991	0.727
F5 (6211)	65.64	0.931	16.01	0.997	2.32	0.999	10.30	0.981	0.802

6.4.8 Biocompatibility study

A cell study was carried out to ensure the biocompatibility of the formulation and to examine whether the HME process has caused any chemical toxicity to the polymer. The results from the cell study in Figure 6.18 shows the number of cells in the well on the first day (day 0), second day (day 1) and fifth day (day 4). The study showed that the cells can still grow in the wells, showing no signs of toxicity from the foreign materials. This confirms that the materials are not cytotoxic and the HME process did not cause any degradation or changes in chemical properties to the bulk materials. Hence, such a formulation is safe for use in pharmaceutical applications.

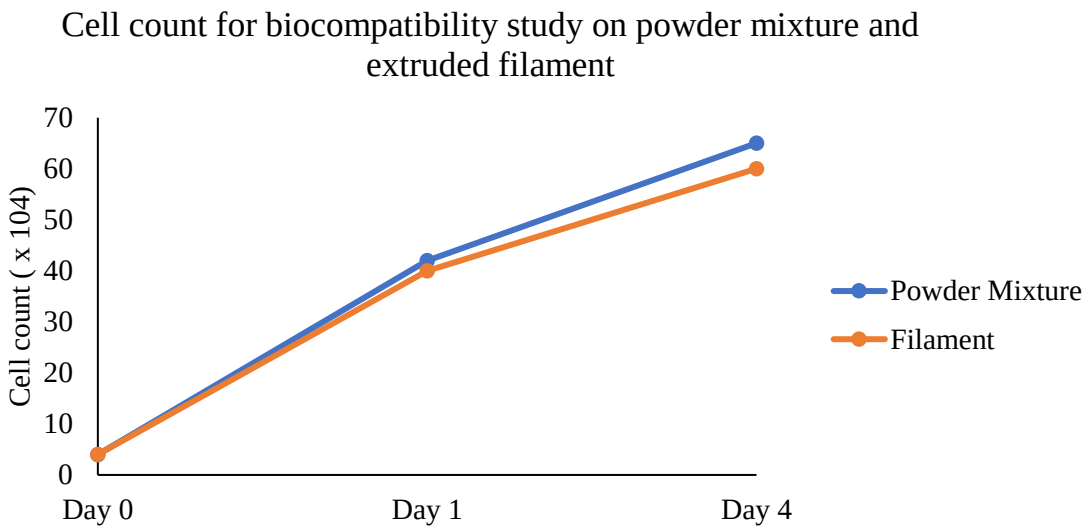

Figure 6.18: Cell count of biocompatibility study on day 0, day 1 and day 4.

6.5 Conclusions

This study showed that when HME is combined with a low-cost FDM 3D printing technique, it can be used as a continuous fabrication process for a sustained release drug delivery device. This is a cost-effective and convenient way to produce drug delivery systems, especially for medications that need to be personalised and customised according to the patients' requirements. The success of this approach allows local hospitals to manufacture their own medical and pharmaceutical products on-site according to their patients' needs. This will help save time from waiting for suitable products to be manufactured off-site or using the traditional manufacturing processes. This technique is particularly useful for hospitals in remote areas as it is able to overcome some distribution and supply chain challenges. The filaments were produced by optimising various compositions of pharmaceutical grade polymers, such as hydroxypropyl cellulose (HPC), Eudragit® (RL PO), polyethylene glycol (PEG) whereas theophylline was used as a model drug. For the purpose of the study, HME was implemented from the view that it would result in the formation of solid dispersion of drug onto the polymeric carrier matrices by means of high shear mixing inside the heated barrel. HME has been used to produce 3D printable filament that can be loaded with any thermally stable API. HME can also effectively convert a crystalline API into amorphous form, forming a solid dispersion. In order to produce FDM 3D printable filaments, the type of polymeric carrier chosen is essential. It must have suitable flexibility and ductility that can withstand the forces experienced during the FDM 3D printing process. The mechanical characterization of the filaments revealed quite robust properties of the

filaments suitable for FDM 3D printing of tablets. The 3D printed tablets showed good consistency and have an elegant appearance for the majority of the filament formulations. Only one formulation (F6) did not produce an acceptable 3D printed tablet as the molten filament was too viscous, causing the 3D printed tablet to stick to the printing surface. Solid state analyses conducted via DSC and XRD showed the amorphous nature of the crystalline drug dispersed onto the polymeric matrices. The surface analysis conducted via SEM showed smooth surfaces of the produced filaments as well as tablets, where no drug crystals were visible.

In-vitro dissolution was carried out for the tablets to study the drug release profiles. The 3D printed tablets showed promising results in controlling the release rate of the drug. The *in-vitro* drug release study showed a sustained release profile over 10 hours, where about 80% of the drug was released from the printed dosage forms. This indicates that the optimised 3D printed tablets are suitable for the development of sustained-release personalised delivery systems. The dissolution efficiencies for the dissolution profiles were calculated and the release mechanism of the 3D printed tablets were determined by fitting the dissolution data to mathematical kinetic models. As the 3D printed tablet formulations consist of different polymeric mixture, the Korsmeyer-Peppas law may be the most appropriate model to describe the drug release kinetics of the 3D printed tablets. Cell study was carried out the bulk materials and the extruded filaments to ensure the biocompatibility of the materials. The study showed that the materials are biocompatible and do not have any cytotoxic effect on living cells. Therefore, this polymeric mixture can be used for printing not just tablets but also drug-loaded implants. The study also confirms that the thermal process of HME also did not induce any toxicity or degradation to the polymeric mixture.

Chapter 7 : Development of metformin-loaded filaments for 3D printing of sustained release drug delivery system

7.1 Introduction

A sustained-release drug delivery system is a purposefully designed system where the drug is released at a predetermined rate in order to maintain a constant drug level over a period of time [638]. The benefits of sustain release drug delivery system include the reduced frequency of medication intake required reduced side effects and improved patient compliance [639]. Sustained release drug delivery systems have been designed to solve problems that arises from drugs that have short half-lives and are eliminate quickly from blood circulation [640]. Such drugs required patients to increase the frequency of intake, which could increase the side effect and cause much inconvenience to the patients. Much effort has been put into designing sustained-release formulations as such formulations are able the most effective treatment using the smallest quantity of a drug at the shortest possible time. The primary aim of this system is to improve the efficacy of drugs and patient compliance.

Traditionally, sustained release dosage forms are prepared by applying a coating of pharmaceutical excipient that act as a protective membrane on a tablet [641]. The type of polymers used also plays an important role in sustaining the release of a formulation. Some of the polymers that have been successfully used for sustained release formulations include hydroxypropyl methylcellulose (HPMC), hydroxypropyl cellulose (HPC), polyvinylpyrrolidone (PVP), Eudragit, and polyethylene oxide (PEO) [642–646]. The suitability of the polymers used can also depend on the physicochemical properties of the drug.

Metformin hydrochloride (HCl) is a highly soluble active pharmaceutical ingredient (API) and is one of the most studied API for prolonged-release formulations [647]. The chemical structure of metformin is shown in Figure 7.1. Due to its high water solubility, metformin is often available as an immediate release formulation. As a result, it is prescribed 2-3 times daily for diabetic patients.

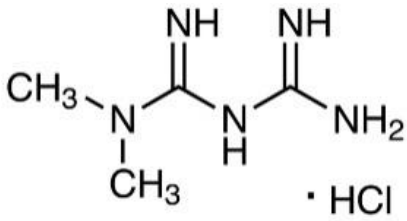

Figure 7.1: Chemical structure of diabetic drug Metformin Hydrochloride (HCl).

Freely water-soluble Metformin is the most commonly used drug as a first-line treatment for newly diagnosed Type II diabetes patients [648]. There are several ways where metformin can help lower blood glucose levels in diabetic patients. Metformin can reduce hepatic glucose production in the liver, increases insulin sensitivity by improving the skeletal muscle uptake and utilisation of glucose, and reduce the intestinal absorption of glucose [649]. However, the treatment of metformin is often insufficient and additional drug such as gliclazide is often prescribed additional treatment to improve the convenience and adherence to the prescribed therapy and to contribute to better glucose control [650,651]. It has also been reported that patients with type II diabetes mellitus typically achieve better glucose control when received two combined medications [652–654]. However, metformin will often be used as the first option of treatment particularly for newly diagnosed patients as it is still considered the most effective treatment [655]. Metformin is normally absorbed in the upper gastrointestinal (GI) tract [656]. Formulating metformin as a sustained release dosage form can allow metformin to be released in the upper GI tract over a longer period of time and can help address issues of gastrointestinal intolerability [656,657]. This can help avoid multiple daily dosing and improve patient adherence. With an extended-release metformin, the patient could experience fewer GI side effects as only one pill is taken per day but the daily dose remain the same [658,659]. This will not only benefit the patients by improving glycaemic control but will also help reduce the burden on health care usage and overall costs [660]. In order to achieve a prolonged release metformin formulation, the polymeric excipients used play a crucial role. Studies have shown that polymer such as HPMC and Eudragit have successfully been used to prolong the release of metformin release [169,661]. Nanjwade *et al*. also designed a metformin extended-release table using a combination of a hydrophobic carrier (stearic acid) and a hydrophilic polymer (PEO) [662].

One of the innovative techniques to formulate sustained release drug delivery systems is via 3D printing [663–666]. In the past decade, the research on 3D printing for biomedical

and pharmaceutical applications has received a tremendous amount of interests. This is because there has been increasing need to customised products according to the requirements of patients and 3D printing seems to be the most cost-effective production method for such products. Pharmaceutical products use a lot of polymers and some may be suitable for 3D printing processes, in particular fused deposition modelling (FDM) 3D printing. Suitable polymers loaded with a desired API can be formed into filaments using hot-melt extrusion (HME) and the filaments can be used as a feedstock for FDM 3D printing. This technique has been proven feasible and simple in the earlier chapters. Studies have also shown that the parameters of the 3D printing process and the shape of the printed tablet may have an effect on the release profile of the drug [79,612,613,667].

The polymeric composition study carried out from Chapter 6 exhibit sustained-release properties for the incorporated API. This is particularly true for composition with higher Eudragit® RL PO. The results suggested that the formulations with a high concentration of Eudragit provides a sustained release profile for the drug theophylline. Hence, an attempt to apply the two compositions that showed the slowest drug release profile from the HPC and Eudragit compositions in the previous chapter to produce sustained release metformin formulations. A study by Gioumouxouzis *et al*. also showed that metformin was loaded onto Eudragit® RL PO to achieve a prolonged release pattern [169]. In this chapter, metformin will also be loaded onto another type of biodegradable polymer, polycaprolactone (PCL). PCL is commonly used in biomedical applications and also widely available as a 3D printing filament.

Poly-ε-caprolactone (PCL) is a synthetic, semicrystalline polymer that exhibit very low glass transition temperature (T_g) and low melting temperature (T_m). The T_g of PCL is typically around -60 °C to -65 °C and the T_m is around 60 °C [668]. PCL is synthesised through ring-opening polymerisation of ε-caprolactone as shown in Figure 7.2 [669]. The main basic building blocks of PCL are esters and ethe groups and its chemical structure is depicted in Figure 7.3. The high mobility of the polymeric chain and the low molecular interaction of PCL allows it to have very low melting and glass transition temperatures [670].

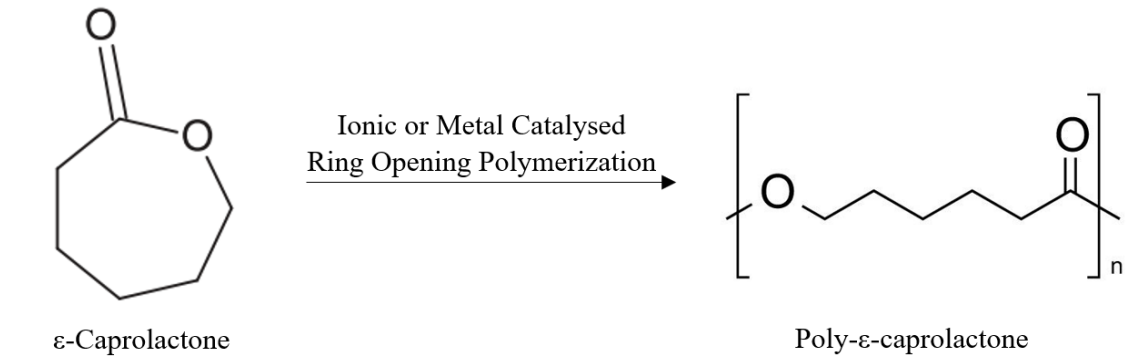

ε-Caprolactone Poly-ε-caprolactone

Figure 7.2: Ring opening polymerisation of ε-caprolactone producing poly-ε-caprolactone (PCL) [671].

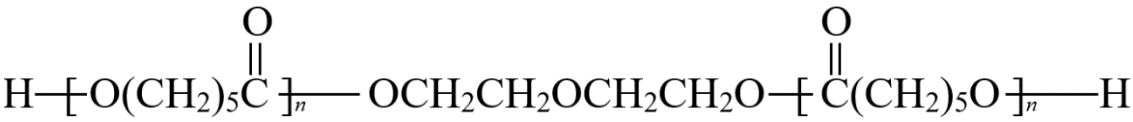

Figure 7.3: Chemical structure of polycaprolactone (PCL) [672].

PCL is considered non-toxic and is a biodegradable material by hydrolysis of its ester bonds [672,673]. The degradation time of PCL can be over 3-4 years [674]. PCL has been used in a wide range of medical applications including tissue engineering [675], drug delivery systems [676,677], regenerative medicines [678] and various implants [679–681]. Apart from medical applications, PCL has also been used in the polymer industries as hot-melt adhesives, food packaging, model making and laminating pouches [682–684]. PCL is non-hazardous and has received U.S. Food and Drug Administration (FDA) approval for use in a large number of drug delivery and medical devices. It has been reported in the literature that PCL exhibit a typical modulus of elasticity of ~440 MPa and tensile strength of ~16MPa [685]. Some other properties of PCL include resistance to water, oil, solvent and chlorine [668].

PCL has shown great potential to be used for biomedical applications including implants and drug delivery systems due to its biocompatibility and biodegradability [686,687]. Some examples of PCL-based implants include implantable contraceptive devices and stents [71,677,688]. PCL has been used to produce drug delivery systems that exhibit long sustained drug attributed to the properties of the polymer [71,689,690]. This is because PCL is a hydrophobic polymer, which could act as a protective layer to freely soluble drugs. The excellent mechanical properties of PCL also allowed the material to be produced into filaments that are suitable to be used for Fused Deposition Modelling (FDM) 3D printing.

In this study, metformin will be loaded onto a polymeric matrix consists of PCL and polyethylene glycol (PEG) in addition to the sustained release Eudragit compositions. PEG is highly water soluble and has been widely used as a drug carrier [691]. As PCL is hydrophobic, PEG will improve its hydrophilicity and drug loading ability. Four different polymeric compositions will be processed with HME to form into 3D printing filaments. Two formulations are Eudragit-based and two PCL-based. The extruded filaments will be used to 3D print metformin loaded tablets and drug release studies will be carried out to investigate the sustain release properties of the polymeric compositions.

Both PCL and PEG has a very low melting point which could prevent thermal degradation of thermosensitive drugs. This could be highly beneficial especially when thermal processes such as HME and FDM 3D printing are involved. Due to the low melting point and low glass transition temperature of PCL, the polymer can be soft and flexible even at room temperature.

7.2 Materials

Nisso Hydroxy Propyl Cellulose (HPC) (Grade SSL) was purchased from Nippon Soda Co., LTD. (Tokyo, Japan). Eudragit® RL PO powder was purchased from Evonik Industries (Darmstadt, Germany). Poly (ethylene glycol), average molecular weight (M.W.) 6000 g/mol was purchased from Fisher Scientific (Loughborough, UK). Polycaprolactone (PCL) in powdered form with average M.W. 50000 g/mol was purchased from Polysciences Europe GmbH (Hirschberg an der Bergstrasse, Germany). Metformin Hydrochloride purchased from Tokyo Chemical Industry UK Ltd. (Oxford, UK) was used as a model drug. All materials were used as received.

7.3 Experimental Methods

7.3.1 Preparation of metformin-loaded filaments

Two types of metformin-loaded filaments were produced. The material compositions were shown in Table 7.1. The materials in powder form were first mixed together in a pestle and mortar. The mixed powder was then transferred into a bottle and further mixing was carried out using a Turbula shaker mixer, Eskens (Alphen aan den Rijn, Netherlands) for 15 mins. The mixed powder was then produced into filaments using a table-top custom-built L/D 10 twin-screw extruder by Twin Tech Extrusion Limited (Stoke-on-Trent, UK), assembled by Point1Controls/R Controls (Stoke-on-Trent, UK). The extruder consists of 4 zones: Z1, Z2, Z3, Z4 in which the temperature of each zone can be

controlled independently. The extruding temperatures set were different for each formulation. For M1 and M2, the temperatures at the 4 zones (Z1 : Z2 : Z3 : Z4) were (70°C : 100°C : 110°C : 110°C) and the die was set to 110°C. For M3 and M4, the temperatures were (40°C : 50°C : 65°C : 65°C) and the die was set to 65°C. The heat soak time was set to 5 minutes for all formulations. The extruding hole on the die has a diameter of 2.0 mm and the extrusion speed was set to 60 rpm. A standalone filament winder was used to collect the filaments extruded. A Vernier calliper was used to measure the diameter of the filaments and only filaments with a diameter of 1.75 mm were used for 3D printing as the size of the 3D printing nozzle can only fit filaments with diameter below 1.75 mm.

Table 7.1: Percentage of composition in different formulation of metformin-loaded filaments. The quantities are in percentage (w/w).

Compound	**Formulation Code**			
	M1	**M2**	**M3**	**M4**
Metformin HCl	10	10	10	10
Hydroxy Propyl Cellulose (HPC)	20	-	-	-
Eudragit® RL PO	60	80	-	-
PEG 6000	10	10	20	10
Polycaprolactone (PCL)	-	-	70	80

7.3.2 3D printing process

The extruded filaments were used for 3D printing using a Makerbot Replicator 2X (Makerbot Inc., NY, USA) FDM 3D printer. The CAD model of a drug delivery device (tablet shape) was designed using Solidworks (Dassault Systemes, Waltham, MA, USA). Figure 1 shows a computer-generated 3D model of the tablet used for 3D printing. The 3D model was then saved as an .STL file and imported to Makerbot Desktop software (Makerbot Inc., NY, USA) for slicing. The tablet has a height of 5 mm, width of 10 mm and length of 20 mm. The layer height for printing was set to 0.15 mm. Tablet infill for printing was set to 100%.

7.3.3 Differential Scanning Calorimetry (DSC)

A DSC 4000 system (Perkin Elmer, Waltham, MA, USA) was used to study the glass transition temperature and the melting temperature of all the filaments. The samples used were about 5mg. The samples were placed in an aluminium pan, and an empty aluminium pan was used as a reference. Nitrogen gas was used as the purged gas at a flow rate of 20

mL/min in all the DSC experiments. The data were collected and analysed with Pyris software (Perkin Elmer, Waltham, MA, USA).

7.3.4 Thermogravimetric analysis (TGA)

TGA was carried out using a Q40 Thermogravimetric analyser (TA Instruments, New Castle, DE, US) to obtain the degradation profile of the filaments. The samples used were about 10mg and were placed in an open aluminium pan. The furnace was then heated from 30°C to 550°C at a rate of 10°C/min. Nitrogen gas was used as purge gas at a flow rate of 20mL/min. Data were collected and analysed using the Advantage/Universal Analysis Software (TA Instruments).

7.3.5 X-ray Powder Diffraction

The crystallinity of the individual compound and the extruded filaments were assessed using a Siemens D500 X-ray Diffractometer (Siemens, Germany). The samples were scanned between 2 Theta(θ)=5° to 50° using 0.01° step width and 1s time count. The divergence slit was 1mm and the scatter slit was 0.6mm. The X-ray wavelength was 0.154 nm in Cu source and at a voltage of 40 kV.

7.3.6 *In-vitro* Drug Release Study

In-vitro dissolution test was carried out on three randomly selected tablets from each formulation for drug release study. The mass of the samples was first weighed before dissolution and then weighed again after the dissolution test when the samples were dried. Determination of the In-Vitro drug release was performed using USP type I dissolution apparatus (708-DS Dissolution Apparatus, Agilent Technologies, Santa Clara, CA, USA) in 1000mL of 0.05M phosphate buffer solution (pH 6.8) at 37±0.3◦C with a rotation speed of 100 rpm. The drug concentration of the dissolution medium was measured using a Cary 60 UV-Vis Spectrophotometer (Agilent Technologies, Santa Clara, CA, USA) at a wavelength of 232 nm in a 2 mm cell versus a blank solution consisting of a phosphate buffer (pH 6.8). The samples were drawn automatically using an Agilent 810 peristaltic pump (Agilent Technologies, Santa Clara, CA, USA) and sampling was done every 5 min for the first hour, every 20 min of the following 2 hours and every 60 min for the last 10 hours. The release profiles were plotted as a percentage of cumulative drug release versus time.

7.4 Results and Discussion

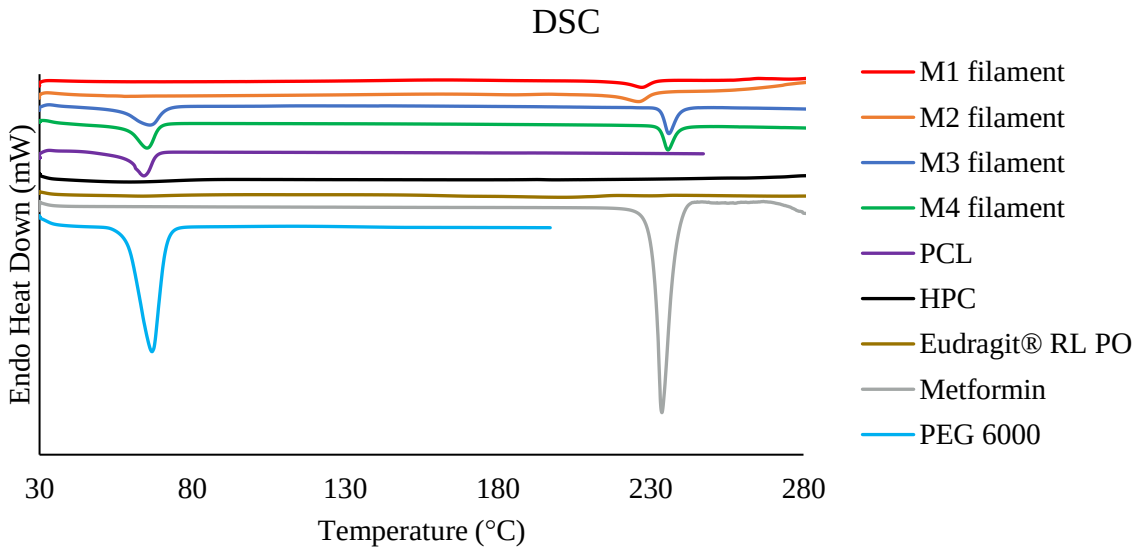

Figure 7.4: DSC thermograms for all four metformin filaments and the bulk material used: Polycaprolactone (PCL), Hydroxypropyl cellulose (HPC), Eudragit® RL PO, Metformin HCl and PEG 6000.

DSC analysis was carried out for the extruded metformin filaments and the materials used to fabricate the filaments which include PCL, HPC, Eudragit, Metformin and PEG. The DSC profiles for all materials analysed were shown in Figure 7.4. The DSC thermograms for HPC and Eudragit did not show any thermal events due to their amorphicity in nature. Metformin is a highly crystalline drug and showed a large endothermic peak which reflects its melting point at around 233.7 °C. Due to the high melting point of metformin, it can be used in thermal processes such as HME and 3D printing as it will be able to withstand the temperature of the processes. The DSC results confirmed that PEG has a melting point of around 66 °C. Similarly, PCL also has a very low melting point at 64.2 °C. The use of PCL and PEG as drug carrier means that the processing temperature can be very low, which could prevent any thermal degradation of the materials. The melting temperature and the melting enthalpy of the materials were displayed in Table 7.2.

The composition of M1 and M2 filaments were made of HPC, Eudragit and PEG, similar to the composition being studied in Chapter 6. The two formulations that showed the slowest drug release from Chapter 6 were chosen to investigate the effect of such composition for a readily soluble drug, metformin. The DSC curves for M1 and M2 filaments showed small endothermic peaks at 227 °C and 226.2 °C respectively. These two endothermic events represent the melting point of metformin in the filament

formulation. This confirms the presence of metformin in the filaments. The melting temperatures were actually lower than the pure metformin. This is because the polymeric composition was able to suppress the melting point of metformin when it has been processed with the carriers. Apart from that, the energy required to melt metformin in M1 and M2 were lower as compared to pure metformin. The DSC for M1 and M2 suggest that the filaments may have high amorphous content. However, there is still some crystallinity due to the presence of metformin. Similar to the formulations in Chapter 6, M1 and M2 filaments can be prepared using twin-screw extrusion at a maximum temperature of 110 °C. This processing temperature was required to melt/soften HPC and Eudragit to a suitable viscosity that can be mixed with other materials and processed into 3D printable filaments. The filaments, M1 and M2, can be 3D printed at a printing temperature of 195 °C.

M3 and M4 filaments contain PCL, PEG and metformin as a drug. The DSC analysis for these two filaments showed two endothermic events. The first endothermic event corresponds to the melting of PCL as it happened around 68.2 °C and 66.1 °C for M3 and M4 respectively. The second endothermic event corresponds to the melting of metformin. The results suggest that both filaments may have high crystallinity due to the nature of compositions. PCL, PEG and metformin are materials that contain high crystallinity. Due to the low melting point of PCL, the processing temperature of the PCL filaments were also low. The maximum temperature required to extrude metformin-loaded PCL filaments was 65 °C. The temperature used for the 3D printing of M3 and M4 filaments was 70 °C. This printing temperature was much lower than M1 and M2 filaments. Such formulation may be suitable for thermosensitive materials and active ingredients as the processing temperatures were relatively low. This can be attractive as the formulation can offer the benefit of 3D printing of personalised tablets and implants for thermal sensitive and low melting point drugs.

Table 7.2: Melting temperature (T_m) and the measured heat enthalpy value for melting extracted from the DSC profiles for all metformin filaments and individual materials.

Sample	**Melting point T_m (°C)**	**Heat enthalpy value (ΔH) for T_m (J/g)**
HPC	-	-
Eudragit® RL PO	-	-
PCL	64.2	102.7
Metformin	233.7	283.7

PEG	66.7	252.7
M1	227.0	30.9
M2	226.2	47.3
M3	68.2 / 235.1	174.1 / 69.8
M4	66.1 / 236.0	119.1 / 56.4

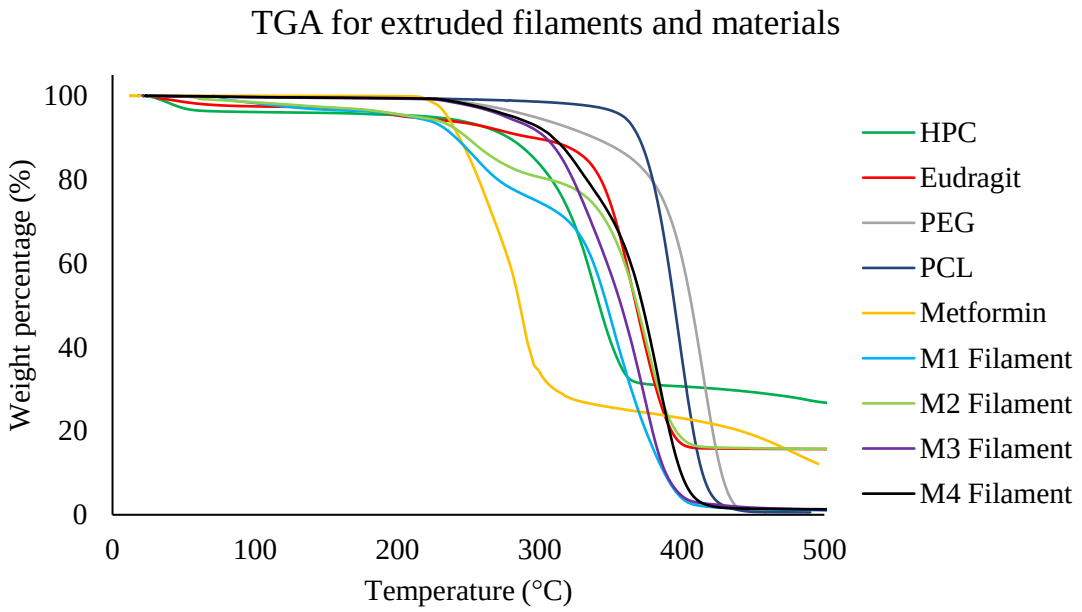

Figure 7.5: TGA profiles for all extruded metformin filaments and individual materials.

The thermal degradation profiles of the extruded filaments and the individual materials were displayed in Figure 7.5. Three different degradation points t_{90}, t_{50}, and t_{10} were extracted from the profiles representing the temperature when 10%, 50% and 90% of the sample has degraded respectively. The exact values of the temperatures at these degradation points were displayed in Table 7.3. The active ingredient used, metformin, degraded at the lowest temperature amongst all the materials used. At around 243 °C, 10% of the metformin has degraded. However, the drug is still considered thermally stable as the maximum temperature of the twin-screw extrusion process was 110 °C and the maximum temperature of the FDM 3D printing process was 195 °C. Metformin only fully degrades at a temperature above 495 °C. All other materials used also only start to degrade at above 270 °C. The four filaments produced also showed good thermal stability. The TGA analysis confirmed that the components were suitable for the twin-screw extrusion and the filaments produced from the extrusion were suitable to be used for 3D printing.

Table 7.3: Temperature at three degradation points (t_{90} = 90%, t_{50} = 50%, t_{10} = 10% wt. remaining) for all filaments and the individual materials.

Samples	t_{90} (°C)	t_{50} (°C)	t_{10} (°C)
HPC	269.9	363.3	-
Eudragit	293.4	367.7	-
PEG	338.3	406.7	427.8
PCL	369.5	394.7	414.2
Metformin	243.2	286.2	495.7
M1 Filament	240.8	347.2	387.5
M2 Filament	249.5	368.4	-
M3 Filament	303.5	357.1	388.5
M4 Filament	309.4	372.2	399.4

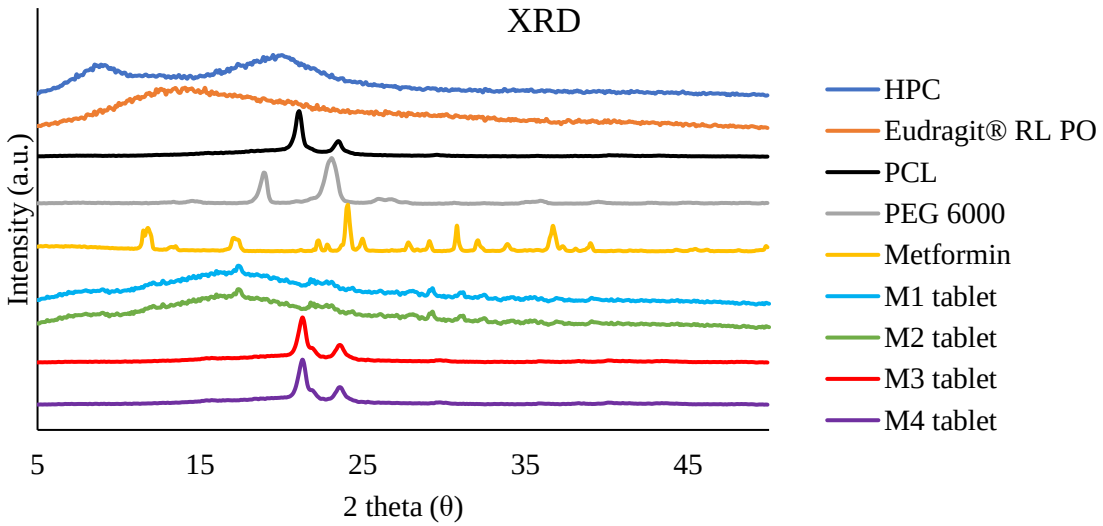

Figure 7.6: XRD analysis on the 3D printed metformin tablets and their individual materials.

Figure 7.6 shows the XRD analysis for all 3D printed metformin tablets using the twin-screw extruded filaments, and the individual materials that made up the tablets. The XRD spectra for HPC and Eudragit showed that these two materials contain high amorphous content. On the other hand. PCL, PEG and metformin are highly crystalline. As for the 3D printed tablets using the M1 and M2 formulations, the XRD spectra suggest that there were some amorphicity and crystallinity in the tablets. The crystallinity was due to the presence of metformin as the crystallinity peaks on the spectra corresponds to the peaks that can be found on the metformin spectrum. However, the peaks were much smaller as the percentage of the drug present in the polymeric composition was just 10 %. Apart from that, the polymeric mixture of HPC and Eudragit are mainly amorphous. This finding was consistent to the DSC results as the DSC recorded the melting point of

metformin in both M1 and M2 filaments. This suggests that the crystalline drug still maintained its crystallinity even though it has been processed using twin-screw extrusion. Hence, the drug has not been converted to amorphous form. The spectra for M3 and M4 tablets showed that both tablets contain high crystallinity as well. The crystallinity peaks present were mainly attributed to the crystallinity peaks from PCL and PEG. As the concentration of metformin in the compositions were low, the peaks may not be obvious. This could also be that the crystalline peaks of PCL and PEG were much larger than the metformin crystalline peaks, hence the smaller peaks of metformin were not as evident. Nevertheless, the presence of Metformin in the M3 and M4 formulations were confirmed in the DSC analysis. In general, the results from the XRD analysis and DSC analysis were consistent with each other.

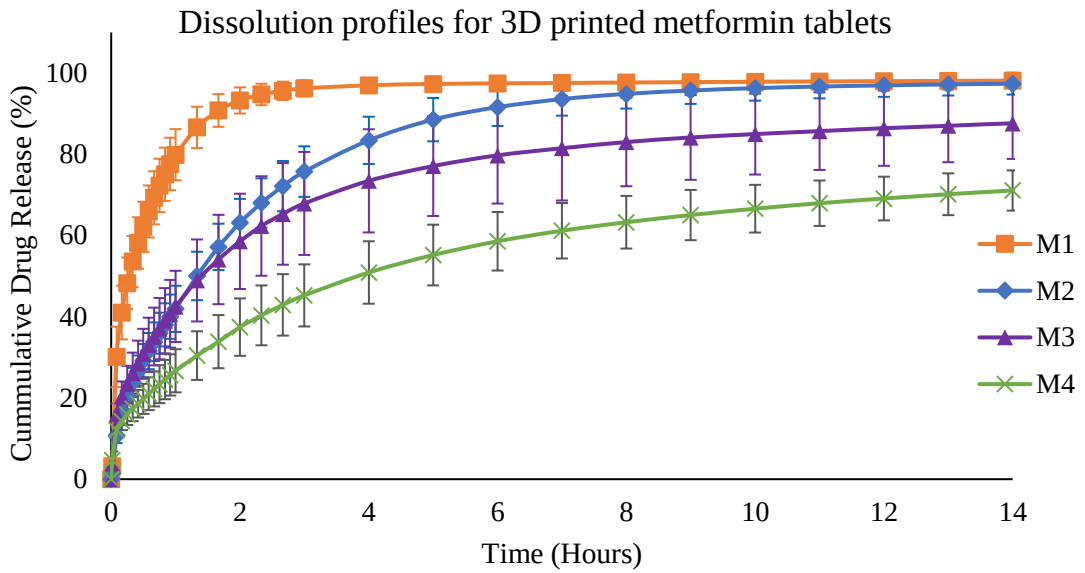

Figure 7.7: In-vitro drug release study on the 3D printed metformin tablets.

The four metformin-loaded filaments were used to 3D print tablets. The drug release profiles of the 3D printed tablets were obtained via drug dissolution testing and the results were shown in Figure 7.7. Formulation M1 showed the quickest release where more than 80 % of the drug was released within the first 2 hours, whereas M4 showed the slowest release where the drug release only started to plateau after 10 hours. Metformin is a highly soluble drug. The results suggest that the formulations made of PCL and PEG were capable of sustaining the release of metformin. HPC and Eudragit are highly amorphous polymer and were mainly used to improve the solubility of poorly water-soluble drugs. Hence, the formulation which contains HPC in its composition, M1, showed the quickest drug release as HPC is water soluble as well. Formulation M2 consists of Eudragit and

PEG but bot HPC as the polymeric matrix. Eudragit has been used mainly for sustained-release products. It is permeable to water but not soluble. Therefore, M2 formulation exhibit a more prolonged release profile and the drug release reach 80 % after 3 hours.

Formulations M3 and M4 were made of PCL and PEG, both components exhibit high crystallinity. As the drug metformin is also high crystalline, the formulation also showed high crystallinity content as suggested in the XRD analysis. A study has reported that 3D printed implant with a low degree of crystallinity showed faster drug release profiles [179]. These dissolution studies confirmed that PCL is capable of producing a sustained-release product, and formulation with higher concentration PCL, M4, had the slowest drug release profile. PCL is also not soluble in water; hence the drug release mechanism was mainly due to diffusion. Nevertheless, PCL showed drug loading capability and can be suitable to be used for sustained release applications as it is also a biodegradable material.

Table 7.4: Difference factor (f_1) for dissolution of 3D printed metformin tablets

Formulation No. Compared	**M1**	**M2**	**M3**	**M4**
M1	-	48.30	56.17	63.39
M2	44.48	-	25.36	36.32
M3	103.93	33.55	-	14.75
M4	140.03	56.39	14.77	-

Table 7.5: Similarity factor (f_2) for dissolution of 3D printed metformin tablets

Formulation No. Compared	**M1**	**M2**	**M3**	**M4**
M1	-	25.95	20.37	17.66
M2	25.60	-	41.96	34.18
M3	20.89	41.25	-	61.02
M4	17.92	34.18	61.02	-

The dissolution profiles for each of the 3D printed metformin tablets obtained in Figure 7.7 were compared with each other to determine their similarities. A mathematical analysis was carried out on the dissolution data and two common parameters were obtained, difference factor (f_1) and similarity factor (f_2). f_1 measures the percentage difference between the two compared dissolution curves. f_1 value is 0 represents the percentage difference between two dissolution profiles is zero. This means the two dissolution profiles are identical. In general, f_1 values between 0 and 15 indicates that the two dissolution profiles can be considered similar. f_2 is also commonly used to determine

the similarity of two dissolution profiles, hence called the similarity factor. Two profiles are considered identical when f_2 = 100. However, an f_2 value of between 50 to 100 will be enough to indicate the similarity between the two dissolution profiles. The is because an f_2 value of between 50 and 100 indicates that the average difference of the dissolution at each sampling point is less than 10%. The obtained values for f_1 and f_2 were displayed in Table 7.4 and

Table 7.5 respectively. The values shown are comparison of two dissolution profiles at a time. The results suggest that the dissolution characteristics of the formulations did not show similarities to each other, particularly for M1 and M2. This can also be reflected in the dissolution profiles in Figure 7.7. M1 and M2 did not show similarity as the absence of HPC in M2 had made a huge difference to the drug release in the formulation. M1 and M2, when compared to M3 and M4 are completely different polymeric compositions that exhibit different physicochemical properties. Hence, they were not comparable. On the other hand, M3 and M4 showed some similarity as the f_1 values were below 15 and f_2 values were above 50. These two formulations have the same polymeric mixture at different concentrations, hence they showed similarities.

Table 7.6: The Mean Percentage Error (MPE), Coefficient of determinations (R2/RSQ), Diffusion exponent (n) of the dissolution profiles for all 3D printed metformin tablets when fitted to the different dissolution kinetic models.

Formulation	**Zero order**		**First order**		**Higuchi**		**Korsmeyer-Peppas**		
No.	**MPE%**	**RSQ**	**MPE%**	**RSQ**	**MPE%**	**RSQ**	**MPE%**	**RSQ**	**n**
M1	91.18	0.493	89.18	0.815	64.33	0.728	23.40	0.921	0.891
M2	95.87	0.798	56.56	0.983	37.57	0.945	14.12	0.953	0.718
M3	36.60	0.829	31.40	0.933	15.84	0.958	3.35	0.989	0.449
M4	36.87	0.757	35.39	0.809	17.44	0.887	4.33	0.989	0.415

Dissolution theories and kinetic models are often used to describe the drug release characteristics of the tablets by using the dissolution data obtained. The dissolution data for all four 3D printed tablets were fitted to four mathematical models to determine which model is most suitable to describe the release mechanism of the formulations. In general, the model that shows the highest coefficient of determinations (RSQ) and the smallest mean percentage error (MPE) can be considered as the closest representation of the drug release mechanism for the formulation. The results from the kinetic model analysis were shown in Table 7.6. The results suggest that all four metformin formulations seem to best fit the Korsmeyer-Peppas model, also known as the Power law model. According to the

Korsmayer-Peppas equation, when the value of n falls between 0.45 and 0.89, the drug release mechanism can be described as non-Fickian (anomalous). This means that the drug release can be caused by diffusion and swelling of polymer matrix [635]. This phenomenon can only be seen in M1 and M2 tablets. This could be caused by the presence of Eudragit. Eudragit is permeable to water but not dissolvable. Hence, the swelling of the polymer occurs. When *n* value is below 0.45, the drug release mechanism is diffusion-controlled, representing a Fickian diffusion release mechanism [636]. This means that the drug release from M3 and M4 were diffusion. Unlike formulations M1 and M2, there was no swelling of polymer in M3 and M4 as PCL is hydrophobic and PEG is highly soluble in water. Hence, metformin was released through diffusion. In general, the Korsmeyer-Peppas model is a more comprehensive and suitable model to describe the drug release mechanism for polymeric systems.

7.5 Conclusion

Sustained release drug delivery systems can offer several advantages to patients as it can reduce the frequency of medication intake, improve the therapeutic efficacy of a medication, and reduce the side effects that can be caused by the drug. An attempt to sustain the release of metformin using four different polymeric composition was investigated. The polymeric compositions were loaded with metformin using HME in the form 3D printable filaments. The filaments were then used as feedstock for the 3D printing of metformin tablets. The study showed that PCL based filaments were more effective in sustaining the release of metformin than the Eudragit based filaments. The higher the percentage of PCL, the slower the drug release. This is because PCL is hydrophobic and the drug release study suggests that metformin was released through diffusion. The advantage of using PCL is that it has a very low melting point at around 60 °C. Therefore, the HME and 3D printing processes can be operated at a temperature as low as 65 °C, which could prevent any possible thermal degradation. This could is particularly beneficial for pharmaceutical applications as this offer an opportunity to process some excipients and API are thermosensitive. Due to the low processing temperatures, thermal degradation can be prevented.

3D printing was chosen as it offers great flexibility in the type of drug delivery devices that can be produced. Apart from that, 3D printing is very effective at producing customised products as each print can be controlled and adjusted accordingly to achieve

the desired outcome. Although a tablet has been chosen to be 3D printed, other drug delivery systems such as transdermal patches and microneedles can also be easily produced due to the flexibility of 3D printing. The 3D printing technology also allows the incorporation of more than one API into a formulation. This can be easily achieved using printers with more than one printing head, where different filaments containing different APIs can be printed one after the other. However, the filaments containing different APIs can also be changed around to achieve a dosage form containing multiple APIs. With the use of HME, the release pattern and the dose can be tailored according to the patient's specific needs. This can increase patient compliance and improve the effectiveness of treatment.

Chapter 8 : Fabrication of flexible Resistance Temperature Detectors (RTDs) temperature sensors via FDM 3D printing and thin-film fabrication technology

8.1 Introduction

Continuous health monitoring has received a significant amount of interest from consumers to technology development companies. Due to the advancement in technology, people are now able to measure and monitor their own health status without needing to attend clinics appointment in person. Therefore, healthcare resources can be reserved for those when it is absolutely necessary. Being able to monitor vital signs ourselves via some healthcare technology can help us to track how our lifestyle is affecting our health and allow us to make changes accordingly. These technologies may help revolutionise our healthcare systems to make them more accessible and also reduce the ever-increasing pressure that is put on healthcare services due to our ageing society. Hence, much effort has been put into improving the reliability of these technologies.

One simple but important parameter that needs to be frequently monitored is our body temperature. Our body regulates its temperature so that it could stay constant at around 37 °C and other organs can function normally. A constant body temperature can be highly important and a slight shift for just a couple of degrees can cause serious health problems, affecting the normal functions of our body such as enzyme activity, hormones etc [692]. Some of the factors that may cause a disruption to our body temperature include abnormal metabolic function, elevated glucose levels or even side effect of some medications [207,693,694].

Heat is often produced through the metabolic reactions that happen in our body. As heat is produced, an equal amount of heat needs to be dissipated to ensure our body temperature stays constant [695]. Heat dissipation often occurs through our skin as it is a superior thermoregulator [696]. However, the glucose level in our body can disrupt the heat balance as an increase in glucose level can cause an increase in body temperature [697,698]. This is because the active oxidation process of glucose produce heat. This can be more evident in diabetic patients as they often have issues with dissipating heat and keeping their body temperature in control [694]. For instance, when a diabetic patient carries out physical exercise, their body temperature tends to be higher as there is a greater

heat production than heat dissipation [699]. Hence, constant monitoring of body temperature can be useful for diabetic patients as it can give an indication of their daily glucose level. This method of glucose monitoring has been proven feasible and can be highly preferred as it is not invasive, reusable and cost less than using a traditional lancet and test strip [700].

Apart from that, skin temperature can be used as a parameter to early detect any underlying health issues. For example it can be used to detect wound or other infections, and predict the occurrence of diabetic foot ulcers [701–705]. This can help avoid and act as warning signs for any life-threatening conditions. A study has reported that local skin temperature assessment can be an effective way for the early detection of diabetes-related foot complications. The difference in the mean temperature values of the two feet at any spot may be used to determine the urgency of treatment [706]. Besides the skin, some other parts of the human body which may be suitable temperature measurement include the forearm, wrist and fingertips [700].

The purpose of this study is to fabricate a simple and low-cost temperature sensor that exhibit flexibility and stability to be used as a skin temperature sensor. The flexible sensor fabricated could have the potential of being integrated with the 3D printed drug delivery systems as described in the previous chapters, forming a smart drug delivery system. This can potentially be in the form of an implant or a smart electronic tattoo that can be attached to the skin [341,707–709]. The function of smart medical systems relies heavily upon the sensors integrated into the systems. This is because the sensor in the system detects signals it is purposed to sense, then feeds the information to the system for it to respond as being programmed. The fabrication of flexible sensors has received much research interest in particular for biomedical sensing applications. This is because not a part of the human body is completely flat and flexible sensors can conform to the curvature of the human body whilst retaining its function.

In this study, the flexible temperature sensors were designed to be Resistance Temperature Detectors (RTDs). RTD temperature sensor is a common device used for temperature measurement and is usually made of materials that have a positive temperature coefficient. A material that exhibit a positive temperature coefficient means that the electrical resistance of the material will increase with an increase in temperature. This change in resistance is then used to detect and measure temperature changes. An

RTD is often more accurate and stable as compared to a thermocouple and thermistor [212,710]. It is more suitable when high precision and accuracy is required. Platinum is often used in RTDs as it has excellent corrosion resistance, excellent long-term stability and measures a wide range of temperature (-200 °C to 850 °C) [711].

Two fabrication methods were used to fabricate the temperature sensors; Fused Deposition Modelling (FDM) 3D printing method and a thin-film fabrication technique called the lift-off process. The 3D printed sensors were printed using two different conductive Polylactic acid (PLA) filaments that are commercially available. The sensors were printed on flexible mylar substrate. Both conductive filaments used were commercially available, one contained carbon black (CB) and the other contained graphene. The exact percentage of compositions for these conductive PLA filaments were not available publicly due to intellectual property protections. The product information of the CB PLA filament shows that the filaments were made up of Natureworks 4043D PLA, a dispersant and conductive CB. It was suggested that the percentage of CB present was ~20% via thermal degradation analysis on the filament [712]. The filament showed excellent flexibility and its measured resistance is 1.8 kΩ at 10 cm length for a 1.75 mm thick filament. Its volume resistivity is 15 Ω-cm. On the other hand, the graphene PLA may contain graphene of ~8% in its composition and contain other additives as well [713]. The resistance of the graphene filament is 4 kΩ at a length of 1 meter and has a volume resistivity of 0.6 Ω-cm. The performance of the two 3D printed temperature sensors was measured and compare.

Furthermore, thin-film temperature sensors were fabricated on a flexible polyimide substrate using a thin layer of gold. The performance of all fabricated sensors was measured. Thin film flexible sensors were preferred as they can be more suitable for biomedical applications, in particular for non-invasive monitoring on human skin. Thin film sensors are typically smaller and have faster response time, which is desirable in many applications, particularly for biomedical applications. Thin-film fabrication is very effective for the fabrication of thin and flexible sensors. Some of the advantages of this fabrication method includes low cost, large area compatibility and high scalability [327,714]. This study will also demonstrate how a flexible resistive temperature sensor can be easily fabricated by patterning gold on flexible polyimide thin films. The thin-film fabricated sensor may offer better flexibility than the 3D printed sensor as the thin-film sensor is much thinner than the 3D printed sensor.

8.2 Materials

DuPont™ Kapton® E polyimide film with a thickness of 50 μm was purchased from RS Components Ltd. (Corby, UK). ma-N 1420 negative photoresist and ma-D 533 developer for photoresist from micro resist technology was purchased from A-GAS (Rugby, UK). Isopropanol (IPA) was purchased from VWR chemicals (East Grinstead, UK). Acetone was purchase from Sigma Aldrich (Gillingham, UK). Gold (Au) Pellets up to 4 mm with 99.99% purity suitable for thermal evaporation were purchased from Kurt J. Lesker Company® (Hastings, UK). Conductive Polylactide (PLA) Filaments from Protopasta were purchased from 3DFilaPrint (Southend on Sea, UK). This conductive filament was also referred to as carbon black (CB) PLA. Conductive graphene (G) PLA filaments from BlackMagic3D were purchased from graphene supermarket (NY, US). Mylar polyester film with a thickness of 0.25 mm was purchased from RS Component (Corby, UK). Deionised water was prepared using Merck Millipore Milli-Q™ ultrapure water purification system from Fisher Scientific (Loughborough, UK). All materials and chemicals were used as received.

8.3 Experimental methods

8.3.1 3D printing of temperature sensor

The CAD model of an RTD sensor was created in Solidworks (Dassault Systemes, Waltham, MA, US). The 3D model was then saved as an .STL file and imported to Cura for Robo 2.5.0 software (Robo3D, San Diego, CA, US) for slicing. The sliced 3D model saved as .gcode file and was printed using a Robo R2 FDM 3D printer (Robo3D, San Diego, CA, US). The layer height for printing was set to 0.1 mm, the printing temperature for both filaments was 225°C and the print bed temperature was set to 70°C. The designed structure for 3D printing of the sensor is depicted in Figure 8.1.

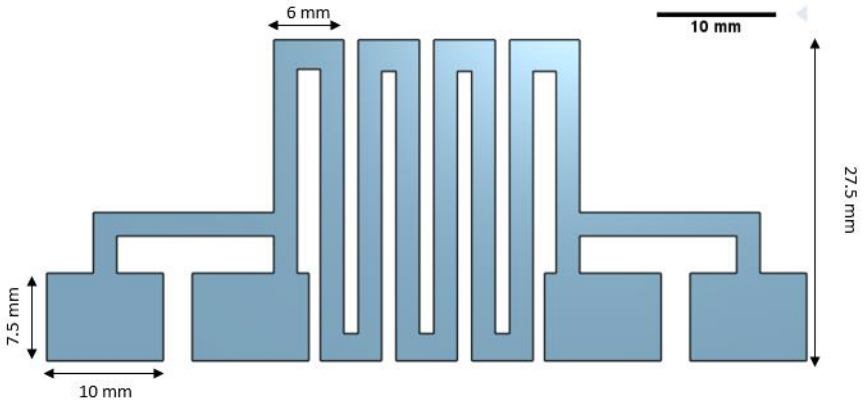

Figure 8.1: CAD model designed to be used for 3D printing of RTD sensors

8.3.2 Thin-film fabrication of flexible resistance temperature detectors (RTDs)

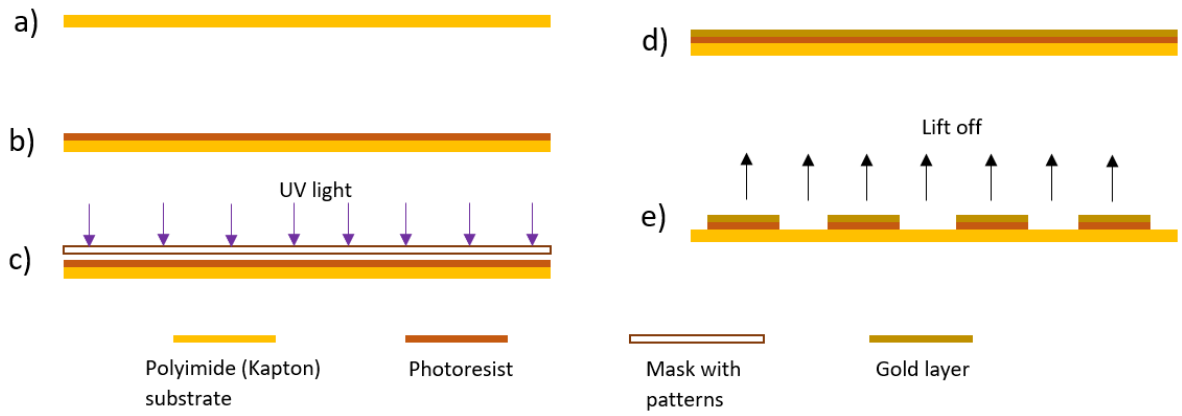

Figure 8.2: Schematic diagram for the fabrication process of a thin-film temperature sensor via the lift-off method a) clean polyimide substrate, b) polyimide substrate spin coated with a layer of photoresist solution, c) mask with sensor structures aligned with polyimide substrate coated with photoresist for UV exposure, d) deposition of gold layer, e) removing of unwanted gold layer with uncured photoresist in an acetone bath to form sensor structures required on the substrate.

The fabrication technique for the flexible temperature sensors is called the lift-off technique. The simplified steps for the process are shown in Figure 8.2. Firstly, a polyimide substrate of 60 mm x 60 mm was first cleaned in an acetone bath with a beaker was placed in an ultrasonic cleaner (Cole-Parmer, St. Neots, UK) for 5 mins. The substrate was then transferred to an IPA bath and sonicated for another 5 mins. The residue solvents were removed from the substrate by rinsing it with deionised water. The wet substrate was then blow dry with compressed air. The cleaned substrate was then placed on a pre-heated hotplate at 150 °C for 5 mins to completely remove the moisture and contaminants on the surface. After heating, the substrate was allowed to cool down on a clean metal cooling plate for 1 min. Once cooled, ma-N 1420 negative photoresist

was dropped onto the substrate surface using a pipette and spin-coated at 3000 rpm for 30 s. The substate coated with ma-N 1420 was then placed on a hotplate at 100 °C for 2 mins.

After the coating of ma-N 1420 negative photoresist on the polyimide substrate, a chromium mask with RTDs structures pattern on a glass substrate produced by Masken Lithograhie und Consulting GmbH (ML&S, Jena, Germany) (depicted in Figure 8.3) was aligned with the coated PI substrate using a manual mask aligner MJB3 (Karl Suss, Garching, Germany). Once aligned, the substrate was exposed to Ultraviolet (UV) light for 28 s to crosslink the photoresist with the substrate. After crosslinking the photoresist with the PI substrate, the substrate was immersed in a ma-D 533 developer bath for 150 s. After the development, the substrate was then cleaned with deionised water and dried with an air gun for gold deposition. The gold deposition was carried out using an Edwards Auto 306 Vacuum Thermal Evaporator (Island Scientific Ltd, Isle of Wight, UK). The current for gold deposition was set to between 3 A and 4 A, and the thickness of the gold deposited was 50 nm. The lift-off process was then carried out after gold deposition. The gold deposited PI substrate with developed negative photoresist was placed in an acetone bath for 20 mins to remove the gold layer where the photoresist was not crosslinked. This process was repeated 3 times to ensure all unwanted gold surfaces had been removed. The remaining gold surface would form the pattern of the RTD sensors.

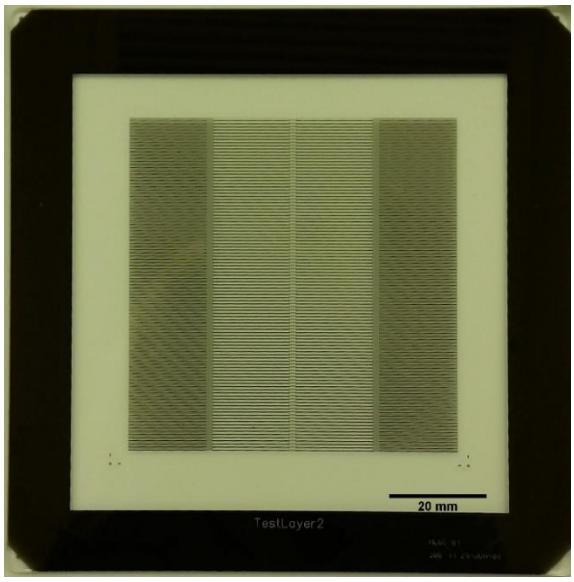

Figure 8.3: Mask used for UV patterning of the RTDs structure for the fabrication of thin-film temperature sensor.

8.3.3 Characterisation of temperature sensors

The electrical conductivity of the 3D printed and the thin film temperature sensors were determined by carrying out a current-voltage characterisation using the Keysight B1500A Semiconductor Device Analyzer (California, USA). A voltage of 5 V to -5 V double sweep was applied and the current flow of the devices were measured. The data were collected and analysed using the Easy EXPERT group+ software (Keysight, California, USA).

8.3.3.1 Response of sensors to temperature change

The resistance of the 3D printed temperature sensors and the thin film temperature sensor were measured at different temperatures (15 °C, 20 °C, 25 °C, 30 °C, 35 °C, 40 °C, 45 °C, 50 °C, 55 °C, 60 °C, 65 °C, 70 °C, 75 °C, 80 °C). The sensors were placed on an Ecotherm digital chilling/heating dry bath (Torrey Pines Scientific, Carlsbad, CA, US), also referred to a hot plate, at the temperatures aforementioned and the change in resistance was measured using a tabletop digital multimeter Keysight 34465A (Keysight Technologies, Wokingham, UK).

8.3.3.2 Temperature cyclic test

Furthermore, temperature cyclic tests were then carried out on both the 3D printed sensors and thin film temperature sensors. The sensors were attached to a hot plate and the temperature of the plate was cycled from 20 °C to 40 °C for 5 cycles. Each cycle was

kept for 5 mins and the change in resistance of the sensors were captured at a rate of every second.

8.4 Results and discussion

8.4.1 3D printed temperature sensors

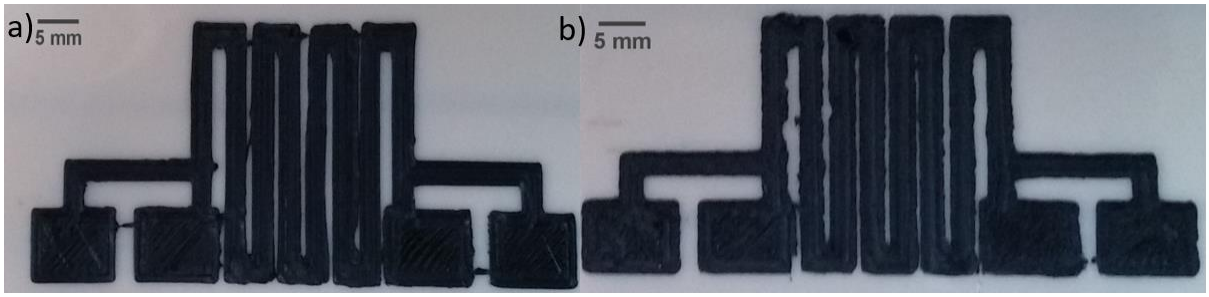

Figure 8.4: 3D printed RTD sensors a) printed using conductive carbon black PLA b) printed using conductive graphene PLA.

Figure 8.4 shows the image of the 3D printed RTD sensors in both conductive filaments. The thickness of the sensors was measured at around 0.3 mm. As the 3D printer was set to print at a resolution of 0.1 mm, three layers of materials were printed in total for both 3D printed RTD sensors. The thin meander structures at the centre were designed for temperature sensing. These thin oscillating patterns were to ensure the resistance of the sensor to be as high as possible. The temperature sensors were designed to have four larger square contact pads which were used for measurements. This is known as the Kelvin setup and it is aimed to reduce the influence of resistance at the contacts in order to get a more accurate measurement. Due to the poor resolution and printing technique of Fused Deposition Modelling (FDM) 3D printing, the printed structures may not be perfectly straight and some bits were connected to each other as seen in Figure 8.4. The connected bits were carefully cut using a knife to ensure they are not connected to each other.

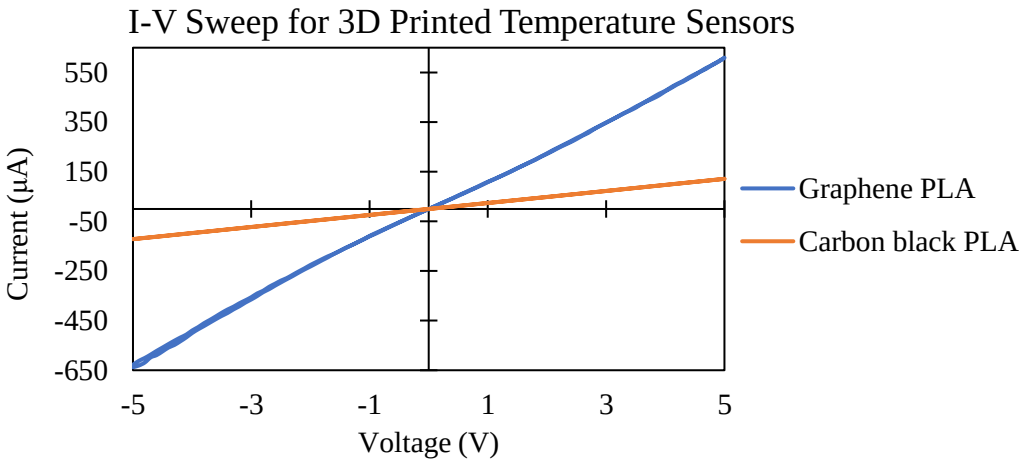

Figure 8.5: Voltage of -5V to 5V applied to obtain the obtain the current vs voltage of the 3D printed sensors.

The conductivity of the 3D printed temperature sensors was measured by applying a voltage of -5 V to 5V to the sensors through the contact pads. Figure 8.5 shows the comparisons of the current vs voltage plots for the 3D printed temperature sensors printed with both G and CB PLA. The graph shows the relationship between the electric current through the device at the corresponding voltage applied. Both sensors showed linear behaviour obeying Ohm's law, where the current is proportional to the applied voltage.

$$\text{Ohm's Law: V (Voltage)} = \text{I (Current) x R (Resistance)} \quad \text{(Equation 8.1)}$$

The G PLA shows better conductivity than the CB PLA. The maximum current that it reaches is much higher than CB PLA. The maximum current that G PLA can achieve is around 550 μA whereas the CB PLA can only achieve a maximum of around 150 μA. The conductivity of the sensors can be further quantified by calculating the conductance of the sensors using the resistance measured. The electrical conductance of can be calculated using the inverse of the resistance ($^{1}/_{R}$). Electrical conductance is a measurement of how easily electricity can flow along an electrically conductive path [715]. The calculated conductance of the CB PLA sensor and the G PLA sensor was 0.0238 mS and 0.1042 mS respectively. This shows that G has superior conductivity than CB, making it very suitable to be used for electronics applications. The current vs voltage plot showed no hysteresis for both materials, which means the current-voltage relationship does not depend on the history but only the present voltage applied. This characteristic is highly desirable for the fabrication of a sensor with high sensitivity in order to achieve better reproducibility and reliability.

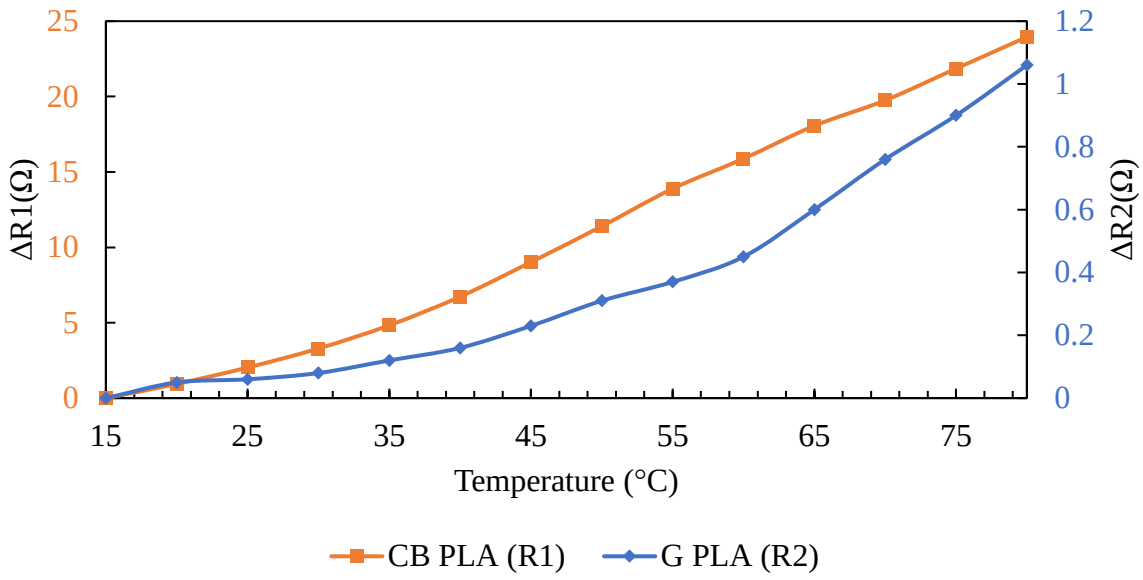

Figure 8.6: The change in resistance of the 3D printed temperature sensors as temperature increases from 15 °C to 80 °C.

Figure 8.6 shows the change in resistance of the 3D printed temperature sensors when the temperature changes. The results showed here confirmed that the 3D printed temperature sensors are working as the resistance increases as the temperature increases. This shows that both materials have a positive temperature coefficient, where the resistance increase with temperature. The maximum resistance of the G sensor is much lower than the maximum resistance of the CB sensor. This finding is coherent with the results in Figure 8.5, showing G has better conductivity than CB as the overall resistance measured in the graphene sensor was lower than the CB sensor. However, the increase in resistance with temperature for the sensor printed with CB PLA was more linear than the G PLA. It seems that CB was more responsive to the change in temperature than graphene. This may suggest that CB may be more suitable for temperature sensing than graphene as it may have better sensitivity to temperature change. The sensitivity of the temperature sensors can be measured using the temperature coefficient of resistance for the sensors. This can be calculated using the following equation:

$$R_t = R_{ref}(1 + \alpha(T - T_{ref}) \quad \text{(Equation 8.2)}$$

where R_t is the resistance at temperature T in °C, R_{ref} is the resistance at 20 °C, α is the temperature coefficient resistance, and T_{ref} is the temperature at 20 °C [716]. The CB PLA sensor has a sensitivity of 0.01416 ± 0.00004 $°C^{-1}$ whereas the G PLA sensor has a sensitivity of 0.00498 ± 0.00004 $°C^{-1}$. The calculation suggests that the CB PLA sensor

has a higher sensitivity than the G PLA sensor. The is as reflected in Figure 8.6, where the increase in resistance with temperature of CB PLA sensor was more linear than the G PLA.

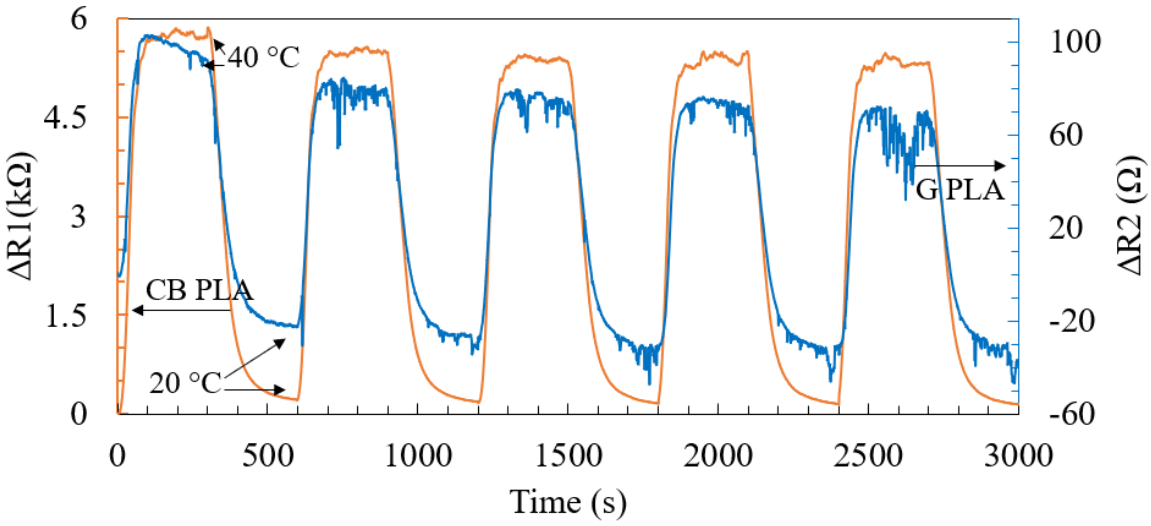

Figure 8.7: 5 cycles of resistance measurements from 20 °C to 40 °C for both 3D printed temperature sensors.

Temperature cyclic tests were carried out on the 3D printed temperatures that were made of two different conductive materials and the results were shown in Figure 8.7. It is important for a temperature sensor to be able to produce repeatable measurements. The purpose of the cyclic test was to confirm whether the temperature sensors are responsive and sensitive enough to the change in temperature. The temperature range of 20 °C to 40 °C was chosen for the test as this is within the fluctuation of skin temperature range, depending on the activities being carried out [717]. The sensors were placed on a hot plate and the temperature was set to increase from 20 °C to 40 °C. The change in resistance was measured for 5 mins at every second. After 5 mins, the plate was cooled down to 20 °C. The results showed that the CB PLA printed temperature sensor was more stable and repeatable when heated. This is because the changes in resistance of the CB PLA sensor were similar throughout the cycles when heated up to 40 °C. When cooled to 20 °C, the CB PLA sensor also return to its original resistance value as indicated in Figure 8.7, showing the change in resistance was close to zero. On the other hand, the cyclic response of the temperature sensor printed using G PLA was not as reliable and repeatable. The resistance of the sensor did not return to the value when it was first measured at the end of the cycle and there were some small fluctuations during the measurements. This finding was consistent with the temperature response test shown in Figure 8.6. The

change in resistance of G PLA seemed to experience a lag as the temperature change, whereas the response of CB was quicker. Although G PLA has better conductivity, CB PLA seems to exhibit better sensitivity and reliability as a temperature sensor.

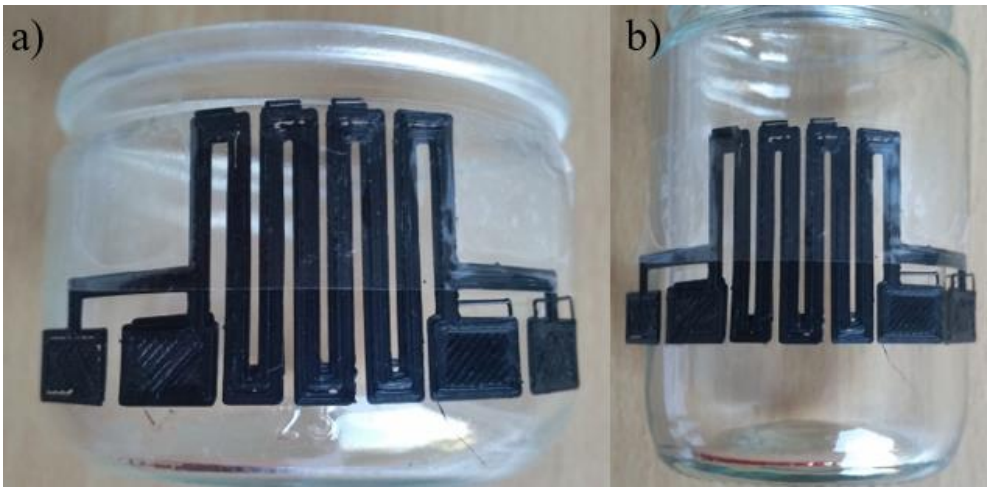

Figure 8.8: Bending test on curved surface with a radius of a) 3.5 cm b) 2.55 cm.

Table 8.1: Resistance measurement for the bending cycles of 3D printed temperature sensors at room temperature.

Resistance of 3D printed temperature sensors (kΩ)							
R = 3.5 cm				**R = 2.55 cm**			
Carbon black PLA		Graphene PLA		Carbon black PLA		Graphene PLA	
Flat	Bend	Flat	Bend	Flat	Bend	Flat	Bend
30.18	30.56	4.14	5.05	30.21	30.68	2.91	3.12
30.26	30.54	4.19	5.18	30.48	30.63	2.92	3.39
30.28	30.74	4.09	4.52	30.34	30.68	2.98	3.38
30.24	30.76	4.03	4.55	30.52	30.78	2.95	3.31
30.34	30.72	3.98	4.61	30.38	30.59	2.94	3.11

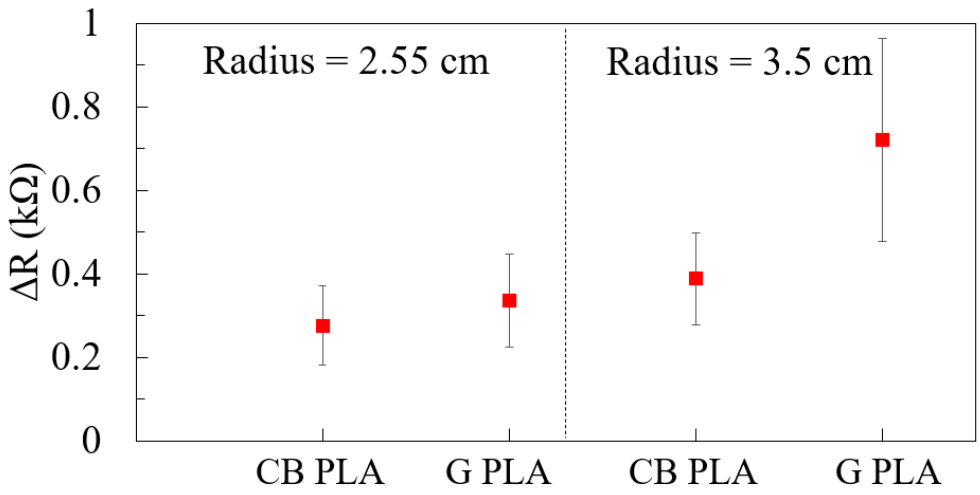

Figure 8.9: Change in resistance for 5 bending cycles of the 3D printed temperature sensors.

A bending test was carried out to investigate the flexibility of the 3D printed sensors. The sensors were first peeled from its original mylar substrate and positioned over two curved surfaces with radii of 3.5 cm and 2.5 cm at room temperature for the bending test. The set-up of the bending for the 3D printed sensors were as shown in Figure 8.8. The strain on the surface of the sensors were estimated using the following equation:

$$\varepsilon = \frac{df + ds}{2R} \quad \text{(Equation 8.3)}$$

where df is the thickness of the sensor, ds is the thickness of the substrate and R is the radius of curvature [718]. The estimated strain on the surface of the sensors when being bent over the surfaces with radii 3.5 cm and 2.55 cm were 0.0715 % and 0.0981 % respectively. The resistance values of both the 3D printed sensors when they were flat and bent throughout 5 cycles were recorded and displayed in Table 8.1. The results showed that there were very subtle changes to the resistance as the sensors were bent. Generally, the resistance of the sensors increased slightly as it was bent over a curved surface. This could be due to the thickness of the 3D printed sensors. The sensors were relatively thick which means they could be more resistant to bending. Hence, the change in resistance was small. However, the increase in resistance when bent was more obvious in the G PLA sensors than the CB PLA sensors. The average values of the change in resistance during the bending cycles were shown in Figure 8.9. The results showed that CB PLA sensors were more stable in the bending test than G PLA sensors. This indicates that CB PLA may have better flexibility and more suitable to be used for flexible sensing applications as the change in resistance is generally smaller even at a higher radius

curvature. On the other hand, the resistance G PLA sensor had a larger increase when the radius of curvature increase. Nevertheless, the sensors showed good stability and flexibility which make the sensors suitable to be used on curved surfaces. This could be particularly beneficial for biomedical applications such as measuring skin temperature as the sensor may be able to conform to the skin surface.

As the sensors were peeled off from their substrate and attached to a curved surface, this shows that the sensors offer the advantage of being transferrable to other substrate after being fabricated. The resistance of the sensors still remained consistent and stable even after being transferred. Hence, the 3D printed sensors also exhibit good stability and modularity for use in biomedical applications. To demonstrate further the ability of the 3D printed sensors to perform as temperature sensors on different substrate surface, the printed sensors were attached to wood and plastic surfaces at room temperature (Figure 8.10). The resistance of the sensors was then measured and the results were shown in Table 8.2. The resistance values shown were an average value of resistance over 1 minute. The results showed the stability of both 3D printed sensors when being used to measure the temperature at different surfaces. Both the wood and plastic surface were at room temperature of around 20 °C. The resistance values for both CB and graphene PLA sensors were considered consistent as both the sensors measured similar resistance values for different surfaces at the same temperature.

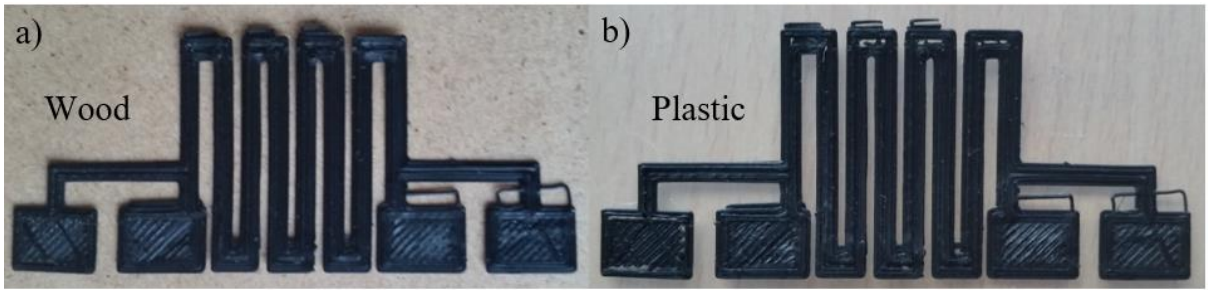

Figure 8.10: Temperature sensing of different substrate surface at room temperature a) wood surface b) plastic surface.

Table 8.2: The resistance of the 3D printed temperature sensors when attached to wood and plastic as new substrate.

Substrate	**Resistance (kΩ)**	
	Carbon Black PLA	**Graphene PLA**
Wood	30.52 ± 0.07	3.52 ± 0.04
Plastic	30.53 ± 0.05	3.50 ± 0.03

Figure 8.11: 3D printed temperature sensors attached on the outer surface of glass vial filled with water at 3 temperature points for temperature sensing.

To measure the response of both 3D printed temperature sensors at different temperatures, the sensors were attached to the outer surface of a glass vial (Figure 8.11). The glass vial was then filled with water at 3 different temperature: room temperature water (~ 25 °C), warm water (~ 40 °C), and boiling water (~ 100 °C). The resistance of the 3D printed temperature sensors was then measured for a duration of 1 min. The results in Table 8.3 show the average resistance of the sensors when the vial was filled with water at 3 temperature points. The temperature sensors were responsive to the temperature of the water. However, the resistance measured does not reflect the temperature of the water but of the outer surface of the glass vial. This is because heat energy was lost through conduction when heating up the glass. Hence, the temperature of the glass could a lower than the water itself.

The measurements here may not be directly comparable to the measurements shown in Figure 8.6. This is because the measurements from Figure 8.6 were only taken up to a maximum temperature of 80 °C. Apart from that, the sensors were placed on a flat surface for the measurements in Figure 8.6. However, the measurements tabulated in Table 8.3 were recorded when the sensors were attached to a curved surface. This means that the sensors were bent on the surface and the bending of the sensors can cause the resistance to increase due to the strain exerted on the sensors. The resistance values in Table 8.3 have accounted for the bending of the sensors and the higher temperature detected by the sensors. A more accurate comparison for the performance of the sensors may be calculating the temperature coefficient resistance, α. The calculated α for the CB PLA sensor and graphene PLA sensor was 0.0141473 ± 0.0003 $°C^{-1}$ and 0.00404 ± 0.0006 $°C^{-}$

[1], which corresponds to the measurement using the data as in Figure 8.6 above. This shows the stability of the temperature sensors even under bent conditions.

Table 8.3: The resistance of 3D printed sensors when attached to the outer surface of a glass vial filled with water at 3 different temperatures.

Water Temperature	Carbon Black PLA	Graphene PLA
Room temperature (~ 25 °C)	31.2 ± 0.2	3.19 ± 0.08
Warm (~ 45 °C)	51.9 ± 0.9	3.42 ± 0.09
Boiling (~ 100 °C)	64.7 ± 0.5	4.16 ± 0.08

8.4.2 Thin-film temperature sensors

Figure 8.12: Images of the fabricated thin-film RTDs a) image of the whole film pattern with RTD structures in gold, b) zoom in image of a), c) enlarged image for the resistor

structure on the left, d) enlarged image of the resistor structure in the centre, e) enlarged image of the resistor structure on the right.

Figure 8.12 shows the images of the flexible temperature sensors fabricated on the polyimide substrate. Figure 8.12a shows the arrays of temperature sensors, where the substrate consists of many rows of the single temperature sensor. The temperature sensors are made of gold layers at a thickness of 50 nm. A single sensor strip has a width of 500 µm and a length of 67.5 mm. Each sensor strips are separated with a gap of 200 µm. Similar to the 3D printed temperature sensors, the structure of the sensors consists of resistors that have very thin oscillating lines. There are three resistors in a single strip which is shown in Figure 8.12b-e. The very thin structures of the temperature sensor can enhance the response time and resolution for temperature sensing. The thin-film structures were fabricated via the lift-off technique, which is a simple, easy and efficient technique to pattern metals without the use of any strong chemicals. As the method can eliminate the use of strong and hazardous chemicals, this method could be highly desirable particularly for the fabrication of biomedical sensors. This is because most biomedical sensors will have close contact with the human body and must not pose any health hazards to the human body. Apart from that, sensors fabricated using this technique can be compatible with pharmaceutics fabrication as some pharmaceutical materials can be chemically sensitive and can degrade in the presence of hazardous chemicals.

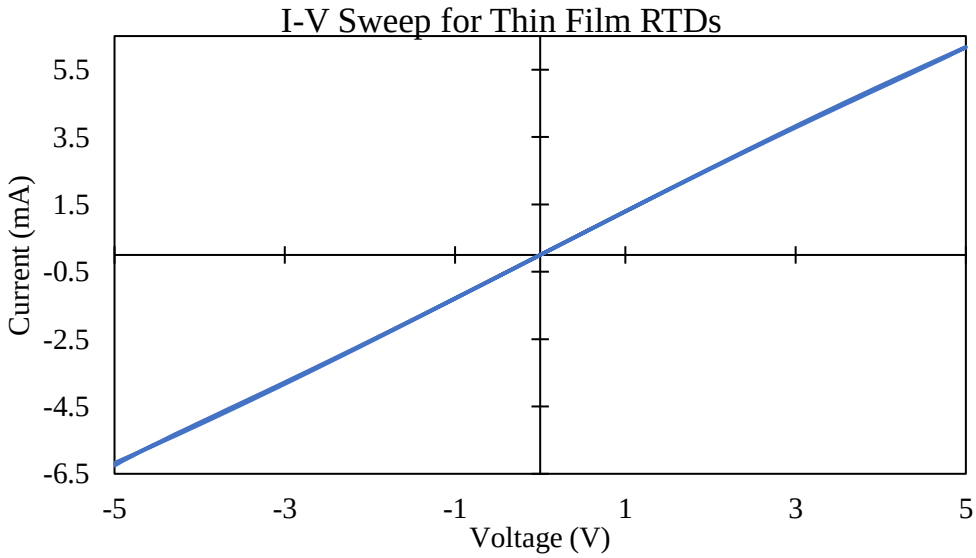

Figure 8.13: The average current vs voltage sweep and average resistance for a bunch of 10 thin film RTD strips

The curent-voltage characteristics of the flexible temperature sensors were measured and the average resistance and current flow measured from -5 V to 5 V for 10 sensor strips

tested is shown in Figure 8.13. The measurements were taken only from the resistors at the centre (Figure 8.12d) using the larger long contact pads on the left and right. The fabricated gold thin-film temperature sensors showed excellent conductivity reaching a maximum current of around 5.5 mA at 5 V and around -6 mA at -5 V. The maximum average resistance measured was around 900 Ω. The temperature sensors also showed no hysteresis in the double I-V sweep as the current flow follows the same straight line when the voltage of -5 V to 5 V was applied twice.

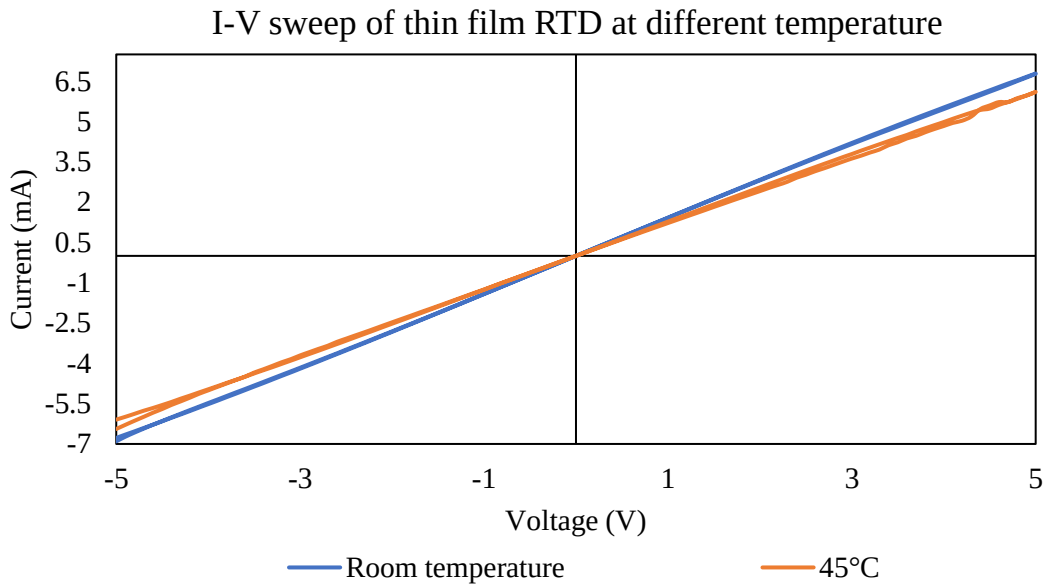

Figure 8.14: The I-V sweeps for a single thin film RTD strip at two different temperatures (room temperature and 45 °C).

The current-voltage characteristic at two different temperatures for the same single flexible temperature sensor strip was then measured. Measurements were taken when the sensor was place on the plate of the probe station at room temperature (~ 20 °C) and at ~ 45 °C. To obtain a temperature of 45 °C, a heating element with a temperature sensor was attached to the plate to heat up the plate. The current-voltage measurement was taken when the temperature of the plate was stabilised. Figure 8.14 shows the I-V sweeps for the thin-film temperature sensor at both temperatures. The maximum current flow in the sensor was higher at room temperature than at 45 °C. At room temperature, the current flow was around 6.5 mA at 5 V and -7 mA at -5 V. On the other hand, the current flow temperature at 45 °C reached only around 5.5 mA at 5 V and -6 mA at 5V. This also means that the resistance at 45 °C is higher than at room temperature, showing that the resistance of the sensor is higher at higher temperature. The resistance at room temperature was around 700 Ω whereas it was around 800 Ω at 45 °C. The response of

the thin-film temperature sensor were then further confirmed with a temperature response experiment by increasing the temperature it was measuring more systematically.

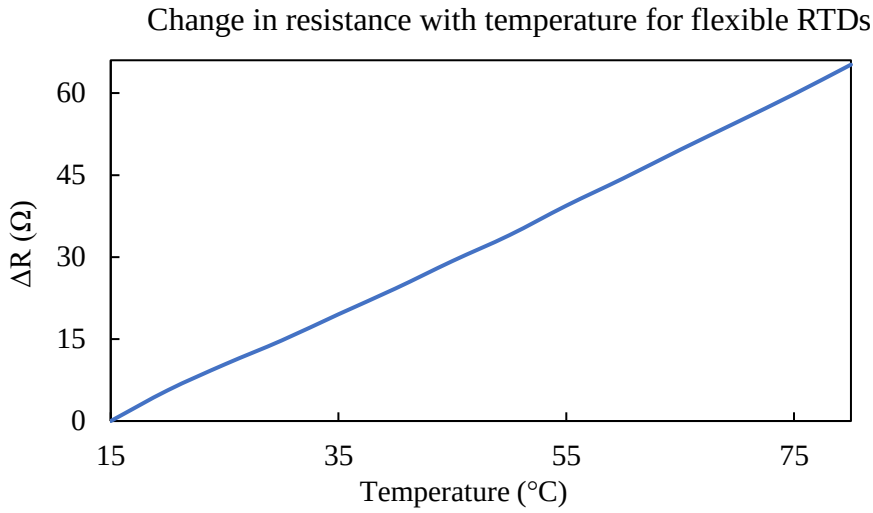

Figure 8.15: The change in resistance of thin film RTDs as temperature increases from 15 °C to 80 °C.

To verify the positive temperature coefficient response of the thin-film RTDs, the resistance of a bunch of 20 RTDs were measured at the same time as temperature increase from 15 °C to 80 °C. The result is shown in Figure 8.15 as a resistance vs temperature plot. The resistance of the RTDs increase linearly as the temperature increase. This showed that gold is very responsive to change in temperature and is very suitable to be used as a temperature sensor. The sensitivity of the thin film temperature sensor was calculated using $R_t = R_{ref}(1 + \alpha(T - T_{ref})$ (Equation 8.2). The calculate sensitivity was 0.00167 ± 0.00001 $°C^{-1}$.

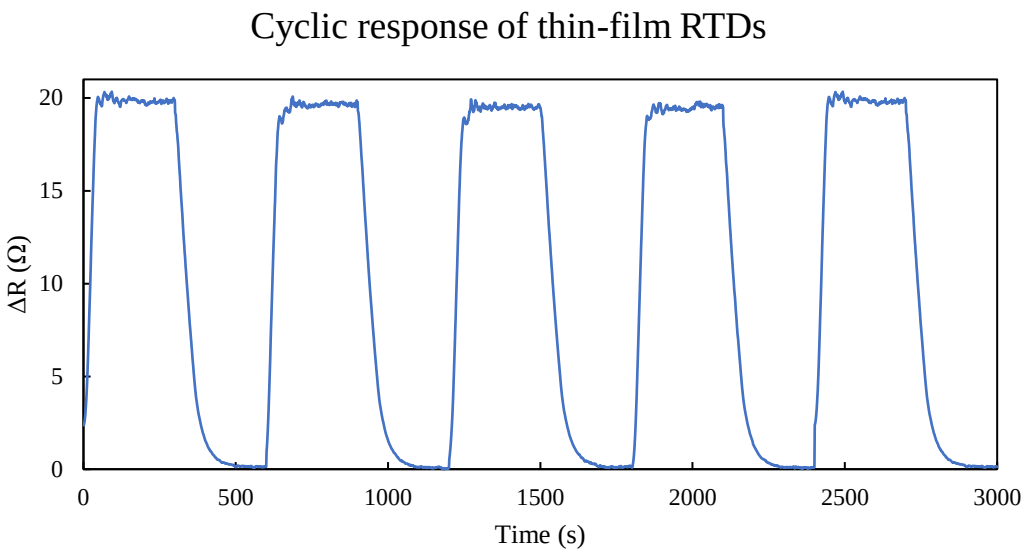

Figure 8.16: change in resistance for thin-film RTDs for cyclic test from 20 °C to 40 °C.

The temperature cyclic test result for the thin-film RTDs was shown in Figure 8.16. The test showed that these thin-film RTDs made of gold were responsive and sensitive to the change in temperature. These sensors had good repeatability as the resistance at 20 °C and 40 °C were consistent throughout the cycle. The thin-film RTDs also had excellent sensitivity as the temperature increased from 20 °C to 40 °C, the change in resistance was instant and showed minimum lag time. These RTDs will be suitable to be used for skin temperature sensing as they were fabricated on a flexible substrate that is conformable to human skin. Pasindu *et al*. showed the effectiveness of a similar flexible temperature sensor which was integrated into a textile yarn [719]. The temperature sensing yarns have a very fast response time, even faster than the rate of change in skin temperature. This shows that such temperature sensors can accurately acquire temperature data and can be used as continuous temperature measurement.

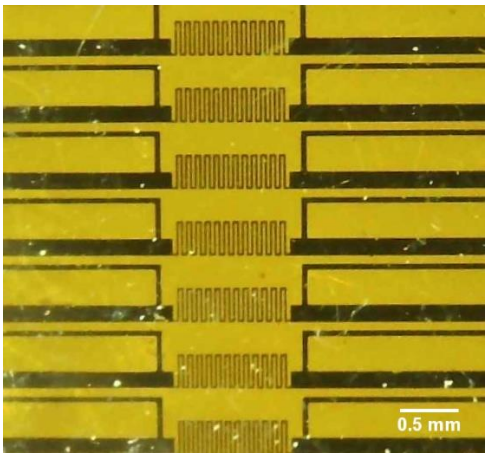

Figure 8.17: Optical image taken after measurements.

During the characterisation of the thin-film RTDs, the sensor strips that were made up of thin gold layer were exposed to friction with metal contacts for measuring the conductivity and resistance. Figure 8.17 shows the image of the RTDs after measurements were carried out. It can be seen metal contacts were scratched but gold layers were still intact on the polyimide substrate. Unlike platinum sensors from Kinkeldei *et al*., platinum lines will crack after deformation [711]. It was then suggested that more ductile metals such as gold, copper and aluminium can be used to overcome the issue of cracking on the sensors [711]. Therefore, the thin-film sensors made of gold may be more durable and were still working even after the surface was slightly scratched.

As mentioned, these thin-film RTDs were very small and it was possible to fabricate up to 100 strip of sensors on a piece of polyimide film of approximately 60 mm x 60 mm. Although 100 sensors were fabricated on a single film, it was also possible to cut the sensors into single strips and function independently. This shows the modularity of the sensors. Similar to the 3D printed sensors, the thin-film sensors can also easily be transferrable to other surfaces but with the polyimide substrate. These thin-film sensors are highly integrable with many other applications, particularly for the smart textile and wearable devices applications [720–723]. The thin-film sensors exhibit better conductivity and temperature sensing response than the 3D printed sensors. This is mainly due to the excellent electrical properties of gold. The thin-film sensors were also more flexible due to the thinner structure.

8.5 Conclusion

Temperature is one of the most simple but important signals to be measured for health monitoring. For example, skin temperature can be used as a vital sign for the early

detection of diabetic foot problems. RTD temperature sensors were fabricated here using two different fabrication methods. Both 3D printing and thin-film deposition are simple and low-cost fabrication method. The 3D printed temperature sensors were printed using conductive PLA filaments. CB PLA filaments and G PLA filaments were used for the 3D printing of sensors and the temperature sensing performance were compared. The 3D printed G PLA showed better electrical conductivity than the CB PLA. However, the CB PLA temperature sensor showed better linearity and sensitivity than the G PLA sensor. The cyclic response test also confirms that the CB PLA temperature sensor was more stable responsive than the G PLA sensor. The CB PLA sensor showed better flexibility and stability after a few bending cycles. A batch of thin-film RTD sensors was also fabricated using a thin-film fabrication technique that involves the lift-off process. This thin-film RTD is made of a thin layer of gold, which was only 50 nm thick. The gold is deposited onto a flexible film that is 50 µm thick. Hence, the sensors showed high flexibility. As the thin-film sensors were much thinner than the 3D printed sensors, they offer better flexibility than the 3D printed sensors. The thin-film temperature sensors were also more conductive than the 3D printed sensors as they were made of gold. They also exhibit excellent linearity and cyclic response.

The benefit of the 3D printed sensor is that it can be produced in one automated process through 3D printing. As in previous chapters, 3D printing has been used to produce drug delivery systems. This 3D printed sensor added to the drug delivery system to form a sensor integrated drug delivery device. The benefit of a temperature sensor can be used to detect and inflammation or infection on the site of drug delivery when being integrated with a drug delivery device such as a transdermal patch. Both 3D printed temperature sensors and thin-film temperature sensors showed great modularity. They can be easily attached to another substrate or system for temperature sensing. Hence, the fabricated temperature sensors showed practicality, particularly for biomedical applications.

Chapter 9 : Fabrication of a MoS_2-based thin-film glucose sensing device

9.1 Introduction

Diabetes is one of the top ten chronic diseases in the world and is caused by the uncontrolled elevation of blood glucose levels. According to the World Health Organization (WHO), there are around 422 million people suffering from diabetes mellitus around the world and this number is still steadily increasing [293]. Diabetes can cause serious health consequences and can cause damage to the heart, blood vessels, eyes, kidneys and nerves. Therefore, diabetic patients are required to monitor their blood glucose levels regularly as the glucose level needs to be corrected immediately in order to prevent any diabetes-related complications. By regularly testing blood glucose levels, diabetic patients can monitor how their diets, medications and activities affect their diabetes. It is also important for doctors to manage the treatment plan according to the patient's condition.

The most commonly used technology for blood glucose monitoring is by using a glucometer. The glucometers analyse a small amount of blood on a paper strip drawn from the diabetic patient. This method involves regular finger pricking, in which a small drop of blood is drawn using a lancet and the blood is then dropped onto an enzymatic strip to generate a reading on a glucometer. This method has been very convenient and has improved over the years, but it is still not very patient compliance as diabetes is a lifetime chronic disease. Not only does finger pricking may cause pain, but it also creates a wound on the skin which may increase the risk of infection when proper hygiene is not kept. Besides that, the sensitivity of the fingertip may be impaired and the patient may often forget to measure their glucose level as this needs to be done regularly throughout the day. Continuous glucose monitoring has therefore received growing interest as it provides a continuous profile of a patients glucose level, allowing patients to identify glycaemic spikes and administer the right amount of insulin at the right time [724].

Currently, continuous glucose monitors are implanted under the skin and can send glucose levels information to a display device via a transmitter. This information can also be accessed by the healthcare team remotely so that the diabetic patient is closely monitored and treatment can be adjusted accordingly. As these devices are implanted

under the skin, the glucose levels being measured are actually from the interstitial fluids rather than the blood. The advantage of continuous glucose monitoring is that it shows the trend of glucose levels in diabetic patients so that the patients can take action early. As a result, it can help to reduce the possibility of hypo or hyperglycaemic events. However, current continuous glucose monitoring systems require implantation and is a very expensive technology. Some are also not patient-friendly as it requires frequent calibration. Most of the transmitter in the glucose monitoring devices are operated by batteries and the batteries life often last for only a few weeks or months [725,726]. The batteries will need to be replaced or recharge. The glucose sensors in these devices often have a short lifetime of a few days or weeks which also requires frequent replacing [727].

Therefore, a minimally or non-invasive glucose measurement has attracted much attention from researchers to health technology companies. The work to improve the sensitivity and reliability of the sensor has been ongoing. Many have shown improved performance but has been their usability has been limited due to the high cost. Not only does the development of a glucose biosensor need to be highly sensitive and have a quick response time, but much focus has also been put on low-cost fabrication as well. To achieve non-invasive glucose monitoring, an alternative to blood glucose measurements is required. Some has suggested that tear fluid is an attractive option due to easy accessibility of the samples and evidence that have shown a correlation between tear glucose and blood glucose [728]. Other biofluids that have shown potential include sweat, saliva and interstitial fluid [729–732].

In general, the glucose-sensing ability of the glucose sensors can be simplified into two categories: enzyme-based and non-enzyme-based glucose sensors [733,734]. Enzyme-based glucose sensors are the gold standard as enzymes are sensitive to glucose and can create a rapid electrochemical response accurately in the presence of glucose [733,735,736]. One of the most widely used enzymes in the glucose biosensor industry is glucose oxidase (GOx), which is a glucose-sensing protein [303,737]. GOx is a typical flavin enzyme with flavin adenine dinucleotide (FAD) and it's normally isolated from fungi such as *Aspergillus niger* and *Penicillium* [738,739]. It has also been reported that GOx exhibits antibacterial activity in the presence of oxygen and glucose [740]. For glucose sensing, GOx oxidises glucose to gluconic acid and hydrogen peroxide [741]. The electrochemical mechanism of glucose oxidation can be simply represented by the following equations:

$$\text{glucose} + \text{GOx} \rightarrow \text{gluconic acid} + \text{hydrogen peroxide} \quad \text{(Equation 9.1)}$$

$$\text{hydrogen peroxide} \rightarrow 2e^- + O_2 + 2H^+ \quad \text{(Equation 9.2)}$$

Typically, enzymatic glucose sensors detect the presence of glucose by measuring the rate of glucose oxidation. The reactions describe from the equations above transfer electrons to a sensing electrode. The electronic current produced on the electrode will be measured and will correspond to the glucose concentration detected [742]. Such glucose biosensors are called amperometric biosensor as it is based on the direct electron transfer between an electrode and immobilised GOx. This has been a promising method for glucose sensing and GOx is widely used because it is inexpensive, stable and its catalytic ability to glucose [743,744].

One of the widely known issues with enzyme-based glucose biosensors is the low electron-transfer rate causing low electrochemical signal in glucose biosensors [745]. Improving the electron transfer on the biosensor can enhance the sensitivity and accuracy of the sensors. Hence, much effort has been focused on improving the surface to improve electron transfer efficiency between the enzyme and the electrode. One innovative method that has been discovered is utilising the excellent chemical properties of advanced nanostructures and their nanocomposites. Some examples of the nanomaterials that have been used include metal nanoparticles, carbon nanotubes, graphene and many more [746–750]. Nanomaterials have received much attention as it has become an attractive material in bioelectrochemistry, and also for the direct electrochemistry of GOx. This is because nanomaterials could provide an environment similar to the redox proteins in the native systems and give the protein molecules more freedom in orientation, which could reduce the insulating property of the protein, resulting in a better electron transfer [751,752]. In recent years, one class of nanomaterials, known as two-dimensional (2D) materials, has been of great interest particularly in many electronic applications [753]. 2D materials can include graphene and 2D transition metal dichalcogenides (TMDs) materials.

Molybdenum Disulphide (MoS_2) is one of the most popular TMDs being studied [754]. These materials are usually in layered positions where the Mo atoms and S atoms are covalently bound, and each layer is separated by van der Waals interactions [755]. MoS_2 exhibit unique electronic properties and high electron mobility, making it an interesting 2D materials to be studied for use in wide range of applications [756]. Some of the most studied applications include solar energy devices [757,758], gas sensors [759,760] and

photo-active materials [761]. Apart from the high electron transfer abilities, the biocompatibility and high electrochemical catalytic activities of MoS_2 makes it suitable for biosensor device applications [762].

There have been several interests in using MoS_2 for glucose biosensor. Su *et al*. has developed an electrochemical glucose biosensor by using a glass carbon electrode that was modified with MoS_2 and decorated with gold nanoparticles [763]. Shan *et al*. developed a back-gated FET-based MoS_2 glucose biosensor that is capable of detecting glucose at very low concentration [430]. A systematic study to investigate the effect of different MoS_2 morphologies on its glucose-sensing ability was carried out by Tuan *et al*. [764]. The study showed that MoS_2 nanoplatelets-based glucose biosensor had a higher sensitivity than MoS_2 nanoparticles and MoS_2 nanoflowers-based glucose biosensors. The layered structure of MoS_2 allowed it to exhibit excellent mechanical properties and flexibility. Studies have shown that modification of MoS_2 nanosheets with gold nanoparticles has increased the effective surface area and improve the conductivity of the material as it promotes electron transfer reactions [765–768]. The presence of MoS_2 is able to improve the electron transfer rate and the electrochemical signal, hence improving the sensitivity and accuracy of the sensors.
Due to the layered structure of MoS_2, the material also exhibits high flexibility. The flexibility of such materials offers the opportunity to develop more reliable flexible sensors. This is because the increasing interest in wearable and point-of-care diagnostics devices have contributed to the need for flexible biosensors [769,770]. Flexible sensors are highly desirable especially for biomedical applications as they are more conformable to the human body.

In this study, a flexible electrochemical glucose biosensor was developed via a simple thin-film fabrication method using easily accessible Kapton® polyimide film. Flexible electrodes have the potential to be used in wearable and flexible biosensing systems for biomedical applications [771]. Typically, flexibility can be achieved by using bendable polymers as the sensing electrode. However, most polymers are electrically insulators instead of conductors. Hence, the flexible polymer used was coated with materials that exhibit excellent electrical property to provide a flexible biosensor platform [772]. The electrode of the thin-film glucose biosensor was made of thin layers of gold and MoS_2 nanosheets. A synergistic effect can be achieved when using gold and MoS_2 as the sensing electrode as such combination can potentially improve enzyme immobilisation and

enhance electron transfer on the electrode surface [773]. GOx was then immobilised onto the surface of the electrode for glucose sensing. MoS_2 has also attracted much attention and has been promising for the fabrication of flexible electronics. The MoS_2 layer was prepared using a simple liquid-based exfoliation method, forming a MoS_2 dispersion which can be utilised easily.

MoS_2 dispersion which was prepared was characterised using the Atomic Force Microscopy (AFM) and Transmission Electron Microscopy (TEM). Studies have shown that MoS_2 has been the potential for biosensing applications for the detection of biomolecules [426]. The bandgap in TMDs allows it to be sensitive in detecting biomolecular targets. The hydrophobic nature of MoS_2 also allows better adsorption of biomolecule [774]. A study by Parlak *et al*. showed that MoS_2 is an ideal semiconductor interface, and when assembled with gold nanoparticles can enhance electrocatalytic reactions as well as providing excellent electrochemical properties [775]. The MoS_2 prepared here is in the form of liquid and can be easily deposited onto the electrode via spin coating to achieve a homogenous layer as the electrode. As MoS_2 is in the form of ink/dispersion, it also offers the potential to be used for printing electronics in the future. The advancement of 3D printing technologies has opened up the possibility of printing electronics material. The fabrication of functional electronics through printing can be a more low-cost fabrication method as the process is fully automated and can be completed in a single step without any post-processing steps [776].

The glucose-sensing ability of the fabricated thin-film glucose biosensors was investigated via cyclic voltammetry (CV) measurements. CV is a type of potentiometry electrochemical measurement that applies low to high voltages and vice versa on an electrode to obtain analytical, thermodynamic, kinetic and mechanistic information about chemical systems involving redox reactions [777]. The constant voltage sweep is applied to a working electrode that is connected to a reference electrode to produce a resulting current. The oxidation and reduction reactions that occurred on the electrode produces a current which could be used to indicate the concentration of an analyte. The current is measured as a function of potential and this measurement is commonly performed in electroanalytical chemistry.

9.2 Materials

Molybdenum (IV) sulphide (MoS_2) powder, Phosphate Buffer Saline (PBS) tablets pH 7.4, Glucose Oxidase (GOx) from *Aspergillus niger* powder with 100,000-250,000 units/g, 6-Mercaptohexanoic acid (6-MHA), Nafion^{TM} perfluorinated resin solution, acetone and glucose solution with 20% concentration in water were purchased from Sigma Aldrich (Gillingham, UK). Ethylcellulose, ethoxyl content 48%, 22 cps and microscope glass slides were purchased from Fisher Scientific, (Loughborough, UK). Isopropanol (IPA) was purchased from VWR chemicals (East Grinstead, UK). Gold (Au) Pellets up to 4mm with 99.99% purity suitable for thermal evaporation were purchased from Kurt J. Lesker Company® (Hastings, UK). DuPont^{TM} Kapton® E polyimide film with a thickness of 50 μm and copper tape were purchased from RS Components Ltd. (Corby, UK). Deionised water was prepared using Merck Millipore Milli-QTM ultrapure water purification system from Fisher Scientific (Loughborough, UK). All materials and chemicals were used as received.

9.3 Experimental methods

9.3.1 Preparation of MoS_2 ink/dispersion

Ethyl cellulose (EC) was mixed with Isopropanol (IPA). The IPA with EC was placed on a hot plate of 60°C and was stirred using a magnetic stirrer at 600 rpm until the EC is fully dissolved. The MoS_2 powder was then added to the IPA with dissolved EC. The concentration of EC in IPA is ~4 wt% and the initial concentration of MoS_2/IPA was 10mg/ml. The MoS_2 was then dispersed into the solvent through 24 hours of sonication using a Fisherbrand® FB15051 bath sonicator (Fisher Scientific, Loughborough, UK). The dispersion was then centrifuged at 1000 rpm for 10 minutes to remove larger MoS_2 flakes that are not properly exfoliated using a Thermo Fisher Scientific Sorvall^{TM} ST8 benchtop centrifuge (Fisher Scientific, Loughborough, UK). After centrifugation, around 45 ml of the supernatant was transferred to a fresh bottle and the sediments obtained through centrifugation were discarded. Fresh 5 ml of 5 mg/ml MoS_2 solution was prepared and added to the 45 ml of the MoS_2 solution remained. The bottle of MoS_2 solution was then sonicated for another 24 hours. After the sonication process, the MoS_2 ink was left at a standstill for 24 hours to allow the sedimentation of larger MoS_2 flakes which have not been properly dispersed before being used. Only the supernatant of the MoS_2 solution was used.

9.3.2 Deposition MoS_2 dispersion onto a glass slide

Two small pieces of copper tape, roughly 0.5 cm x 0.5 cm, were cut and stuck onto a microscope glass slide parallel to each other, leaving a gap of approximately 0.5 cm between the two copper tapes. A 1ml micropipette (Gilson Scientific, Dunstable, UK) was used to take the prepared MoS_2 dispersion and dropped onto the glass substrate to fill the gap between the two copper tapes. The glass slide with MoS_2 dispersion between two copper tapes was placed in an oven at a temperature of 330°C for 3h for the annealing of MoS_2. This sample was then used to measure the conductivity of the deposited MoS_2.

9.3.3 Fabrication of thin-film glucose sensor

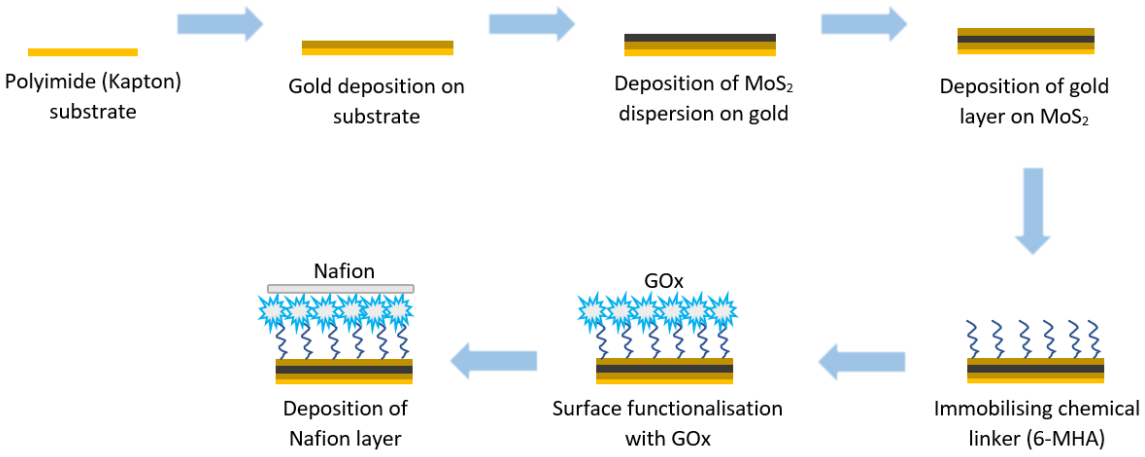

Figure 9.1: Schematic diagram of the fabrication of thin-film flexible electrochemical glucose biosensor made of gold/MoS_2/gold layer functionalised with glucose oxidase.

A piece of polyimide (PI) substrate was first cleaned in an acetone bath using ultrasound for 5 mins. The substrate is then transferred to an Isopropanol (IPA) bath and sonicated for another 5 mins. The residue solvents were removed from the substrate by rinsing it with deionised water. The wet substrate was then blow dry with compressed air. The cleaned substrate was then placed on pre-heated hotplate at 150 °C for 5 mins to completely remove the moisture and contaminants on the surface. After heating, the substrate is allowed to cool down on a clean metal cooling plate for 1 min. Once cooled, the substrate is deposited with the first layer of gold in an Edwards Auto 306 Vacuum Thermal Evaporator (Island Scientific Ltd, Isle of Wight, UK). The current for gold deposition was set to between 3 and 4 amps and the thickness of the gold deposited was 50 nm. After that, MoS_2 dispersion was spin-coated on top of the gold layer at 3000 rpm

for 30 s. The substrate was then placed in an oven at a temperature of 330 °C for 3h for the annealing of MoS_2. A final layer of gold was then coated on top of the MoS_2 layer.

9.3.4 Functionalisation of glucose sensing device

For the functionalisation of the glucose biosensor, the surface of the fabricated thin-film device was cleaned using ethanol and deionised water. 6-MHA was dissolved in ethanol at a concentration of 4 mM. The device was then immersed into the 6-MHA solution for 3h at 4 °C. The enzyme glucose oxidase was dissolved in PBS pH 7.4 at a concentration of 5 mg/ml. Once the surface of the sensor was immobilised with 6-MHA as a chemical linker, 50 µl of dissolved GOx was dropped onto the surface and left for another for 3h at 4 °C. Finally, 5 µl of 0.05% Nafion was dropped onto functionalised surface to form a protective layer. The complete process of fabricating a flexible glucose biosensor is depicted in Figure 9.1.

9.3.5 Characterisation studies

9.3.5.1 Viscosity testing of MoS_2 dipsersion

A Brookfield DV2T Touch Screen Viscometer (Brookfield Ametek Inc., Middleborough, MA, USA) attached with an LV Spindle 61 was used to measure the viscosity of the MoS_2 ink with a speed of 100 rpm for 30 seconds at room temperature. The accuracy of the viscometer is ±0.60 cP. The viscosity of the MoS_2 ink straight after the sonication process and after 24 hours of sedimentation were measured.

9.3.5.2 Conductivity measurement

The electrical property of MoS_2 and the glucose biosensors fabricated were measured using the Keysight B1500A Semiconductor Device Analyzer (California, USA). A 3V to -3V of potential difference was applied. The data were collected and analysed using the Easy EXPERT group+ software (Keysight, California, USA).

9.3.5.3 Atomic Force Microscopy (AFM)

AFM was carried out to study the surface morphology of the thin-film devices using the Bruker Dimension Icon XR AFM (Bruker, MA, USA). The surface characterisation was carried out using the non-contact Kelvin Probe Force Microscopy (KPFM) technique. AFM data were collected using the software Nanoscope Bruker (Bruker, MA, USA) and were analysed using Gwyddion (Czech Metrology Institute, Brno, Czech Republic).

9.3.5.4 Transmission Electron Microscopy (TEM)

TEM was carried out on a 120 kV JEOL JEM1400-Plus (JEOL, Peabody, MA, USA) equipped with a Gatan OneView 4K camera (Gatan Inc., Pleasanton, CA, USA) for the MoS_2 samples. Samples were prepared by pipetting 3-5 µL of MoS_2 ink onto carbon square mesh (CF300CUUL) and ultrathin carbon grids by Electron Microscopy Sciences (CN Technical Services, Ltd., Wisbech, UK). The samples were allowed to dry before characterisation. The TEM data were collected and analysed using the Gatan Microscopy Suite Software (Gatan Inc, CA, USA).

9.3.5.5 Electrochemical measurement of flexible glucose sensor

The electrochemical investigation was done using a conventional three-electrode system with a PBS pH7.4 solution used as the electrolyte. The flexible glucose sensor was used as the working electrode, a silver/silver chloride (Ag/AgCl) double-juction reference electrode was used as the reference electrode and a platinum (Pt) wire electrode was used as the counter electrode. Cyclic voltammetry (CV) measurement and the amperometric response of the glucose sensor were measured at room temperature. The parameters for sampling interval was set to 2 mV/s, and a scan rate of 10 mV/s was used for the CV measurements. The applied voltage range was 600 mV to -800 mV. Three samples shown in Table 9.1 were used in the CV measurement for comparisons.

For the amperometric response, the same three samples were first measured in the electrolyte without the presence of glucose. After the first measurement, 1 mM of glucose was added to the electrolyte and the change in current on the working electrode was measured. An initial potential of -0.8 V, and a sampling interval of 0.2 s were set as the parameter for the amperometric response measurements. All data were collected and analysed using the Gamry Data Acquisition and EChem Analyst software (Gamry Instruments, Warminster, PA, USA).

Table 9.1: Three different glucose biosensors prepared for comparisons.

Sample	Glucose sensing surface
A	Gold surface functionalised with GoX protected with Nafion layer
B	Gold/MoS_2/Gold surface functionalised with GoX protected with Nafion layer
C	Gold/MoS_2/Gold surface functionalised with GoX without Nafion layer

9.4 Results and Discussion

9.4.1 Viscosity testing of MoS_2 dispersion

Table 9.2: Viscosity of MoS_2 Ink after the sonication process

Test run	Viscosity (cP)
Test 1	15.36
Test 2	15.39
Test 3	15.48
Average	15.41 ± 0.06
After 24 hours sedimentation	
Test 1	11.16
Test 2	11.88
Test 3	11.88
Average	11.64 ± 0.42

The viscosity of the MoS_2 ink prepared was measured at room temperature on the results were shown in Table 9.2. The viscosity of the MoS_2 ink was first measured after it was freshly prepared. The ink was then left to settle for 24 hours before a second viscosity measurement was taken. The results showed that the viscosity of the ink was slightly higher when it was freshly prepared than after being left to settle for a day. This shows that the MoS_2 ink contains some larger MoS_2 particles. The exfoliation process through sonication was to separate the layers of MoS_2 to thinner layers by breaking the interactive forces between the layers. After 24 hours of leaving the ink to settle, some heavier MoS_2 layers sediment. Hence, the viscosity was slight lower. However, the difference in viscosity was not large, showing that the liquid exfoliation method was a simple and effective method preparing MoS_2 dispersion which could stay relatively stable over time. The presence of EC as a surfactant in the ink also contributed to the stability of the ink. The MoS_2 ink prepared was shown in Figure 9.2.

The results from viscosity testing also suggested the suitability of MoS_2 ink for use in printing applications. Ink viscosity plays a vital role in the reliability and repeatability of the printing of functional electronics as the viscosity affects the form and volume of the ink droplet [778,779]. A high viscosity ink can cause clogging of the printer nozzle. Surfactant and dispersing agents can reduce aggregation and sedimentation. Inkjet printing typically requires ink at a viscosity of around 10 cP [780]. Another attractive printing method which may be suitable is the aerosol-jet printing technique. This printing technology is a more versatile non-contact printing method as it is capable of printing on non-planar surfaces. It uses an atomiser to disperse the ink during the printing, an

ultrasonic atomiser and a pneumatic atomiser. The ultrasonic atomiser is typically suitable for ink viscosity with 1-10 cP and the pneumatic atomiser can print ink with viscosity ranging from 1 to 1000 cP [781].

Figure 9.2: MoS_2 ink/dispersion.

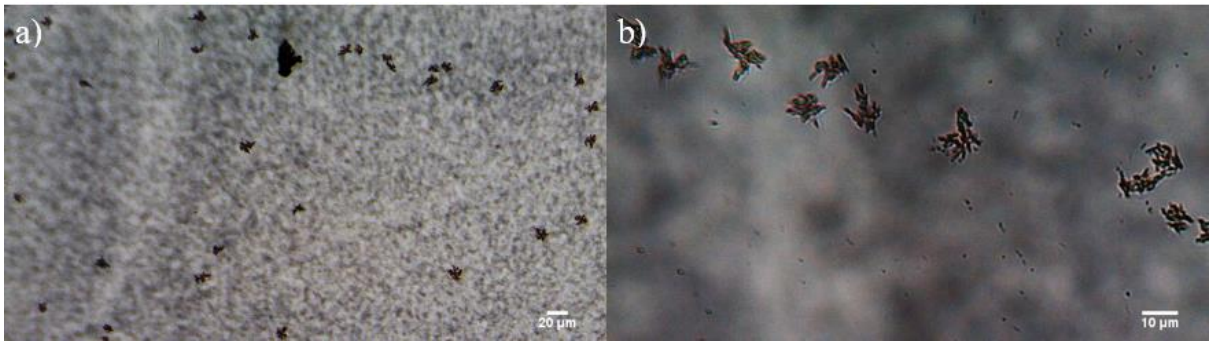

Figure 9.3: Optical images of MoS_2 dispersion a) 4X magnification b) 10X magnification.

A microscopic image of a drop of MoS_2 dispersion on a glass slide was shown in Figure 9.3. The images showed the formation of the MoS_2 flakes in the dispersion after exfoliation. It can be seen that some particles are larger. In general, the liquid exfoliation has been effective in separating the MoS_2 particles into thin sheets. The MoS_2 were originally in the form of powder with average an particle size of below 2 µm. The exfoliation method uses ultrasound forces to break the particles that have agglomerated and the solvent keeps the thin sheets of MoS_2, forming a percolation of MoS_2 network. However, there is not much control over the size of the flakes using this method.

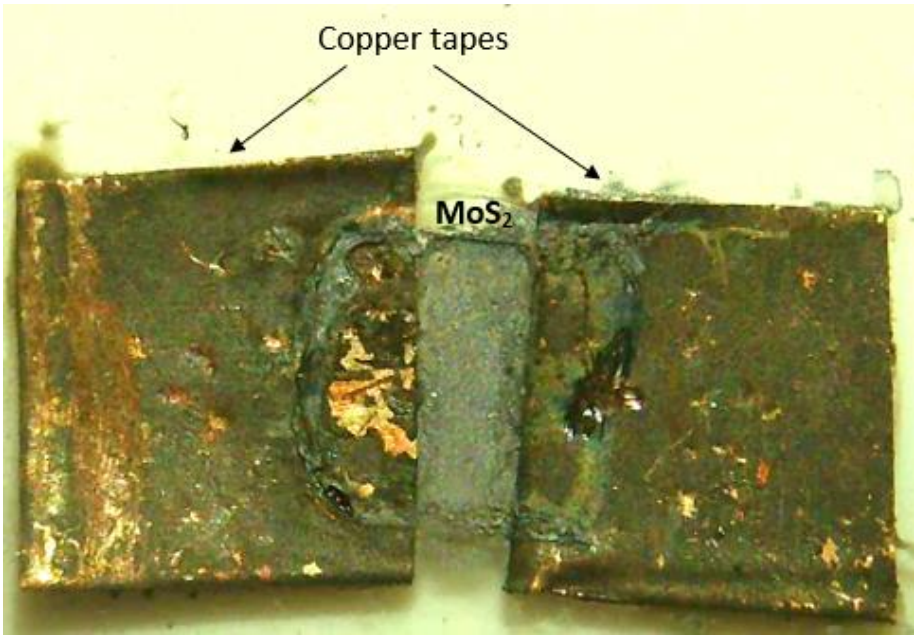

Figure 9.4: Set up for conductivity measurement of prepared MoS_2 dispersion.

The conductivity of the MoS_2 dispersion was tested by depositing the ink onto a glass slide between two copper tapes. The copper tapes act as contact pads for the measuring probes to be placed to achieve a more reliable measurement of the conductivity. The MoS_2 was required to be annealed at 330 °C for 3 hours to ensure its electrical conductivity and remove any excess solvents. After annealing the conductivity measurement was carried out the results were shown in Figure 9.3. The measurements were carried out in a bright and dark environment for comparisons. In the conductivity measurements, a 3V to -3V of potential difference was applied and the current (I) values were recorded. It showed that in a dark environment, the current is lower and the current increases in the presence of light. This shows the reaction of MoS_2 to the presence of light and can be used as a light sensor. MoS_2 is known to have photoluminescence properties and have been successfully used in retinal implant application [782]. Therefore, the measurement here was consistent with the findings in the literature. This study has shown that the liquid exfoliation method can be a low-cost and effective method to prepare MoS_2 dispersion with electrical conductivity, which could be further used for other electronic applications.

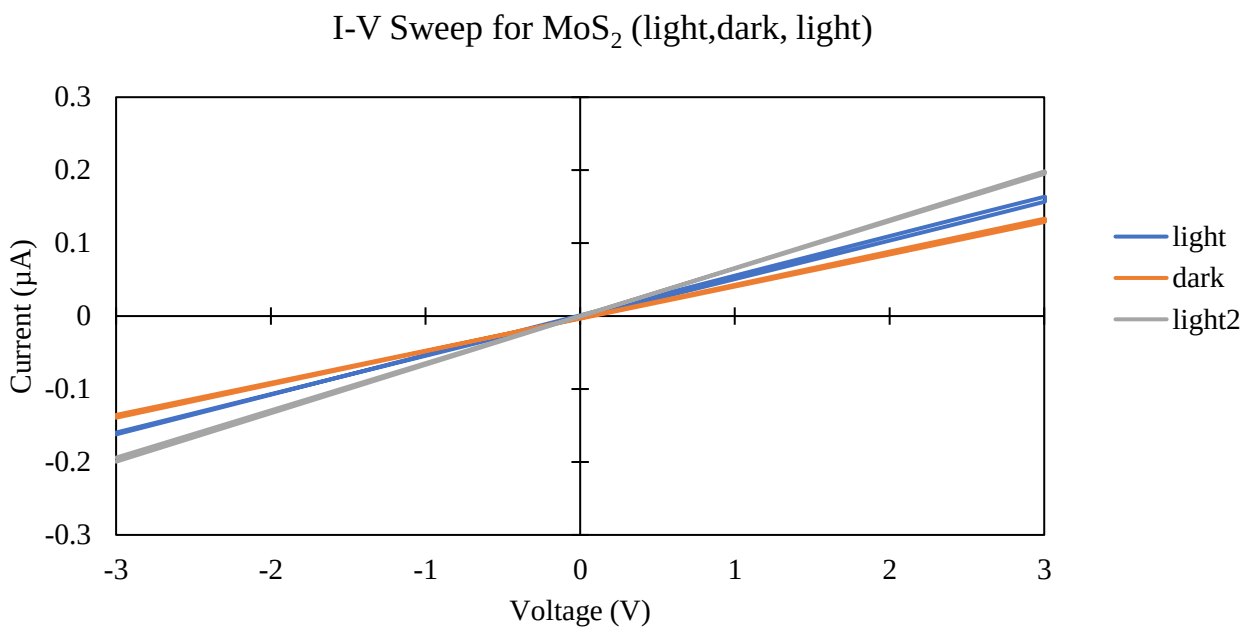

Figure 9.5: I-V Sweep for the conductivity measurement of annealed MoS_2 in the presence of light and in dark environment.

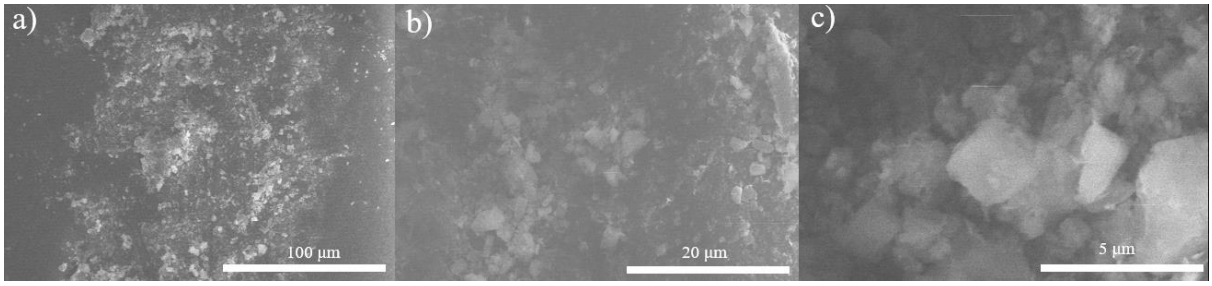

Figure 9.6: SEM images of MoS_2 after annealing a) magnification of 500X b) 2000X c) 10,000X.

The surface morphology of the deposited MoS_2 dispersion on the glass slide was then studied using SEM. The SEM images at several magnifications were shown in Figure 9.6. The SEM images in Figure 9.6 b and c clearly showed the shape of the MoS_2, which are in the form of thin layers of sheets. This further confirms that the exfoliation method of separating the layers was efficient and simple. The MoS_2 layers formed a network, allowing the annealed patch of MoS_2 to be conductive.

AFM was carried out to further study the morphology of MoS_2. The sample used for AFM was prepared using the spin coating method. This was to achieve the thinnest layer of MoS_2 on a smooth surface. A pipette was used to drop 100 µl of MoS_2 ink onto a flexible polyimide film with a thickness of 50 µm. The film was then spun at 2000 rpm for 10 s in a spin coater. Similarly, the MoS_2 coated film was then annealed in an oven before

characterising using the AFM. The AFM image of the MoS_2 film was shown in Figure 9.7. The image showed the MoS_2 flakes on the film, which was consistent with the study using SEM. The AFM image in Figure **9.7** showed that there was a layer of gold on the polyimide film. This is because the polyimide film used had a layer of gold coated onto some parts of the film before the film was spin-coated with MoS_2. However, the purpose of the AFM study here is not to measure the gold surface but only the coated MoS_2 flakes. The AFM measurement showed that the maximum thickness of the spin-coated MoS_2 layer was up to 70 nm. It has been reported that a single layer MoS_2 has a thickness of around 0.7 nm [379]. Therefore, the liquid exfoliated MoS_2 solution here contains multiple layers of MoS_2, where up to 100 layers can be found. Nevertheless, the spin coating is a simple and effective way of achieving a very thin and homogenous layer of MoS_2.

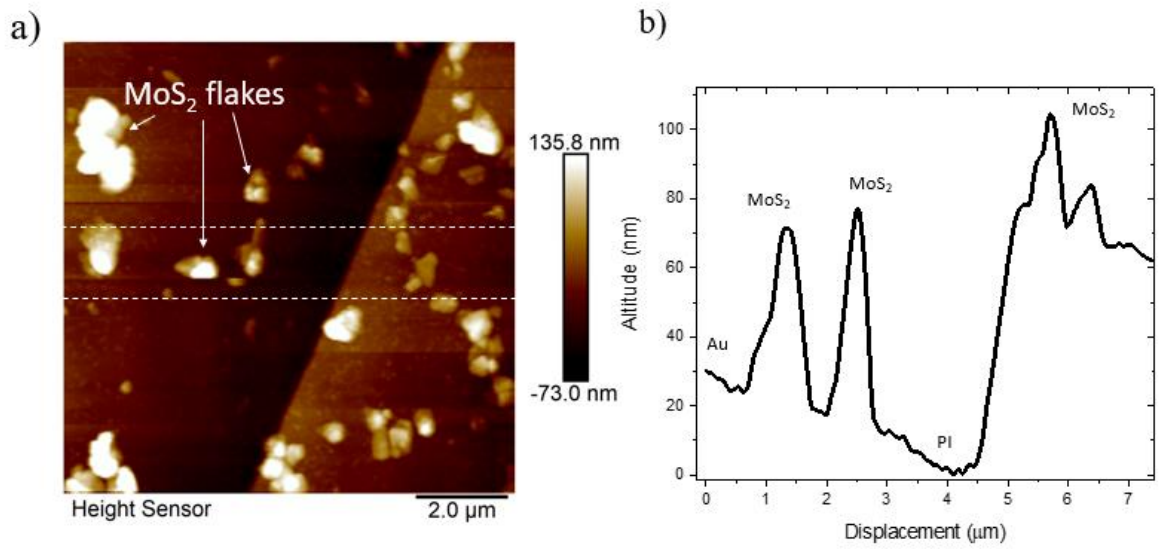

Figure 9.7: a) AFM image of spin coated MoS_2 layer on flexible substrate, b) Average height profile of the MoS_2 layer deposited in the rectangular region marked in (a).

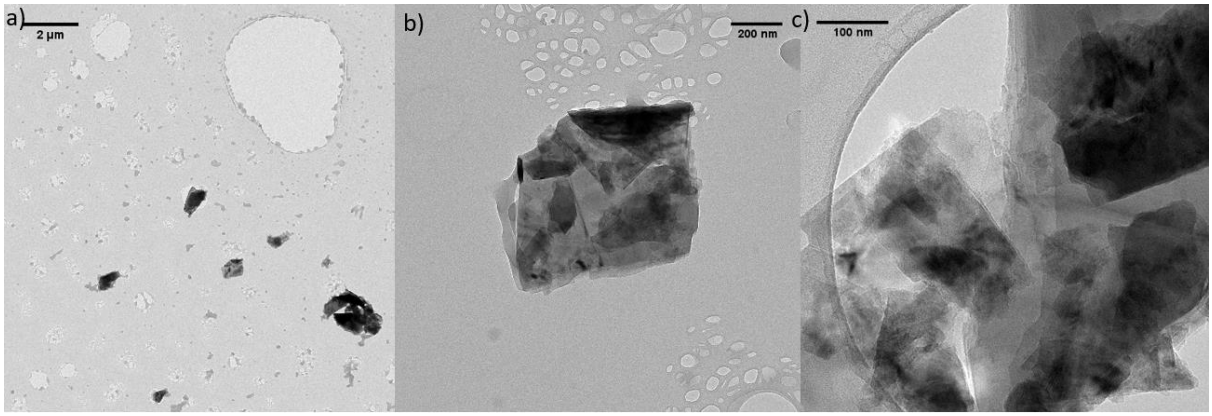

Figure 9.8: TEM images of exfoliated MoS_2 flakes a) magnification: 3000X b) 30,000X, c) 80,000X.

TEM was carried out to investigate the lateral thickness of the exfoliated MoS_2 dispersion. The MoS_2 dispersion were dropped onto carbon grids specifically for TEM imaging. The TEM images of the exfoliated MoS_2 at different magnification were shown in Figure 9.8. The lateral size of the MoS_2 flake in Figure 9.8b is around 690 nm. The TEM shows the exfoliation method can effectively produce several thin layers of MoS_2. The structure of MoS_2 is very similar to graphene, shown in Figure 9.9. Several studies have shown that the structure MoS_2 has advantages of being used to fabricate flexible biosensors with high selectivity and sensitivity [426,430,783]. As such, MoS_2 is a promising material that can be used for the fabrication of modern electronic products such as microelectronics, flexible electronics.

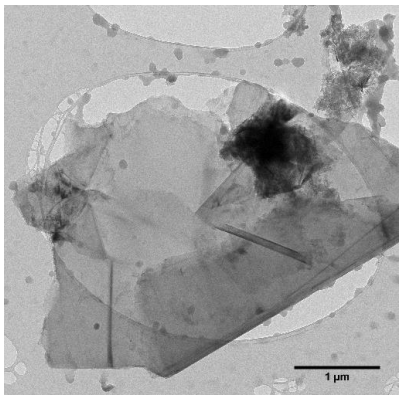

Figure 9.9: TEM of exfoliated graphene layer at a magnification of 10,000X.

9.4.2 Fabrication of glucose biosensor

An enzymatic glucose biosensor was prepared using a simple thin-film fabrication method by first depositing a thin layer of gold (~50 nm) on a flexible polyimide substrate, then spin coating a layer of MoS_2 dispersion, and finally another layer of gold (~50 nm) on top of the MoS_2. The surface was immobilised with glucose oxidase so that it could perform as a glucose-sensing device. As a comparison, another glucose sensor was prepared by just depositing a layer of gold onto the polyimide substrate. The microscopic images of these two glucose sensors were shown in Figure 9.10. The image in Figure 9.10a shows the sensor made up of just a gold layer on a flexible polyimide substrate, and the sensor Figure 9.10b consisted of a gold layer, MoS_2 layer, and another gold layer. Both the sensor surfaces were functionalised with GOx for glucose sensing. The surface morphology and the glucose-sensing performance of the sensors were studied.

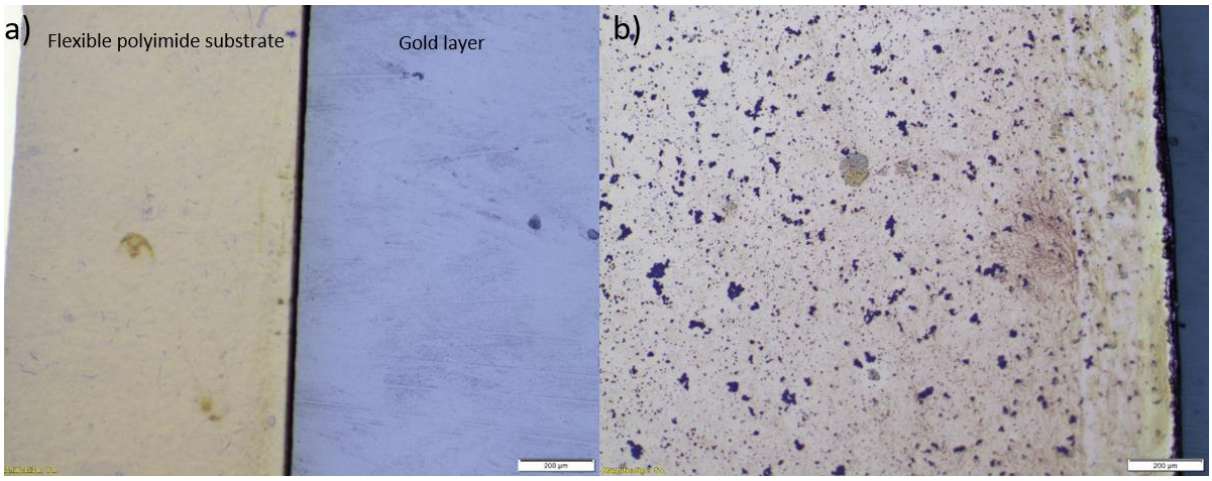

Figure 9.10: Microscopic images of the surface of glucose biosensors at 5X magnification. a) gold only (sample A), b) gold/MoS_2/gold glucose sensor (sample B).

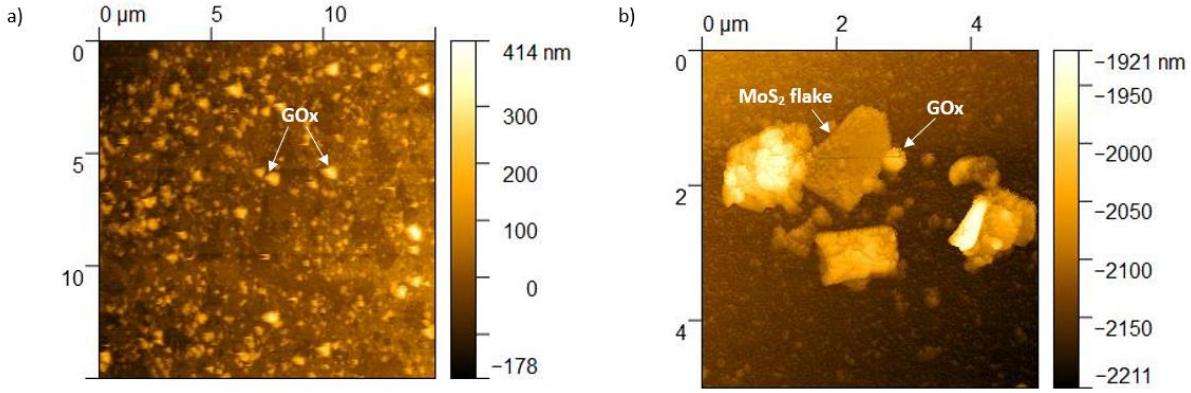

Figure 9.11: AFM study on the surface of glucose biosensors for a) sample A, b) sample B.

The surface morphology of the two glucose biosensors (sample A and B) was obtained using AFM. The results were displayed in Figure 9.11. AFM is a common technique for nanoscale surface characterisation of a sample by making probe scans over a surface in a surface plane x-y while the distance between the surface and the probe is being controlled [784,785]. It is also capable of taking topographic images and can be used to measure the surface roughness of the thin-film glucose biosensors fabrication. Surface roughness is often referred to as the variation in the height of the surface relative to a reference plane [786]. It can usually be calculated and presented as an arithmetical mean deviation of the mean (R_a) or a root mean square deviation for the mean (R_q). For an image where the area is being analysed, the R_a and R_q can be defined as the equations below:

$$R_a = \frac{1}{n}\sum_{i=1}^{n}|y_i| \text{ (Equation 9.3)}$$

$$R_q = \sqrt{\frac{1}{n}\sum_{i=1}^{n} y_i^2} \text{ (Equation 9.4)}$$

where y is the height at a given pixel (i) in the image. The AFM surface topography measurement uses a tapping mode, which is a gentler mode where the measuring tip is oscillated at a resonance frequency as the top gently interacts with the surface at a constant amplitude of oscillation. The method of measuring used here is non-destructive to the surface of the sample. The results for the surface roughness measurements were displayed in Table 9.3. The surface roughness for both glucose biosensors were also compared with the surface of the flexible polyimide film without any materials deposited on its surface. The results showed that the clean polyimide film that was 50 μm thick has a very smooth surface which was excellent for the deposition of nanoparticles. The glucose sensor with the gold surface was smoother than the glucose sensor containing gold/MoS_2/gold layers. This was as expected as the gold surface was smoother than MoS_2 flakes. However, the results showed that both sensors have rather smooth surfaces with could help maintain their function whilst being bent.

Table 9.3: Surface roughness parameters of the glucose biosensors from AFM measurements R_a represents the arithmetic average of the absolute values of the surface height deviations measured from the mean plane, R_q represents the root mean square average of height deviation from the mean image data plane.

Sample no.	**R_a (nm)**	**R_q (nm)**
Clean polyimide film	2.25	3.32
Sample A (Au only)	18.16	19.86
Sample B (Au/MoS_2/Au)	21.43	23.89

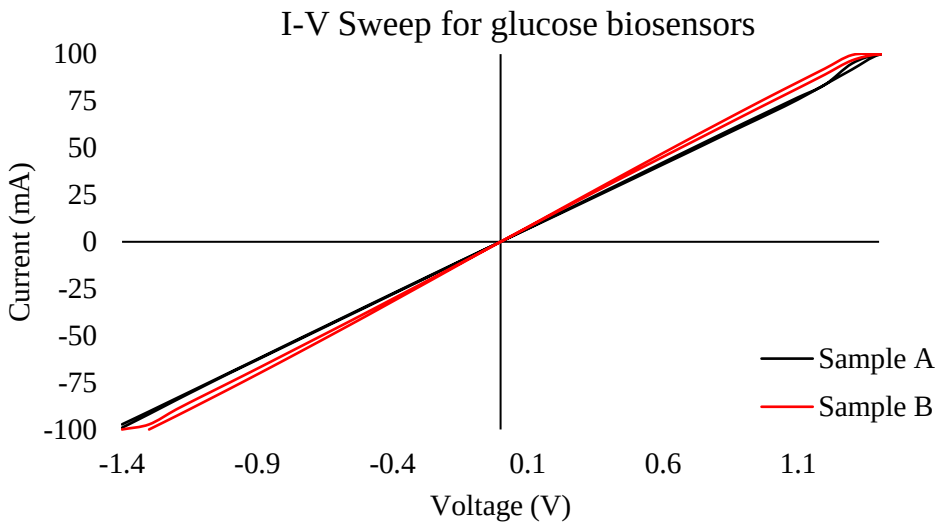

Figure 9.12: Conductivity measurement of the glucose biosensors.

The conductivity of two glucose biosensors was measured and the current vs voltage (I-V) plot was displayed in Figure 9.12. Both biosensors have good conductivity between the applied voltage of -1.4 V to 1.4 V. The maximum current flow for both sensors were around 100 mA. The resistance of the biosensors can be calculated using the gradient of the I-V curve, where resistance R = $\frac{V}{I}$. The calculated resistance for sample A is 13.6 Ω whereas for sample B is 14.6 Ω. The slightly higher resistance in sample B could be due to the presence of a MoS_2 layer sandwiched in between two gold layers. Gold has very high conductivity as it is a metal in nature. The results showed that even with the presence of MoS_2, the biosensor still showed excellent conductivity, which is vital for electron transport during glucose sensing.

9.4.3 Glucose sensing

The flexible glucose biosensor contains gold/MoS_2/gold layers as the electrode. The surface of the electrode was functionalised with the enzyme GOx through gold-thiol interaction. The flexible electrode was first deposited with a thin layer of 6-MHA, which provides a bonding to bind the enzyme GOx onto the electrode surface through electrostatic interactions. The electrochemical reaction of the electrode was measured using the cyclic voltammetry (CV) method. CV is a widely used electroanalytical technique for a systematic study on the electrochemical behaviour of a system through the study of the current-voltage measurements [787]. This technique is relatively simple and provides high information content regarding the qualitative kinetic from an

electrochemical reaction, where each peak corresponds to a particular electrochemical process [788].

The set-up for a CV measurement typically requires a working electrode, reference electrode and a counter electrode immersed in an electrolyte. In this study, the flexible glucose biosensor is the working electrode, an Ag/AgCl electrode is the reference electrode, a platinum wire used as a counter electrode, and PBS pH 7.4 used as the electrolyte. During the CV measurement, the potential/voltage at the working electrode is controlled against the reference electrode. A controlling potential is also applied across the working electrode and the counter electrodes, producing an excitation signal. The excitation signal is varied linearly with time, carrying a forward scan and a backward scan from a range of potential to complete a cycle. The completed cycle can be used to form a plot called the cyclic voltammogram, which represents the current at the working electrode against the applied excitation potential [789].

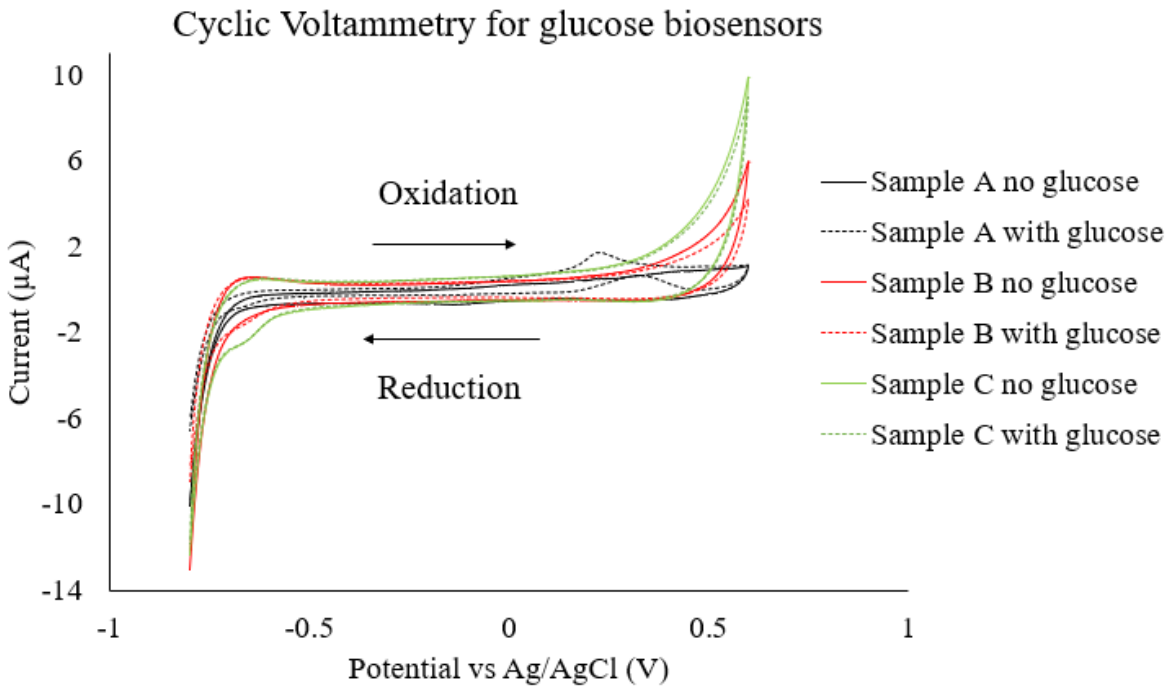

Figure 9.13: Cyclic voltammograms of the glucose biosensors.

The presence of glucose oxidase (GOx) on the surfaces of the sensors can be verified through the detection of the redox peak via cyclic voltammetry. Figure 9.13 shows the cyclic voltammograms of three glucose biosensors samples which were immobilised with GOx. As the glucose biosensor acts as the working electrode, it is an oxidant and an anodic current is produced during oxidation. This is the forward scan on the

voltammograms and is called the anodic process. The scan direction is then switched to a reverse direction, producing a cathodic process as reduction occurs. Sample A was made of only a gold layer immobilised with GOx plus an additional Nafion layer for protection. There wasn't much of an anodic current peak recorded. Sample B was made of gold/MoS_2/gold layers immobilised with GOx and protected with a Nafion layer. Sample C was the same composition as sample B but without the Nafion layer. This was to compare the effectiveness of Nafion as a protective layer for enzyme-based sensors. Sample C has a higher oxidation peak than sample B at the anodic process. The anodic currents start to decrease as the scanning potential was reversed. The peak reduction current of the sensors was around -600 mV as shown in Figure 9.13. The values of peak reduction currents for all samples were displayed in Table 9.4. Both sample B and C showed an increase in the reduction peak current compared to sample A. This showed the presence of MoS_2 improved the redox peak current, which would improve the performance of the electrochemical reaction of the sensors. This also showed that the presence of MoS_2 can improve the electrocatalytic activity towards the oxidation of glucose as the immobilised GOx could electrocatalyse the reduction of the dissolved oxygen, causing an increase in the reduction peak current.

The presence of Nafion can act as a perm-selective outer membrane and it can be used to improve the performance of glucose sensing [790]. Nafion can also reduce the interference from other physiological chemicals. GOx can leach off the sensor without Nafion, which can reduce the sensitivity of the sensor [791]. Upon addition of 1mM glucose, the reduction peak current decreased, which showed the sensors can effectively detect the presence of glucose. This is because the addition of glucose restrained the electrocatalytic reaction and led to the decrease of the reduction current.

The presence of O_2 can be a natural mediator for the catalytic reaction between GOx and glucose. GOx glucose biosensor can catalyse the electron transfer from glucose to oxygen, which is accompanied by the production of gluconolactone and hydrogen peroxide. The biosensors immobilised with GOx detects H_2O_2 concentration which is obtained from the GOx enzymatic reaction with glucose. The enzymatic and electrochemical reactions of the biosensors were demonstrated as the following equations [743,792]:

$$GOx(FAD) + glucose \rightarrow GOx(FADH_2) + gluconolactone\ (enzymatic)\ (Equation\ 9.5)$$

$$GOx(FADH_2) + O_2 \rightarrow GOx(FAD) + H_2O_2\ (enzymatic)\ (Equation\ 9.6)$$

$$GOx(FADH_2) \rightarrow GOx(FAD) + 2e + 2H^+\ (electrochemical)\ (Equation\ 9.7)$$

$$GOx(FAD) + 2e + 2H^+ \rightarrow GOx(FADH_2)\ (electrochemical)\ (Equation\ 9.8)$$

where FAD represents flavine adenine dinucleotide (FAD) cofactors, which are found in GOx, GOx(FAD) represents the oxidised form of GOx and GOx($FADH_2$) represents the reduced form of GOx [793]. GOx(FAD) accepts an electron and is reduced to GOx($FADH_2$). GOx($FADH_2$) is oxidised by oxygen in which oxygen is then reduced to hydrogen peroxide (H_2O_2).

Table 9.4: Reduction peak currents of glucose oxidase on the glucose biosensors during cyclic voltammetry.

Sample no.	**Peak current at reduction (μA)**	
	No glucose	**With glucose**
Sample A	10.03	6.53
Sample B	13.00	8.94
Sample C	12.32	11.82

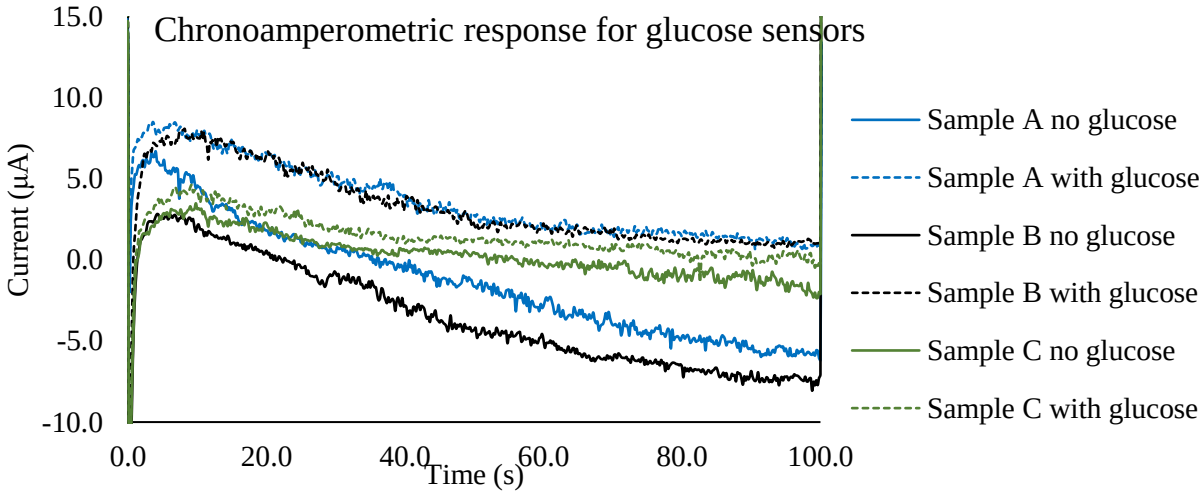

Figure 9.14: Amperometeric response of glucose biosensors upon addition of 1mM glucose solution to the electrolyte.

Amperometry electrochemical measurement measures the electric current of the glucose biosensor over time at a constant electric potential and can be used to detect the glucose sensing performance of the sensors [794]. The amperometric response curves were

presented as current vs time of the biosensors. The amperometry measurements were obtained for the glucose biosensors without glucose and with the addition of 1mM glucose. The chronoamperometric response curves were shown in Figure 9.14. The results can confirm the glucose-sensing abilities of all three samples as the current in all three biosensors increased upon addition of glucose. The magnitude of current increased in sample B is the largest among the three, which could indicate that the sensors are the most sensitive. This could be attributed to the additional MoS_2 layer when compared to sample A. However, the increase in current in sample C was very small upon the addition of glucose. Sample C is without Nafion and this showed the effectiveness of Nafion as a protective layer. As sample C was immersed into the electrolyte for testing, it is possible that some of the enzyme GOx might have leached during the redox reactions. Nevertheless. The fabricated glucose biosensors have shown stability and glucose sensing abilities.

9.5 Conclusion

A simple enzymatic flexile glucose biosensor has been fabricated using a simple thin-film fabrication technique. The surface of the glucose biosensor is made of three thin layers of materials, gold, MoS_2, and gold. The thin layers of sensing materials ensured the flexibility of the sensor. The biosensor was functionalised with enzyme GOx for glucose sensing due to the stability and availability of GOx. The glucose sensors utilised the concept of electrochemistry where glucose is oxidised by the enzyme GOx for glucose measurement. Therefore, the electrons produced on the biosensors were measured by utilising techniques of voltammetry and amperometry. The deposition technique of gold and MoS_2 layers to form the sensing electrode is an easy and practical approach. The glucose biosensor can benefit from the synergistic combination of gold and MoS_2 as the glucose sensor with MoS_2 showed an improved performance of when compared to a pure gold glucose sensor. This is because the excellent electrical properties of 2D MoS_2 produce faster direct electron transfer on the surface of the biosensor. The effect of a Nafion protective layer was also investigated and the results showed that the biosensors with Nafion showed better performance. This is because Nafion can act as a permselective membrane that could prevent any potential interferences from other compounds in the solution [795,796]. Although enzymatic glucose sensors are highly sensitive, the lifetime of these sensors is limited by decreasing enzymatic activity with time. This lifespan is typically one to two weeks. The biosensors here are based on the adsorption of protein,

hence the performance is highly dependent on the amount of immobilised enzymes on the surface of the sensors. The sensitivity is often directly proportional to the enzyme surface density, hence an increase in enzyme could possibly improve the sensitivity of the biosensor [797]. Apart from that, the magnitude of the measured current of the biosensors can change at different glucose concentrations. However, this has not been investigated here and could be useful to determine the sensitivity of the sensor in detecting different glucose levels. Other parameters such as pH and temperature may affect the biosensor response. This is because enzymatic biosensors can be highly sensitive to the surrounding environmental factors which may limit their sensing performance. Although enzymatic glucose sensors are highly sensitive but the lifetime of these sensors is limited by decreasing enzymatic activity with time, this lifespan is typically one to two weeks. The flexibility of the sensors allows it to be used as a wearable device that can conform to the shape of the skin.

Chapter 10 : Conclusions and future work

10.1 Summary of key findings

The research work in this thesis can be split into two different aspects. The first part focused on the development of biocompatible polymeric compositions which are suitable to be made into 3D printable filaments. The developed polymeric compositions were developed using biocompatible and pharmaceutical grade materials. The different polymeric materials were mixed together using the hot-melt extruder technique to achieve enhanced physicochemical properties as well as to produce 3D printable filaments. These polymeric compositions can also be used for drug loading and can be modified to achieve different drug release patterns for patients.

Firstly, a study on improving the physicochemical properties of a widely recognised biocompatible polymer, polylactic acid (PLA), was carried out. PLA is a hydrophobic thermoplastic polymer which has been widely used in food packaging and also as filaments for 3D printing. However, it exhibits poor flexibility and ductility due to its semicrystalline nature. The properties of PLA are required to be enhanced to improve its usability for a wide range of biomedical applications. In this study, polyethylene glycol (PEG) was mixed with PLA to enhance the properties of pure PLA. PEG is often found in pharmaceutical products as an excipient and can act as a plasticiser when mixed with other polymers. The role of a plasticiser can be to increase flexibility and reduce the hardness of a polymeric material. The effect of different PEG grades on PLA was investigated by mixing PEG with PLA using the solvent casting method. The study showed that PEG showed excellent compatibility with PLA as the PEG/PLA mixture did not show any changes in the chemical interactions between the two polymers. The presence of PEG has caused a reduction in the glass transition temperature and the melting temperature of the PEG/PLA mixture. The lower molecular weights PEGs seem to have a more evidence plasticising effect in the blend. This could be due to the smaller molecular chains of PEG which allows an easier interaction within the intermolecular spaces of PLA. Nevertheless, PEG is an effective plasticiser when blended with PLA.

A study to produce biocompatible PEG/PLA filaments then follow. A benchtop FilaFab filament extruder was used to produce the filaments that can be used for 3D printing. PEG 6000 was mixed with PLA to form PEG/PLA filaments. PEG 6000 exists in solid powder

form and PLA exists as solid pellets at room temperature. Due to the difficulty in griding the PLA pellets into powder form, the large difference in size between the PLA and PEG can prevent a homogeneous mixing when being fed into a single-screw filament extruder. This is because the large pitch on the screw can cause segregation between the materials instead of mixing them together. Therefore, a simple coating process was carried out by first dissolving PEG in water, then coating the PEG solution onto the surface of PLA pellets. The coated PLA pellets were allowed to dry and to solidify the PEG on the surface of the pellets before processing. Three different concentrations of PEG/PLA blends (10%, 20%, 30% w/w PEG/PLA) were produced into filaments. The characterisation studies showed that the higher the concentration of PEG, the more evident the plasticising effect. The filament with 30% PEG showed the highest thermal degradation temperature and highest elongation strain. The filaments were also tested for their printability by printing a cylindrical-shaped object. The printing temperature of the PEG/PLA filaments were slightly lower than the pure PLA and commercial PLA filaments. The print quality was also comparable to the commercial filaments. Although the single-screw extrusion can produce filaments that can be used for 3D printing, the mixing efficiency may not be the best. This is because the single-screw extrusion often does not produce homogeneous mixing when the mixing of material is involved in the extrusion process as the single-screw was not capable to provide intimate shear mixing between materials.

To improve the mixing efficiency of the polymeric mixture when producing filament compositions, the use of a twin-screw extruder was investigated. The twin-screw extruder provides a more intimate mixing between different materials due to the twin-screw configuration. It also allows more control of the temperature and speed of the extrusion by the user. The same PEG/PLA blends were extruded into filaments using the twin-screw extruder. However, the preparation work for the PEG/PLA mixture was slightly different due to the difference in the screw size and feeding zone of the extruder. The twin-screw extruder used was designed to process powder materials. Therefore, the feeding zone is very close to the screws which did not allow enough space for the PLA pellets to be conveyed down the extruder. The PEG/PLA blends were first processed into films using the solvent casting method. The solvent cast films were then mechanically ground into finer particles that can be fed into the twin-screw extruder. The characterisation studies on the twin-screw extruded PEG/PLA filaments showed that the plasticising effect of PEG was more evident when compared to the single-screw extruded

PEG/PLA filaments. As expected, the presence of PEG has lowered the glass transition temperature and melting temperature of the PEG/PLA blends. The mechanical test carried out showed that the elongation ability of the PEG/PLA filaments were at least 5 times better than the pure PLA filaments and 50 times better than a commercially available filament. However, it was noticed that as the concentration of PEG increases, the plasticising effect did not increase. There seemed to be a slight decrease in the plasticising effect as the PEG concentration increase which could be caused by a saturation of PEG in the polymer matrix. When PEG in PLA reaches its saturation point, the PEG/PLA blend may become brittle. This is shown by the increase in crystallinity of the PEG/PLA blend and the slight decrease in strength of the filaments. However, the strength of the twin-screw extruded filaments was still more superior to the single-screw extruded filaments, pure PLA filaments and the commercially available filament.

Due to the excellent mixing efficiency of twin-screw extrusion, it was used to develop some drug-loaded filaments that can be used to 3D print drug delivery devices with adjustable release systems. The materials used to produce the drug-loaded filaments were common pharmaceutical grade polymers but were not conventional materials used to produce commercially available filaments. The filaments were composed of HPC, Eudragit® RL PO, and PEG. The drug loaded onto the filament was theophylline, which is a poorly soluble drug. The effect of changing the percentage of HPC and Eudragit on theophylline release was being investigated. The drug release profiles were obtained by carried out *in-vitro* dissolution studies on the 3D printed tablets. The results showed that the higher the percentage of Eudragit, the more sustained the release of theophylline. The Korsmeyer-Peppas model may be the most appropriate model to describe the drug release kinetics of the 3D printed tablets. The cell studies carried out on the materials and tablets also confirmed that the 3D printed tablets did not induce any toxicity to living cells.

Furthermore, an attempt to sustain the release of readily soluble metformin in the composition with high Eudragit concentration was investigated. A completely different composition which contained only PCL and PEG was also loaded with metformin for comparison. The PCL-based filaments were more successful at sustaining the release of PCL. PCL filaments also offer the advantage of being able to be printed at a temperature of around 68 °C. This would be ideal for pharmaceutical applications when dealing with thermally sensitive materials.

The second part focused on the fabrication of flexible sensors for biomedical applications. Two types of sensors were fabricated: temperature sensor and glucose biosensor. The aim was to utilise simple and cost-effective fabrication technique to produce flexible sensors with good stability and reliability. Two fabrication techniques were used to produce RTD temperature sensors. The two techniques were FDM 3D printing and a thin-film fabrication technique called the lift-off process. FDM 3D printing is now an established simple and low-cost fabrication technique. The recent developments of conductive thermoplastic filaments open up the possibility of using FDM 3D printing for electronic applications. The lift-off technique involves several simple steps such as deposition of gold on a substrate, patterning of sensors using UV light, and removing the unwanted structures using acetone. Both techniques were simple and cost-effective for the fabrication of flexible temperature sensors. The 3D printed sensors were printed with two different conductive PLA filaments: carbon black PLA and graphene PLA. The 3D printed graphene PLA showed better electrical conductivity than the carbon black PLA. However, the carbon black PLA temperature sensors showed better linearity and sensitivity for temperature sensing. The carbon black PLA temperature sensors also exhibit better flexibility and stability as shown in the bending test and temperature cyclic test. On the other hand, the thin-film temperature sensors were much smaller in size and more delicate due to the different fabrication technique. The thin-film sensors also showed excellent stability, linearity and flexibility. Both the 3D printed sensors and thin-film temperature sensors are easily transferable to other substrates. The only disadvantage of the 3D printed sensors was its size is limited due to the resolution of FDM 3D printing at 0.1 mm. This means that the 3D printed sensors cannot have a thickness of below 0.1 mm and is difficult to miniaturise.

A similar thin-film fabrication technique was used to produce a glucose biosensor. However, the glucose biosensor was produced only via deposition of materials without the need for the solvent removal of material. The glucose biosensor contained gold and MoS_2 as the conductive electrode. The performance of the glucose sensing containing MoS_2 and without MoS_2 was compared. The results showed that the presence of MoS_2 can enhance electron transfer during glucose oxidation. The enhancement of electron transfer help improves the sensitivity of the sensor.

In summary, regarding the aim and objectives set out in Chapter 2, the following have been achieved and delivered.

- Physicochemical properties of pure PLA can be enhanced by blending it with plasticisers such as PEG
- Twin-screw extrusion is much preferred than single-screw extrusion especially when mixing of materials is required
- Coupling twin-screw extrusion and FDM 3D printing is an effective method to produce personalised drug delivery systems
- PCL blended with PEG can be used for drug loading and the composition can achieve sustained-release systems. The printing temperature of PCL-based filaments was much lower.
- FDM 3D printing can be used to produce flexible and transferable RTD temperature sensors
- Thin-film fabrication technique is a cost-effective technique to produce high quality RTD temperature sensors and glucose biosensors
- The use of MoS_2 can improve electron transfer of the sensor, which could improve sensitivity
- Findings and results obtained have been reported in peer-reviewed literature and at scientific conferences

10.2 Suggestions for future work

The development of smart and personalised medical devices is highly beneficial to our society as this can improve treatment efficacy and reduce on-going pressure on our healthcare systems. As we now live in a world with a wide range of smart technologies around us, having reliable smart medical devices for continuous health monitoring and diagnostic can greatly improve our healthcare systems and quality of life. With the help of advanced healthcare technology, healthcare resources can be better utilised and the ever-increasing pressure on healthcare services can be relieved. This is particularly beneficial in the long term when the life expectancy of our society is constantly increasing. However, one of the main issues that have prevented the wide usage of such medical technology is that most of these advanced technologies are not affordable to the members of the public. These technologies are often too expensive and are only affordable for rich patients. This phenomenon is not encouraged as it can cause further division and inequality in our society. Everyone should have equal opportunity to access the best healthcare available regardless of their social status.

As proposed, the personalisation of drug delivery systems can be easily achievable when integrating the HME with the FDM 3D printing technology. This could be the most cost-effective method as it allows the fabrication of personalised medicines in-house. As 3D printing is not suitable for mass production, it is also ideal for personalised medicines as the personalised medicines are typically required in a small amount for specific patients only. Apart from the fabrication of personalised tablets with customised drug release, 3D printing can also be used to produce different drug delivery devices such as transdermal patches [452,798], microneedles [799,800], orodispersible films [176] and various implants [178,179,801]. Therefore, 3D printing has proven to have a great potential for a wide range of biomedical applications. More studies are still required to prove the reliability and feasibility of 3D printing in producing various drug delivery systems that are safe in order to promote the translation of laboratory research to clinical applications. The developed glucose biosensor in this work is enzyme based. Enzymatic glucose biosensors have been well established and have the advantages of simplicity, efficiency, high sensitivity and selectivity. However, enzymatic glucose biosensors often suffer from high cost and instability [783]. Enzymes are often sensitive to temperature, humidity, and pH. Hence, storing and transporting enzymes can add to the cost. Enzymes also degrade over time and hence the sensors also have a limited lifetime. Therefore, the study of developing non-enzymatic glucose biosensor can be highly desirable. One approach to produce enzyme-free sensors involves the use of nanostructured material modified electrodes as electrochemical sensors for direct oxidation of glucose. For example, a non-enzymatic glucose biosensor was developed by Anderson *et al.* by nucleating colloidal silver nanoparticles on MoS_2 [802]. Another study by Huang *et al.* showed copper nanoparticles can be decorated onto MoS_2 nanosheets and has showen electrocatalytic activity towards glucose oxidation [803]. An alternative for the fabrication of an enzyme-free glucose biosensor involves the use of synthetic receptors [804]. For examples, a synthetic peptide can be designed as a glucose receptor to mimic the glucose binding sites for glucose sensing [805]. The sensors fabricated using peptides offer significant advantages over proteins as peptides can be immobilized at high density but still preserve their stability and specificity of binding [806–809].

A minimally or non-invasive monitoring approach can also be explored for ease of use and patient comfort. Examples of body fluids that can be measured non-invasively are sweat and interstitial fluid. These fluids contain metabolites (such as glucose, lactate and

alcohol), electrolytes, trace elements and some large molecules (such as proteins or cytokines) which could provide useful information for physiological health status and disease diagnosis and management. Interstitial fluid is particularly attractive as the concentration of the analytes in the interstitial fluid correlates well with the blood. This is because the components in the interstitial fluid diffuse directly from the capillary endothelium. On the other hand, sweat can be easily obtained as it is produced naturally on the skin. Even when there is limited sweat produced due to inactivity, an iontophoresis technique can be used to extract sweat through the surface of the skin in a non-invasive manner (Figure 10.1). The iontophoresis process applies a mild current across the skin to induce ion migration between the two electrodes on the wearable biosensor and can be accomplished at rest. It transports the molecules without harming the skin surface or contacting the blood.

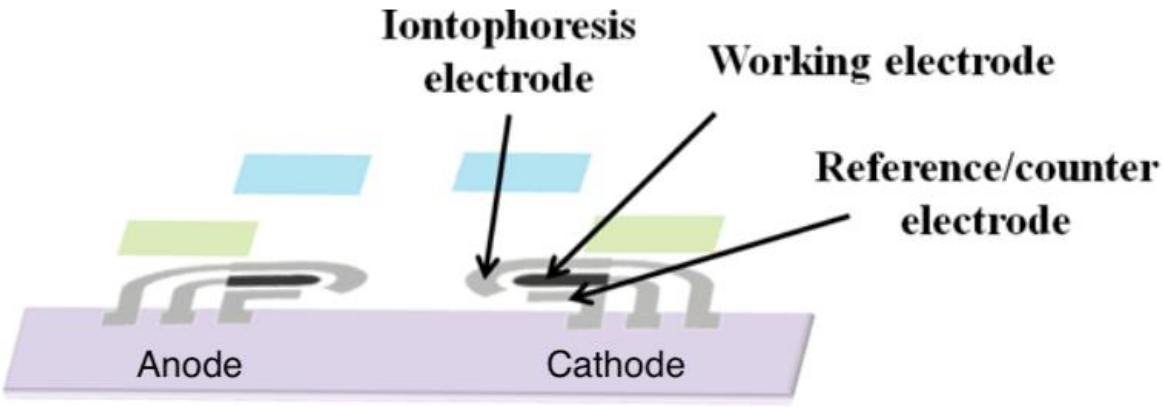

Figure 10.1: Schematic diagram of an iontophoretic-based biosensor. The working electrode will be made of functionalised MoS_2 for biosensing application (adapted with permission from reference [346]).

Similarly, reverse iontophoresis can be used to extract interstitial fluids, where the application of a low current induces a flux of positively charged ions towards the negatively charged skin surface, and also causes an electro-osmotic flow from anode to cathode. The flow results in the movement of neutral molecules, such as glucose, toward the cathode.

Another interesting exploration is related to the study of MoS_2 as a material for biosensor. MoS_2 is expected to possess similar advantages as graphene and graphene derivatives as it shares the materials properties of graphene. Many research and work have proven that MoS_2 is a promising material and exhibit significant potential for the fabrication of next-

generation low-cost biosensors with high biosensing capabilities. Studies have shown that MoS_2-based biosensors can be used for sensing several important parameters such as pH [810], temperature [811], oxygen level [812], antigen level [432] and many more [813]. Due to the mechanical properties of MoS_2, it is also highly suitable to be used a material for the flexible sensor. As MoS_2 can be effectively processed into solution, the MoS_2 solution can be adjusted to exhibit the properties of functional inks that can be used for printing applications. For example, inkjet printing or aerosol-jet printing can print in very high resolution which could be ideal for the fabrication of miniaturised sensors.

The development of smart pills for better drug delivery can also be explored. This can possibly be achieved by integrating the 3D printed personalised drug delivery systems with the fabricated flexible. The integration can potentially be achieved in a single fabrication process by utilising the FDM 3D printing technique. Some 3D printers can have more than one printing nozzle, which means the printer can print using at least two different materials in a single print without being disrupted. Some studies have proven that printers with multiple print heads can be used for the printing of novel drug delivery devices such as polypills [814–816]. The work here showed that it is possible to print reliable temperature sensors using conductive filaments. Hence, the desired object can be creatively designed to print the drug delivery device and integrate the sensor onto the printed drug delivery device in a single print. Such smart drug delivery systems can be highly beneficial to detect the effects of the drug.

A smart drug delivery system will be suitable for a wide range of applications and enable therapies not possible with conventional means. As an example, a smart drug delivery system for diabetic care can be achieved by integrating the wearable glucose biosensor with a transdermal drug delivery system. The biosensor can measure the fluctuation of the glucose of the patient, as well as the pH and temperature non-invasively. When the glucose level is too high, insulin or other anti-diabetic drugs will be released through a polymeric microneedle to regulate the glucose level. The rate of drug release and the dose will be controlled through a micropump in the smart system. However, the design of such systems is highly complex as it involves the use of microelectronics and the selection of suitable biomaterials. Computer modelling and testing will be required to simulate the environment, response and drug release of the smart pill. Computer simulation will help decide several important parameters when designing the smart pill such as the pressure required of drug release, drug flow rate, desired drug volume etc. A novel self-powering

method for this multifunctional wearable device such as using piezoelectric could also be explored. A self-powering device will obviate the need for power supply or battery which could miniaturise the device for better patient comfort. There is also a need for wireless communication of the device to send its recorded data to be displayed on a user device. This novel smart device would also require unique and state-of-the-art fabrication techniques.

The development of a state-of-the-art smart medical device is a highly complex task. This is considered cutting-edge research that requires experts from different fields to ensure the success of the project. To this day, there is still no such smart integrated medical device that can act as a continuous health monitoring system as well as a smart drug delivery system available on the market.

Appendix: List of publications and conference proceedings

Tan DK., Maniruzzaman M., and Nokhodchi A., Advanced pharmaceutical applications of hot-melt extrusion coupled with fused deposition modelling (FDM) 3D printing for personalised drug delivery," Pharmaceutics, vol. 10, no. 4, 2018 (Special Issue Best Paper Award)

Tan DK., Maniruzzaman M., and Nokhodchi A., Development and optimisation of novel polymeric compositions for sustained release theophylline caplets (PrintCap) via FDM 3D printing," Polymers, vol. 12, no. 1, 2019

Tan DK., Nokhodchi A., and Maniruzzaman M., 3D and 4D printing technologies: Innovative process engineering and smart additive manufacturing," in 3D and 4D Printing in Biomedical Applications: Process Engineering and Additive Manufacturing, ch. 2, pp. 25-52, John Wiley & Sons, Ltd, 2019

Wallis M., Al-Dulimi Z., **Tan DK.**, Maniruzzaman M., and Nokhodchi A., 3D printing for enhanced drug delivery: current state-of-the-art and challenges," Drug Development and Industrial Pharmacy, vol. 46, no. 9, pp. 1385-1401, 2020

Tan DK., Davis D., Miller D., Williams III R., and Nokhodchi A., Innovations in thermal processing: Hot-melt extrusion and KinetiSol® dispersing," AAPS PharmSciTech, 2020

Tan DK., Münzenrieder N., Maniruzzaman M., and Nokhodchi A., A low-cost method to prepare biocompatible filaments with enhanced physico-mechanical properties for FDM 3D printing," Current Drug Delivery, vol. 17, 2020

Al-Dulimi Z., Wallis M., **Tan DK.**, Maniruzzaman M., and Nokhodchi A., 3D printing technology as innovative solutions for biomedical applications," Drug Discovery Today, vol: 26, 2020

Conference Proceedings

Deck K Tan, Niko Münzenrieder, Mohammed Maniruzzaman, Ali Nokhodchi. "3D printing of smart medical implants for biomedical applications", C3Bio conference on Biosensors, Bioelectronics and Biodevices Sept 2019 & C3Bio/IBST joint event, Bath UK

Deck K Tan. "Coupling Hot-Melt Extrusion with Fused Deposition Modelling 3D Printing for the Fabrication of Pharmaceutical Tablets", University of Sussex Chemistry PhD Colloquium, Sep 2020, virtual symposium

Deck K Tan, Mohammed Maniruzzaman, Ali Nokhodchi. "Development of novel polymeric compositions for 3D printing of personalised drug delivery systems and implants", 7th International Pharmaceutical Federation (FIP) Pharmaceutical science World Congress PSWC Oct 2020, virtual conference

Deck K Tan, Niko Münzenrieder, Ali Nokhodchi. "Fabrication of Flexible and Transferable RTDs via Fused Deposition Modelling 3D Printing", IEEE International Conference on Flexible, Printable Sensors and Systems, June 2021, virtual conference

Bibliography

1. Vaz VM, Kumar L. 3D Printing as a Promising Tool in Personalized Medicine. AAPS PharmSciTech. 2021;22:49.

2. Al-Dulimi Z, Wallis M, Tan DK, Maniruzzaman M, Nokhodchi A. 3D printing technology as innovative solutions for biomedical applications. Drug Discov Today. Elsevier Ltd 2021;26:360–83.

3. Ponmozhi J, Frias C, Marques T, Frazão O. Smart sensors/actuators for biomedical applications: Review. Measurement. 2012;45:1675–88.

4. Goyanes A, Det-Amornrat U, Wang J, Basit AW, Gaisford S. 3D scanning and 3D printing as innovative technologies for fabricating personalized topical drug delivery systems. J Control Release. Elsevier B.V. 2016;234:41–8.

5. Ventola CL. Medical Applications for 3D Printing: Current and Projected Uses. P T. 2014;39:704–11.

6. Hoffman AN. 3D Systems: “Stuck In The Middle” of the 3D Printer Boom? Rotterdam Sch Manag Erasmus Univ SAGE Knowl. Rotterdam School of Management, Erasmus University 2014;1–9.

7. Siddique THM, Sami I, Nisar MZ, Naeem M, Karim A, Usman M. Low Cost 3D Printing for Rapid Prototyping and its Application. In: 2019 Second International Conference on Latest trends in Electrical Engineering and Computing Technologies (INTELLECT). IEEE 2019. p. 1–5.

8. Lemu HG, Kurtovic S. 3D Printing for Rapid Manufacturing: Study of Dimensional and Geometrical Accuracy. In: Frick J, Laugen BT, editors. IFIP International Conference on Advances in Production Management Systems. Springer Berlin Heidelberg 2012. p. 470–9.

9. Manda VR, Kampurath V, Msrk C. 3D printing and its effect on outsourcing: A study of the Indian aircraft industry. J Aerosp Technol Manag. 2018;10:1–22.

10. Diment LE, Thompson MS, Bergmann JHM. Clinical efficacy and effectiveness of 3D printing: a systematic review. BMJ Open. 2017;7:e016891.

11. Tofail SAM, Koumoulos EP, Bandyopadhyay A, Bose S, O'Donoghue L, Charitidis C. Additive manufacturing: scientific and technological challenges, market uptake and opportunities. Mater Today. 2018;21:22–37.

12. Yan Q, Dong H, Su J, Han J, Song B, Wei Q, et al. A Review of 3D Printing Technology for Medical Applications. Engineering. Elsevier 2018;4:729–42.

13. Chung P, Heller JA, Etemadi M, Ottoson PE, Liu JA, Rand L, et al. Rapid and Low-cost Prototyping of Medical Devices Using 3D Printed Molds for Liquid Injection Molding. J Vis Exp. 2014;88:517453791–51745.

14. Pham DT, Gault RS. A comparison of rapid prototyping technologies. Int J Mach Tools Manuf. 1998;38:1257–87.

15. Fisher T. Welcome to the Third Industrial Revolution: The Mass-Customisation of Architecture, Practice and Education. Archit Des. 2015;85:40–5.

16. Gosselin C, Duballet R, Roux P, Gaudillière N, Dirrenberger J, Morel P. Large-scale 3D printing of ultra-high performance concrete - a new processing route for architects and builders. Mater Des. Elsevier Ltd 2016;100:102–9.

17. Murr LE. Frontiers of 3D Printing/Additive Manufacturing: from Human Organs to Aircraft Fabrication. J Mater Sci Technol. Elsevier Ltd 2016;32:987–95.

18. Lipton JI, Cutler M, Nigl F, Cohen D, Lipson H. Additive manufacturing for the food industry. Trends Food Sci Technol. Elsevier Ltd 2015;43:114–23.

19. Končić J, Ščapec J, Miyake I, Suit R. 3D print additive technology as a form of textile material substitute in clothing design - Interdisciplinary approach in designing corsets and fashion accessories. Ind Textila. 2018;69:190–6.

20. Liaw C-Y, Guvendiren M. Current and emerging applications of 3D printing in medicine. Biofabrication. IOP Publishing 2017;9:024102.

21. Kaye R, Goldstein T, Zeltsman D, Grande DA, Smith LP. Three dimensional printing: A review on the utility within medicine and otolaryngology. Int J Pediatr Otorhinolaryngol. Elsevier Ltd 2016;89:145–8.

22. Tetsuka H, Shin SR. Materials and technical innovations in 3D printing in biomedical applications. J Mater Chem B. Royal Society of Chemistry 2020;8:2930–50.

23. Alhnan MA, Okwuosa TC, Sadia M, Wan KW, Ahmed W, Arafat B. Emergence of 3D Printed Dosage Forms: Opportunities and Challenges. Pharm Res. Pharmaceutical Research 2016;33:1817–32.

24. Bhise NS, Manoharan V, Massa S, Tamayol A, Ghaderi M, Miscuglio M, et al. A liver-on-a-chip platform with bioprinted hepatic spheroids. Biofabrication. 2016;8:014101.

25. Yang Q, Lian Q, Xu F. Perspective: Fabrication of integrated organ-on-a-chip via bioprinting. Biomicrofluidics. 2017;11:031301.

26. Lind JU, Busbee TA, Valentine AD, Pasqualini FS, Yuan H, Yadid M, et al. Instrumented cardiac microphysiological devices via multimaterial three-dimensional printing. Nat Mater. 2017;16:303–8.

27. Ma X, Liu J, Zhu W, Tang M, Lawrence N, Yu C, et al. 3D bioprinting of functional tissue models for personalized drug screening and in vitro disease modeling. Adv Drug Deliv Rev. 2018;132:235–51.

28. Thomas RC, Vu P, Modi SP, Chung PE, Landis RC, Khaing ZZ, et al. Sacrificial Crystal Templated Hyaluronic Acid Hydrogels As Biomimetic 3D Tissue Scaffolds for Nerve Tissue Regeneration. ACS Biomater Sci Eng. 2017;3:1451–9.

29. Matai I, Kaur G, Seyedsalehi A, McClinton A, Laurencin CT. Progress in 3D bioprinting technology for tissue/organ regenerative engineering. Biomaterials. 2020;226:119536.

30. Kim SH, Yeon YK, Lee JM, Chao JR, Lee YJ, Seo YB, et al. Precisely printable and biocompatible silk fibroin bioink for digital light processing 3D printing. Nat Commun. 2018;9:1620.

31. Gu Z, Fu J, Lin H, He Y. Development of 3D bioprinting: From printing methods to biomedical applications. Asian J Pharm Sci. 2020;15:529–57.

32. Ng WL, Lee JM, Zhou M, Chen Y-W, Lee K-XA, Yeong WY, et al. Vat polymerization-based bioprinting—process, materials, applications and regulatory challenges. Biofabrication. IOP Publishing 2020;12:022001.

33. Medellin A, Du W, Miao G, Zou J, Pei Z, Ma C. Vat Photopolymerization 3D Printing of Nanocomposites: A Literature Review. J Micro Nano-Manufacturing. 2019;7:031006.

34. Bagheri A, Jin J. Photopolymerization in 3D Printing. ACS Appl Polym Mater. 2019;1:593–611.

35. Sirrine JM, Zlatanic A, Meenakshisundaram V, Messman JM, Williams CB, Dvornic PR, et al. 3D Printing Amorphous Polysiloxane Terpolymers via Vat Photopolymerization. Macromol Chem Phys. 2019;220:1800425.

36. Aduba DC, Margaretta ED, Marnot AEC, Heifferon K V., Surbey WR, Chartrain NA, et al. Vat photopolymerization 3D printing of acid-cleavable PEG-methacrylate networks for biomaterial applications. Mater Today Commun. 2019;19:204–11.

37. Datsiou KC, Saleh E, Spirrett F, Goodridge R, Ashcroft I, Eustice D. Additive manufacturing of glass with laser powder bed fusion. J Am Ceram Soc. 2019;102:4410–4.

38. King WE, Anderson AT, Ferencz RM, Hodge NE, Kamath C, Khairallah SA, et al. Laser powder bed fusion additive manufacturing of metals; physics, computational, and materials challenges. Appl Phys Rev. 2015;2:041304.

39. Zavala-Arredondo M, London T, Allen M, Maccio T, Ward S, Griffiths D, et al. Use of power factor and specific point energy as design parameters in laser powder-bed-fusion (L-PBF) of AlSi10Mg alloy. Mater Des. 2019;182:108018.

40. Bhavar V, Kattire P, Patil V, Khot S, Gujar K. A review on powder bed fusion technology of metal additive manufacturing. In: 4th International conference and exhibition on Additive Manufacturing Technologies-AM-2014. 2014.

41. Vock S, Klöden B, Kirchner A, Weißgärber T, Kieback B. Powders for powder

bed fusion: a review. Prog Addit Manuf. 2019;4:383–97.

42. Santecchia E, Mengucci P, Gatto A, Bassoli E, Denti L, Rutkowski B, et al. Laser Powder Bed Fusion: tailoring the microstructure of alloys for biomedical applications. Mater Today Proc. 2019;19:24–32.

43. Yang H, Lim JC, Liu Y, Qi X, Yap YL, Dikshit V, et al. Performance evaluation of ProJet multi-material jetting 3D printer. Virtual Phys Prototyp. 2017;12:95–103.

44. Yap YL, Wang C, Sing SL, Dikshit V, Yeong WY, Wei J. Material jetting additive manufacturing: An experimental study using designed metrological benchmarks. Precis Eng. 2017;50:275–85.

45. Tsai M-J, Mei C-W, Cheng Y-L, Chen F, Hu Z-Y, Huang K-C. A study of a material jetting based color 3d printing system by using multiple piezoelectric heads. In: 2017 International Conference on Machine Learning and Cybernetics (ICMLC). IEEE 2017. p. 664–9.

46. Saijo H, Igawa K, Kanno Y, Mori Y, Kondo K, Shimizu K, et al. Maxillofacial reconstruction using custom-made artificial bones fabricated by inkjet printing technology. J Artif Organs. 2009;12:200–5.

47. Tappa K, Jammalamadaka U. Novel Biomaterials Used in Medical 3D Printing Techniques. J Funct Biomater. 2018;9:17.

48. Whyman S, Arif KM, Potgieter J. Design and development of an extrusion system for 3D printing biopolymer pellets. Int J Adv Manuf Technol. 2018;96:3417–28.

49. Gibson MA, Mykulowycz NM, Shim J, Fontana R, Schmitt P, Roberts A, et al. 3D printing metals like thermoplastics: Fused filament fabrication of metallic glasses. Mater Today. 2018;21:697–702.

50. Azad MA, Olawuni D, Kimbell G, Badruddoza AZ, Hossain S, Sultana T. Polymers for Extrusion-Based 3D Printing of Pharmaceuticals : A Holistic Materials – Process Perspective. 1–34 p.

51. Beck RCR, Chaves PS, Goyanes A, Vukosavljevic B, Buanz A, Windbergs M, et al. 3D printed tablets loaded with polymeric nanocapsules: An innovative approach

to produce customized drug delivery systems. Int J Pharm. Elsevier B.V. 2017;528:268–79.

52. Dass A, Moridi A. State of the Art in Directed Energy Deposition: From Additive Manufacturing to Materials Design. Coatings. 2019;9:418.

53. Saboori A, Aversa A, Marchese G, Biamino S, Lombardi M, Fino P. Application of Directed Energy Deposition-Based Additive Manufacturing in Repair. Appl Sci. 2019;9:3316.

54. Jinoop A, Paul C, Bindra K. Laser-assisted directed energy deposition of nickel super alloys: A review. Proc Inst Mech Eng Part L J Mater Des Appl. 2019;233:2376–400.

55. Lores A, Azurmendi N, Agote I, Zuza E. A review on recent developments in binder jetting metal additive manufacturing: materials and process characteristics. Powder Metall. 2019;62:267–96.

56. Miyanaji H, Orth M, Akbar JM, Yang L. Process development for green part printing using binder jetting additive manufacturing. Front Mech Eng. 2018;13:504–12.

57. Szymczyk-Ziółkowska P, Łabowska MB, Detyna J, Michalak I, Gruber P. A review of fabrication polymer scaffolds for biomedical applications using additive manufacturing techniques. Biocybern Biomed Eng. 2020;40:624–38.

58. Lv X, Ye F, Cheng L, Fan S, Liu Y. Binder jetting of ceramics: Powders, binders, printing parameters, equipment, and post-treatment. Ceram Int. 2019;45:12609–24.

59. RepRap Contributors. RepRap [Internet]. RepRap. 2018 Jun 22; https://reprap.org/mediawiki/index.php?title=RepRap&oldid=182586 p. 182586.

60. Goole J, Amighi K. 3D printing in pharmaceutics: A new tool for designing customized drug delivery systems. Int J Pharm. Elsevier B.V. 2016;499:376–94.

61. Robo3D. Robo R2 Quick Start Guide [Internet]. robo. 2020 May 5; https://robo3d.com/pages/r2-qsg.

62. Kim K, Park J, Suh J, Kim M, Jeong Y, Park I. 3D printing of multiaxial force sensors using carbon nanotube (CNT)/thermoplastic polyurethane (TPU) filaments. Sensors Actuators A Phys. 2017;263:493–500.

63. Pavon C, Aldas M, López-Martínez J, Ferrándiz S. New Materials for 3D-Printing Based on Polycaprolactone with Gum Rosin and Beeswax as Additives. Polymers (Basel). 2020;12:334.

64. Deshmukh K, Basheer Ahamed M, Deshmukh RR, Khadheer Pasha SK, Bhagat PR, Chidambaram K. Biopolymer Composites With High Dielectric Performance: Interface Engineering. In: Biopolymer Composites in Electronics. Elsevier 2017. p. 27–128.

65. Dizon JRC, Espera AH, Chen Q, Advincula RC. Mechanical characterization of 3D-printed polymers. Addit Manuf. Elsevier B.V. 2018;20:44–67.

66. Xiaoyong S, Liangcheng C, Honglin M, Peng G, Zhanwei B, Cheng L. Experimental analysis of high temperature PEEK materials on 3D printing test. Proc - 9th Int Conf Meas Technol Mechatronics Autom ICMTMA 2017. 2017;13–6.

67. Molitch-Hou M. 3D Printing Filaments: What's the Deal with ULTEM and PEEK? [Internet]. Engineering.com. 2018 Jun 26; https://www.engineering.com/3DPrinting/3DPrintingArticles/ArticleID/14465/3D-Printing-Filaments-Whats-the-Deal-with-ULTEM-and-PEEK.aspx.

68. INTAMSYS. INTAMSYS Launches PEEK 3D Printer [Internet]. 2018 Jun 26; https://www.intamsys.com/intamsys-launches-peek-3d-printer/.

69. Roopavath UK, Kalaskar DM. Introduction to 3D printing in medicine. In: 3D Printing in Medicine. Elsevier Ltd 2017. p. 1–20.

70. Khaled SA, Burley JC, Alexander MR, Yang J, Roberts CJ. 3D printing of five-in-one dose combination polypill with defined immediate and sustained release profiles. J Control Release. 2015;217:308–14.

71. Fu J, Yu X, Jin Y. 3D printing of vaginal rings with personalized shapes for

controlled release of progesterone. Int J Pharm. Elsevier 2018;539:75–82.

72. Rajic A, Desnica E, Palinkas I, Nedelcu D, Vulicevic LL. 3D printing technology with plastic materials for hip implant master patterns manufacturing. Mater Plast. 2019;56:882–90.

73. Hedayati SK, Behravesh AH, Hasannia S, Bagheri Saed A, Akhoundi B. 3D printed PCL scaffold reinforced with continuous biodegradable fiber yarn: A study on mechanical and cell viability properties. Polym Test. Elsevier Ltd 2020;83:106347.

74. Rajzer I, Kurowska A, Jabłoński A, Kwiatkowski R, Piekarczyk W, Hajduga MB, et al. Scaffolds modified with graphene as future implants for nasal cartilage. J Mater Sci. 2020;55:4030–42.

75. SPRITAM. Spritam (levetiracetam) Tablets for Oral Suspension [Internet]. Aprecia Pharmaceuticals. 2020 May 5; https://www.spritam.com/#/patient.

76. Scoutaris N, Ross SA, Douroumis D. 3D Printed "Starmix" Drug Loaded Dosage Forms for Paediatric Applications. Pharm Res. Pharmaceutical Research 2018;35:1–11.

77. Sadia M, Arafat B, Ahmed W, Forbes RT, Alhnan MA. Channelled tablets: An innovative approach to accelerating drug release from 3D printed tablets. J Control Release. Elsevier 2018;269:355–63.

78. Goyanes A, Buanz ABMM, Basit AW, Gaisford S. Fused-filament 3D printing (3DP) for fabrication of tablets. Int J Pharm. 2014;476:88–92.

79. Goyanes A, Robles Martinez P, Buanz A, Basit AW, Gaisford S. Effect of geometry on drug release from 3D printed tablets. Int J Pharm. Elsevier 2015;494:657–63.

80. Damon A, Clifton W, Valero-Moreno F, Nottmeier E. Orientation Planning in the Fused Deposition Modeling 3D Printing of Anatomical Spine Models. Cureus. 2020;12:1–6.

81. Waran V, Narayanan V, Karuppiah R, Pancharatnam D, Chandran H, Raman R, et

al. Injecting Realism in Surgical Training—Initial Simulation Experience With Custom 3D Models. J Surg Educ. 2014;71:193–7.

82. Luque MC, Calleja-Hortelano A, Romero PE. Use of 3D Printing in Model Manufacturing for Minor Surgery Training of General Practitioners in Primary Care. Appl Sci. 2019;9:5212.

83. Rendón-Medina MA, Hanson-Viana E, Palacios-Juarez J, Sandoval-Rodriguez JI. Application of low-cost fused deposition modeling additive manufacturing rapid anatomic models in patients with rhino-cerebral mucormycosis treated with maxillectomy. Eur J Plast Surg. European Journal of Plastic Surgery 2019;42:299–304.

84. Domínguez-Robles J, Mancinelli C, Mancuso E, García-Romero I, Gilmore BF, Casettari L, et al. 3D Printing of Drug-Loaded Thermoplastic Polyurethane Meshes: A Potential Material for Soft Tissue Reinforcement in Vaginal Surgery. Pharmaceutics. 2020;12:63.

85. Domínguez-Robles J, Martin N, Fong M, Stewart S, Irwin N, Rial-Hermida M, et al. Antioxidant PLA Composites Containing Lignin for 3D Printing Applications: A Potential Material for Healthcare Applications. Pharmaceutics. 2019;11:165.

86. Huang JJ, Ren JA, Wang GF, Li ZA, Wu XW, Ren HJ, et al. 3D-printed “fistula stent” designed for management of enterocutaneous fistula: An advanced strategy. World J Gastroenterol. 2017;23:7489–94.

87. Santerre JP, Woodhouse K, Laroche G, Labow RS. Understanding the biodegradation of polyurethanes: From classical implants to tissue engineering materials. Biomaterials. 2005;26:7457–70.

88. Kim T, Lee YG. Shape transformable bifurcated stents. Sci Rep. Springer US 2018;8:1–9.

89. Rahman Z, Barakh Ali SF, Ozkan T, Charoo NA, Reddy IK, Khan MA. Additive Manufacturing with 3D Printing: Progress from Bench to Bedside. AAPS J. The AAPS Journal 2018;20:101.

90. Khodaei M, Amini K, Valanezhad A. Fabrication and Characterization of Poly Lactic Acid Scaffolds by Fused Deposition Modeling for Bone Tissue Engineering. J Wuhan Univ Technol Mater Sci Ed. 2020;35:248–51.

91. Monshi M, Esmaeili S, Kolooshani A, Moghadas BK, Saber-Samandari S. A novel three-dimensional printing of electroconductive scaffolds for bone cancer therapy application. Nanomed. 2020;7:138–48.

92. Shin SR, Li Y-C, Jang HL, Khoshakhlagh P, Akbari M, Nasajpour A, et al. Graphene-based materials for tissue engineering. Adv Drug Deliv Rev. 2016;105:255–74.

93. Pang L, Dai C, Bi L, Guo Z, Fan J. Biosafety and Antibacterial Ability of Graphene and Graphene Oxide In Vitro and In Vivo. Nanoscale Res Lett. 2017;12:564.

94. Zou X, Zhang L, Wang Z, Luo Y. Mechanisms of the Antimicrobial Activities of Graphene Materials. J Am Chem Soc. 2016;138:2064–77.

95. BBC. Engineering enthusiasts 3D print thousands of face shields [Internet]. BBC News. https://www.bbc.co.uk/news/av/uk-scotland-52294799/engineering-enthusiasts-3d-print-thousands-of-face-shields.

96. Carlota V. How is the 3D printing community responding to COVID-19? [Internet]. 3dnatives. 2020 May 5; https://www.3dnatives.com/en/3d-printed-masks-and-ventilators-200320204/.

97. Carlota V. Medically approved emergency 3D printed ventilator goes into production [Internet]. 3dnatives. 2020 May 5; https://www.3dnatives.com/en/3d-printed-respirator-230320205/.

98. Zhang J, Feng X, Patil H, Tiwari R V., Repka MA. Coupling 3D printing with hot-melt extrusion to produce controlled-release tablets. Int J Pharm. 2017;519:186–97.

99. Patil H, Tiwari R V., Repka MA. Hot-Melt Extrusion: from Theory to Application in Pharmaceutical Formulation. AAPS PharmSciTech. 2016;17:20–42.

100. Crowley MM, Zhang F, Repka MA, Thumma S, Upadhye SB, Kumar Battu S, et

al. Pharmaceutical Applications of Hot-Melt Extrusion: Part I. Drug Dev Ind Pharm. 2007;33:909–26.

101. Martin C. Melt Extrusion [Internet]. Repka MA, Langley N, DiNunzio J, editors. Melt Extrusion: Materials, Technology and Drug Product Design. Springer New York 2013. 47–79 p. (AAPS Advances in the Pharmaceutical Sciences Series; vol. 9).

102. Gürses A, Açıkyıldız M, Güneş K, Gürses MS. Dyes and Pigments: Their Structure and Properties. In: Gürses A, Açıkyıldız M, Güneş K, Gürses MS, editors. Dyes and Pigments. Springer International Publishing 2016. p. 13–29.

103. Kumar M, Bhatia R, Rawal RK. Applications of various analytical techniques in quality control of pharmaceutical excipients. J Pharm Biomed Anal. Elsevier B.V. 2018;157:122–36.

104. Li M, Gogos CG, Ioannidis N. Improving the API dissolution rate during pharmaceutical hot-melt extrusion I: Effect of the API particle size, and the co-rotating, twin-screw extruder screw configuration on the API dissolution rate. Int J Pharm. Elsevier B.V. 2015;478:103–12.

105. Particle Sciences. Hot Melt Extrusion. Tech Br 2011 vol 3. 2011;3:2.

106. Feng X, Zhang F. Twin-screw extrusion of sustained-release oral dosage forms and medical implants. Drug Deliv Transl Res. Drug Delivery and Translational Research 2017;8:1694–713.

107. Ohtsubo K, Suzuki K, Yasui Y, Kasumi T. Bio-functional components in the processed pre-germinated brown rice by a twin-screw extruder. J Food Compos Anal. 2005;18:303–16.

108. Wiedmann W, Strobel E. Compounding of Thermoplastic Starch with Twin-screw Extruders. Starch - Stärke. 1991;43:138–45.

109. Chokshi R, Hossein Z. Hot-Melt Extrusion Technique: A Review. Iran J Pharm Res. 2004;3:3–16.

110. Breitenbach J. Melt extrusion: from process to drug delivery technology. Eur J

Pharm Biopharm. 2002;54:107–17.

111. Montiel R, Patiño-Herrera R, Gonzalez-Calderón JA, Pérez E. Novel Twin Screw Co-Extrusion-Electrospinning Apparatus. Am J Biomed Eng. 2016;6:19–24.

112. Patel A, Sahu D, Dashora A, Garg R, Agraval P, Patel PP, et al. A Review of Hot Melt Extrusion Technique. Int J Innov Res Sci Eng Technol. 2013;2:2194–8.

113. Kallakunta VR, Sarabu S, Bandari S, Tiwari R, Patil H, Repka MA. An update on the contribution of hot-melt extrusion technology to novel drug delivery in the twenty-first century: part I. Expert Opin Drug Deliv. Taylor & Francis 2019;16:539–50.

114. Maniruzzaman M, Boateng JS, Snowden MJ, Douroumis D. A Review of Hot-Melt Extrusion: Process Technology to Pharmaceutical Products. ISRN Pharm. 2012;2012:1–9.

115. Genina N, Hadi B, Löbmann K. Hot Melt Extrusion as Solvent-Free Technique for a Continuous Manufacturing of Drug-Loaded Mesoporous Silica. J Pharm Sci. 2018;107:149–55.

116. Sarabu S, Bandari S, Kallakunta VR, Tiwari R, Patil H, Repka MA. An update on the contribution of hot-melt extrusion technology to novel drug delivery in the twenty-first century: part II. Expert Opin Drug Deliv. Taylor & Francis 2019;16:567–82.

117. Hitzer P, Bäuerle T, Drieschner T, Ostertag E, Paulsen K, van Lishaut H, et al. Process analytical techniques for hot-melt extrusion and their application to amorphous solid dispersions. Anal Bioanal Chem. Analytical and Bioanalytical Chemistry 2017;409:4321–33.

118. Repka MA, Majumdar S, Kumar Battu S, Srirangam R, Upadhye SB. Applications of hot-melt extrusion for drug delivery. Expert Opin Drug Deliv. 2008;5:1357–76.

119. Schlindwein W, Bezerra M, Almeida J, Berghaus A, Owen M, Muirhead G. In-Line UV-Vis Spectroscopy as a Fast-Working Process Analytical Technology (PAT) during Early Phase Product Development Using Hot Melt Extrusion

(HME). Pharmaceutics. 2018;10:166.

120. Repka MA, Battu SK, Upadhye SB, Thumma S, Crowley MM, Zhang F, et al. Pharmaceutical applications of hot-melt extrusion: Part II. Drug Dev Ind Pharm. 2007;33:1043–57.

121. Jani R, Patel D. Hot melt extrusion: An industrially feasible approach for casting orodispersible film. Asian J Pharm Sci. 2015;10:292–305.

122. Mehuys E, Vervaet C, Remon J. Hot-melt extruded ethylcellulose cylinders containing a HPMC–Gelucire® core for sustained drug delivery. J Control Release. 2004;94:273–80.

123. Simons FJ, Wagner KG. Modeling, design and manufacture of innovative floating gastroretentive drug delivery systems based on hot-melt extruded tubes. Eur J Pharm Biopharm. 2019;137:196–208.

124. Kelleher JF, Madi AM, Gilvary GC, Tian YW, Li S, Almajaan A, et al. Metformin Hydrochloride and Sitagliptin Phosphate Fixed-Dose Combination Product Prepared Using Melt Granulation Continuous Processing Technology. AAPS PharmSciTech. 2020;21:23.

125. Repka MA, Bandari S, Kallakunta VR, Vo AQ, McFall H, Pimparade MB, et al. Melt extrusion with poorly soluble drugs – An integrated review. Int J Pharm. Elsevier 2018;535:68–85.

126. Maddineni S, Battu SK, Morott J, Majumdar S, Murthy SN, Repka MA. Influence of Process and Formulation Parameters on Dissolution and Stability Characteristics of Kollidon® VA 64 Hot-Melt Extrudates. AAPS PharmSciTech. 2015;16:444–54.

127. Kate L, Gokarna V, Borhade V, Prabhu P, Deshpande V, Pathak S, et al. Bioavailability enhancement of atovaquone using hot melt extrusion technology. Eur J Pharm Sci. 2016;86:103–14.

128. Sareen S, Mathew G, Joseph L. Improvement in solubility of poor water-soluble drugs by solid dispersion. Int J Pharm Investig. 2012;2:12–7.

129. De Brabander C, Vervaet C, Fiermans L, Remon JP. Matrix mini-tablets based on starch/microcrystalline wax mixtures. Int J Pharm. 2000;199:195–203.

130. De Brabander C, Vervaet C, Remon JP. Development and evaluation of sustained release mini-matrices prepared via hot melt extrusion. J Control Release. 2003;89:235–47.

131. Roblegg E, Jäger E, Hodzic A, Koscher G, Mohr S, Zimmer A, et al. Development of sustained-release lipophilic calcium stearate pellets via hot melt extrusion. Eur J Pharm Biopharm. 2011;79:635–45.

132. Clark MR, Johnson TJ, Mccabe RT, Clark JT, Tuitupou A, Elgendy H, et al. A Hot-Melt Extruded Intravaginal Ring for the Sustained Delivery of the Antiretroviral Microbicide UC781. J Pharm Sci. 2012;101:576–87.

133. Vithani K, Maniruzzaman M, Slipper IJ, Mostafa S, Miolane C, Cuppok Y, et al. Sustained release solid lipid matrices processed by hot-melt extrusion (HME). Colloids Surfaces B Biointerfaces. Elsevier B.V. 2013;110:403–10.

134. Bruce LD, Shah NH, Waseem Malick A, Infeld MH, McGinity JW. Properties of hot-melt extruded tablet formulations for the colonic delivery of 5-aminosalicylic acid. Eur J Pharm Biopharm. 2005;59:85–97.

135. Keating A V, Soto J, Tuleu C, Forbes C, Zhao M, Craig DQM. Solid state characterisation and taste masking efficiency evaluation of polymer based extrudates of isoniazid for paediatric administration. Int J Pharm. 2018;536:536–46.

136. Ghalanbor Z, Körber M, Bodmeier R. Improved lysozyme stability and release properties of Poly(lactide-co- glycolide) implants prepared by hot-melt extrusion. Pharm Res. 2010;27:371–9.

137. Bode C, Kranz H, Fivez A, Siepmann F, Siepmann J. Often neglected: PLGA/PLA swelling orchestrates drug release: HME implants. J Control Release. 2019;306:97–107.

138. Salmoria G V., Ghizoni GB, Gindri IM, Marques MS, Kanis LA. Hot extrusion of

PE/fluorouracil implantable rods for targeted drug delivery in cancer treatment. Polym Bull. Springer Berlin Heidelberg 2019;76:1825–38.

139. Musazzi UM, Khalid GM, Selmin F, Minghetti P, Cilurzo F. Trends in the production methods of orodispersible films. Int J Pharm. 2020;576:118963.

140. Pimparade MB, Vo A, Maurya AS, Bae J, Morott JT, Feng X, et al. Development and evaluation of an oral fast disintegrating anti-allergic film using hot-melt extrusion technology. Eur J Pharm Biopharm. Elsevier B.V. 2017;119:81–90.

141. Speer I, Preis M, Breitkreutz J. Prolonged drug release properties for orodispersible films by combining hot-melt extrusion and solvent casting methods. Eur J Pharm Biopharm. Elsevier 2018;129:66–73.

142. Musazzi UM, Selmin F, Ortenzi MA, Mohammed GK, Franzé S, Minghetti P, et al. Personalized orodispersible films by hot melt ram extrusion 3D printing. Int J Pharm. Elsevier 2018;551:52–9.

143. Wesholowski J, Prill S, Berghaus A, Thommes M. Inline UV/Vis spectroscopy as PAT tool for hot-melt extrusion. Drug Deliv Transl Res. Drug Delivery and Translational Research 2018;8:1595–603.

144. Almeida J, Bezerra M, Markl D, Berghaus A, Borman P, Schlindwein W. Development and Validation of an in-line API Quantification Method Using A QbD Principles Based on UV-Vis Spectroscopy to Monitor and Optimise Continuous Hot Melt Extrusion Process. Pharmaceutics. 2020;12:150.

145. Vo AQ, He H, Zhang J, Martin S, Chen R, Repka MA. Application of FT-NIR Analysis for In-line and Real-Time Monitoring of Pharmaceutical Hot Melt Extrusion: a Technical Note. AAPS PharmSciTech. 2018;19:3425–9.

146. Islam MT, Scoutaris N, Maniruzzaman M, Moradiya HG, Halsey SA, Bradley MSA, et al. Implementation of transmission NIR as a PAT tool for monitoring drug transformation during HME processing. Eur J Pharm Biopharm. Elsevier B.V. 2015;96:106–16.

147. Arnfast L, van Renterghem J, Aho J, Bøtker J, Raijada D, Baldursdóttir S, et al.

Exploring the Complexity of Processing-Induced Dehydration during Hot Melt Extrusion Using In-Line Raman Spectroscopy. Pharmaceutics. 2020;12:116.

148. Guo X, Lin Z, Wang Y, He Z, Wang M, Jin G. In-Line Monitoring the Degradation of Polypropylene under Multiple Extrusions Based on Raman Spectroscopy. Polymers (Basel). 2019;11:1698.

149. Patel PS, Raval JP, Patel H V. Review on the pharmaceutical applications of hot melt extruder. Asian J Pharm Clin Res. 2010;3:80–3.

150. Smith DM, Kapoor Y, Klinzing GR, Procopio AT. Pharmaceutical 3D printing: Design and qualification of a single step print and fill capsule. Int J Pharm. 2018;544:21–30.

151. Melocchi A, Parietti F, Maroni A, Foppoli A, Gazzaniga A, Zema L. Hot-melt extruded filaments based on pharmaceutical grade polymers for 3D printing by fused deposition modeling. Int J Pharm. Elsevier B.V. 2016;509:255–63.

152. Okwuosa TC, Pereira BC, Arafat B, Cieszynska M, Isreb A, Alhnan MA. Fabricating a Shell-Core Delayed Release Tablet Using Dual FDM 3D Printing for Patient-Centred Therapy. Pharm Res. Pharmaceutical Research 2017;34:427–37.

153. Okwuosa TC, Stefaniak D, Arafat B, Isreb A, Wan KW, Alhnan MA. A Lower Temperature FDM 3D Printing for the Manufacture of Patient-Specific Immediate Release Tablets. Pharm Res. Pharmaceutical Research 2016;33:2704–12.

154. Sadia M, Sośnicka A, Arafat B, Isreb A, Ahmed W, Kelarakis A, et al. Adaptation of pharmaceutical excipients to FDM 3D printing for the fabrication of patient-tailored immediate release tablets. Int J Pharm. 2016;513:659–68.

155. Zhang J, Yang W, Vo AQ, Feng X, Ye X, Kim DW, et al. Hydroxypropyl methylcellulose-based controlled release dosage by melt extrusion and 3D printing: Structure and drug release correlation. Carbohydr Polym. Elsevier 2017;177:49–57.

156. Goyanes A, Chang H, Sedough D, Hatton GB, Wang J, Buanz A, et al. Fabrication of controlled-release budesonide tablets via desktop (FDM) 3D printing. Int J

Pharm. 2015;496:414–20.

157. Okwuosa TC, Soares C, Gollwitzer V, Habashy R, Timmins P, Alhnan MA. On demand manufacturing of patient-specific liquid capsules via co-ordinated 3D printing and liquid dispensing. Eur J Pharm Sci. Elsevier 2018;118:134–43.

158. Chai X, Chai H, Wang X, Yang J, Li J, Zhao Y, et al. Fused deposition modeling (FDM) 3D printed tablets for intragastric floating delivery of domperidone. Sci Rep. 2017;7:1–9.

159. Goyanes A, Fina F, Martorana A, Sedough D, Gaisford S, Basit AW. Development of modified release 3D printed tablets (printlets) with pharmaceutical excipients using additive manufacturing. Int J Pharm. Elsevier B.V. 2017;527:21–30.

160. Li Q, Wen H, Jia D, Guan X, Pan H, Yang Y, et al. Preparation and investigation of controlled-release glipizide novel oral device with three-dimensional printing. Int J Pharm. Elsevier B.V. 2017;525:5–11.

161. Verstraete G, Van Renterghem J, Van Bockstal PJ, Kasmi S, De Geest BG, De Beer T, et al. Hydrophilic thermoplastic polyurethanes for the manufacturing of highly dosed oral sustained release matrices via hot melt extrusion and injection molding. Int J Pharm. 2016;506:214–21.

162. Verstraete G, Samaro A, Grymonpré W, Vanhoorne V, Van Snick B, Boone MN, et al. 3D printing of high drug loaded dosage forms using thermoplastic polyurethanes. Int J Pharm. Elsevier 2018;536:318–25.

163. Kempin W, Domsta V, Grathoff G, Brecht I, Semmling B, Tillmann S, et al. Immediate Release 3D-Printed Tablets Produced Via Fused Deposition Modeling of a Thermo-Sensitive Drug. Pharm Res. Pharmaceutical Research 2018;35:124.

164. Kollamaram G, Croker DM, Walker GM, Goyanes A, Basit AW, Gaisford S. Low temperature fused deposition modeling (FDM) 3D printing of thermolabile drugs. Int J Pharm. Elsevier 2018;545:144–52.

165. Solanki NG, Tahsin M, Shah A V., Serajuddin ATM. Formulation of 3D Printed Tablet for Rapid Drug Release by Fused Deposition Modeling: Screening

Polymers for Drug Release, Drug-Polymer Miscibility and Printability. J Pharm Sci. Elsevier Ltd 2018;107:390–401.

166. Webster R, Castellano JM, Onuma OK. Putting polypills into practice: challenges and lessons learned. Lancet. 2017;389:1066–74.

167. Huffman MD, Xavier D, Perel P. Uses of polypills for cardiovascular disease and evidence to date. Lancet. 2017;389:1055–65.

168. Barrios V, Kaskens L, Castellano JM, Cosin-Sales J, Ruiz JE, Zsolt I, et al. Usefulness of a Cardiovascular Polypill in the Treatment of Secondary Prevention Patients in Spain: A Cost-effectiveness Study. Rev Española Cardiol (English Ed. 2017;70:42–9.

169. Gioumouxouzis CI, Baklavaridis A, Katsamenis OL, Markopoulou CK, Bouropoulos N, Tzetzis D, et al. A 3D printed bilayer oral solid dosage form combining metformin for prolonged and glimepiride for immediate drug delivery. Eur J Pharm Sci. Elsevier 2018;120:40–52.

170. Goyanes A, Wang J, Buanz A, Martínez-Pacheco R, Telford R, Gaisford S, et al. 3D Printing of Medicines: Engineering Novel Oral Devices with Unique Design and Drug Release Characteristics. Mol Pharm. 2015;12:4077–84.

171. Maroni A, Melocchi A, Parietti F, Foppoli A, Zema L, Gazzaniga A. 3D printed multi-compartment capsular devices for two-pulse oral drug delivery. J Control Release. Elsevier 2017;268:10–8.

172. Tagami T, Nagata N, Hayashi N, Ogawa E, Fukushige K, Sakai N, et al. Defined drug release from 3D-printed composite tablets consisting of drug-loaded polyvinylalcohol and a water-soluble or water-insoluble polymer filler. Int J Pharm. Elsevier 2018;543:361–7.

173. Melocchi A, Parietti F, Loreti G, Maroni A, Gazzaniga A, Zema L. 3D printing by fused deposition modeling (FDM) of a swellable/erodible capsular device for oral pulsatile release of drugs. J Drug Deliv Sci Technol. Elsevier Ltd 2015;30:360–7.

174. Pereira BC, Isreb A, Forbes RT, Dores F, Habashy R, Petit JB, et al. ‘Temporary

Plasticiser': A novel solution to fabricate 3D printed patient-centred cardiovascular 'Polypill' architectures. Eur J Pharm Biopharm. Elsevier 2019;135:94–103.

175. Arafat B, Qinna N, Cieszynska M, Forbes RT, Alhnan MA. Tailored on demand anti-coagulant dosing: An in vitro and in vivo evaluation of 3D printed purpose-designed oral dosage forms. Eur J Pharm Biopharm. Elsevier 2018;128:282–9.

176. Jamróz W, Kurek M, Łyszczarz E, Szafraniec J, Knapik-Kowalczuk J, Syrek K, et al. 3D printed orodispersible films with Aripiprazole. Int J Pharm. 2017;533:413–20.

177. Kempin W, Franz C, Koster LC, Schneider F, Bogdahn M, Weitschies W, et al. Assessment of different polymers and drug loads for fused deposition modeling of drug loaded implants. Eur J Pharm Biopharm. Elsevier B.V. 2017;115:84–93.

178. Genina N, Holländer J, Jukarainen H, Mäkilä E, Salonen J, Sandler N. Ethylene vinyl acetate (EVA) as a new drug carrier for 3D printed medical drug delivery devices. Eur J Pharm Sci. Elsevier B.V. 2016;90:53–63.

179. Holländer J, Genina N, Jukarainen H, Khajeheian M, Rosling A, Mäkilä E, et al. Three-Dimensional Printed PCL-Based Implantable Prototypes of Medical Devices for Controlled Drug Delivery. J Pharm Sci. 2016;105:2665–76.

180. Stewart S, Domínguez-Robles J, McIlorum V, Mancuso E, Lamprou D, Donnelly R, et al. Development of a Biodegradable Subcutaneous Implant for Prolonged Drug Delivery Using 3D Printing. Pharmaceutics. 2020;12:105.

181. Melocchi A, Inverardi N, Uboldi M, Baldi F, Maroni A, Pandini S, et al. Retentive device for intravesical drug delivery based on water-induced shape memory response of poly(vinyl alcohol): design concept and 4D printing feasibility. Int J Pharm. Elsevier 2019;559:299–311.

182. Shin D-G, Kim T-H, Kim D-E. Review of 4D printing materials and their properties. Int J Precis Eng Manuf Technol. 2017;4:349–57.

183. Zhou Y, Huang WM, Kang SF, Wu XL, Lu HB, Fu J, et al. From 3D to 4D printing: approaches and typical applications. J Mech Sci Technol. 2015;29:4281–8.

184. Huang WM, Ding Z, Wang CC, Wei J, Zhao Y, Purnawali H. Shape memory materials. Mater Today. Elsevier Ltd 2010;13:54–61.

185. Ge Q, Dunn CK, Qi HJ, Dunn ML. Active origami by 4D printing. Smart Mater Struct. 2014;23:094007.

186. National Research Council. Chapter 1: Introduction to Sensors. In: Expanding the Vision of Sensor Materials. National Academies Press 1995. p. 9–18.

187. Zhou G, Wang Y, Cui L. Biomedical Sensor, Device and Measurement Systems. In: Serra PA, editor. Advances in Bioengineering. InTech 2015.

188. Singh S, Kapoor N. Health Implications of Electromagnetic Fields, Mechanisms of Action, and Research Needs. Adv Biol. 2014;2014:1–24.

189. Hieda I, Nam KC. Electric Field Measurement of the Living Human Body for Biomedical Applications: Phase Measurement of the Electric Field Intensity. Int J Antennas Propag. 2013;2013:1–6.

190. Zheng Y, Zhang H, Yip K, Zheng Z, Yang S. Preliminary Measurement of Electromagnetic Fields and Microdischarges From the Human Body. Altern Ther Health Med. 2016;22:20–31.

191. Sharma NK, Singh S. Designing a non invasive blood glucose measurement sensor. In: 2012 IEEE 7th International Conference on Industrial and Information Systems (ICIIS). IEEE 2012. p. 1–3.

192. Ahn SR, An JH, Lee SH, Song HS, Jang J, Park TH. Peptide hormone sensors using human hormone receptor-carrying nanovesicles and graphene FETs. Sci Rep. 2020;10:388.

193. Ali MA, Hu C, Jahan S, Yuan B, Saleh MS, Ju E, et al. Sensing of COVID-19 Antibodies in Seconds via Aerosol Jet Nanoprinted Reduced-Graphene-Oxide-Coated 3D Electrodes. Adv Mater. 2021;33:2006647.

194. Sameh R, Genedy M, Abdeldayem A, Abdel azeem MH. Design and Implementation of an SPO2 Based Sensor for Heart Monitoring Using an Android Application. J Phys Conf Ser. 2020;1447:012004.

195. Sepulveda AT, Pontes AJ, Viana JC, de Villoria RG, Fachin F, Wardle BL, et al. Flexible sensor for blood pressure measurement. In: 2011 Annual International Conference of the IEEE Engineering in Medicine and Biology Society. IEEE 2011. p. 512–5.

196. Farin NJ, Sharif SMA, Mobin I. An Intelligent Sensor Based System for Real Time Heart Rate Monitoring (HRM). Intell Control Autom. 2016;07:55–62.

197. Bhalla N, Jolly P, Formisano N, Estrela P. Introduction to biosensors. Essays Biochem. Portland Press Limited 2016;60:1–8.

198. Idros N, Ho M, Pivnenko M, Qasim M, Xu H, Gu Z, et al. Colorimetric-Based Detection of TNT Explosives Using Functionalized Silica Nanoparticles. Sensors. 2015;15:12891–905.

199. Yáñez-Sedeño P, Agüí L, Villalonga R, Pingarrón JM. Biosensors in forensic analysis. A review. Anal Chim Acta. Elsevier 2014;823:1–19.

200. Justino CIL, Duarte AC, Rocha-Santos TAP. Recent Progress in Biosensors for Environmental Monitoring: A Review. Sensors (Basel). MDPI 2017;17:2918.

201. Bhide A, Muthukumar S, Saini A, Prasad S. Simultaneous lancet-free monitoring of alcohol and glucose from low-volumes of perspired human sweat. Sci Rep. Springer US 2018;8:1–11.

202. Lee H, Song C, Hong YS, Kim MS, Cho HR, Kang T, et al. Wearable/disposable sweat-based glucose monitoring device with multistage transdermal drug delivery module. Sci Adv. 2017;3:1–9.

203. Curto VF, Coyle S, Byrne R, Angelov N, Diamond D, Benito-Lopez F. Concept and development of an autonomous wearable micro-fluidic platform for real time pH sweat analysis. Sensors Actuators B Chem. Elsevier 2012;175:263–70.

204. Sund-Levander M, Grodzinsky E. Assessment of body temperature measurement options. Br J Nurs. 2013;22:942–50.

205. Centre for Clinical Practice at NICE (UK). Acutely Ill Patients in Hospital: Recognition of and Response to Acute Illness in Adults in Hospital [Internet].

London: National Institute for Health and Clinical Excellence (UK). 2021 Feb 5; https://pubmed.ncbi.nlm.nih.gov/21204323/.

206. Tortora GJ, Derrickson BH. Principles of Anatomy and Physiology. 15th ed. Wiley 2016. 1288 p.

207. Osilla; E V., Sharma JLMS. Physiology, Temperature Regulation [Internet]. StatPearls. 2021 Jan 8; https://www.ncbi.nlm.nih.gov/books/NBK507838/.

208. Pocock; G, Richards C. The Human Body: An introduction for the biomedical and health science. 1st ed. OUP Oxford 1753.

209. Cheshire WP. Thermoregulatory disorders and illness related to heat and cold stress. Auton Neurosci. 2016;196:91–104.

210. Konishi S, Hirata A. Flexible Temperature Sensor Integrated with Soft Pneumatic Microactuators for Functional Microfingers. Sci Rep. 2019;9:15634.

211. Wang C-C, Hou Z-Y, You J-C. A High-Precision CMOS Temperature Sensor with Thermistor Linear Calibration in the (−5 °C, 120 °C) Temperature Range. Sensors. 2018;18:2165.

212. Santos EJP, Vasconcelos IB. RTD-based smart temperature sensor: Process development and circuit design. In: 2008 26th International Conference on Microelectronics. IEEE 2008. p. 333–6.

213. Schena E, Tosi D, Saccomandi P, Lewis E, Kim T. Fiber Optic Sensors for Temperature Monitoring during Thermal Treatments: An Overview. Sensors. 2016;16:1144.

214. Keranen K, Makinen J-T, Korhonen P, Juntunen E, Heikkinen V, Makela J. Improved infrared temperature sensing system for mobile devices. In: 2008 2nd Electronics Systemintegration Technology Conference. IEEE 2008. p. 809–14.

215. Ross-Pinnock D, Maropoulos PG. Review of industrial temperature measurement technologies and research priorities for the thermal characterisation of the factories of the future. Proc Inst Mech Eng Part B J Eng Manuf. 2016;230:793–806.

216. Papaioannou N, Leach F, Davy M. Effect of Thermocouple Size on the Measurement of Exhaust Gas Temperature in Internal Combustion Engines. In: International Powertrains, Fuels & Lubricants Meeting. 2018.

217. Liu B, Huang Q, Wang P. Analysis of surrounding gas temperature influence on thermocouple measurement temperature. J Phys Conf Ser. 2020;1509:012004.

218. Grassini S, Parvis M, Barresi AA. Inert Thermocouple With Nanometric Thickness for Lyophilization Monitoring. IEEE Trans Instrum Meas. 2013;62:1276–83.

219. Zell M, Lyng JG, Morgan DJ, Cronin DA. Development of rapid response thermocouple probes for use in a batch ohmic heating system. J Food Eng. 2009;93:344–7.

220. Lebedev V, Laukhina E, Laukhin V, Somov A, Baranov A, Rovira C, et al. Approach to Engineering the Temperature Sensing E-textile: A Lightweight Thermistor as an Active Sensing Element. In: Lecture Notes of the Institute for Computer Sciences, Social Informatics and Telecommunications Engineering. Springer, Cham 2016. p. 223–34.

221. Hughes-Riley T, Lugoda P, Dias T, Trabi C, Morris R. A Study of Thermistor Performance within a Textile Structure. Sensors. 2017;17:1804.

222. Kim JC, Park GH, Nam JD. A study on the PTC thermistor characteristics of polyethylene and polyethylene copolymer composite systems in melt and solution manufacturing method. Polym Korea. 2002;26:812–20.

223. Arathy K, Ansari S, Malini KA. High reliability thermistor probes for early detection of breast cancer using skin contact thermometry with thermal imaging. Mater Express. 2020;10:620–8.

224. Zát'ura F, Ramert B, Scheinar J, Reif R, Výborný K. Kidney temperature measurement. Thermistors for temperature measurement. Acta Univ Palacki Olomuc Fac Med. 1994;138:45–8.

225. Aleksic OS, Nikolic PM, Lukovic D, Savic S, Pejovic VZ, Radojcic BM. A thick film NTC thermistor air flow sensor. In: 24th International Conference on

Microelectronics (IEEE Cat No04TH8716). IEEE 2004. p. 185–8.

226. Martin PE, Richards H. Thermistors as Cryogenic Temperature Sensors. In: Advances in Cryogenic Engineering. Springer US 1962. p. 522–6.

227. Wang X, Xie Z, Huang H, Liu Z, Chen D, Shen G. Gas sensors, thermistor and photodetector based on ZnS nanowires. J Mater Chem. 2012;22:6845.

228. Kim J, Kim J, Shin Y, Yoon Y. A study on the fabrication of an RTD (resistance temperature detector) by using Pt thin film. Korean J Chem Eng. 2001;18:61–6.

229. Cheng C-C, Lee D. Enabling Smart Air Conditioning by Sensor Development: A Review. Sensors. 2016;16:2028.

230. Berk Z. Elements of Process Control. In: Food Process Engineering and Technology. Elsevier 2009. p. 129–51.

231. Kang L, Shi Y, Zhang J, Huang C, Zhang N, He Y, et al. A flexible resistive temperature detector (RTD) based on in-situ growth of patterned Ag film on polyimide without lithography. Microelectron Eng. 2019;216:111052.

232. Kerlin TW, Upadhyaya BR. Nuclear plant instrumentation. In: Dynamics and Control of Nuclear Reactors. Elsevier 2019. p. 213–35.

233. Roriz P, Silva S, Frazão O, Novais S. Optical Fiber Temperature Sensors and Their Biomedical Applications. Sensors. 2020;20:2113.

234. Shah RY, Agrawal YK. Introduction to fiber optics: Sensors for biomedical applications. Indian J Pharm Sci. 2011;73:17–22.

235. Christensen DA. Fiberoptic Temperature Sensing For Biomedical Applications. In: Proc SPIE 0906, Optical Fibers in Medicine III. 1988. p. 108.

236. Poeggel S, Tosi D, Duraibabu D, Leen G, McGrath D, Lewis E. Optical Fibre Pressure Sensors in Medical Applications. Sensors. 2015;15:17115–48.

237. Jensen SC, Tilstra SD, Barnabo GA, Thomas DC, Phillips RW. Fiber optic temperature sensor for aerospace applications. In: Lewis NE, Moore EL, editors. SPIE Microelectronic Interconnect and Integrated Processing Symposium. 1990.

p. 87–95.

238. García I, Zubia J, Durana G, Aldabaldetreku G, Illarramendi MA, Villatoro J. Optical fiber sensors for aircraft structural health monitoring. Sensors (Switzerland). 2015;15:15494–519.

239. Coscetta A, Minardo A, Olivares L, Mirabile M, Longo M, Damiano M, et al. Wind Turbine Blade Monitoring with Brillouin-Based Fiber-Optic Sensors. J Sensors. 2017;2017:1–5.

240. Brown G, Hartog A. Optical Fiber Sensors in Upstream Oil & Gas. J Pet Technol. 2002;54.

241. Wang Y, Zhang W-H. The Development of Infrared Temperature Sensor Based on Thermopile Detector TPS334 and PGA309. In: 2009 International Conference on Measuring Technology and Mechatronics Automation. IEEE 2009. p. 62–5.

242. O'Shaughnessy SA, Hebel MA, Evett SR, Colaizzi PD. Evaluation of a wireless infrared thermometer with a narrow field of view. Comput Electron Agric. 2011;76:59–68.

243. Zhao L, Zhang J, Shen Y, Wu W. Design and Implementation of Energy Saving Controller for Air-Conditioner in Building. Int J Smart Home. 2015;9:47–54.

244. Xiong Z, Sun D-W, Pu H, Gao W, Dai Q. Applications of emerging imaging techniques for meat quality and safety detection and evaluation: A review. Crit Rev Food Sci Nutr. 2017;57:755–68.

245. Costa N, Stelletta C, Cannizzo C, Gianesella M, Lo Fiego P, Morgante M. The use of thermography on the slaughter-line for the assessment of pork and raw ham quality. Ital J Anim Sci. 2007;6:704–6.

246. Bulanon DM, Burks TF, Alchanatis V. Study on temporal variation in citrus canopy using thermal imaging for citrus fruit detection. Biosyst Eng. 2008;101:161–71.

247. Gutiérrez S, Diago MP, Fernández-Novales J, Tardaguila J. Vineyard water status assessment using on-the-go thermal imaging and machine learning. Gerós H,

editor. PLoS One. 2018;13:e0192037.

248. Kim C, Chean M. Development of a Constant Temperature Control Light Emitting Diode Light Cold Mask Reflecting Real-Time Skin Temperature Change. J Nanosci Nanotechnol. 2021;21:1789–94.

249. Kolomiets O, Hoffmann U, Geladi P, Siesler HW. Quantitative Determination of Pharmaceutical Drug Formulations by Near-Infrared Spectroscopic Imaging. Appl Spectrosc. 2008;62:1200–8.

250. Camuffo D. Measuring Temperature. In: Microclimate for Cultural Heritage. Elsevier 2019. p. 383–429.

251. Pflug IJ, Berry MR. Using Thermocouples to Measure Temperatures during Retort or Autoclave Validation1. J Food Prot. 1987;50:975–81.

252. Lecigne R, Garnon J, Cazzato RL, Auloge P, Dalili D, Koch G, et al. Transforaminal Insertion of a Thermocouple on the Posterior Vertebral Wall Combined with Hydrodissection during Lumbar Spinal Radiofrequency Ablation. Am J Neuroradiol. 2019;40:1786–90.

253. Scervini M, Rae C, Lindley B. Transmutation of thermocouples in thermal and fast nuclear reactors. In: 2013 3rd International Conference on Advancements in Nuclear Instrumentation, Measurement Methods and their Applications (ANIMMA). IEEE 2013. p. 1–8.

254. George EI, Brand TC, LaPorta A, Marescaux J, Satava RM. Origins of Robotic Surgery: From Skepticism to Standard of Care. JSLS J Soc Laparoendosc Surg. 2018;22:e2018.00039.

255. Park P, Ruffieux D, Makinwa KAA. A Thermistor-Based Temperature Sensor for a Real-Time Clock With 2 ppm Frequency Stability. IEEE J Solid-State Circuits. 2015;50:1571–80.

256. Jagtap S, Rane S, Mulik U, Amalnerkar D. Thick film NTC thermistor for wide range of temperature sensing. Microelectron Int. 2007;24:7–13.

257. Shenep JL, Adair JR, Hughes WT, Roberson PK, Flynn PM, Brodkey TO, et al.

lnfrared, Thermistor, and Glass-Mercury Thermometry for Measurement of Body Temperature in Children With Cancer. Clin Pediatr (Phila). 1991;30:36–41.

258. Gautherie M. Thermopathology of Breast Cancer: Measurement and Analysis of In Vivo Temperature and Blood Flow. Ann N Y Acad Sci. 1980;335:383–415.

259. Keyserlingk JR, Ahlgren PD, Yu E, Belliveau N, Yassa M. Functional infrared imaging of the breast. IEEE Eng Med Biol Mag. 2000;19:30–41.

260. Lim R, Cheng M-Y, Chen W, Choong DSW, Park JH, Oh JS, et al. Development of Integrated Thermistor Sensor and Heating Electrode for Renal Denervation Procedure. In: 2018 IEEE 68th Electronic Components and Technology Conference (ECTC). IEEE 2018. p. 777–82.

261. Barvik D, Kubicek J, Malinova N, Augustynek M, Vilimek D, Penhaker M. Analysis and Measurement of Cardiac Output Based on Pulmonary Artery Thermodilution in Laboratory Conditions. In: 8th European Medical and Biological Engineering Conference. 2021. p. 73–83.

262. Hong Cao, Vorperian VR, Jang-Zem Tsai, Tungjitkusolmun S, Eung Je Woo, Webster JG. Temperature measurement within myocardium during in vitro RF catheter ablation. IEEE Trans Biomed Eng. 2000;47:1518–24.

263. Yang Z, Zhang Y, Itoh T. A flexible implantable micro temperature sensor on polymer capillary for biomedical applications. In: 2013 IEEE 26th International Conference on Micro Electro Mechanical Systems (MEMS). IEEE 2013. p. 889–92.

264. Inci MN, Yoshino T. A Fiber Optic Wavelength Modulation Sensor Based on Tantalum Pentoxide Coatings for Absolute Temperature Measurements. Opt Rev. 2000;7:205–8.

265. Roriz P, Ramos A, Santos JL, Simões JA. Fiber optic intensity-modulated sensors: A review in biomechanics. Photonic Sensors. 2012;2:315–30.

266. Zhang Y, Su H, Ma K, Zhu F, Guo Y, Jiang W. Optic-Fiber Temperature Sensor. In: Temperature Sensing. InTech 2018.

267. Vengsarkar AM, Murphy KA, Claus RO. Stable phase-modulated fiber-optic sensors for senior electrical engineering laboratory curricula. IEEE Trans Educ. 1992;35:69–75.

268. Sahota JK, Gupta N, Dhawan D. Fiber Bragg grating sensors for monitoring of physical parameters: a comprehensive review. Opt Eng. 2020;59:1.

269. Hartog AH. Principles of optical fibre temperature sensors. Sens Rev. 1987;7:197–9.

270. Tosi D, Macchi E, Gallati M, Braschi G, Cigada A, Poeggel S, et al. Optical fiber sensors for monitoring of thermal ablation procedure applied to interventional cancer care: results and future prospects. In: Nanotech Italy. 2014.

271. Duraibabu D, Kelly N, Poeggel S, Flood H, Yuan H, Dooly G, et al. Optical fibre pressure and temperature sensor system designed for urodynamic applications. In: Lewis E, editor. Sixth European Workshop on Optical Fibre Sensors (EWOFS'2016). 2016. p. 991617.

272. Zheng H, Hao L, He H. A Kind of Fluorescent Optical Fiber Temperature Sensor Applied for Cancer Knub. In: 2009 Pacific-Asia Conference on Knowledge Engineering and Software Engineering. IEEE 2009. p. 18–20.

273. Dziuda Ł. Fiber-optic sensors for monitoring patient physiological parameters: a review of applicable technologies and relevance to use during magnetic resonance imaging procedures. J Biomed Opt. 2015;20:1.

274. Schaafsma DT, Palmer G, Bechtel JH. Fiber optic temperature sensors for medical applications. In: Gannot I, editor. 2003. p. 162.

275. Correia R, James S, Lee SW, Morgan SP, Korposh S. Biomedical application of optical fibre sensors. J Opt (United Kingdom). IOP Publishing 2018;20.

276. Saccomandi P, Frauenfelder G, Massaroni C, Caponera MA, Polimadei A, Taffoni F, et al. Temperature monitoring during radiofrequency ablation of liver: In vivo trials. In: 2016 38th Annual International Conference of the IEEE Engineering in Medicine and Biology Society (EMBC). IEEE 2016. p. 344–7.

277. Taffoni F, Formica D, Saccomandi P, Pino G, Schena E. Optical Fiber-Based MR-Compatible Sensors for Medical Applications: An Overview. Sensors. 2013;13:14105–20.

278. Tosi D, Macchi EG, Cigada A. Fiber-Optic Temperature and Pressure Sensors Applied to Radiofrequency Thermal Ablation in Liver Phantom: Methodology and Experimental Measurements. J Sensors. 2015;2015:1–22.

279. Yoo WJ, Seo JK, Cho DH, Jang KW, Heo JY, Jun JH, et al. Infrared Fiber-Optic Temperature Array Sensor for Radiofrequency Ablation. In: 2009 2nd International Conference on Biomedical Engineering and Informatics. IEEE 2009. p. 1–4.

280. Limab®. Luxtron Fiber Optic Thermometer [Internet]. LIMAB UK Ltd. 2021 Feb 9; https://www.limab.co.uk/product/luxtron-fiber-optic-thermometer/.

281. Ning B, Wu Y. Research on Non-Contact Infrared Temperature Measurement. In: 2010 International Conference on Computational Intelligence and Software Engineering. IEEE 2010. p. 1–4.

282. Havens KJ, Sharp EJ. Thermal Imagers and System Considerations. In: Thermal Imaging Techniques to Survey and Monitor Animals in the Wild. Elsevier 2016. p. 101–19.

283. Meola C, Carlomagno GM. Recent advances in the use of infrared thermography. Meas Sci Technol. 2004;15:R27–58.

284. Chen H-Y, Chen A, Chen C. Investigation of the Impact of Infrared Sensors on Core Body Temperature Monitoring by Comparing Measurement Sites. Sensors. 2020;20:2885.

285. Gómez-de-Gabriel J, Harwin W. Evaluation of Sensor Configurations for Robotic Surgical Instruments. Sensors. 2015;15:27341–58.

286. Agnihotri A. Human Body Respiration Measurement Using Digital Temperature Sensor with I2c Interface. Int J Sci Res Publ. 2013;3:2–8.

287. Boccanfuso L, O'Kane JM. Remote measurement of breathing rate in real time

using a high precision, single-point infrared temperature sensor. In: 2012 4th IEEE RAS & EMBS International Conference on Biomedical Robotics and Biomechatronics (BioRob). IEEE 2012. p. 1704–9.

288. Xu W, Gao B, Ma S, Zhang A, Chiu Y, Lee Y-K. Low-cost temperature-compensated thermoresistive micro calorimetric flow sensor by using 0.35μm CMOS MEMS technology. In: 2016 IEEE 29th International Conference on Micro Electro Mechanical Systems (MEMS). IEEE 2016. p. 189–92.

289. Rajan G, Callaghan D, Semenova Y, Farrell G. Miniature temperature insensitive fiber optic sensors for minimally invasive surgical devices. In: 21st International Conference on Optical Fiber Sensors. 2011. p. 77536Z.

290. NICE. Type 2 diabetes: prevention in people at high risk [Internet]. NICE National Institute of Health and Care Excellence. 2012.

291. NHS. Diabetes [Internet]. National Health Service. 2019 Aug 1; https://www.nhs.uk/conditions/diabetes/.

292. Diabetes: the basics [Internet]. Diabetes UK. 2019 Aug 1; https://www.diabetes.org.uk/diabetes-the-basics.

293. WHO. Diabetes [Internet]. World Health Organization. 2019 Aug 1; https://www.who.int/news-room/fact-sheets/detail/diabetes.

294. Hayes C, Kriska A. Role of Physical Activity in Diabetes Management and Prevention. J Am Diet Assoc. Elsevier 2008;108:S19–23.

295. Ley SH, Hamdy O, Mohan V, Hu FB. Prevention and management of type 2 diabetes: dietary components and nutritional strategies. Lancet. Elsevier 2014;383:1999–2007.

296. Clarke SF, Foster JR. A history of blood glucose meters and their role in self-monitoring of diabetes mellitus. Br J Biomed Sci. 2012;69:83–93.

297. Villena Gonzales W, Mobashsher A, Abbosh A. The Progress of Glucose Monitoring—A Review of Invasive to Minimally and Non-Invasive Techniques, Devices and Sensors. Sensors. 2019;19:800.

298. Yoon J, Lee SN, Shin MK, Kim H-W, Choi HK, Lee T, et al. Flexible electrochemical glucose biosensor based on GOx/gold/MoS2/gold nanofilm on the polymer electrode. Biosens Bioelectron. Elsevier 2019;140:111343.

299. Du X, Li Y, Motley JR, Stickle WF, Herman GS. Glucose Sensing Using Functionalized Amorphous In-Ga-Zn-O Field-Effect Transistors. ACS Appl Mater Interfaces. 2016;8:7631–7.

300. Williams DL, Doig AR, Korosi A. Electrochemical-enzymatic analysis of blood glucose and lactate. Anal Chem. 1970;42:118–21.

301. Bandodkar AJ, Jeerapan I, Wang J. Wearable Chemical Sensors: Present Challenges and Future Prospects. ACS Sensors. 2016;1:464–82.

302. Updike SJ, Hicks GP. The Enzyme Electrode. Nature. 1967;214:986–8.

303. Yoo E-H, Lee S-Y. Glucose biosensors: an overview of use in clinical practice. Sensors (Basel). 2010/05/04. Molecular Diversity Preservation International (MDPI) 2010;10:4558–76.

304. Cappon G, Acciaroli G, Vettoretti M, Facchinetti A, Id GS. Wearable Continuous Glucose Monitoring Sensors: A Revolution in Diabetes Treatment. Electronics. 2017;6:65.

305. Srivastava A, Chowdhury K, Sharma S, Sharma N. Blood Glucose Monitoring Using Non Invasive Optical Method: Design Limitations and Challenges. Int J Adv Res Electr Electron Instrum Eng. 2013;2:615–20.

306. Ben Mohammadi L, Klotzbuecher T, Sigloch S, Welzel K, Göddel M, Pieber TR, et al. In vivo evaluation of a chip based near infrared sensor for continuous glucose monitoring. Biosens Bioelectron. Elsevier 2014;53:99–104.

307. Mortellaro M, DeHennis A. Performance characterization of an abiotic and fluorescent-based continuous glucose monitoring system in patients with type 1 diabetes. Biosens Bioelectron. Elsevier 2014;61:227–31.

308. Salam NABA, Saad WHBM, Manap ZB, Bte Salehuddin F. The evolution of non-invasive blood glucose monitoring system for personal application. J Telecommun

Electron Comput Eng. 2016;8:59–65.

309. Joshi K, Sumant O. Continuous Glucose Monitoring Systems Market by Components (Sensors, Transmitters & Receivers, and Integrated Insulin Pumps), Demographics (Child Population (<=14years), and Adult Population (>14years), and End User (Clinics and Diagnostics Centers, ICUs, [Internet]. 2020.

310. Wang J. Electrochemical glucose biosensors. Electrochem Sensors, Biosens their Biomed Appl. 2008;57–69.

311. Care AD. FreeStyle, Libre [Internet]. 2019 Sep 17; https://www.freestylelibre.co.uk/libre/.

312. Dexcom. Introducing the new Dexcom G6® CGM System. Experience the power of what Dexcom G6 can do for you. [Internet]. 2019 Sep 17; https://www.dexcom.com/en-GB/uk-dexcom-g6-cgm-system.

313. Prabhakaran A, Nayak P. Surface Engineering of Laser-Scribed Graphene Sensor Enables Non-Enzymatic Glucose Detection in Human Body Fluids. ACS Appl Nano Mater. 2020;3:391–8.

314. Zhu X, Ju Y, Chen J, Liu D, Liu H. Nonenzymatic wearable sensor for electrochemical analysis of perspiration glucose. ACS Sensors. 2018;3:1135–41.

315. Manesh KM, Kim HT, Santhosh P, Gopalan AI, Lee K-P. A novel glucose biosensor based on immobilization of glucose oxidase into multiwall carbon nanotubes–polyelectrolyte-loaded electrospun nanofibrous membrane. Biosens Bioelectron. 2008;23:771–9.

316. Welch ME, Doublet T, Bernard C, Malliaras GG, Ober CK. A glucose sensor via stable immobilization of the GOx enzyme on an organic transistor using a polymer brush. J Polym Sci Part A Polym Chem. 2015;53:372–7.

317. Gellynck K, Kodeck V, Van De Walle E, Kersemans K, De Vos F, Declercq H, et al. First step toward near-infrared continuous glucose monitoring: in vivo evaluation of antibody coupled biomaterials. Exp Biol Med (Maywood). 2014/10/10. SAGE Publications 2015;240:446–57.

318. Ben Mohammadi L, Klotzbuecher T, Sigloch S, Welzel K, Goeddel M, Pieber TR, et al. Clinical performance of a low cost near infrared sensor for continuous glucose monitoring applied with subcutaneous microdialysis. Biomed Microdevices. 2015;17:73.

319. Pandey R, Paidi SK, Valdez TA, Zhang C, Spegazzini N, Dasari RR, et al. Noninvasive Monitoring of Blood Glucose with Raman Spectroscopy. Acc Chem Res. 2017/01/10. 2017;50:264–72.

320. Milenko K, Fuglerud SS, Jernelv IL, Aksnes A, Ellingsen R, Hjelme DR. Towards Fiber-Optic Raman Spectroscopy for Glucose Sensing. In: Advanced Photonics 2018 (BGPP, IPR, NP, NOMA, Sensors, Networks, SPPCom, SOF). Optical Society of America 2018. p. JTu2A.70.

321. Kinnamon D, Ghanta R, Lin K-C, Muthukumar S, Prasad S. Portable biosensor for monitoring cortisol in low-volume perspired human sweat. Sci Rep. 2017;7:13312.

322. Gao W, Emaminejad S, Nyein HYY, Challa S, Chen K, Peck A, et al. Fully integrated wearable sensor arrays for multiplexed in situ perspiration analysis. Nature. 2016;529:509–14.

323. Munje RD, Muthukumar S, Prasad S. Lancet-free and label-free diagnostics of glucose in sweat using Zinc Oxide based flexible bioelectronics. Sensors Actuators, B Chem. Elsevier B.V. 2017;238:482–90.

324. Abellán-Llobregat A, Jeerapan I, Bandodkar A, Vidal L, Canals A, Wang J, et al. A stretchable and screen-printed electrochemical sensor for glucose determination in human perspiration. Biosens Bioelectron. 2017;91:885–91.

325. The Juvenile Diabetes Research Foundation Continuous Glucose Monitoring Study Group. Continuous Glucose Monitoring and Intensive Treatment of Type 1 Diabetes. N Engl J Med. 2008;359:1464–76.

326. Nam H, Oh B-RR, Chen P, Chen M, Wi S, Wan W, et al. Multiple MoS2 transistors for sensing molecule interaction kinetics. Sci Rep. Nature Publishing Group 2015;5:04017010.

327. Nathan A, Ahnood A, Cole MT, Lee S, Suzuki Y, Hiralal P, et al. Flexible electronics: The next ubiquitous platform. Proc IEEE. 2012;100:1486–517.

328. Petti L, Münzenrieder N, Vogt C, Faber H, Büthe L, Cantarella G, et al. Metal oxide semiconductor thin-film transistors for flexible electronics. Appl Phys Rev. 2016;3:021303.

329. Sung J. End of paper labels: Emerging smart labels toward Internet of Things. In: 2015 IEEE 2nd World Forum on Internet of Things (WF-IoT). IEEE 2015. p. 216–21.

330. Brodnjak U, Muck D, Tomc H, Karlovits I, Gregor-Svetec D, Starešinič M. Printed Smart Labels in Packaging. In: Printed Electronics: Technologies, Applications and Challenges. 2017.

331. Gong S, Schwalb W, Wang Y, Chen Y, Tang Y, Si J, et al. A wearable and highly sensitive pressure sensor with ultrathin gold nanowires. Nat Commun. 2014;5:3132.

332. Gu Y, Zhang T, Chen H, Wang F, Pu Y, Gao C, et al. Mini Review on Flexible and Wearable Electronics for Monitoring Human Health Information. Nanoscale Res Lett. 2019;14:263.

333. Li D, Yu H, Pu Z, Lai X, Sun C, Wu H, et al. Flexible Microfluidics for Wearable Electronics. In: Wang G, Hou C, Wang H, editors. Flexible and Wearable Electronics for Smart Clothing. Wiley 2020. p. 213–35.

334. van den Brand J, de Kok M, Koetse M, Cauwe M, Verplancke R, Bossuyt F, et al. Flexible and stretchable electronics for wearable health devices. Solid State Electron. 2015;113:116–20.

335. Natta L, Mastronardi VM, Guido F, Algieri L, Puce S, Pisano F, et al. Soft and flexible piezoelectric smart patch for vascular graft monitoring based on Aluminum Nitride thin film. Sci Rep. 2019;9:8392.

336. Takei K. Human Interactive Wearable Devices: Applications of Artificial Electronic Skins and Smart Bandages. In: Design, User Experience, and Usability

User Experience Design for Everyday Life Applications and Services. Springer, Cham 2014. p. 710–8.

337. Yin F, Yang J, Peng H, Yuan W. Flexible and highly sensitive artificial electronic skin based on graphene/polyamide interlocking fabric. J Mater Chem C. 2018;6:6840–6.

338. Almansoori MT, Li X, Zheng L. A Brief Review on E-skin and its Multifunctional Sensing Applications. Curr Smart Mater. 2019;4:3–14.

339. Williams NX, Noyce S, Cardenas JA, Catenacci M, Wiley BJ, Franklin AD. Silver nanowire inks for direct-write electronic tattoo applications. Nanoscale. 2019;11:14294–302.

340. Wang Y, Qiu Y, Ameri SK, Jang H, Dai Z, Huang Y, et al. Low-cost, μm-thick, tape-free electronic tattoo sensors with minimized motion and sweat artifacts. npj Flex Electron. Springer US 2018;2:6.

341. Nicholas X. Williams ADF. Electronic Tattoos: A Promising Approach to Real-time Theragnostics. J Dermatology Ski Sci. 2020;2:5–16.

342. Kim D-H, Ghaffari R, Lu N, Rogers JA. Flexible and Stretchable Electronics for Biointegrated Devices. Annu Rev Biomed Eng. 2012;14:113–28.

343. Roh KS, Yoon S, Do Kwon Y, Shim Y, Kim Y-J. Single-Port Surgical Robot System with Flexible Surgical Instruments. In: Intelligent Robotics and Applications. Springer Cham 2015. p. 447–59.

344. Kassanos P, Seichepine F, Wales D, Yang G-Z. Towards a Flexible/Stretchable Multiparametric Sensing Device for Surgical and Wearable Applications. In: 2019 IEEE Biomedical Circuits and Systems Conference (BioCAS). IEEE 2019. p. 1–4.

345. Nag A, Mukhopadhyay SC. Wearable flexible sensors : fabrication and characterization. In: Mukhopadhyay SC, Islam T, editors. Wearable Sensors Applications, design and implementation. IOP Publishing 2017. p. 1–27. (2053-2563).

346. Bandodkar AJ, Jia W, Yardimci C, Wang X, Ramirez J, Wang J. Tattoo-based noninvasive glucose monitoring: A proof-of-concept study. Anal Chem. 2015;87:394–8.

347. Nesaei S, Song Y, Wang Y, Ruan X, Du D, Gozen A, et al. Micro additive manufacturing of glucose biosensors: A feasibility study. Anal Chim Acta. Elsevier Ltd 2018;1043:142–9.

348. Vamvakaki V, Chaniotakis NA. Immobilization of enzymes into nanocavities for the improvement of biosensor stability. Biosens Bioelectron. Elsevier 2007;22:2650–5.

349. Stern E, Klemic JF, Routenberg DA, Wyrembak PN, Turner-Evans DB, Hamilton AD, et al. Label-free immunodetection with CMOS-compatible semiconducting nanowires. Nature. Nature Publishing Group 2007;445:519.

350. Sarkar D, Banerjee K. Proposal for tunnel-field-effect-transistor as ultra-sensitive and label-free biosensors. Appl Phys Lett. American Institute of Physics 2012;100:143108.

351. Chen Y, Ren R, Pu H, Guo X, Chang J, Zhou G, et al. Field-Effect Transistor Biosensor for Rapid Detection of Ebola Antigen. Sci Rep. 2017;7:10974.

352. Zheng C, Jin X, Li Y, Mei J, Sun Y, Xiao M, et al. Sensitive Molybdenum Disulfide Based Field Effect Transistor Sensor for Real-time Monitoring of Hydrogen Peroxide. Sci Rep. 2019;9:1–9.

353. Wang H, Yu L, Lee Y-H, Shi Y, Hsu A, Chin ML, et al. Integrated Circuits Based on Bilayer MoS2 Transistors. Nano Lett. American Chemical Society 2012;12:4674–80.

354. Klasens HA, Koelmans H. A tin oxide field-effect transistor. Solid State Electron. 1964;7:701–2.

355. Rim YS. Review of metal oxide semiconductors-based thin-film transistors for point-of-care sensor applications. J Inf Disp. Taylor & Francis 2020;21:203–10.

356. Smith JT, Shah SS, Goryll M, Stowell JR, Allee DR. Flexible ISFET biosensor

using IGZO metal oxide TFTs and an ITO sensing layer. IEEE Sens J. IEEE 2014;14:937–8.

357. Rim YS, Chen H, Zhu B, Bae S-H, Zhu S, Li PJ, et al. Interface Engineering of Metal Oxide Semiconductors for Biosensing Applications. Adv Mater Interfaces. 2017;4:1700020.

358. Jia X, Fuentes-Hernandez C, Wang C-Y, Park Y, Kippelen B. Stable organic thin-film transistors. Sci Adv. 2018;4:eaao1705.

359. Reese C, Roberts M, Ling M, Bao Z. Organic thin film transistors. Mater Today. 2004;7:20–7.

360. Chandar Shekar B, Lee J, Rhee S-W. Organic thin film transistors: Materials, processes and devices. Korean J Chem Eng. 2004;21:267–85.

361. Wang N, Yang A, Fu Y, Li Y, Yan F. Functionalized Organic Thin Film Transistors for Biosensing. Acc Chem Res. American Chemical Society 2019;52:277–87.

362. Timko BP, Cohen-Karni T, Qing Q, Tian B, Lieber CM. Design and Implementation of Functional Nanoelectronic Interfaces With Biomolecules, Cells, and Tissue Using Nanowire Device Arrays. IEEE Trans Nanotechnol. 2010;9:269–80.

363. Huang Y, Sudibya HG, Fu D, Xue R, Dong X, Li L-J, et al. Label-free detection of ATP release from living astrocytes with high temporal resolution using carbon nanotube network. Biosens Bioelectron. 2009;24:2716–20.

364. Duan X, Li Y, Rajan NK, Routenberg DA, Modis Y, Reed MA. Quantification of the affinities and kinetics of protein interactions using silicon nanowire biosensors. Nat Nanotechnol. Nature Publishing Group 2012;7:401.

365. Sudibya HG, Ma J, Dong X, Ng S, Li L-J, Liu X-W, et al. Interfacing Glycosylated Carbon-Nanotube-Network Devices with Living Cells to Detect Dynamic Secretion of Biomolecules. Angew Chemie Int Ed. John Wiley & Sons, Ltd 2009;48:2723–6.

366. Vashist YK, Uzungolu G, Kutup A, Gebauer F, Koenig A, Deutsch L, et al. Heme oxygenase-1 germ line GTn promoter polymorphism is an independent prognosticator of tumor recurrence and survival in pancreatic cancer. J Surg Oncol. John Wiley & Sons, Ltd 2011;104:305–11.

367. Park H, Oh DS, Lee KJ, Jung DY, Lee S, Yoo S, et al. Flexible and Transparent Thin-Film Transistors Based on Two-Dimensional Materials for Active-Matrix Display. ACS Appl Mater Interfaces. 2020;12:4749–54.

368. Lee GH, Cui X, Kim YD, Arefe G, Zhang X, Lee CH, et al. Highly Stable, Dual-Gated MoS2 Transistors Encapsulated by Hexagonal Boron Nitride with Gate-Controllable Contact, Resistance, and Threshold Voltage. ACS Nano. American Chemical Society 2015;9:7019–26.

369. Lee GH, Yu YJ, Cui X, Petrone N, Lee CH, Choi MS, et al. Flexible and transparent MoS2 field-effect transistors on hexagonal boron nitride-graphene heterostructures. ACS Nano. American Chemical Society 2013;7:7931–6.

370. Jeong HM, Lee JW, Shin WH, Choi YJ, Shin HJ, Kang JK, et al. Nitrogen-Doped Graphene for High-Performance Ultracapacitors and the Importance of Nitrogen-Doped Sites at Basal Planes. Nano Lett. 2011;11:2472–7.

371. Atta NF, Galal A, El-Ads EH. Graphene — A Platform for Sensor and Biosensor Applications. In: Biosensors - Micro and Nanoscale Applications. InTech 2015. p. 13.

372. Peña-Bahamonde J, Nguyen HN, Fanourakis SK, Rodrigues DF. Recent advances in graphene-based biosensor technology with applications in life sciences. J Nanobiotechnology. BioMed Central 2018;16:1–17.

373. Krishnan SK, Singh E, Singh P, Meyyappan M, Nalwa HS. A review on graphene-based nanocomposites for electrochemical and fluorescent biosensors. RSC Adv. Royal Society of Chemistry 2019;9:8778–81.

374. López Marzo AM, Mayorga-Martinez CC, Pumera M. 3D-printed graphene direct electron transfer enzyme biosensors. Biosens Bioelectron. 2020;151:111980.

375. Lin Y-M, Valdes-Garcia A, Han S-J, Farmer DB, Meric I, Sun Y, et al. Wafer-Scale Graphene Integrated Circuit. Science (80-). American Association for the Advancement of Science 2011;332:1294–7.

376. Chhowalla M, Shin HS, Eda G, Li LJ, Loh KP, Zhang H. The chemistry of two-dimensional layered transition metal dichalcogenide nanosheets. Nat Chem. Nature Publishing Group 2013;5:263–75.

377. Chang HY, Yang S, Lee J, Tao L, Hwang WS, Jena D, et al. High-performance, highly bendable MoS2 transistors with high-K dielectrics for flexible low-power systems. ACS Nano. 2013;7:5446–52.

378. Mak KF, Lee C, Hone J, Shan J, Heinz TF. Atomically Thin MoS2: A New Direct-Gap Semiconductor. Phys Rev Lett. American Physical Society 2010;105:136805.

379. Radisavljevic B, Radenovic A, Brivio J, Giacometti V, Kis A. Single-layer MoS2 transistors. Nat Nanotechnol. Nature Publishing Group 2011;6:147–50.

380. Li SL, Tsukagoshi K, Orgiu E, Samorì P. Charge transport and mobility engineering in two-dimensional transition metal chalcogenide semiconductors. Chem Soc Rev. 2016;45:118–51.

381. Chhowalla M, Liu Z, Zhang H. Two-dimensional transition metal dichalcogenide (TMD) nanosheets. Chem Soc Rev. Royal Society of Chemistry 2015;44:2584–6.

382. Novoselov KS, Jiang D, Schedin F, Booth TJ, Khotkevich V V, Morozov S V, et al. Two-dimensional atomic crystals. Proc Natl Acad Sci U S A. 2005/07/18. National Academy of Sciences 2005;102:10451–3.

383. Ren X, Zhao Q, McCulloch WD, Wu Y. MoS2 as a long-life host material for potassium ion intercalation. Nano Res. 2017;10:1313–21.

384. Zou J, Li F, Bissett MA, Kim F, Hardwick LJ. Intercalation behaviour of Li and Na into 3-layer and multilayer MoS2 flakes. Electrochim Acta. 2020;331:135284.

385. Liu L, Wu J, Wu L, Ye M, Liu X, Wang Q, et al. Phase-selective synthesis of 1T′ MoS2 monolayers and heterophase bilayers. Nat Mater. 2018;17:1108–14.

386. Jin Q, Liu N, Chen B, Mei D. Mechanisms of Semiconducting 2H to Metallic 1T Phase Transition in Two-dimensional MoS 2 Nanosheets. J Phys Chem C. 2018;122:28215–24.

387. Mintz L. Molybdenum Disulphide (MoS2) Nanosheet Inks Evaluated for Printed Electronics and Application to Thin-Film Transistors. 2017.

388. Sarkar D, Liu W, Xie X, Anselmo AC, Mitragotri S, Banerjee K. MoS2 field-effect transistor for next-generation label-free biosensors. ACS Nano. 2014;8:3992–4003.

389. Lv R, Robinson JA, Schaak RE, Sun D, Sun Y, Mallouk TE, et al. Transition metal dichalcogenides and beyond: Synthesis, properties, and applications of single- and few-layer nanosheets. Acc Chem Res. 2015;48:56–64.

390. Yang H, Giri A, Moon S, Shin S, Myoung JM, Jeong U. Highly Scalable Synthesis of MoS2 Thin Films with Precise Thickness Control via Polymer-Assisted Deposition. Chem Mater. 2017;29:5772–6.

391. Nicolosi V, Chhowalla M, Kanatzidis MG, Strano MS, Coleman JN. Liquid Exfoliation of Layered Materials. Science (80-). American Association for the Advancement of Science 2013;340:1226419–1226419.

392. Zhang W, Zhang P, Su Z, Wei G. Synthesis and sensor applications of MoS2-based nanocomposites. Nanoscale. Royal Society of Chemistry 2015;7:18364–78.

393. Li H, Wu J, Yin Z, Zhang H. Preparation and Applications of Mechanically Exfoliated Single-Layer and Multilayer MoS2 and WSe2 Nanosheets. Acc Chem Res. American Chemical Society 2014;47:1067–75.

394. Wei Y, Tran V-T, Zhao C, Liu H, Kong J, Du H. Robust Photodetectable Paper from Chemically Exfoliated MoS2–MoO3 Multilayers. ACS Appl Mater Interfaces. American Chemical Society 2019;11:21445–53.

395. King LA, Zhao W, Chhowalla M, Riley DJ, Eda G. Photoelectrochemical properties of chemically exfoliated MoS2. J Mater Chem A. The Royal Society of Chemistry 2013;1:8935–41.

396. Samad L, Bladow SM, Ding Q, Zhuo J, Jacobberger RM, Arnold MS, et al. Layer-Controlled Chemical Vapor Deposition Growth of MoS2 Vertical Heterostructures via van der Waals Epitaxy. ACS Nano. American Chemical Society 2016;10:7039–46.

397. Liu K-KK, Zhang W, Lee Y-HH, Lin Y-CC, Chang M-TT, Su C-YY, et al. Growth of Large-Area and Highly Crystalline MoS2 Thin Layers on Insulating Substrates. Nano Lett. American Chemical Society 2012;12:1538–44.

398. Zeng Z, Yin Z, Huang X, Li H, He Q, Lu G, et al. Single-Layer Semiconducting Nanosheets: High-Yield Preparation and Device Fabrication. Angew Chemie Int Ed. 2011;50:11093–7.

399. Joensen P, Frindt RF, Morrison SR. Single-layer MoS2. Mater Res Bull. 1986;21:457–61.

400. Jiménez Sandoval S, Yang D, Frindt RF, Irwin JC. Raman study and lattice dynamics of single molecular layers of MoS2. Phys Rev B. 1991;44:3955–62.

401. Ramakrishna Matte HSS, Gomathi A, Manna AK, Late DJ, Datta R, Pati SK, et al. MoS2 and WS2 Analogues of Graphene. Angew Chemie Int Ed. 2010;49:4059–62.

402. Yu L, Lee YH, Ling X, Santos EJG, Shin YC, Lin Y, et al. Graphene/MoS2 Hybrid technology for large-scale two-dimensional electronics. Nano Lett. 2014;14:3055–63.

403. Lee YH, Zhang XQ, Zhang W, Chang MT, Lin C Te, Chang K Di, et al. Synthesis of large-area MoS 2 atomic layers with chemical vapor deposition. Adv Mater. John Wiley & Sons, Ltd 2012;24:2320–5.

404. Yu Y, Li C, Liu Y, Su L, Zhang Y, Cao L. Controlled scalable synthesis of uniform, high-quality monolayer and few-layer MoS2 films. Sci Rep. 2013;3:1–6.

405. Lin Y-C, Zhang W, Huang J-K, Liu K-K, Lee Y-H, Liang C-T, et al. Wafer-scale MoS2 thin layers prepared by MoO3 sulfurization. Nanoscale. 2012;4:6637.

406. Balendhran S, Ou JZ, Bhaskaran M, Sriram S, Ippolito S, Vasic Z, et al. Atomically

thin layers of MoS 2 via a two step thermal evaporation–exfoliation method. Nanoscale. 2012;4:461–6.

407. Ganatra R, Zhang Q. Few-layer MoS2: A promising layered semiconductor. ACS Nano. 2014;8:4074–99.

408. Choudhary N, Park J, Hwang JY, Choi W. Growth of Large-Scale and Thickness-Modulated MoS2 Nanosheets. ACS Appl Mater Interfaces. American Chemical Society 2014;6:21215–22.

409. Coleman JN, Lotya M, O'Neill A, Bergin SD, King PJ, Khan U, et al. Two-dimensional nanosheets produced by liquid exfoliation of layered materials. Science (80-). 2011;331:568–71.

410. Backes C, Szydłowska BM, Harvey A, Yuan S, Vega-Mayoral V, Davies BR, et al. Production of highly monolayer enriched dispersions of liquid-exfoliated nanosheets by liquid cascade centrifugation. ACS Nano. 2016;10:1589–601.

411. Zhang W, Wang Y, Zhang D, Yu S, Zhu W, Wang J, et al. A one-step approach to the large-scale synthesis of functionalized MoS2 nanosheets by ionic liquid assisted grinding. Nanoscale. Royal Society of Chemistry 2015;7:10210–7.

412. Zhou K, Jiang S, Bao C, Song L, Wang B, Tang G, et al. Preparation of poly(vinyl alcohol) nanocomposites with molybdenum disulfide (MoS2): structural characteristics and markedly enhanced properties. RSC Adv. The Royal Society of Chemistry 2012;2:11695–703.

413. Eksik O, Gao J, Shojaee SA, Thomas A, Chow P, Bartolucci SF, et al. Epoxy Nanocomposites with Two-Dimensional Transition Metal Dichalcogenide Additives. ACS Nano. American Chemical Society 2014;8:5282–9.

414. Wang S, Ang PK, Wang Z, Tang ALL, Thong JTL, Loh KP. High mobility, printable, and solution-processed graphene electronics. Nano Lett. 2010;10:92–8.

415. Bonaccorso F, Bartolotta A, Coleman JN, Backes C. 2D-Crystal-Based Functional Inks. Adv Mater. John Wiley & Sons, Ltd 2016;28:6136–66.

416. Smith RJ, King PJ, Lotya M, Wirtz C, Khan U, De S, et al. Large-Scale Exfoliation

of Inorganic Layered Compounds in Aqueous Surfactant Solutions. Adv Mater. 2011;23:3944–8.

417. Choucair M, Thordarson P, Stride JA. Gram-scale production of graphene based on solvothermal synthesis and sonication. Nat Nanotechnol. Nature Publishing Group 2008;4:30.

418. Wang QH, Kalantar-Zadeh K, Kis A, Coleman JN, Strano MS. Electronics and optoelectronics of two-dimensional transition metal dichalcogenides. Nat Nanotechnol. Nature Publishing Group, a division of Macmillan Publishers Limited. All Rights Reserved. 2012;7:699.

419. Wang T, Zhu H, Zhuo J, Zhu Z, Papakonstantinou P, Lubarsky G, et al. Biosensor based on ultrasmall MoS2 nanoparticles for electrochemical detection of H2O2 released by cells at the nanomolar level. Anal Chem. 2013;85:10289–95.

420. Lotya M, Hernandez Y, King PJ, Smith RJ, Nicolosi V, Karlsson LS, et al. Liquid Phase Production of Graphene by Exfoliation of Graphite in Surfactant/Water Solutions. J Am Chem Soc. 2009;131:3611–20.

421. Bertolazzi S, Brivio J, Kis A. Stretching and Breaking of Ultrathin MoS2. ACS Nano. American Chemical Society 2011;5:9703–9.

422. Cheng R, Jiang S, Chen Y, Liu Y, Weiss N, Cheng HC, et al. Few-layer molybdenum disulfide transistors and circuits for high-speed flexible electronics. Nat Commun. Nature Publishing Group 2014;5:1–9.

423. Yin Z, Li H, Li H, Jiang L, Shi Y, Sun Y, et al. Single-Layer MoS2 Phototransistors. ACS Nano. American Chemical Society 2012;6:74–80.

424. Kim S, Konar A, Hwang W-S, Lee JH, Lee J, Yang J, et al. High-mobility and low-power thin-film transistors based on multilayer MoS2 crystals. Nat Commun. Nature Publishing Group, a division of Macmillan Publishers Limited. All Rights Reserved. 2012;3:1011.

425. Late DJ, Huang Y-K, Liu B, Acharya J, Shirodkar SN, Luo J, et al. Sensing Behavior of Atomically Thin-Layered MoS2 Transistors. ACS Nano. American

Chemical Society 2013;7:4879–91.

426. Lee J, Dak P, Lee Y, Park H, Choi W, Alam MA, et al. Two-dimensional layered MoS2biosensors enable highly sensitive detection of biomolecules. Sci Rep. 2014;4:1–7.

427. Perkins FK, Friedman AL, Cobas E, Campbell PM, Jernigan GG, Jonker BT. Chemical vapor sensing with monolayer MoS2. Nano Lett. 2013;13:668–73.

428. Akinwande D, Huyghebaert C, Wang CH, Serna MI, Goossens S, Li LJ, et al. Graphene and two-dimensional materials for silicon technology. Nature. Springer US 2019;573:507–18.

429. Li T, Wan B, Du G, Zhang B, Zeng Z. Electrical performance of multilayer MoS2 transistors on high-κ Al2O3 coated Si substrates. AIP Adv. 2015;5:057102.

430. Shan J, Li J, Chu X, Xu M, Jin F, Wang XX, et al. High sensitivity glucose detection at extremely low concentrations using a MoS 2 -based field-effect transistor. RSC Adv. 2018;8:7942–8.

431. Park H, Han G, Lee SW, Lee H, Jeong SH, Naqi M, et al. Label-Free and Recalibrated Multilayer MoS 2 Biosensor for Point-of-Care Diagnostics. ACS Appl Mater Interfaces. 2017;9:43490–7.

432. Yoo G, Park H, Kim M, Song WG, Jeong S, Kim MH, et al. Real-time electrical detection of epidermal skin MoS2 biosensor for point-of-care diagnostics. Nano Res. 2017;10:767–75.

433. Gupta A, Arunachalam V, Vasudevan S. Liquid-Phase Exfoliation of MoS2 Nanosheets: The Critical Role of Trace Water. J Phys Chem Lett. 2016;7:4884–90.

434. Forsberg V. Liquid Exfoliation of Molybdenum Disulfide for Inkjet Printing. Mid Sweden University 2016.

435. Sharafeldin M, Jones A, Rusling JF. 3D-printed biosensor arrays for medical diagnostics. Micromachines. 2018;9:1–22.

436. Ahn BY, Walker SB, Slimmer SC, Russo A, Gupta A, Kranz S, et al. Planar and Three-Dimensional Printing of Conductive Inks. J Vis Exp. MyJove Corporation 2011;1–8.

437. Khan S, Lorenzelli L, Dahiya RS. Technologies for printing sensors and electronics over large flexible substrates: A review. IEEE Sens J. 2015;15:3164–85.

438. Pease RF, Chou SY. Lithography and Other Patterning Techniques for Future Electronics. Proc IEEE. 2008;96:248–70.

439. Dahiya RS, Mittendorfer P, Valle M, Cheng G, Lumelsky VJ. Directions Toward Effective Utilization of Tactile Skin: A Review. IEEE Sens J. 2013;13:4121–38.

440. Dahiya RS. Epidermal electronics – flexible electronics for biomedical applications. In: Iniewski K, Carrara S, editors. Handbook of Bioelectronics: Directly Interfacing Electronics and Biological Systems. Cambridge University Press 2015. p. 245–55.

441. Søndergaard RR, Hösel M, Krebs FC. Roll-to-Roll fabrication of large area functional organic materials. J Polym Sci Part B Polym Phys. John Wiley & Sons, Ltd 2013;51:16–34.

442. Subramanian V, Chang JB, Vornbrock A de la F, Huang DC, Jagannathan L, Liao F, et al. Printed electronics for low-cost electronic systems: Technology status and application development. In: ESSCIRC 2008 - 34th European Solid-State Circuits Conference. 2008. p. 17–24.

443. Leenen MAM, Arning V, Thiem H, Steiger J, Anselmann R. Printable electronics: flexibility for the future. Phys status solidi. John Wiley & Sons, Ltd 2009;206:588–97.

444. Moonen PF, Yakimets I, Huskens J. Fabrication of Transistors on Flexible Substrates: from Mass-Printing to High-Resolution Alternative Lithography Strategies. Adv Mater. John Wiley & Sons, Ltd 2012;24:5526–41.

445. Kelly AG, Hallam T, Backes C, Harvey A, Esmaeily AS, Godwin I, et al. All-

printed thin-film transistors from networks of liquid-exfoliated nanosheets. Science (80-). 2017;356:69–73.

446. Li J, Lemme MC, Östling M. Inkjet Printing of 2D Layered Materials. ChemPhysChem. 2014;15:3427–34.

447. Li J, Naiini MM, Vaziri S, Lemme MC, Östling M. Inkjet printing of MoS2. Adv Funct Mater. 2014;24:6524–31.

448. Nam H, Wi S, Rokni H, Chen M, Priessnitz G, Lu W, et al. MoS2 transistors fabricated via plasma-assisted nanoprinting of few-layer MoS2 flakes into large-area arrays. ACS Nano. 2013;7:5870–81.

449. Zhuo B, Chen S, Zhao M, Guo X. High Sensitivity Flexible Capacitive Pressure Sensor Using Polydimethylsiloxane Elastomer Dielectric Layer Micro-Structured by 3-D Printed Mold. IEEE J Electron Devices Soc. IEEE 2017;5:219–23.

450. Nag A, Feng S, Mukhopadhyay SC, Kosel J, Inglis D. 3D printed mould-based graphite/PDMS sensor for low-force applications. Sensors Actuators, A Phys. Elsevier B.V. 2018;280:525–34.

451. Kaidarova A, Alsharif N, Oliveira BNM, Marengo M, Geraldi NR, Duarte CM, et al. Laser-Printed, Flexible Graphene Pressure Sensors. Glob Challenges. 2020;4:2000001.

452. Didier C, Kundu A, Rajaraman S. Capabilities and limitations of 3D printed microserpentines and integrated 3D electrodes for stretchable and conformable biosensor applications. Microsystems Nanoeng. Springer US 2020;6:15.

453. Cao L, Han GC, Xiao H, Chen Z, Fang C. A novel 3D paper-based microfluidic electrochemical glucose biosensor based on rGO-TEPA/PB sensitive film. Anal Chim Acta. Elsevier Ltd 2020;1096:34–43.

454. Adams A, Malkoc A, La Belle JT. The Development of a Glucose Dehydrogenase 3D-Printed Glucose Sensor: A Proof-of-Concept Study. J Diabetes Sci Technol. 2018;12:176–82.

455. Li K, Wei H, Liu W, Meng H, Zhang P, Yan C. 3D printed stretchable capacitive

sensors for highly sensitive tactile and electrochemical sensing. Nanotechnology. IOP Publishing 2018;29:185501.

456. Wei H, Li K, Liu WG, Meng H, Zhang PX, Yan CY. 3D Printing of Free-Standing Stretchable Electrodes with Tunable Structure and Stretchability. Adv Eng Mater. 2017;19:1–6.

457. Kim K, Choi J, Jeong Y, Cho I, Kim M, Kim S, et al. Correction to: Highly Sensitive and Wearable Liquid Metal-Based Pressure Sensor for Health Monitoring Applications: Integration of a 3D-Printed Microbump Array with the Microchannel (Advanced Healthcare Materials, (2019), 8, 22, (1900978), 10.1002/adhm.20. Adv Healthc Mater. 2020;9:2000313.

458. Chang Y-H, Wang K, Wu C, Chen Y, Zhang C, Wang B. A facile method for integrating direct-write devices into three-dimensional printed parts. Smart Mater Struct. IOP Publishing 2015;24:065008.

459. Vatani M, Lu Y, Engeberg ED, Choi JW. Combined 3D printing technologies and material for fabrication of tactile sensors. Int J Precis Eng Manuf. 2015;16:1375–83.

460. Emon MOF, Alkadi F, Philip DG, Kim DH, Lee KC, Choi JW. Multi-material 3D printing of a soft pressure sensor. Addit Manuf. Elsevier B.V. 2019;28:629–38.

461. Sirringhaus H, Kawase T, Friend RH, Shimoda T, Inbasekaran M, Wu W, et al. High-resolution inkjet printing of all-polymer transistor circuits. Science (80-). American Assoc for the Advancement of Science 2000;290:2123–6.

462. Dankoco MD, Tesfay GY, Benevent E, Bendahan M. Temperature sensor realized by inkjet printing process on flexible substrate. Mater Sci Eng B Solid-State Mater Adv Technol. Elsevier Ltd 2016;205:1–5.

463. Briand D, Molina-Lopez F, Quintero AV, Mattana G, De Rooij NF. Printed sensors on smart RFID labels for logistics. In: 2012 IEEE 10th International New Circuits and Systems Conference, NEWCAS 2012. 2012. p. 449–52.

464. Subramanya SB, Neella N, Anantha AP, Nayak MM. Study and tailoring of

screen-printed resistive films for disposable strain gauges. Sensors Actuators, A Phys. Elsevier B.V. 2019;295:380–95.

465. Kwok SW, Goh KHH, Tan ZD, Tan STM, Tjiu WW, Soh JY, et al. Electrically conductive filament for 3D-printed circuits and sensors. Appl Mater Today. Elsevier Ltd 2017;9:167–75.

466. Gowers SAN, Curto VF, Seneci CA, Wang C, Anastasova S, Vadgama P, et al. 3D Printed Microfluidic Device with Integrated Biosensors for Online Analysis of Subcutaneous Human Microdialysate. Anal Chem. American Chemical Society 2015;87:7763–70.

467. Hampson SM, Rowe W, Christie SDR, Platt M. 3D printed microfluidic device with integrated optical sensing for particle analysis. Sensors Actuators B Chem. 2018;256:1030–7.

468. Ho CMB, Ng SH, Li KHH, Yoon Y-J. 3D printed microfluidics for biological applications. Lab Chip. 2015;15:3627–37.

469. Weisgrab G, Ovsianikov A, Costa PF. Functional 3D Printing for Microfluidic Chips. Adv Mater Technol. 2019;4:1900275.

470. Zips S, Wenzel OJ, Rinklin P, Grob L, Terkan K, Adly NY, et al. Direct Stereolithographic 3D Printing of Microfluidic Structures on Polymer Substrates for Printed Electronics. Adv Mater Technol. 2019;4:1800455.

471. Waheed S, Cabot JM, Macdonald NP, Lewis T, Guijt RM, Paull B, et al. 3D printed microfluidic devices: enablers and barriers. Lab Chip. 2016;16:1993–2013.

472. Bishop GW, Satterwhite-Warden JE, Bist I, Chen E, Rusling JF. Electrochemiluminescence at Bare and DNA-Coated Graphite Electrodes in 3D-Printed Fluidic Devices. ACS Sensors. American Chemical Society 2016;1:197–202.

473. Li F, MacDonald NP, Guijt RM, Breadmore MC. Multimaterial 3D Printed Fluidic Device for Measuring Pharmaceuticals in Biological Fluids. Anal Chem. 2019;91:1758–63.

474. Xu Y, Liu M, Kong N, Liu J. Lab-on-paper micro- and nano-analytical devices: Fabrication, modification, detection and emerging applications. Microchim Acta. 2016;183:1521–42.

475. Muth JT, Vogt DM, Truby RL, Mengüç Y, Kolesky DB, Wood RJ, et al. Embedded 3D printing of strain sensors within highly stretchable elastomers. Adv Mater. Wiley-VCH Verlag 2014;26:6307–12.

476. Kim JY, Ji S, Jung S, Ryu BH, Kim HS, Lee SS, et al. 3D printable composite dough for stretchable, ultrasensitive and body-patchable strain sensors. Nanoscale. Royal Society of Chemistry 2017;9:11035–46.

477. Dirkzwager RM, Liang S, Tanner JA. Development of Aptamer-Based Point-of-Care Diagnostic Devices for Malaria Using Three-Dimensional Printing Rapid Prototyping. ACS Sensors. American Chemical Society 2016;1:420–6.

478. Koschinsky T, Heinemann L. Sensors for glucose monitoring: Technical and clinical aspects. Diabetes Metab Res Rev. 2001;17:113–23.

479. Sokolov AN, Roberts ME, Bao Z. Fabrication of low-cost electronic biosensors. Mater Today. 2009;12:12–20.

480. Alam AU, Clyne D, Jin H, Hu N-X, Deen MJ. Fully Integrated, Simple, and Low-Cost Electrochemical Sensor Array for in Situ Water Quality Monitoring. ACS Sensors. 2020;5:412–22.

481. Myung N V., Jung S, Kim J. Application of Low-Cost, Easy-to-Use, Portable Biosensor Systems for Diagnosing Bladder Dysfunctions. Int Neurourol J. 2019;23:86–7.

482. Attoye B, Pou C, Blair E, Rinaldi C, Thomson F, Baker MJ, et al. Developing a Low-Cost, Simple-to-Use Electrochemical Sensor for the Detection of Circulating Tumour DNA in Human Fluids. Biosensors. 2020;10:156.

483. Schiemann L, Moritz K. Polymer foils used in construction. In: Textiles, Polymers and Composites for Buildings. Elsevier 2010. p. 189–226.

484. Li S. Fundamentals of Polymerization Reaction Engineering. In: Chemical

Reaction Engineering. Elsevier 2017. p. 541–98.

485. Selvamurugan Muthusamy M, Pramasivam S. Bioplastics – An Eco-friendly Alternative to Petrochemical Plastics. Curr World Environ. 2019;14:49–59.

486. Muhammad Shamsuddin I. Bioplastics as Better Alternative to Petroplastics and Their Role in National Sustainability: A Review. Adv Biosci Bioeng. 2017;5:63.

487. Folino A, Karageorgiou A, Calabrò PS, Komilis D. Biodegradation of wasted bioplastics in natural and industrial environments: A review. Sustain. 2020;12:1–37.

488. Luengo JM, García B, Sandoval A, Naharro G, Olivera ER. Bioplastics from microorganisms. Curr Opin Microbiol. 2003;6:251–60.

489. Krishnamurthy A, Amritkumar P. Synthesis and characterization of eco-friendly bioplastic from low-cost plant resources. SN Appl Sci. 2019;1:1432.

490. Song JH, Murphy RJ, Narayan R, Davies GBH. Biodegradable and compostable alternatives to conventional plastics. Philos Trans R Soc B Biol Sci. 2009;364:2127–39.

491. Narancic T, Cerrone F, Beagan N, O'Connor KE. Recent Advances in Bioplastics: Application and Biodegradation. Polymers (Basel). 2020;12:920.

492. Cinar SO, Chong ZK, Kucuker MA, Wieczorek N, Cengiz U, Kuchta K. Bioplastic production from microalgae: A review. Int J Environ Res Public Health. 2020;17:1–21.

493. Sidek IS, Draman SFS, Abdullah SRS, Anuar N. Current Development on Bioplastics and Its Future Prospects: an Introductory Review. INWASCON Technol Mag. 2019;1:03–8.

494. Bano K, Pandey R. New Advancements of Bioplastics in Medical Applications. Int J Pharm Sci Res. 2018;9:402.

495. Marin E, Boschetto F, Pezzotti G. Biomaterials and biocompatibility: An historical overview. J Biomed Mater Res - Part A. 2020;108:1617–33.

496. Pandey E, Srivastava K, Gupta S, Srivastava S, Mishra N. Some Biocompatible Materials Used in Medical Practices-a Review. Int J Pharm Sci Res IJPSR. 2016;7:2748–55.

497. Morão A, de Bie F. Life Cycle Impact Assessment of Polylactic Acid (PLA) Produced from Sugarcane in Thailand. J Polym Environ. Springer US 2019;27:2523–39.

498. García Ibarra V, Sendón R, Rodríguez-Bernaldo de Quirós A. Antimicrobial Food Packaging Based on Biodegradable Materials. In: Antimicrobial Food Packaging. Elsevier 2016. p. 363–84.

499. Singhvi MS, Zinjarde SS, Gokhale DV. Polylactic acid: synthesis and biomedical applications. J Appl Microbiol. 2019;127:1612–26.

500. N. M, J.H.Y. K, E. M, A.K. T. Poly (lactic-acid) Production from Monomer to Polymer : A Review. SciFed J Polym Sci. 2017;1:1–15.

501. Hong CH, Kim SH, Seo J-Y, Han DS. Development of Four Unit Processes for Biobased PLA Manufacturing. ISRN Polym Sci. 2012;2012:1–6.

502. Jamshidian M, Tehrany EA, Imran M, Jacquot M, Desobry S. Poly-Lactic Acid: Production, Applications, Nanocomposites, and Release Studies. Compr Rev Food Sci Food Saf. 2010;9:552–71.

503. Conn RE, Kolstad JJ, Borzelleca JF, Dixler DS, Filer LJ, Ladu BN, et al. Safety assessment of polylactide (PLA) for use as a food-contact polymer. Food Chem Toxicol. 1995;33:273–83.

504. Ciriminna R, Pagliaro M. Biodegradable and Compostable Plastics: A Critical Perspective on the Dawn of their Global Adoption. ChemistryOpen. 2020;9:8–13.

505. Lagarón J-M. Polylactic acid (PLA) nanocomposites for food packaging applications. In: Multifunctional and Nanoreinforced Polymers for Food Packaging. Elsevier 2011. p. 485–97.

506. Auras R, Harte B, Selke S. An Overview of Polylactides as Packaging Materials. Macromol Biosci. 2004;4:835–64.

507. Lunt J, Shafer AL. Polylactic Acid Polymers from Com. Applications in the Textiles Industry. J Ind Text. 2000;29:191–205.

508. Mohiti-Asli M, Pourdeyhimi B, Loboa EG. Skin Tissue Engineering for the Infected Wound Site: Biodegradable PLA Nanofibers and a Novel Approach for Silver Ion Release Evaluated in a 3D Coculture System of Keratinocytes and Staphylococcus aureus. Tissue Eng Part C Methods. 2014;20:790–7.

509. Liu S, Wu G, Zhang X, Yu J, Liu M, Zhang Y, et al. Preparation and properties of poly (lactic acid) (PLA) suture loaded with PLA microspheres enclosed drugs (PM-Ds). J Text Inst. 2019;110:1596–605.

510. Bakola V, Karagkiozaki V, Tsiapla AR, Pappa F, Moutsios I, Pavlidou E, et al. Dipyridamole-loaded biodegradable PLA nanoplatforms as coatings for cardiovascular stents. Nanotechnology. 2018;29:275101.

511. Rodrigues N, Benning M, Ferreira AM, Dixon L, Dalgarno K. Manufacture and Characterisation of Porous PLA Scaffolds. Procedia CIRP. 2016;49:33–8.

512. Kim YM, Lee JH. Clinical courses and degradation patterns of absorbable plates in facial bone fracture patients. Arch Craniofacial Surg. 2019;20:297–303.

513. Deng K, Chen H, Zhao Y, Zhou Y, Wang Y, Sun Y. Evaluation of adaptation of the polylactic acid pattern of maxillary complete dentures fabricated by fused deposition modelling technology: A pilot study. Mattoli V, editor. PLoS One. 2018;13:e0201777.

514. Buhecha MD, Lansley AB, Somavarapu S, Pannala AS. Development and characterization of PLA nanoparticles for pulmonary drug delivery: Co-encapsulation of theophylline and budesonide, a hydrophilic and lipophilic drug. J Drug Deliv Sci Technol. 2019;53:101128.

515. Fattahi FS, Khoddami A, Avinc O. Poly (Lactic Acid) Nano-fibers as Drug-delivery Systems: Opportunities and challenges. Nanomedicine Res J. 2019;4:130–40.

516. Singh NA, Mandal AKA, Khan ZA. Fabrication of PLA-PEG Nanoparticles as

Delivery Systems for Improved Stability and Controlled Release of Catechin. J Nanomater. 2017;2017:1–9.

517. Liu S, Yu J, Li H, Wang K, Wu G, Wang B, et al. Controllable Drug Release Behavior of Polylactic Acid (PLA) Surgical Suture Coating with Ciprofloxacin (CPFX)—Polycaprolactone (PCL)/Polyglycolide (PGA). Polymers (Basel). 2020;12:288.

518. Abd Alsaheb RA, Aladdin A, Othman NZ, Abd Malek R, Leng OM, Aziz R, et al. Recent applications of polylactic acid in pharmaceutical and medical industries. J Chem Pharm Res. 2015;7:51–63.

519. Emami F, Mostafavi Yazdi SJ, Na DH. Poly(lactic acid)/poly(lactic-co-glycolic acid) particulate carriers for pulmonary drug delivery. J Pharm Investig. 2019;49:427–42.

520. da Silva D, Kaduri M, Poley M, Adir O, Krinsky N, Shainsky-Roitman J, et al. Biocompatibility, biodegradation and excretion of polylactic acid (PLA) in medical implants and theranostic systems. Chem Eng J. 2018;340:9–14.

521. Rong X, Yuan W, Lu Y, Mo X. Safety evaluation of poly(lactic-co-glycolic acid)/poly(lactic-acid) microspheres through intravitreal injection in rabbits. Int J Nanomedicine. 2014;9:3057–68.

522. Bijarimi M, Ahmad S, Rasid R, Khushairi MA, Zakir M. Poly(lactic acid) / Poly(ethylene glycol) blends: Mechanical, thermal and morphological properties. In: AIP Conference Proceedings. 2016. p. 020002.

523. Chieng BW, Ibrahim NA, Yunus WMZW, Hussein MZ. Plasticized poly(lactic acid) with low molecular weight poly(ethylene glycol): Mechanical, thermal, and morphology properties. J Appl Polym Sci. 2013;130:4576–80.

524. Vieira MGA, Da Silva MA, Dos Santos LO, Beppu MM. Natural-based plasticizers and biopolymer films: A review. Eur Polym J. Elsevier Ltd 2011;47:254–63.

525. Sejidov FT, Mansoori Y, Goodarzi N. Esterification reaction using solid

heterogeneous acid catalysts under solvent-less condition. J Mol Catal A Chem. 2005;240:186–90.

526. Tauer K. Fundamental principles of polymeric materials, second edition. Stephen L. Rosen. A volume in the SPE monograph series. [Internet]. Vol. 44, Acta Polymerica. John Wiley & Sons, Ltd 1993. 210 p.

527. Białecka-Florjańczyk E, Florjańczyk Z. Solubility of Plasticizers, Polymers and Environmental Pollution. In: Thermodynamics, Solubility and Environmental Issues. Elsevier 2007. p. 397–408.

528. Ljungberg N, Wesslén B. Tributyl citrate oligomers as plasticizers for poly (lactic acid): Thermo-mechanical film properties and aging. Polymer (Guildf). 2003;44:7679–88.

529. Maru SM, de Matas M, Kelly A, Paradkar A. Characterization of thermal and rheological properties of zidovidine, lamivudine and plasticizer blends with ethyl cellulose to assess their suitability for hot melt extrusion. Eur J Pharm Sci. 2011;44:471–8.

530. Li L, Guan S, Yang L, Qin X, Feng W. Mechanical and Adhesive Properties of Poly(ethylene glycerol) Diacrylate Based Hydrogels Plasticized with PEG and Glycerol. Chem Res Chinese Univ. 2018;34:311–7.

531. Rowe RC, Sheskey PJ, Quinn ME. Polyethylene Glycol. In: Handbook of Pharmaceutical Excipients. 6th ed. Pharmaceutical Press 2009. p. 517–22.

532. Thompson MS, Vadala TP, Vadala ML, Lin Y, Riffle JS. Synthesis and applications of heterobifunctional poly(ethylene oxide) oligomers. Polymer (Guildf). 2008;49:345–73.

533. Zarrintaj P, Saeb MR, Jafari SH, Mozafari M. Application of compatibilized polymer blends in biomedical fields. In: Compatibilization of Polymer Blends. Elsevier 2020. p. 511–37.

534. Bolourchian N, Mahboobian MM, Dadashzadeh S. The effect of PEG molecular weights on dissolution behavior of simvastatin in solid dispersions. Iran J Pharm

Res. 2013;12:9–18.

535. Rotthäuser B, Kraus G, Schmidt PC. Optimization of an effervescent tablet formulation using a central composite design optimization of an effervescent tablet formulation containing spray dried l-leucine and polyethylene glycol 6000 as lubricants using a central composite design. Eur J Pharm Biopharm. 1998;46:85–94.

536. Hadi IA, Ugriné HE, Farouk AM, Shayoub M. Formulation of polyethylene glycol ointment bases suitable for tropical and subtropical climates. I. Acta Pharm Hung. 1989;59:137–42.

537. Akhtarl M, Akhtar N, Ahmad M, Arif S, Shah P. Drug release from PEG Suppository bases and from their combination with polymers. J Fac Pharm Istanbul. 2000;33:7–16.

538. Qussi B, Suess WG. The Influence of Different Plasticizers and Polymers on the Mechanical and Thermal Properties, Porosity and Drug Permeability of Free Shellac Films. Drug Dev Ind Pharm. 2006;32:403–12.

539. Sakr A. Effect of molecular weight of polyethylene glycol binders on acetaminophen tablets. Pharm Ind. 2001;63:974–84.

540. D'souza AA, Shegokar R. Polyethylene glycol (PEG): a versatile polymer for pharmaceutical applications. Expert Opin Drug Deliv. 2016;13:1257–75.

541. Ljungberg N, Wesslén B. Preparation and properties of plasticized poly(lactic acid) films. Biomacromolecules. 2005;6:1789–96.

542. Tusing TW, Elsea JR, Sauveur AB. The Chronic Dermal Toxicity of a Series of Polyethylene Glycols. J Am Pharm Assoc (Scientific ed). 1954;43:489–90.

543. Pillin I, Montrelay N, Grohens Y. Thermo-mechanical characterization of plasticized PLA: Is the miscibility the only significant factor? Polymer (Guildf). 2006;47:4676–82.

544. Chieng BW, Ibrahim NA, Yunus WMZW, Hussein MZ. Poly(lactic acid)/poly(ethylene glycol) polymer nanocomposites: Effects of graphene

nanoplatelets. Polymers (Basel). 2014;6:93–104.

545. Park B-S, Song JC, Park DH, Yoon K-B. PLA/chain-extended PEG blends with improved ductility. J Appl Polym Sci. 2012;123:2360–7.

546. Septevani AA, Bhakri S. Plasticization of poly(lactic acid) using different molecular weight of Poly(ethylene glycol). In: AIP Conference Proceedings. 2017. p. 020038.

547. Çelebi H, Kurt A. Thermal and mechanical properties of PLA/PEG blend and its nanocomposites. In: 16th European Conference on Composite Materials, ECCM 2014. 2014. p. 22–6.

548. International Chemical Safety Cards Database (ICSCs). POLYETHYLENE GLYCOL (200-600) [Internet]. International Labour Organization (ILO). 2021 Jan 6; https://www.ilo.org/dyn/icsc/showcard.display?p_lang=en&p_card_id=1517&p_version=2.

549. Armentano I, Fortunati E, Burgos N, Dominici F, Luzi F, Fiori S, et al. Processing and characterization of plasticized PLA/PHB blends for biodegradable multiphase systems. Express Polym Lett. 2015;9:583–96.

550. Giita Silverajah VS, Ibrahim NA, Zainuddin N, Wan Yunus WMZ, Hassan HA. Mechanical, thermal and morphological properties of poly(lactic acid)/epoxidized palm olein blend. Molecules. 2012;17:11729–47.

551. Li FJ, Zhang SD, Liang JZ, Wang JZ. Effect of polyethylene glycol on the crystallization and impact properties of polylactide-based blends. Polym Adv Technol. 2015;26:465–75.

552. Vialva T. KOLMAR KOREA AND SAMYOUNG MACHINERY DEVELOP 3D PRINTED SKIN CARE CREAM [Internet]. 3D Printing Industry. 2020 May 12; https://3dprintingindustry.com/news/kolmar-korea-and-samyoung-machinery-develop-3d-printed-skin-care-cream-150425/.

553. Lin K-W, Hu C-J, Yang W-W, Chou L-W, Wei S-H, Chen C-S, et al.

Biomechanical Evaluation and Strength Test of 3D-Printed Foot Orthoses. Appl Bionics Biomech. 2019;2019:1–8.

554. 3D Printing Market by Offering (Printer, Material, Software, Service), Process (Binder Jetting, Direct Energy Deposition, Material Extrusion, Material Jetting, Powder Bed Fusion), Application, Vertical, Technology, and Geography - Global Forecast to 2024 [Internet]. 2019 Apr 24; https://www.marketsandmarkets.com/Market-Reports/3d-printing-market-1276.html?gclid=EAIaIQobChMIjZTxxMfo4QIVw7ztCh0XXALzEAAYASAAEgIzXPD_BwE.

555. Joung Y-H. Development of Implantable Medical Devices: From an Engineering Perspective. Int Neurourol J. 2013;17:98.

556. McAlister C, Wood J. The potential of 3D printing to reduce the environmental impacts of production. ECEEE 2014 Ind Summer Study Proc. 2014;213–21.

557. Xu W, Wang X, Sandler N, Willför S, Xu C. Three-Dimensional Printing of Wood-Derived Biopolymers: A Review Focused on Biomedical Applications. ACS Sustain Chem Eng. 2018;6:5663–80.

558. Sungyeap Hong CL. An Overview of the Synthesis and Synthetic Mechanism of Poly (Lactic acid). Mod Chem Appl. 2014;02:1000144.

559. Obayemi JD, Jusu SM, Salifu AA, Ghahremani S, Tadesse M, Uzonwanne VO, et al. Degradable porous drug-loaded polymer scaffolds for localized cancer drug delivery and breast cell/tissue growth. Mater Sci Eng C. 2020;112:110794.

560. Ren Y, Shen M, Ding Y, Yuan M, Jiang L, Li H, et al. Study on preparation and controlled release in vitro of bergenin-amino polylactic acid polymer. Int J Biol Macromol. 2020;153:650–60.

561. Ge H, Lin P, Luo T, Yan Z, Xiao J, Miao S, et al. Fabrication of Ligusticum chuanxiong polylactic acid microspheres: A promising way to enhance the hepatoprotective effect on bioactive ingredients. Food Chem. 2020;317:126377.

562. Serra T, Mateos-Timoneda MA, Planell JA, Navarro M. 3D printed PLA-based

scaffolds: A versatile tool in regenerative medicine. Organogenesis. 2013;9:239–44.

563. Rowe RC, Sheskey PJ, Quinn ME. Poly(DL-Lactic Acid). In: Rowe RC, Sheskey PJ, Quinn ME, editors. Handbook of Pharmaceutical Excipients. 6th ed. Pharmaceutical Press 2009. p. 515–7.

564. Savioli Lopes M, Jardini AL, Maciel Filho R. Poly (lactic acid) production for tissue engineering applications. Procedia Eng. 2012;42:1402–13.

565. Lasprilla AJR, Martinez GAR, Lunelli BH, Jardini AL, Filho RM. Poly-lactic acid synthesis for application in biomedical devices - A review. Biotechnol Adv. Elsevier Inc. 2012;30:321–8.

566. Pivsa-Art W, Fujii K, Nomura K, Aso Y, Ohara H, Yamane H. The effect of poly(ethylene glycol) as plasticizer in blends of poly(lactic acid) and poly(butylene succinate). J Appl Polym Sci. 2015;133:43044.

567. Yuniarto K, Purwanto YA, Purwanto S, Welt BA, Purwadaria HK, Sunarti TC. Infrared and Raman studies on polylactide acid and polyethylene glycol-400 blend. In: AIP Conference Proceedings. 2016. p. 020101.

568. Perkin Elmer. Tg and Melting Point of a Series of Polyethylene Glycols Using the Material Pocket [Internet]. Perkin Elmer. 2020 Apr 28; http://www.perkinelmer.com/CMSResources/Images/44-74297APP_TgandMeltofPolyethylene.pdf p. 1–2.

569. Faucher JA, Koleske J V., Santee ER, Stratta JJ, Wilson CW. Glass transitions of ethylene oxide polymers. J Appl Phys. 1966;37:3962–4.

570. Catoni SEM, Trindade KN, Gomes CAT, Schneider ALS, Pezzin APT, Soldi V. Influence of poly(Ethylene Glycol) - (PEG) on the properties of influence of poly(3-Hydroxybutyrate-CO-3-Hydroxyvalerate) - PHBV. Polimeros. 2013;23:320–5.

571. Xu R, Xie J, Lei C. Influence of melt-draw ratio on the crystalline behaviour of a polylactic acid cast film with a chi structure. RSC Adv. Royal Society of Chemistry

2017;7:39914–21.

572. Claisse PA. Strength of materials. In: Civil Engineering Materials. Elsevier 2016. p. 9–22.

573. Chemical Book. Poly(ethylene glycol) [Internet]. ChemicalBook Inc. 2021 Jan 6; https://www.chemicalbook.com/ProductChemicalPropertiesCB6145866_EN.htm .

574. Maniruzzaman M, Douroumis D, S. J, J. M. Hot-Melt Extrusion (HME): From Process to Pharmaceutical Applications. In: Sezer AD, editor. Recent Advances in Novel Drug Carrier Systems. InTech 2012.

575. Simões MF, Pinto RMA, Simões S. Hot-melt extrusion in the pharmaceutical industry: toward filing a new drug application. Drug Discov Today. Elsevier Ltd 2019;24:1749–68.

576. Goyanes A, Kobayashi M, Martínez-Pacheco R, Gaisford S, Basit AW. Fused-filament 3D printing of drug products: Microstructure analysis and drug release characteristics of PVA-based caplets. Int J Pharm. Elsevier B.V. 2016;514:290–5.

577. Nurzyńska K, Booth J, Roberts CJ, McCabe J, Dryden I, Fischer PM. Long-Term Amorphous Drug Stability Predictions Using Easily Calculated, Predicted, and Measured Parameters. Mol Pharm. American Chemical Society 2015;12:3389–98.

578. Hotha KK, Roychowdhury S, Subramanian V. Drug-Excipient Interactions: Case Studies and Overview of Drug Degradation Pathways. Am J Anal Chem. 2016;07:107–40.

579. Khatri P, Desai D, Sandhu H, Thongsukmak A, Patel G, Vaghashiya J, et al. Melt Extruded Amorphous Solid Dispersions. In: Ghebre-Sellassie I, Martin CE, Zhang F, DiNunzio J, editors. Pharmaceutical Extrusion Technology. 2nd ed. CRC Press 2018. p. 267–310.

580. Gajda M, Nartowski KP, Pluta J, Karolewicz B. Tuning the cocrystal yield in matrix-assisted cocrystallisation via hot melt extrusion: A case of theophylline-nicotinamide cocrystal. Int J Pharm. Elsevier 2019;569:118579.

581. Thiele W. Twin-Screw Extrusion and Screw Design. In: Ghebre-Sellassie I, Martin CE, Zhang F, DiNunzio J, editors. Pharmaceutical Extrusion Technology. 2nd ed. CRC Press 2018. p. 71–94.

582. Chavan RB, Thipparaboina R, Yadav B, Shastri NR. Continuous manufacturing of co-crystals: challenges and prospects. Drug Deliv Transl Res. Drug Delivery and Translational Research 2018;8:1726–39.

583. Lang B, McGinity JW, Williams RO. Dissolution enhancement of itraconazole by hot-melt extrusion alone and the combination of hot-melt extrusion and rapid freezing-effect of formulation and processing variables. Mol Pharm. American Chemical Society 2014;11:186–96.

584. Martin C. Twin Screw Extruders as Continuous Mixers for Thermal Processing: a Technical and Historical Perspective. AAPS PharmSciTech. 2016;17:3–19.

585. Kallakunta VR, Sarabu S, Bandari S, Batra A, Bi V, Durig T, et al. Stable amorphous solid dispersions of fenofibrate using hot melt extrusion technology: Effect of formulation and process parameters for a low glass transition temperature drug. J Drug Deliv Sci Technol. Elsevier BV 2019;58:101395.

586. Monschke M, Kayser K, Wagner KG. Processing of Polyvinyl Acetate Phthalate in Hot-Melt Extrusion-Preparation of Amorphous Solid Dispersions. Pharmaceutics. MDPI 2020;12:337.

587. Zhang Y, Luo R, Chen Y, Ke X, Hu D, Han M. Application of carrier and plasticizer to improve the dissolution and bioavailability of poorly water-soluble baicalein by hot melt extrusion. AAPS PharmSciTech. Springer New York LLC 2014;15:560–8.

588. Zhao Y, Xie X, Zhao Y, Gao Y, Cai C, Zhang Q, et al. Effect of plasticizers on manufacturing ritonavir/copovidone solid dispersions via hot-melt extrusion: Preformulation, physicochemical characterization, and pharmacokinetics in rats. Eur J Pharm Sci. Elsevier B.V. 2019;127:60–70.

589. Yang J, Chen H, You J, Hwang JC. Miscibility and Crystallization of Poly (L-lactide)/ Poly (ethylene glycol) and Poly (L-lactide) / Poly (s-caprolactone)

Blends PLLA was purchased from Sigma Chemical Company. 1997;29:657–62.

590. National Center for Biotechnology Information. Dichloromethane, CID=6344 [Internet]. PubChem Database. 2020 Jul 1; https://pubchem.ncbi.nlm.nih.gov/compound/Dichloromethane.

591. Zhang J-F, Sun X. Poly(lactic acid)-based bioplastics. In: Biodegradable Polymers for Industrial Applications. Elsevier 2005. p. 251–88.

592. Tsuji H, Tezuka Y, Saha SK, Suzuki M, Itsuno S. Spherulite growth of l-lactide copolymers: Effects of tacticity and comonomers. Polymer (Guildf). 2005;46:4917–27.

593. Lizundia E, Petisco S, Sarasua JR. Phase-structure and mechanical properties of isothermally melt-and cold-crystallized poly (L-lactide). J Mech Behav Biomed Mater. Elsevier 2013;17:242–51.

594. Mohapatra AK, Mohanty S, Nayak SK. Effect of PEG on PLA/PEG blend and its nanocomposites: A study of thermo-mechanical and morphological characterization. Polym Compos. 2014;35:283–93.

595. Athanasoulia IG, Tarantili PA. Preparation and characterization of polyethylene glycol/poly(L-lactic acid) blends. Pure Appl Chem. 2017;89:141–52.

596. Schruben DL, Gonzalez P. Dispersity improvement in solvent casting particle/polymer composite. Polym Eng Sci. 2000;40:139–42.

597. Singh G, Bhunia H, Rajor A, Jana RN, Choudhary V. Mechanical properties and morphology of polylactide, linear low-density polyethylene, and their blends. J Appl Polym Sci. 2010;118:496–502.

598. Witowski JS, Pędziwiatr M, Piotr M, Budzyński A. Cost-effective, personalized, 3D-printed liver model for preoperative planning before laparoscopic liver hemihepatectomy for colorectal cancer metastases. Int J Comput Assist Radiol Surg. 2017;12:2047–54.

599. Osouli-Bostanabad K, Adibkia K. Made-on-demand, complex and personalized 3D-printed drug products. BioImpacts. 2018/03/10. Tabriz University of Medical

Sciences 2018;8:77–9.

600. Agrawal A, Gupta AK. 3D Printing Technology in Pharmaceuticals and Biomedical : A Review. J Drug Deliv Ther Open. 2019;9:1–4.

601. Hsiao WK, Lorber B, Reitsamer H, Khinast J. 3D printing of oral drugs: a new reality or hype? Expert Opin Drug Deliv. Taylor & Francis 2018;15:1–4.

602. Korte C, Quodbach J. Formulation development and process analysis of drug-loaded filaments manufactured via hot-melt extrusion for 3D-printing of medicines. Pharm Dev Technol. Informa Healthcare USA, Inc 2018;23:1–11.

603. kushwaha S. Application of Hot Melt Extrusion in Pharmaceutical 3D Printing. J Bioequiv Availab. 2018;10:54–7.

604. Tan DK, Maniruzzaman M, Nokhodchi A. Development and optimisation of novel polymeric compositions for sustained release theophylline caplets (PrintCap) via FDM 3D printing. Polymers (Basel). 2020;12:27.

605. Tan D, Maniruzzaman M, Nokhodchi A. Advanced Pharmaceutical Applications of Hot-Melt Extrusion Coupled with Fused Deposition Modelling (FDM) 3D Printing for Personalised Drug Delivery. Pharmaceutics. 2018;10:203.

606. Rowe RC, Sheskey PJ, Quinn ME. Hydroxypropyl Cellulose. In: Rowe RC, Sheskey PJ, Quinn ME, editors. Handbook of Pharmaceutical Excipients. 6th ed. Pharmaceutical Press 2009. p. 317–22.

607. Sarode A, Wang P, Cote C, Worthen DR. Low-Viscosity Hydroxypropylcellulose (HPC) Grades SL and SSL: Versatile Pharmaceutical Polymers for Dissolution Enhancement, Controlled Release, and Pharmaceutical Processing. AAPS PharmSciTech. 2012;14:151–9.

608. Thakral S, Thakral NK, Majumdar DK. Eudragit®: a technology evaluation. Expert Opin Drug Deliv. Taylor & Francis 2013;10:131–49.

609. Dave VS, Fahmy RM, Hoag SW. Investigation of the physical-mechanical properties of Eudragit® RS PO/RL PO and their mixtures with common pharmaceutical excipients. Drug Dev Ind Pharm. 2013;39:1113–25.

610. Kotiyan PN, Vavia PR. Eudragits: Role as crystallization inhibitors in drug-in-adhesive transdermal systems of estradiol. Eur J Pharm Biopharm. 2001;52:173–80.

611. Baird JA, Taylor LS. Evaluation of amorphous solid dispersion properties using thermal analysis techniques. Adv Drug Deliv Rev. Elsevier B.V. 2012;64:396–421.

612. Mathew E, Pitzanti G, Larrañeta E, Lamprou DA. Three-dimensional printing of pharmaceuticals and drug delivery devices. Pharmaceutics. 2020;12:1–9.

613. Alhijjaj M, Nasereddin J, Belton P, Qi S. Impact of Processing Parameters on the Quality of Pharmaceutical Solid Dosage Forms Produced by Fused Deposition Modeling (FDM). Pharmaceutics. 2019;11:633.

614. Pietrzak K, Isreb A, Alhnan MA. A flexible-dose dispenser for immediate and extended release 3D printed tablets. Eur J Pharm Biopharm. 2015;96:380–7.

615. Kadry H, Al-Hilal TA, Keshavarz A, Alam F, Xu C, Joy A, et al. Multi-purposable filaments of HPMC for 3D printing of medications with tailored drug release and timed-absorption. Int J Pharm. Elsevier 2018;544:285–96.

616. Nisso. Excipients Nisso HPC Hydroxypropyl Cellulose Technical Data Sheet [Internet]. 2019 Aug 7; http://www.nissoexcipients.com/PDF/TDS-01_version1-1.pdf p. 1–4.

617. Patra CN, Priya R, Swain S, Kumar Jena G, Panigrahi KC, Ghose D. Pharmaceutical significance of Eudragit: A review. Futur J Pharm Sci. Elsevier B.V. 2017;3:33–45.

618. Parikh T, Gupta SS, Meena A, Serajuddin ATM. Investigation of thermal and viscoelastic properties of polymers relevant to hot melt extrusion - III: Polymethacrylates and polymethacrylic acid based polymers. J Excipients Food Chem. 2014;5:56–64.

619. Reitman M, Jaekel DJ, Siskey R, Kurtz SM. Morphology and Crystalline Architecture of Polyaryletherketones. In: PEEK Biomaterials Handbook. Elsevier

2019. p. 53–66.

620. Yang Y, Wang H, Li H, Ou Z, Yang G. 3D printed tablets with internal scaffold structure using ethyl cellulose to achieve sustained ibuprofen release. Eur J Pharm Sci. Elsevier 2018;115:11–8.

621. Clarke JB, Hastie JW, Kihlborg LHE, Metselaar R, Thackeray MM. Definitions of terms relating to phase transitions of the solid state (IUPAC Recommendations 1994). In: Nič M, Jirát J, Košata B, Jenkins A, McNaught A, editors. Pure and Applied Chemistry. 2nd ed. IUPAC 1994. p. 577–94.

622. Siepmann J, Siepmann F. Mathematical modeling of drug dissolution. Int J Pharm. Elsevier B.V. 2013;453:12–24.

623. Dash S, Murthy PN, Nath L, Chowdhury P. Kinetic modeling on drug release from controlled drug delivery systems. Acta Pol Pharm - Drug Res. 2010;67:217–23.

624. Mathematical models of drug release. In: Strategies to Modify the Drug Release from Pharmaceutical Systems. Elsevier 2015. p. 63–86.

625. Siepmann J, Peppas NA. Higuchi equation: Derivation, applications, use and misuse. Int J Pharm. Elsevier B.V. 2011;418:6–12.

626. Korsmeyer RW, Gurny R, Doelker E, Buri P, Peppas NA. Mechanisms of solute release from porous hydrophilic polymers. Int J Pharm. 1983;15:25–35.

627. Ramteke KH, Dighe PA, Kharat AR, Patil SV. Mathematical Models of Drug Dissolution: A Review. Sch Acad J Pharm. 2017;3:388–96.

628. Bravo SA, Lamas MC, Salomon CJ. Swellable Matrices for the Controlled-Release of Diclofenac Sodium: Formulation and In Vitro Studies. Pharm Dev Technol. 2004;9:75–83.

629. Higuchi T. Mechanism of sustained-action medication. Theoretical analysis of rate of release of solid drugs dispersed in solid matrices. J Pharm Sci. 1963;52:1145–9.

630. Lapidus H, Lordi NG. Drug Release from Compressed Hydrophilic Matrices. J

Pharm Sci. 1968;57:1292–301.

631. Peppas NA, Narasimhan B. Mathematical models in drug delivery: How modeling has shaped the way we design new drug delivery systems. J Control Release. 2014;190:75–81.

632. Higuchi T. Rate of Release of Medicaments from Ointment Bases Containing Drugs in Suspension. J Pharm Sci. 1961;50:874–5.

633. Siepmann J, Göpferich A. Mathematical modeling of bioerodible, polymeric drug delivery systems. Adv Drug Deliv Rev. 2001;48:229–47.

634. Supramaniam J, Adnan R, Mohd Kaus NH, Bushra R. Magnetic nanocellulose alginate hydrogel beads as potential drug delivery system. Int J Biol Macromol. Elsevier B.V. 2018;118:640–8.

635. Homaee Borujeni S, Mirdamadian SZ, Varshosaz J, Taheri A. Three-dimensional (3D) printed tablets using ethyl cellulose and hydroxypropyl cellulose to achieve zero order sustained release profile. Cellulose. Springer Netherlands 2020;27:1573–89.

636. Permanadewi I, Kumoro AC, Wardhani DH, Aryanti N. Modelling of controlled drug release in gastrointestinal tract simulation. J Phys Conf Ser. 2019;1295.

637. Giri BR, Song ES, Kwon J, Lee JH, Park JB, Kim DW. Fabrication of intragastric floating, controlled release 3D printed theophylline tablets using hot-melt extrusion and fused deposition modeling. Pharmaceutics. 2020;12.

638. Jethara S, Patel MR, Patel AD. Sustained Release Drug Delivery Systems : A Patent Overview. Aperito J Drug Des Pharmacol. 2015;1:104.

639. Paes AHP, Bakker A, Soe-Agnie CJ. Impact of Dosage Frequency on Patient Compliance. Diabetes Care. 1997;20:1512–7.

640. Mandhar P, Joshi G. Development of Sustained Release Drug Delivery System: A Review. Asian Pacific J Heal Sci. 2015;2:179–85.

641. Modi S, Gaikwad P, Bankar V, Pawar S. Sustained release drug delivery system:

A review. Int J Pharm Res Dev. 2011;2.

642. Jitendra J, Marya BH, Patani M, Patel M. Formulation and evaluation of indomethacin bilayer sustained release tablets. Int J PharmTech Res. 2011;3:1132–8.

643. Senjoti FG, Mahmood S, Jaffri JM, Mandal UK. Design and In-vitro Evaluation of Sustained Release Floating Tablets of Metformin HCl Based on Effervescence and Swelling. Iran J Pharm Res IJPR. Shaheed Beheshti University of Medical Sciences 2016;15:53–70.

644. Rohini D, Sekar A, Mjn C. Preparation and in vitro evaluation of sustained release tablet formulations of metformin HCL. Asian J Pharm Clin Res. 2012;5:45–8.

645. S. H, P. S, Sai G. M. Formulation and Evaluation of Bilayered Tablets Containing Immediate Release Layer of Glimepiride Complexed with Mangifera indica Gum and Sustained Release Layer Containing Metformin HCL by Using HPMC as Release Retardant. Int J Pharm Clin Res. 2017;9.

646. Gangane P, Kadam M, Mahapatra D, Mahajan N, Mahajan U. Design and formulating gliclazide solid dispersion immediate release layer and metformin sustained release layer in bilayer tablet for the effective postprandial management of diabetes mellitus. Int J Pharm Sci Res. 2018;9:3743–56.

647. Wadher K, Umekar M, Kakde R. Study on sustained-release metformin hydrochloride from matrix tablet: Influence of hydrophilic polymers and in vitro evaluation. Int J Pharm Investig. 2011;1:157.

648. Vynckier AK, Voorspoels J, Remon JP, Vervaet C. Co-extrusion as a processing technique to manufacture a dual sustained release fixed-dose combination product. J Pharm Pharmacol. 2016;68:721–7.

649. Derosa G, D'Angelo A, Romano D, Maffioli P. Effects of metformin extended release compared to immediate release formula on glycemic control and glycemic variability in patients with type 2 diabetes. Drug Des Devel Ther. 2017;11:1481–8.

650. Ristic S, Collober-Maugeais C, Cressier F, Tang P, Pecher E. Nateglinide or gliclazide in combination with metformin for treatment of patients with type 2 diabetes mellitus inadequately controlled on maximum doses of metformin alone: 1-year trial results. Diabetes, Obes Metab. 2007;9:506–11.

651. Cho HY, Yoon H, Lim YC, Lee YB. Pharmacokinetics and bioequivalence evaluation of gliclazide/metformin combination tablet and equivalent doses of gliclazide and metformin in healthy Korean subjects. Int J Clin Pharmacol Ther. 2009;47:770–9.

652. Chipkin SR. How to select and combine oral agents for patients with type 2 diabetes mellitus. Am J Med. 2005;118:4–13.

653. Cahn A, Cefalu WT. Clinical Considerations for Use of Initial Combination Therapy in Type 2 Diabetes. Diabetes Care. 2016;39:S137–45.

654. Bailey T. Options for Combination Therapy in Type 2 Diabetes: Comparison of the ADA/EASD Position Statement and AACE/ACE Algorithm. Am J Med. 2013;126:S10–20.

655. Rojas LBA, Gomes MB. Metformin: an old but still the best treatment for type 2 diabetes. Diabetol Metab Syndr. 2013;5:6.

656. Timmins P, Donahue S, Meeker J, Marathe P. Steady-State Pharmacokinetics of a Novel Extended-Release Metformin Formulation. Clin Pharmacokinet. 2005;44:721–9.

657. Garber AJ, Duncan TG, Goodman AM, Mills DJ, Rohlf JL. Efficacy of Metformin in Type II Diabetes. Am J Med. 1997;103:491–7.

658. Chacra AR. Evolving Metformin Treatment Strategies in Type-2 Diabetes. Am J Ther. 2014;21:198–210.

659. Blonde L, Dailey GE, Jabbour SA, Reasner CA, Mills DJ. Gastrointestinal tolerability of extended-release metformin tablets compared to immediate-release metformin tablets: results of a retrospective cohort study. Curr Med Res Opin. 2004;20:565–72.

660. Jabbour S, Ziring B. Advantages of extended-release metformin in patients with type 2 diabetes mellitus. Postgrad Med. 2011;123:15–23.

661. Roy H, Nandi S, Parida K, Brahma C. Formulation and design of sustained release matrix tablets of metformin hydrochloride: Influence of hypromellose and polyacrylate polymers. Int J Appl Basic Med Res. 2013;3:55.

662. Nanjwade B, Mhase S, Manvi F. Formulation of Extended-Release Metformin Hydrochloride Matrix Tablets. Trop J Pharm Res. 2011;10:375–83.

663. Cheng Y, Qin H, Acevedo NC, Shi X. Development of methylcellulose-based sustained-release dosage by semisolid extrusion additive manufacturing in drug delivery system. J Biomed Mater Res Part B Appl Biomater. 2021;109:257–68.

664. Siyawamwaya M, du Toit LC, Kumar P, Choonara YE, Kondiah PPPD, Pillay V. 3D printed, controlled release, tritherapeutic tablet matrix for advanced anti-HIV-1 drug delivery. Eur J Pharm Biopharm. 2019;138:99–110.

665. Pandey M, Choudhury H, Fern JLC, Kee ATK, Kou J, Jing JLJ, et al. 3D printing for oral drug delivery: a new tool to customize drug delivery. Drug Deliv Transl Res. 2020;10:986–1001.

666. Jeong HM, Weon K-Y, Shin BS, Shin S. 3D-Printed Gastroretentive Sustained Release Drug Delivery System by Applying Design of Experiment Approach. Molecules. 2020;25:2330.

667. Xu X, Zhao J, Wang M, Wang L, Yang J. 3D Printed Polyvinyl Alcohol Tablets with Multiple Release Profiles. Sci Rep. 2019;9:12487.

668. Rowe RC, Sheskey PJ, Quinn ME. Aliphatic Polyester. In: Rowe RC, Sheskey PJ, Quinn ME, editors. Handbook of Pharmaceutical Excipients. Pharmaceutical Press 2009. p. 23–8.

669. Arakawa CK, DeForest CA. Polymer Design and Development. In: Biology and Engineering of Stem Cell Niches. Elsevier 2017. p. 295–314.

670. Endres H-J, Siebert-Raths A. Performance Profile of Biopolymers Compared to Conventional Plastics. In: Polymer Science: A Comprehensive Reference. Elsevier

2012. p. 317–53.

671. Guarino V, Gentile G, Sorrentino L, Ambrosio L. Polycaprolactone: Synthesis, Properties, and Applications. In: Encyclopedia of Polymer Science and Technology. 2017. p. 1–36.

672. Manoukian OS, Sardashti N, Stedman T, Gailiunas K, Ojha A, Penalosa A, et al. Biomaterials for Tissue Engineering and Regenerative Medicine. In: Encyclopedia of Biomedical Engineering. Elsevier 2019. p. 462–82.

673. Miller K, Hsu JE, Soslowsky LJ. Materials in Tendon and Ligament Repair. In: Comprehensive Biomaterials. Elsevier 2011. p. 257–79.

674. Koski JA, Ibarra C, Rodeo SA. Tissue-Engineered Ligament. Orthop Clin North Am. 2000;31:437–52.

675. Dwivedi R, Kumar S, Pandey R, Mahajan A, Nandana D, Katti DS, et al. Polycaprolactone as biomaterial for bone scaffolds: Review of literature. J Oral Biol Craniofacial Res. 2020;10:381–8.

676. Stewart SA, Domínguez-Robles J, McIlorum VJ, Gonzalez Z, Utomo E, Mancuso E, et al. Poly(caprolactone)-Based Coatings on 3D-Printed Biodegradable Implants: A Novel Strategy to Prolong Delivery of Hydrophilic Drugs. Mol Pharm. 2020;17:3487–500.

677. Woodruff MA, Hutmacher DW. The return of a forgotten polymer—Polycaprolactone in the 21st century. Prog Polym Sci. 2010;35:1217–56.

678. Tang X, Thankappan SK, Lee P, Fard SE, Harmon MD, Tran K, et al. Polymeric Biomaterials in Tissue Engineering and Regenerative Medicine. In: Natural and Synthetic Biomedical Polymers. Elsevier 2014. p. 351–71.

679. Teo L, Teoh SH, Seah LL. Biointegration of Osteomesh® Polycaprolactone Implants in the Rabbit Eyelid. Invest Ophthalmol Vis Sci. 2013;54:6380.

680. Low SW, Ng YJ, Yeo TT, Chou N. Use of Osteoplug polycaprolactone implants as novel burr-hole covers. Singapore Med J. 2009;50:777–80.

681. Kammerer M, Fabritius M, Carvalho C, Mülhaupt R, Feuerstein TJ, Trittler R. Valproate release from polycaprolactone implants prepared by 3D-bioplotting. Pharmazie. 2011;66:511–6.

682. Choi WY, Lee CM, Park HJ. Development of biodegradable hot-melt adhesive based on poly-ε-caprolactone and soy protein isolate for food packaging system. LWT - Food Sci Technol. 2006;39:591–7.

683. Vignali A, Iannace S, Falcone G, Utzeri R, Stagnaro P, Bertini F. Lightweight Poly(ε-Caprolactone) Composites with Surface Modified Hollow Glass Microspheres for Use in Rotational Molding: Thermal, Rheological and Mechanical Properties. Polymers (Basel). 2019;11:624.

684. Tous L, Ruseckaite RA, Ciannamea EM. Sustainable hot-melt adhesives based on soybean protein isolate and polycaprolactone. Ind Crops Prod. 2019;135:153–8.

685. Daniels AU, Chang MKO, Andriano KP, Heller J. Mechanical properties of biodegradable polymers and composites proposed for internal fixation of bone. J Appl Biomater. 1990;1:57–78.

686. Sinha VR, Bansal K, Kaushik R, Kumria R, Trehan A. Poly-ϵ-caprolactone microspheres and nanospheres: an overview. Int J Pharm. 2004;278:1–23.

687. Merkli A, Tabatabay C, Gurny R, Heller J. Biodegradable polymers for the controlled release of ocular drugs. Prog Polym Sci. 1998;23:563–80.

688. Guerra A, Cano P, Rabionet M, Puig T, Ciurana J. 3D-Printed PCL/PLA Composite Stents: Towards a New Solution to Cardiovascular Problems. Materials (Basel). 2018;11:1679.

689. Li C, Cheng L, Zhang Y, Guo S, Wu W. Effects of implant diameter, drug loading and end-capping on praziquantel release from PCL implants. Int J Pharm. 2010;386:23–9.

690. Cheng L, Guo S, Wu W. Characterization and in vitro release of praziquantel from poly(ε-caprolactone) implants. Int J Pharm. 2009;377:112–9.

691. Soni V, Pandey V, Asati S, Gour V, Tekade RK. Biodegradable Block Copolymers

and Their Applications for Drug Delivery. In: Basic Fundamentals of Drug Delivery. Elsevier 2019. p. 401–47.

692. Ahmed A, Sadaniantz A. Metabolic and electrolyte abnormalities during heat exhaustion. Postgrad Med J. 1996;72:505–6.

693. Cuddy MLS. The Effects of Drugs on Thermoregulation. AACN Clin Issues Adv Pract Acute Crit Care. 2004;15:238–53.

694. Kenny GP, Sigal RJ, McGinn R. Body temperature regulation in diabetes. Temperature. 2016;3:119–45.

695. McCallum L, Higgins D. Measuring body temperature. Nurs Times. 2012;108:20–2.

696. Romanovsky AA. Skin temperature: its role in thermoregulation. Acta Physiol. 2014;210:498–507.

697. Welle S, Campbell RG. Stimulation of thermogenesis by carbohydrate overfeeding. Evidence against sympathetic nervous system mediation. J Clin Invest. 1983;71:916–25.

698. Green JH, Macdonald IA. The influence of intravenous glucose on body temperature. Q J Exp Physiol. 1981;66:465–73.

699. KENNY GP, STAPLETON JM, YARDLEY JE, BOULAY P, SIGAL RJ. Older Adults with Type 2 Diabetes Store More Heat during Exercise. Med Sci Sport Exerc. 2013;45:1906–14.

700. Yap Hui Kit S, Mohd Kassim N. Non-Invasive Blood Glucose Measurement Using Temperature-based Approach. J Teknol. 2013;64:105–10.

701. Chanmugam A, Langemo D, Thomason K, Haan J, Altenburger EA, Tippett A, et al. Relative Temperature Maximum in Wound Infection and Inflammation as Compared with a Control Subject Using Long-Wave Infrared Thermography. Adv Skin Wound Care. 2017;30:406–14.

702. Fierheller M, Sibbald RG. A Clinical Investigation into the Relationship between

Increased Periwound Skin Temperature and Local Wound Infection in Patients with Chronic Leg Ulcers. Adv Skin Wound Care. 2010;23:369–79.

703. Pang Q, Lou D, Li S, Wang G, Qiao B, Dong S, et al. Smart Flexible Electronics-Integrated Wound Dressing for Real-Time Monitoring and On-Demand Treatment of Infected Wounds. Adv Sci. 2020;7:1902673.

704. Lavery LA, Petersen BJ, Linders DR, Bloom JD, Rothenberg GM, Armstrong DG. Unilateral remote temperature monitoring to predict future ulceration for the diabetic foot in remission. BMJ Open Diabetes Res Care. 2019;7:e000696.

705. Roth J, Horowitz M. Inflammation, fever, and body temperature under febrile conditions. Vol. 28, Journal of basic and clinical physiology and pharmacology. 2017. p. 519–20.

706. van Netten JJ, Prijs M, van Baal JG, Liu C, van der Heijden F, Bus SA. Diagnostic Values for Skin Temperature Assessment to Detect Diabetes-Related Foot Complications. Diabetes Technol Ther. 2014;16:714–21.

707. Lee J, Cho HR, Cha GD, Seo H, Lee S, Park C-K, et al. Flexible, sticky, and biodegradable wireless device for drug delivery to brain tumors. Nat Commun. 2019;10:5205.

708. Meetoo D, Wong L, Ochieng B. Smart tattoo: technology for monitoring blood glucose in the future. Br J Nurs. 2019;28:110–5.

709. Bahadur S, Kumar P. Medicated Tattoos: A Recent Drug Delivery Approach in Medical Science. Int J Pharm Sci Res. 2020;11:4174–9.

710. Variohm. Advantages of RTD sensors [Internet]. Variohm Eurosensor. 2021 Jan 8; https://www.variohm.com/news-media/technical-blog-archive/advantages-of-rtd-sensors.

711. Kinkeldei T, Zysset C, Cherenack K, Troester G. Development and evaluation of temperature sensors for textile integration. In: Proceedings of IEEE Sensors Conference. IEEE 2009. p. 1580–3.

712. Sathies T, Senthil P, Prakash C. Application of 3D printed PLA-carbon black

conductive polymer composite in solvent sensing. Mater Res Express. IOP Publishing 2019;6.

713. Foster CW, Down MP, Zhang Y, Ji X, Rowley-Neale SJ, Smith GC, et al. 3D Printed Graphene Based Energy Storage Devices. Sci Rep. 2017;7:1–11.

714. Bauer S, Bauer-Gogonea S, Graz I, Kaltenbrunner M, Keplinger C, Schwödiauer R. 25th anniversary article: A soft future: From robots and sensor skin to energy harvesters. Adv Mater. 2014;26:149–62.

715. Walsh FC. Electrolytic Conductivity and its Measurement. Trans IMF. 1992;70:45–9.

716. Dellinger JH. The temperature coefficient of resistance of copper. J Franklin Inst. 1910;170:213–6.

717. Jones LA, Berris M. The psychophysics of temperature perception and thermal-interface design. In: Proceedings 10th Symposium on Haptic Interfaces for Virtual Environment and Teleoperator Systems HAPTICS 2002. IEEE Comput. Soc 2002. p. 137–42.

718. Suo Z, Ma EY, Gleskova H, Wagner S. Mechanics of rollable and foldable film-on-foil electronics. Appl Phys Lett. 1999;74:1177–9.

719. Lugoda P, Costa JC, Oliveira C, Garcia-Garcia LA, Wickramasinghe SD, Pouryazdan A, et al. Flexible Temperature Sensor Integration into E-Textiles Using Different Industrial Yarn Fabrication Processes. Sensors. 2019;20:73.

720. Lugoda P, Costa JC, Garcia-Garcia LA, Pouryazdan A, Jocys Z, Spina F, et al. Strain Sensors: Coco Stretch: Strain Sensors Based on Natural Coconut Oil and Carbon Black Filled Elastomers. Adv Mater Technol. 2021;6:2170012.

721. Cantarella G, Costa J, Meister T, Ishida K, Carta C, Ellinger F, et al. Review of recent trends in flexible metal oxide thin-film transistors for analog applications. Flex Print Electron. 2020;5:033001.

722. Costa JC, Spina F, Lugoda P, Garcia-Garcia L, Roggen D, Münzenrieder N. Flexible Sensors—From Materials to Applications. Technologies. 2019;7:35.

723. Gonçalves C, da Silva AF, Gomes J, Simoes R. Wearable e-textile technologies: A review on sensors, actuators and control elements. Inventions. 2018;3:1–13.

724. Vaddiraju S, Burgess DJ, Tomazos I, Jain FC, Papadimitrakopoulos F. Technologies for Continuous Glucose Monitoring: Current Problems and Future Promises. J Diabetes Sci Technol. 2010;4:1540–62.

725. Lucisano JY, Routh TL, Lin JT, Gough DA. Glucose Monitoring in Individuals With Diabetes Using a Long-Term Implanted Sensor/Telemetry System and Model. IEEE Trans Biomed Eng. 2017;64:1982–93.

726. Ahmadi MM, Jullien GA. A Wireless-Implantable Microsystem for Continuous Blood Glucose Monitoring. IEEE Trans Biomed Circuits Syst. 2009;3:169–80.

727. Vashist S. Continuous Glucose Monitoring Systems: A Review. Diagnostics. 2013;3:385–412.

728. La Belle JT, Adams A, Lin CE, Engelschall E, Pratt B, Cook CB. Self-monitoring of tear glucose: The development of a tear based glucose sensor as an alternative to self-monitoring of blood glucose. Chem Commun. Royal Society of Chemistry 2016;52:9197–204.

729. Cengiz E, Tamborlane W V. A Tale of Two Compartments: Interstitial Versus Blood Glucose Monitoring. Diabetes Technol Ther. 2009;11:S-11-S-16.

730. Zhang W, Du Y, Wang ML. Noninvasive glucose monitoring using saliva nano-biosensor. Sens Bio-Sensing Res. 2015;4:23–9.

731. Chung M, Fortunato G, Radacsi N. Wearable flexible sweat sensors for healthcare monitoring: a review. J R Soc Interface. 2019;16:20190217.

732. Zhao J, Lin Y, Wu J, Nyein HYY, Bariya M, Tai L-C, et al. A Fully Integrated and Self-Powered Smartwatch for Continuous Sweat Glucose Monitoring. ACS Sensors. 2019;4:1925–33.

733. Lee H, Hong YJ, Baik S, Hyeon T, Kim DH. Enzyme-Based Glucose Sensor: From Invasive to Wearable Device. Adv Healthc Mater. 2018;7:1–14.

734. Strakosas X, Selberg J, Pansodtee P, Yonas N, Manapongpun P, Teodorescu M, et al. A non-enzymatic glucose sensor enabled by bioelectronic pH control. Sci Rep. Springer US 2019;9:1–7.

735. Nery EW, Kundys M, Jeleń PS, Jönsson-Niedziólka M. Electrochemical glucose sensing: Is there still room for improvement? Anal Chem. 2016;88:11271–82.

736. Hagvik J. Glucose Measurement: Time for a Gold Standard. J Diabetes Sci Technol. 2007;1:169–72.

737. Juska VB, Pemble ME. A critical review of electrochemical glucose sensing: Evolution of biosensor platforms based on advanced nanosystems. Sensors (Switzerland). 2020;20:1–28.

738. Hu S, Lu Q, Xu Y. Biosensors based on direct electron transfer of protein. In: Electrochemical Sensors, Biosensors and their Biomedical Applications. Elsevier 2008. p. 531–81.

739. Ferri S, Kojima K, Sode K. Review of Glucose Oxidases and Glucose Dehydrogenases: A Bird's Eye View of Glucose Sensing Enzymes. J Diabetes Sci Technol. 2011;5:1068–76.

740. Wong CM, Wong KH, Chen XD. Glucose oxidase: natural occurrence, function, properties and industrial applications. Appl Microbiol Biotechnol. 2008;78:927–38.

741. Amor-Gutiérrez O, Costa-Rama E, Fernández Abedul MT. Determination of glucose with an enzymatic paper-based sensor. In: Abedul MTF, editor. Laboratory Methods in Dynamic Electroanalysis. Elsevier 2020. p. 257–65.

742. Blanford CF. The birth of protein electrochemistry. Chem Commun. 2013;49:11130.

743. Yusan S, Rahman MM, Mohamad N, Arrif TM, Latif AZA, M. A. MA, et al. Development of an Amperometric Glucose Biosensor Based on the Immobilization of Glucose Oxidase on the Se-MCM-41 Mesoporous Composite. J Anal Methods Chem. 2018;2018:1–8.

744. Kang X, Mai Z, Zou X, Cai P, Mo J. A novel glucose biosensor based on immobilization of glucose oxidase in chitosan on a glassy carbon electrode modified with gold–platinum alloy nanoparticles/multiwall carbon nanotubes. Anal Biochem. 2007;369:71–9.

745. Min J, Lee T, Oh SM, Kim H, Choi JW. Electrochemical biomemory device consisting of recombinant protein molecules. Biotechnol Bioprocess Eng. 2010;15:30–9.

746. Rizwan M, Elma S, Lim SA, Ahmed MU. AuNPs/CNOs/SWCNTs/chitosan-nanocomposite modified electrochemical sensor for the label-free detection of carcinoembryonic antigen. Biosens Bioelectron. 2018;107:211–7.

747. Xu S, Zhang Y, Zhu Y, Wu J, Li K, Lin G, et al. Facile one-step fabrication of glucose oxidase loaded polymeric nanoparticles decorating MWCNTs for constructing glucose biosensing platform: Structure matters. Biosens Bioelectron. 2019;135:153–9.

748. Feng X, Cheng H, Pan Y, Zheng H. Development of glucose biosensors based on nanostructured graphene-conducting polyaniline composite. Biosens Bioelectron. 2015;70:411–7.

749. Baek SH, Roh J, Park CY, Kim MW, Shi R, Kailasa SK, et al. Cu-nanoflower decorated gold nanoparticles-graphene oxide nanofiber as electrochemical biosensor for glucose detection. Mater Sci Eng C. 2020;107:110273.

750. Yuan Y, Wang Y, Wang H, Hou S. Gold nanoparticles decorated on single layer graphene applied for electrochemical ultrasensitive glucose biosensor. J Electroanal Chem. 2019;855:113495.

751. Gu T, Zhang Y, Deng F, Zhang J, Hasebe Y. Direct electrochemistry of glucose oxidase and biosensing for glucose based on DNA/chitosan film. J Environ Sci. The Research Centre for Eco-Environmental Sciences, Chinese Academy of Sciences 2011;23:S66–9.

752. Liu S, Ju H. Reagentless glucose biosensor based on direct electron transfer of glucose oxidase immobilized on colloidal gold modified carbon paste electrode.

Biosens Bioelectron. 2003;19:177–83.

753. Rafiei-Sarmazdeh Z, Morteza Zahedi-Dizaji S, Kafi Kang A. Two-Dimensional Nanomaterials. In: Nanostructures. IntechOpen 2020.

754. Lv R, Terrones H, Elías AL, Perea-López N, Gutiérrez HR, Cruz-Silva E, et al. Two-dimensional transition metal dichalcogenides: Clusters, ribbons, sheets and more. Nano Today. 2015;10:559–92.

755. Wu S, Zeng Z, He Q, Wang Z, Wang SJ, Du Y, et al. Electrochemically Reduced Single-Layer MoS2 Nanosheets: Characterization, Properties, and Sensing Applications. Small. 2012;8:2264–70.

756. Ma K, Sinha A, Dang X, Zhao H. Electrochemical Preparation of Gold Nanoparticles-Polypyrrole Co-Decorated 2D MoS 2 Nanocomposite Sensor for Sensitive Detection of Glucose . J Electrochem Soc. 2019;166:B147–54.

757. Tsai ML, Su SH, Chang JK, Tsai DS, Chen CH, Wu CI, et al. Monolayer MoS2 heterojunction solar cells. ACS Nano. 2014;8:8317–22.

758. Lee SK, Chu D, Song DY, Pak SW, Kim EK. Electrical and photovoltaic properties of residue-free MoS 2 thin films by liquid exfoliation method. Nanotechnology. IOP Publishing 2017;28:195703.

759. Järvinen T, Lorite GS, Peräntie J, Toth G, Saarakkala S, Virtanen VK, et al. WS 2 and MoS 2 thin film gas sensors with high response to NH 3 in air at low temperature. Nanotechnology. 2019;30:405501.

760. Kumar R, Zheng W, Liu X, Zhang J, Kumar M. MoS 2 -Based Nanomaterials for Room-Temperature Gas Sensors. Adv Mater Technol. 2020;5:1901062.

761. Jung KH, Yun SJ, Lim JW, Kim G, Kim SH. Photo-Carrier-Guiding Behavior of Vertically Grown MoS 2 and MoSe 2 in Highly Efficient Low-Light Transparent Photovoltaic Devices on Large-Area Rough Substrates. ACS Appl Mater Interfaces. 2020;12:1368–77.

762. Wang X, Nan F, Zhao J, Yang T, Ge T, Jiao K. A label-free ultrasensitive electrochemical DNA sensor based on thin-layer MoS2 nanosheets with high

electrochemical activity. Biosens Bioelectron. 2015;64:386–91.

763. Su S, Sun H, Xu F, Yuwen L, Fan C, Wang L. Direct electrochemistry of glucose oxidase and a biosensor for glucose based on a glass carbon electrode modified with MoS2 nanosheets decorated with gold nanoparticles. Microchim Acta. 2014;181:1497–503.

764. Van Tuan D, Thuy Ngan DT, Thuy NT, Lan H, Nguyet NT, Van Thu V, et al. Effect of nanostructured MoS2 morphology on the glucose sensing of electrochemical biosensors. Curr Appl Phys. Elsevier B.V. 2020;20:1090–6.

765. Huang K-J, Liu Y-J, Liu Y-M, Wang L-L. Molybdenum disulfide nanoflower-chitosan-Au nanoparticles composites based electrochemical sensing platform for bisphenol A determination. J Hazard Mater. 2014;276:207–15.

766. Lin X, Ni Y, Kokot S. Electrochemical cholesterol sensor based on cholesterol oxidase and MoS2-AuNPs modified glassy carbon electrode. Sensors Actuators B Chem. 2016;233:100–6.

767. Sun H, Chao J, Zuo X, Su S, Liu X, Yuwen L, et al. Gold nanoparticle-decorated MoS2 nanosheets for simultaneous detection of ascorbic acid, dopamine and uric acid. RSC Adv. 2014;4:27625.

768. Wu J, Lu Y, Wu Z, Li S, Zhang Q, Chen Z, et al. Two-dimensional molybdenum disulfide (MoS2) with gold nanoparticles for biosensing of explosives by optical spectroscopy. Sensors Actuators B Chem. 2018;261:279–87.

769. Wang S, Chinnasamy T, Lifson MA, Inci F, Demirci U. Flexible Substrate-Based Devices for Point-of-Care Diagnostics. Trends Biotechnol. 2016;34:909–21.

770. Seshadri DR, Li RT, Voos JE, Rowbottom JR, Alfes CM, Zorman CA, et al. Wearable sensors for monitoring the physiological and biochemical profile of the athlete. npj Digit Med. Springer US 2019;2:72.

771. Kang H, Jung S, Jeong S, Kim G, Lee K. Polymer-metal hybrid transparent electrodes for flexible electronics. Nat Commun. 2015;6:6503.

772. Shafiee H, Asghar W, Inci F, Yuksekkaya M, Jahangir M, Zhang MH, et al. Paper

and flexible substrates as materials for biosensing platforms to detect multiple biotargets. Sci Rep. 2015;5:1–9.

773. Teymourian H, Barfidokht A, Wang J. Electrochemical glucose sensors in diabetes management: An updated review (2010-2020). Chem Soc Rev. Royal Society of Chemistry 2020;49:7671–709.

774. Gaur APS, Sahoo S, Ahmadi M, Dash SP, Guinel MJF, Katiyar RS. Surface energy engineering for tunable wettability through controlled synthesis of MoS2. Nano Lett. 2014;14:4314–21.

775. Parlak O, İncel A, Uzun L, Turner APF, Tiwari A. Structuring Au nanoparticles on two-dimensional MoS2 nanosheets for electrochemical glucose biosensors. Biosens Bioelectron. Elsevier 2017;89:545–50.

776. Tan HW, Tran T, Chua CK. A review of printed passive electronic components through fully additive manufacturing methods. Virtual Phys Prototyp. Taylor & Francis 2016;11:271–88.

777. Nicholson RS. Theory and Application of Cyclic Voltammetry for Measurement of Electrode Reaction Kinetics. Anal Chem. 1965;37:1351–5.

778. Huang L, Huang Y, Liang J, Wan X, Chen Y. Graphene-based conducting inks for direct inkjet printing of flexible conductive patterns and their applications in electric circuits and chemical sensors. Nano Res. 2011;4:675–84.

779. Dybowska-Sarapuk L, Kielbasinski K, Arazna A, Futera K, Skalski A, Janczak D, et al. Efficient inkjet printing of graphene-based elements: Influence of dispersing agent on ink viscosity. Nanomaterials. 2018;8:9–14.

780. Li J, Ye F, Vaziri S, Muhammed M, Lemme MC, Östling M. Efficient inkjet printing of graphene. Adv Mater. 2013;25:3985–92.

781. Saengchairat N, Tran T, Chua C-K. A review: additive manufacturing for active electronic components. Virtual Phys Prototyp. 2017;12:31–46.

782. Hossain RF, Deaguero IG, Boland T, Kaul AB. Biocompatible, large-format, inkjet printed heterostructure MoS2-graphene photodetectors on conformable

substrates. npj 2D Mater Appl. Springer US 2017;1:28.

783. He W, Huang Y, Wu J. Enzyme-Free Glucose Biosensors Based on MoS2 Nanocomposites. Nanoscale Res Lett. Nanoscale Research Letters 2020;15:60.

784. Raposo M, Ferreira Q. A Guide for Atomic Force Microscopy Analysis of Soft-Condensed Matter. In 2007.

785. De Oliveira RRL, Albuquerque DAC, Cruz TGS, Yamaji FM, Leite FL. Measurement of the Nanoscale Roughness by Atomic Force Microscopy: Basic Principles and Applications. In: Atomic Force Microscopy - Imaging, Measuring and Manipulating Surfaces at the Atomic Scale. InTech 2012.

786. Bhushan B. Surface Roughness Analysis and Measurement Techniques. In: Modern Tribology Handbook, Two Volume Set. 1st ed. CRC Press 2000. p. 72.

787. P.S. J, Sutrave DS. A Brief Study of Cyclic Voltammetry and Electrochemical Analysis. Int J ChemTech Res. 2018;11:77–88.

788. Elgrishi N, Rountree KJ, McCarthy BD, Rountree ES, Eisenhart TT, Dempsey JL. A Practical Beginner's Guide to Cyclic Voltammetry. J Chem Educ. 2018;95:197–206.

789. Bilal S. Cyclic Voltammetry. In: Encyclopedia of Applied Electrochemistry. Springer New York 2014. p. 285–9.

790. Vaddiraju S, Tomazos I, Burgess DJ, Jain FC, Papadimitrakopoulos F. Emerging synergy between nanotechnology and implantable biosensors: A review. Biosens Bioelectron. 2010;25:1553–65.

791. Rao AN, Avula MN, Grainger DW. 3.34 Biomaterials Challenges in Continuous Glucose Monitors In Vivo. In: Comprehensive Biomaterials II. Elsevier 2017. p. 755–70.

792. Vaze A, Hussain N, Tang C, Leech D, Rusling J. Biocatalytic anode for glucose oxidation utilizing carbon nanotubes for direct electron transfer with glucose oxidase. Electrochem commun. 2009;11:2004–7.

793. Liu Y, Nan X, Shi W, Liu X, He Z, Sun Y, et al. A glucose biosensor based on the immobilization of glucose oxidase and Au nanocomposites with polynorepinephrine. RSC Adv. 2019;9:16439–46.

794. Adeloju SB. AMPEROMETRY. In: Encyclopedia of Analytical Science. Elsevier 2005. p. 70–9.

795. Kulkarni T, Slaughter G. Application of Semipermeable Membranes in Glucose Biosensing. Membranes (Basel). 2016;6:55.

796. Rishpon J, Gottesfeld S, Campbell C, Davey J, Zawodzinski TA. Amperometric glucose sensors based on glucose oxidase immobilized in nafion. Electroanalysis. 1994;6:17–21.

797. Gao Q, Guo Y, Zhang W, Qi H, Zhang C. An amperometric glucose biosensor based on layer-by-layer GOx-SWCNT conjugate/redox polymer multilayer on a screen-printed carbon electrode. Sensors Actuators B Chem. 2011;153:219–25.

798. Economidou SN, Lamprou DA, Douroumis D. 3D printing applications for transdermal drug delivery. Int J Pharm. Elsevier 2018;544:415–24.

799. Moussi K, Bukhamsin A, Hidalgo T, Kosel J. Biocompatible 3D Printed Microneedles for Transdermal, Intradermal, and Percutaneous Applications. Adv Eng Mater. 2020;22:1901358.

800. Pere CPP, Economidou SN, Lall G, Ziraud C, Boateng JS, Alexander BD, et al. 3D printed microneedles for insulin skin delivery. Int J Pharm. Elsevier 2018;544:425–32.

801. Boetker J, Water JJ, Aho J, Arnfast L, Bohr A, Rantanen J. Modifying release characteristics from 3D printed drug-eluting products. Eur J Pharm Sci. Elsevier B.V. 2016;90:47–52.

802. Anderson K, Poulter B, Dudgeon J, Li S-E, Ma X. A Highly Sensitive Nonenzymatic Glucose Biosensor Based on the Regulatory Effect of Glucose on Electrochemical Behaviors of Colloidal Silver Nanoparticles on MoS2. Sensors. 2017;17:1807.

803. Huang J, Dong Z, Li Y, Li J, Tang W, Yang H, et al. MoS2 nanosheet functionalized with Cu nanoparticles and its application for glucose detection. Mater Res Bull. Elsevier Ltd 2013;48:4544–7.

804. Shirinfar B, Ahmed N. Diabetes Treatment: Selective Synthetic Receptor for Glucose. ChemistryOpen. 2019;8:84–6.

805. Li C, Chen X, Zhang F, He X, Fang G, Liu J, et al. Design of Cyclic Peptide Based Glucose Receptors and Their Application in Glucose Sensing. Anal Chem. 2017;89:10431–8.

806. Groß A, Hashimoto C, Sticht H, Eichler J. Synthetic Peptides as Protein Mimics. Front Bioeng Biotechnol. 2016;3:1–16.

807. Wasilewski T, Szulczyński B, Wojciechowski M, Kamysz W, Gębicki J. A Highly Selective Biosensor Based on Peptide Directly Derived from the HarmOBP7 Aldehyde Binding Site. Sensors. 2019;19:4284.

808. Liu Q, Wang J, Boyd BJ. Peptide-based biosensors. Talanta. 2015;136:114–27.

809. Barbosa AJM, Oliveira AR, Roque ACA. Protein- and Peptide-Based Biosensors in Artificial Olfaction. Trends Biotechnol. 2018;36:1244–58.

810. Wang H, Zhao P, Zeng X, Young CD, Hu W. High-stability pH sensing with a few-layer MoS 2 field-effect transistor . Nanotechnology. IOP Publishing 2019;30:375203.

811. Chen X, Park YJ, Kang M, Kang SK, Koo J, Shinde SM, et al. CVD-grown monolayer MoS 2 in bioabsorbable electronics and biosensors. Nat Commun. Springer US 2018;9:1–12.

812. Kim YH, Kim KY, Choi YR, Shim YS, Jeon JM, Lee JH, et al. Ultrasensitive reversible oxygen sensing by using liquid-exfoliated MoS2 nanoparticles. J Mater Chem A. Royal Society of Chemistry 2016;4:6070–6.

813. Yadav V, Roy S, Singh P, Khan Z, Jaiswal A. 2D MoS2-Based Nanomaterials for Therapeutic, Bioimaging, and Biosensing Applications. Small. 2019;15:1–33.

814. Khaled SA, Burley JC, Alexander MR, Yang J, Roberts CJ. 3D printing of tablets containing multiple drugs with defined release profiles. Int J Pharm. 2015;494:643–50.

815. Trenfield SJ, Tan HX, Goyanes A, Wilsdon D, Rowland M, Gaisford S, et al. Non-destructive dose verification of two drugs within 3D printed polyprintlets. Int J Pharm. 2020;577:119066.

816. Araújo M, Sa-Barreto L, Gratieri T, Gelfuso G, Cunha-Filho M. The Digital Pharmacies Era: How 3D Printing Technology Using Fused Deposition Modeling Can Become a Reality. Pharmaceutics. 2019;11:128.